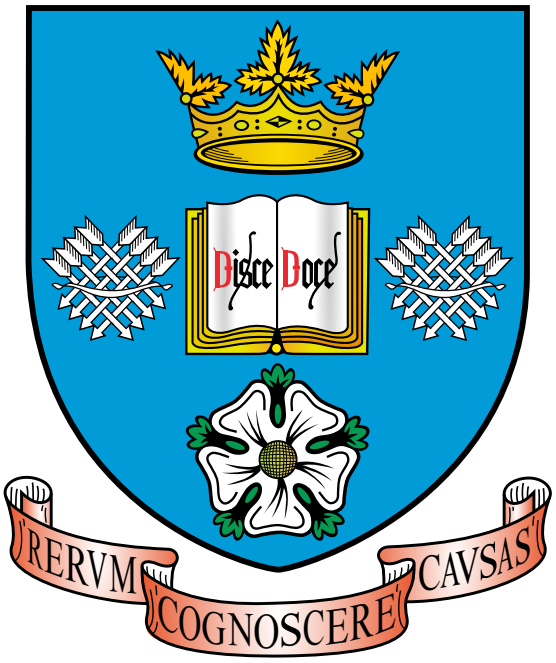

Identifying the residence time distributions of urban drainage structures from solute transport data using maximum entropy deconvolution

A thesis submitted to the University of Sheffield in partial fulfilment of the requirements for the degree of Doctor of Philosophy

Frederick C. Sonnenwald M.Eng. (Hons.)

Supervised by Virginia Stovin and Ian Guymer

Department of Civil and Structural Engineering,
The University of Sheffield

March 2014

Declaration

I declare that the work contained within this thesis has been composed by myself. No portion of the work has been submitted in support of an application for any other degree or qualification at this university, or any other institute of learning. The work is my own except where indicated; all quotations have been distinguished by quotations marks and all sources of information have been acknowledged.

Abstract

Solute transport, the processes of water carrying particles through flow, is affected by the bulk mixing that the flow experiences. Improved understanding of solute transport can therefore lead to improved understanding of bulk mixing processes. The Residence Time Distribution (RTD) is a non-parametric model that more fully describes solute transport than traditional models, and therefore can provide additional insight into the underlying mixing processes. As a predictive model, a downstream concentration profile can be expressed as the convolution of an upstream concentration profile with an RTD. Maximum entropy deconvolution is an optimisation method that can be used to reverse the convolution process and obtain an RTD from paired experimental upstream/downstream concentration profiles. This thesis focuses on the application of maximum entropy deconvolution to solute transport.

As maximum entropy deconvolution is a relatively new method as applied to solute transport data, it has been tested thoroughly. An initial investigation of the effects of outlet angle on short-circuiting (as a mixing process) in surcharged manholes was undertaken to guide further work on maximum entropy deconvolution. Maximum entropy deconvolution was found to make repeated comparisons between recorded and predicted data through a constraint function. A study evaluating 12 potential correlation measures was undertaken, finding 8 measures potentially suitable for inclusion in maximum entropy deconvolution as a constraint function. 3 correlation measures were found to be additionally suitable for independent model evaluation. Several other configuration settings to maximum entropy deconvolution (number and distribution of sample points, and number of iterations) were also found to impact on the deconvolved RTD. These were

examined with different types of input data (e.g. storage tank vs manhole) in order to determine a robust combination of settings for all data types.

Two novel extensions to maximum entropy deconvolution are proposed and examined. The first novel extension involves changing interpolation function and number of sample points to give a smoother RTD. The smoother shape is more realistic and allows for easier interpretation of the RTD. The use of alternative interpolation functions also reduces the impact of over-sampling. The second novel extension is the deconvolution of raw data, i.e. data without pre-processing, reducing potential sources for error and making deconvolution easier to apply. Synthetic raw data was examined to produce guidelines for raw data quality. When the quality limits are exceeded, some minimal pre-processing then becomes necessary.

A large data set, covering both benched and unbenched manholes with 0°, 30°, 60°, and 90° outlet angles at a range of surcharge depths and flow rates, has been re-analysed (as raw data) with deconvolution. The data was previously analysed with Advection Dispersion Equation and Aggregated Dead Zone models. 6 characteristic RTD shapes were observed, from which different flow fields have been inferred. Deconvolved RTDs are shown to provide new insight into mixing processes occurring.

Acknowledgements

A thesis is a big piece of work and there are some people I would like to thank for helping out and making it possible. Thank you to Virginia and Ian, for helping me wrap my head around things and move them away from "Fred-isms". Thanks as well to everyone in D105 for an excellent work environment, and to the Department at large for the same. The Department and University also get a tip of the hat for the fees-reductions that have made these three years doable.

I also spent a year in Germany. While that work does not form a part of my thesis, it was invaluable experience. Thank you to Ralf Walker, Tobias Emilsson, and everyone else at ZinCo GmbH. My time there will stick with me. The funding for my German year is thanks to the EU Marie Curie Industry-Academia Partnerships and Pathways (IAPP) Green Roof Systems Project.

Finally, a big thank you is in order for my parents. When you get down to it, in every sense, it wasn't possible without them.

Preface

The chapters of this thesis consist of standalone reports and papers that have been reformatted and combined. Published or presented papers that are included:

- Sonnenwald, F., Stovin, V., & Guymer, I. (2011). The influence of outlet angle on solute transport in surcharged manholes. In *12th International Conference on Urban Drainage*. Porte Alegre, Brazil.
- Sonnenwald, F., Stovin, V., & Guymer, I. (2013b). Correlation measures for solute transport model identification & evaluation. In P. Rowinski (Ed.), *Experimental and Computational Solutions of Hydraulic Problems*: Springer.
- Sonnenwald, F., Stovin, V., & Guymer, I. (2013a). Configuring maximum entropy deconvolution for the identification of residence time distributions in solute transport applications. *Journal of Hydrologic Engineering*. (Oct. 24, 2013).

Other work published or presented, but not included:

- Sonnenwald, F. (2011). Modelling green roof run-off from storm events. In *1st National Green Roof Student Conference*. Sheffield, UK.
- Vesuviano, G., Sonnenwald, F., & Stovin, V. (2013). A two-stage storage routing model for green roof runoff detention. *Water Science and Technology*, 68(4), 769–775.
- Sonnenwald, F., Stovin, V., Campbell, N., & D'Arcy, B. (2012). Performance evaluation of SUDSButt, a rainfall attenuation device for retrofit in

urban environments. In *9th International Conference on Urban Drainage Modelling*. Belgrade, Serbia. Poster + extended abstract only.

While the reports and papers have been edited to form a whole, some parts appear incomplete. These are questions that are answered in later chapters (and this is indicated). Literature relevant to each topic is placed within the appropriate chapter to form a coherent research story. I hope that this makes for an easily digested thesis. Please enjoy.

Contents

List of Figures

List of Tables

Nomenclature

ADE	Advection-Dispersion Equation
ADZ	Aggregated Dead Zone
APE	Average Percent Error
AT	Above-threshold
A	Sum of the CRTD from 0 to normalised time 1
a	IDW exponent
a	KEM range value
BLC	Burnham-Liard Criterion
BT	Below-threshold
C	Maximum entropy constraint function
C_0	KEM nugget value
C_1	KEM sill value
CFD	Computational Fluid Dynamics
CIS	Cells-in-series
CORR2	MATLAB's 2-D Correlation Coefficient
CRTD	Cumulative Residence Time Distribution
CSO	Combined Sewer Overflow
c	Raw correlation value
$c_{\max}$	Numerically highest correlation value

$c_{\min}$	Numerically lowest correlation value
c_{norm}	Normalised correlation value
c_{perfect}	Perfect correlation value
DC	Double cubic sample point distribution
DuL	Double log sample point distribution
DwL	Downstream log sample point distribution
D	Manhole diameter
D_p	Pipe diameter
d	Distance
ES	Equally spaced sample point distribution
E	The RTD
$\hat{E}$	An estimate of the RTD
$\hat{E}_0$	Initial estimate of the RTD
F	The CRTD
$\hat{F}$	An estimate of the CRTD
f	RTD or CRTD scaling factor
f_0	Initial estimate of the scaling factor
FFCBS	Furthest Fitting Cost Based Similarity
FFT	Fast Fourier Transform
GIE	Gaussian Influence Estimation
G	Energy dissipation
g	Acceleration due to gravity, 9.81 ms^{-2}
H	Shannon entropy function
IDW	Inverse Distance Weighting
ISE	Integral of Squared Error
KEM	Kriging Estimation Method
K	Energy loss coefficient

K_x	Longitudinal dispersion coeffecient
LAMA	Linear interpolation with Applied Moving Average
LFZ	Log from zero sample point distribution
L	End point of the CRTD
N	Number of points
n	Sample point
NIPs	Number of inflection points
PLIF	Planar Laser Induced Fluorescence
PMCC	Pearson's Product Moment Correlation Coefficient
$P(x)$	Probability distribution of x
Q	Volumetric flow rate
r	Base-line prediction of RTD in the absence of other data
R^2	Nash-Sutcliffe Efficiency Index
RMSD	Root Mean Square Deviation
R_t^2	Young's Coefficient of Determination
RTD	Residence Time Distribution
SB	Slope-based sample point distribution
SQP	Sequential Quadratic Programming
S	Cross-sectional averaged concentration
S	Entropy function for deconvolution
s	Surcharge depth above pipe soffit
s'	Surcharge thereshold depth
T	Residence time
T	Length of the input data
t	Time
t_{50}	Time taken for 50% of mass to pass through a system
t_n	Nominal retention time

t_{nz}	Normalised time
$\bar{t}$	Mean travel time
$u(t)$	Upstream concentration profile
V	Mixing volume
V	Volt
V_x	Mean longitudunal velocity
x	Distance
$\hat{y}(t)$	Predicted downstream concentration profile
$y(t)$	Downstream concentration profile
YIC	Young Information Criterion
α	ADZ model coeffecient
$\triangle h$	Head loss
$\triangle t$	Time-step
δ	ADZ time delay offset
$\mathcal{F}$	FFT
λ	Interpolation weighting factor
λ	Langrange multiplier
z_i	A known data point
z_j	Point to be interpolated
μ	Mean
ν	Kinematic viscosity
σ	Standard deviation
$\star$	Cross-correlation
τ	ADZ time delay
τ	Integration variable
χ^2	Chi-Squared Test
γ	Semi-variance

Chapter 1

Introduction

"Identifying the residence time distributions of urban drainage structures from solute transport data using maximum entropy deconvolution."

1.1 Context

Urban drainage structures are devices throughout the urban environment that collect and transport water. They are designed and constructed to ensure sanitary and safe living conditions as part of the built environment. When the toilet is flushed, water begins a long and complex journey through these structures and the drainage network they form. In combined sewer networks (like are used in the UK), rainfall also travels these structures. Example drainage structures include: manholes, green roofs, combined sewer overflows (CSOs), and stilling ponds.

As the built environment spreads, it is becoming increasingly important to fully understand and manage these structures for planning purposes. This is emphasised by climate change. It is generally expected that in some areas rainfall events will become more extreme and rain will fall at greater intensity, e.g. Mailhot *et al.* (2012); Rodda *et al.* (2010). As a result, hydraulic loading on existing infrastructure is likely to significantly increase. An improved understanding of how urban drainage structures function will be critical in this scenario.

Models of drainage networks are routinely used by water companies for planning purposes. They consist of two components: a hydraulic model that predicts flows; and a water quality model for predicting the fate of pollution loads. The latter is particularly important for the evaluation of CSOs. The continued occurrence of CSO spill events (Dirckx *et al.*, 2011) highlights the need to fully understand the solute transport and mixing processes that occur and affect water quality within combined sewer networks so that environmental impacts can be quantified (Lau *et al.*, 2002; Andrés-Doménech *et al.*, 2010). Better understanding can lead to improved models, risk assessments, and management decisions.

Solute transport is the process of water carrying particles through flow, and is affected by the bulk mixing processes that the flow experiences. For example, solute transport through a pipe is different from solute transport through a manhole due to the differences in flow between them. An improved understanding of solute transport can lead to an improved understanding of the bulk mixing processes and therefore flow.

The Residence Time Distribution (RTD) is a non-parametric model that can describe solute transport within a reach or structure, but relies on no assumptions about their operation. As it more fully describes solute transport than traditional models, the RTD can provide new insights into mixing processes. This in turn can improve network quality models.

An RTD can be extracted from recorded data using a process called deconvolution. This allows for laboratory and field solute transport experiments to be analysed to provide more information on the underlying mixing processes.

1.2 Thesis layout

This thesis focuses on the application of type of deconvolution called maximum entropy deconvolution to solute transport. Chapter 2 provides background literature on network modelling, solute transport, and deconvolution. It also states the aims and objectives. Chapter 3 is a initial investigation carried out with maximum entropy deconvolution to guide further work. Chapter 4 contains a review of correlation measures, used to identify the similarity between two time-series in the maximum entropy deconvolution process. Maximum entropy deconvolution

is explored in more detail and a sensitivity analysis of configuration parameters is carried out in Chapter 5. Two improvements to maximum entropy deconvolution are developed in Chapters 6 and 7, focussing on RTD smoothness and deconvolution of raw data respectively. Chapter 8 is an investigation of flow fields in surcharged benched and unbenched manholes with varying outlet angle using maximum entropy deconvolution. The thesis, conclusions, and further work are summarised in Chapter 9.

Chapter 2

Background

This chapter covers background literature on hydraulic, water quality, and solute transport modelling. Solute transport modelling in manholes is introduced specifically, leading to the introduction of Residence Time Distributions as a solute transport model and deconvolution as a means of obtaining a Residence Time Distribution from experimental data. The aims and objectives and introduced More detailed literature review is included in later chapters where relevant.

2.1 Hydraulic modelling

The most commonly used software package for drainage network modelling within the UK is InfoWorks CS (Innovyze, 2010). Other packages available include MIKE (DHI, 2012) and SWMM (U.S. EPA, 2010). Within these packages, a hydraulic model is solved and then calibrated. Calibration is an empirical process, but the underlying model is based on drainage structure hydraulics. The output from the solved and calibrated model is then input into a water quality model.

Principles such as conservation of mass, conservation of energy, and conservation of momentum (Chadwick *et al.*, 2004) underlie all hydraulics. They are applied through formulae like Bernoulli's equation, the Manning formula, and reservoir routing (Chow, 1959). Most structures in sewer networks are simple enough that this basic hydraulics theory can be easily applied and therefore they are easily

modelled, e.g. pipes. Additionally, computational power has made the application of numerically complex methods such as the Hardy-Cross method (Cross, 1936) for solving network flow problems practical.

When urban drainage structures have extremely complex geometries, simpler formulae and methods can no longer be applied as the application of basic hydraulics theory is highly dependent upon simplifying assumptions. These assumptions generally no longer hold true in complex geometry due to correspondingly complex 3-D flow fields. As a result it becomes necessary to create a more detailed model. To date these models are typically either scale physical models or Computational Fluid Dynamics (CFD) models. CFD models implement complex systems of equations, e.g. the Navier-Stokes equations (Chadwick *et al.*, 2004), to determine flow through a structure.

Physical models can be expensive and can require significant expenditures of both time and space to create. CFD models, while requiring less physical space are extremely numerically complex, requiring significant computational time. Both types of model require specialised knowledge. These limitations make including realistic models of more complex urban drainage structures into larger network models nearly impossible on anything other than a case by case basis. Empirical calibration (e.g. for energy losses) will on many occasions alleviate the need for a model.

2.2 Water quality modelling

Water quality modelling is a broad subject area that has many different facets, but in general describes the transport and reactions of substances (dissolved or solid) within water. This covers species transport, whose chemical properties may depend on pH, temperature, and other chemicals present. Substances or particles may or may not interact with the pipe walls in the form of particle build-up or bioflims. Larger particles may flocculate to form suspended solids, but also very small fine particles can be picked up and deposited again depending on flow velocity.

Accurate water quality modelling for urban drainage depends on the accuracy of the underlying hydraulic models as well as the accuracy of the quality models

themselves. The use of simplified hydraulic models, however, inherently results in simplified quality models. This affects their predictive ability, e.g. gauging the impact of a chemical spill, which is of great importance considering the increased awareness of impact on the environment.

2.2.1 Solute transport

Solute transport in an urban drainage context refers to the transportation of solutes in water, i.e. chemicals that can be diluted or dissolved. (Solute transport, however, may also refer to the transport of solutes in other fluids in other contexts.) Solutes in most cases follow the flow field of the water, and therefore as solute transport is generally concerned with understanding how solutes move, it is also by extension concerned with how water moves. Traditionally solute transport is analysed in a one-dimensional context, e.g. Fischer (1979); Rutherford (1994). In one-dimensional solute transport, experiments are typically performed by injecting fluorescent Rhodamine dye and measuring concentration levels with fluorometers. Alternatively, salt or radioactive tracers may be used. This results in a temporal concentration profile, a record of concentration level (e.g. ppm) over time.

Plug flow in pipes occurs when all the solute moves at the average velocity of the water, shown in Figure 2.1a. However, as plug flow does not take into account the velocity distribution across the pipe cross-section it is not a realistic representation in most cases. Figure 2.1b shows longitudinal differential advection, which takes into account the velocity distribution and therefore better represents solute transport processes in pipes. Particles closer to the centre of the pipe travel further with time as the velocity at the centre of the pipe is higher. However, this only occurs in pipes experiencing laminar flow (very low velocities). As velocity increases so does turbulent diffusion, which promotes mixing across the pipe diameter. However, longitudinal differential advection continues to occur, resulting in a combination of the two processes known as longitudinal dispersion. The effects of turbulent flow are shown in Figure 2.1c. Two simple models characterising the laminar and turbulent behaviour in pipes were developed by Taylor (1953) and Taylor (1954), respectively.

It can be inferred from Taylor's work that Fick's Law can be used to model lon-

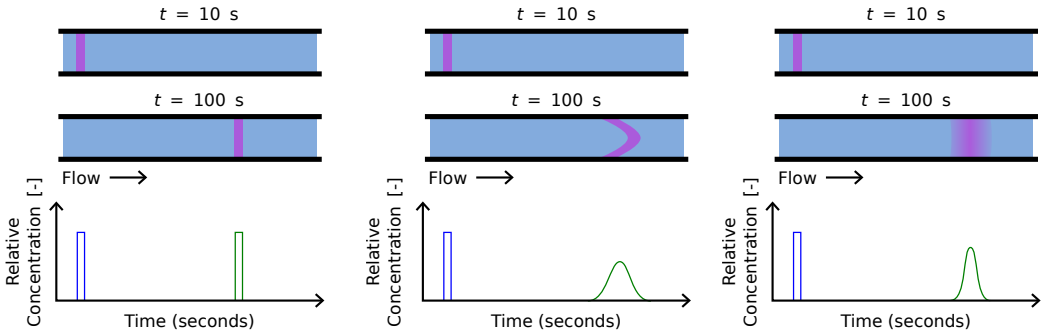

(a) Plug flow (b) Laminar flow (c) Turbulent flow

Figure 2.1: Solute transport in pipes

gitudinal solute transport assuming a constant velocity profile and cross-section, e.g. a pipe (Rutherford, 1994). This leads to the Advection-Dispersion Equation (ADE), shown in Equation 2.1 where S is cross-sectional averaged concentration, t is time, V_x is the mean longitudinal velocity, x is distance, and K_x is the longitudinal dispersion coefficient. The solution of this equation using the "frozen cloud method" is shown in Equation 2.2, where $y(t)$ is the downstream response to an upstream concentration profile $u(t)$, $\bar{t}$ is mean travel time and τ is an integration variable. The ADE model has been applied not only to pipes, but to rivers and other well-mixed structures.

$$\frac{\partial S}{\partial t} + V_x \frac{\partial S}{\partial x} = K_x \frac{\partial^2 S}{\partial x^2} \tag{2.1}$$

$$y(t) = \int_{-\infty}^{\infty} \frac{u(\tau) V_x}{\sqrt{4\pi K_x \bar{t}}} \exp\left[-\frac{V_x^2 (\bar{t} - t + \tau)^2}{4 K_x \bar{t}} \right] d\tau \tag{2.2}$$

Unfortunately, the ADE model is not suitable for systems that contain dead zones. Dead zones are areas of a system that occur outside of the main flow path, where flow velocity is extremely low in comparison to the main channel (Valentine & Wood, 1977). The majority of a solute cloud is carried with the flow past the dead zone while some solute enters the dead zone. Later, after the main bulk of solute has passed, solute will continue to be released from the dead zone, leading to a long tail in concentration profile. This is illustrated in Figure 2.2.

An alternative method for solute transport routing, the Aggregated Dead Zone

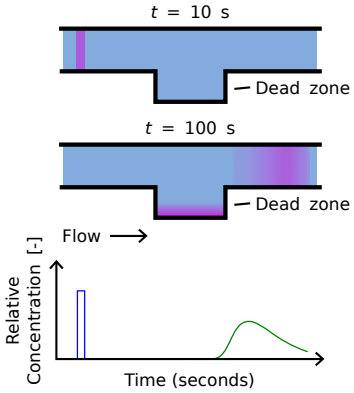

Figure 2.2: Dead-zone mixing

(ADZ) model, was developed as an extension to the simple Cells-in-series (CIS) model (Beer & Young, 1983; Wallis *et al.*, 1989; Rutherford, 1994). The CIS model assumes that solute passes through a sequence of instantaneously mixed reactors, each with an exponential decay and no delay. The ADZ model adds a delay term between each cell to allow for pure advection of the solute. It is convenient to think of the ADZ model of a channel as a series of hypothetical dead zones, where the solute transfers from one zone to the next.

The single-cell ADZ model can be expressed as the discrete time formula shown in Equation 2.3. n is the sample point at time t, $\alpha = -\exp(-\triangle t/T)$, $\triangle t$ is the sampling time-step, T is the residence time $\bar{t} - \tau$, δ is $\tau/\triangle t$ rounded down to the nearest integer, and τ is the time delay or difference in first arrival time. The ADZ model is useful when channels are less homogeneous, i.e. they have dead zones, and so no longer have the consistent mean velocity or cross-sectional area required to apply the ADE model.

$$y(n) = -\alpha y(n-1) + (1+\alpha)u(n-\delta) \tag{2.3}$$

2.3 Solute transport in surcharged manholes

One hydraulic structure of particular interest is the manhole (Figure 2.3). Manholes are introduced to a sewer network at regular intervals to provide access and are present at every change in level and/or direction. After heavy rainfalls, manholes in combined sewer systems (common in the UK) become surcharged,

temporarily storing water. In this condition, flow through the manhole experiences complex mixing processes which affect its solute transport characteristics. These processes are not yet well understood and therefore may be represented unrealistically in water quality models.

Previous research investigating solute transport in surcharged manholes began with ADE and ADZ model parameter analysis (Guymer & O'Brien, 2000). Subsequent research examined the effects of manhole outlet angle and benching (Saiyudthong, 2003). More recent research has included the effects of manhole diameter (Guymer *et al.*, 2005; Lau *et al.*, 2008; Stovin *et al.*, 2013). Figure 2.4 shows experimental upstream and downstream concentration profiles from a manhole with three downstream predictions: one an optimised ADE model; the second an optimised ADZ model; and the last an RTD based prediction (introduced in Section 2.4). This figure shows how ADE model predictions typically result in poor fits. ADZ model predictions can be somewhat better, but that neither model has high overall predictive capability. ADE and ADZ model performance degrades when the underlying assumptions are not met (Davis *et al.*, 2000; Rieckermann *et al.*, 2005).

The manhole diameter analyses have revealed a "hydraulic threshold" (e.g. Guymer *et al.*, 2005). Depending on surcharge depth, there was a significant change in dispersion coefficient, indicating that there was a change in the solute transport characteristics. Guymer *et al.* (2005) theorised that there were two flow regimes, dependent on surcharge depth, resulting in different solute transport characteristics. The two regimes are referred to as the below-threshold condition (Figure 2.5a) and the above-threshold condition (Figure 2.5b). The threshold is the surcharge depth at which the change in flow regime occurs, which Stovin *et al.* (2010a) suggested to occur at $s' = 0.258D$, where s' is threshold surcharge depth and D

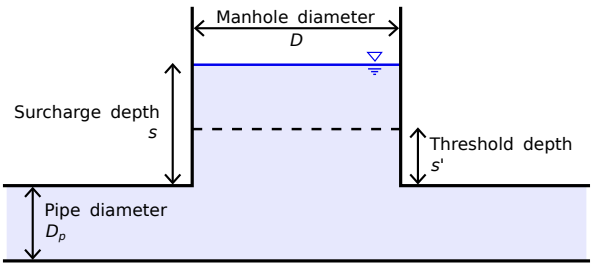

Figure 2.3: Manhole schematic

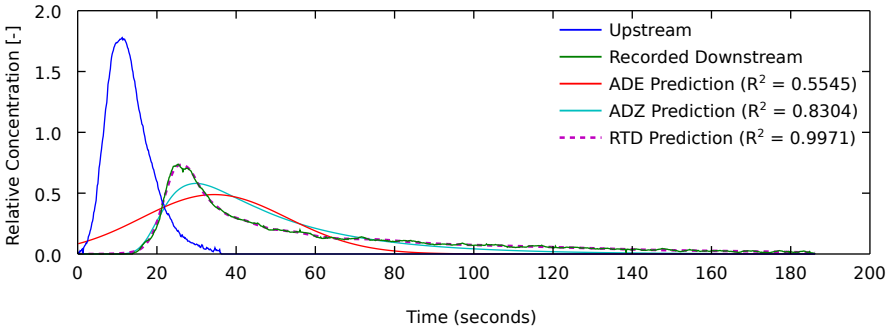

Figure 2.4: Comparison of ADE, ADZ, and RTD model fits for an 800 mm manhole with 1 l/s flow and 31 mm surcharge depth (data from Guymer & Stovin, 2011)

is manhole diameter.

Below-threshold flow is characterised by thorough mixing, while in the above-threshold condition the bulk of the solute passes directly through the manhole without mixing in the surcharge volume. Guymer *et al.* (2005) linked this to jet theory (Albertson *et al.*, 1950), where the jet core creates a "short-circuiting" and dead zone combined flow field. The yellow areas in Figure 2.5 shows this jet effect. In Figure 2.5b, the lighter area above the jet is the manhole's dead zone.

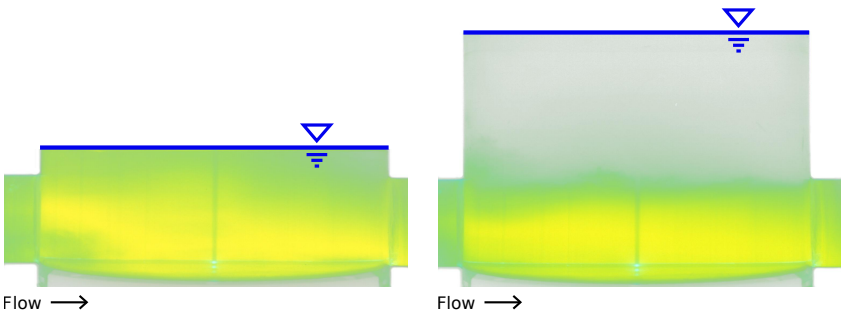

(a) Below-threshold (b) Above-threshold

Figure 2.5: Mixing regimes in a surcharged manhole, shown through (PLIF) images, after Guymer *et al.* (2005)

2.4 The Residence Time Distribution

Due to the poor fit of the traditional ADE and ADZ models in many cases, a new approach to modelling solute transport centred around the Residence Time Distribution (RTD) was developed (Stovin *et al.*, 2010a). An RTD is a non-parametric model that can describe the mixing (hydrodynamic) processes taking place in a river reach or urban drainage structure. Figure 2.4 shows how the RTD based prediction clearly provides a better fit than either an ADE or a single-cell ADZ model can for that data.

"Residence time" in general refers to the amount of time a volume of solute may reside within a structure before continuing. In Figures 2.2 and 2.5b, water swirls around within the dead zone, and then continues onwards. Considering multiple single particles passing through a dead zone, each particle may have a separate path and therefore residence time. The RTD describes the range of times a particle may take and is in effect a probability distribution of residence times.

The RTD is commonly used in Chemical Engineering as the E curve, where it describes mixing in chemical reactors in response to a Dirac pulse (instantaneous input) (Levenspiel, 1972; Denbigh & Turner, 1984). The RTD may also be referred to as an exit distribution, age function, or transfer function. It is considered analogous to the instantaneous unit hydrograph (Sherman, 1932).

Using the RTD as a predictive model, the relationship between the upstream and downstream concentration profiles is defined by the convolution integral, shown in Equation 2.4. A simplified convolution process is shown in Figure 2.6. Each point of the upstream profile is multiplied by the RTD, creating a scaled RTD. This scaled RTD is then placed in the downstream profile so that it starts at upstream profile point and continues to the end of the scaled RTD. For example, Point 1 in upstream profile ($t = 1$) becomes the green curve in the downstream profile, starting at $t = 1$ and continuing until $t = 5$. This process is repeated for Point 2, etc., of the upstream profile. The convolved profile is the summation of all the scaled RTDs. The principle of convolution, or super-positioning, is also used in ADE model routing (Equation 2.2).

$$y(t) = \int_{-\infty}^{\infty} E(\tau)u(t-\tau)d\tau \tag{2.4}$$

Figure 2.7a shows what could be a typical upstream/downstream concentration profile pair. The solute disperses and spreads out as it travels downstream. Going backwards in time, i.e. upstream, leads towards a reverse of this and the concentration profile increases in peakiness (Figure 2.7b). Eventually the peakiness reaches infinity, i.e. an instantaneous pulse. If the downstream profile is shifted backwards in time simultaneously with the upstream profile, when the upstream profile is instantaneous, the downstream profile is the RTD.

Figure 2.8 shows an arbitrary example RTD. It displays the primary characteristics of the RTD. By definition, the sum of the RTD is 1, i.e. $\int_0^{\infty} E(\tau)d\tau = 1$, when the solute transport routing is a mass conservation (non-reactive) system. The shaded area represents the fraction of particles input that have not yet exited at time t and hence are older than t. This RTD in general indicates that the concentration of particles to pass through a system increases slowly, peaks, then decreases slowly, similar to the Gaussian profile that describes Fickian processes.

The primary benefit of the RTD is that, as it is a non-parametric model, it makes no assumptions about how a system operates. It can therefore describe any arbitrary mixing regime. An additional feature of the RTD is that it can be normalised along the x-axis by Equation 2.5, where t_{nz} is normalised time, Q is the volumetric flow rate, and V is the mixing volume (volume of water between the upstream and downstream boundaries of the system under study, e.g. between fluorometers) (Danckwerts, 1953). By taking into account different flow rates and volumes (e.g. surcharge depths in manholes), different physical scales and experimental configurations can be compared directly.

$$t_{nz} = tQV^{-1} \tag{2.5}$$

Stovin *et al.* (2010a) illustrate the difference between the below-threshold and above-threshold mixing regimes by calculating RTDs from CFD models. This comparison between different manholes was made, in part, through the use of the Cumulative Residence Time Distribution (CRTD). The CRTD is a sum over time of the RTD. The y-axis of a CRTD plot shows the relative amount of solute

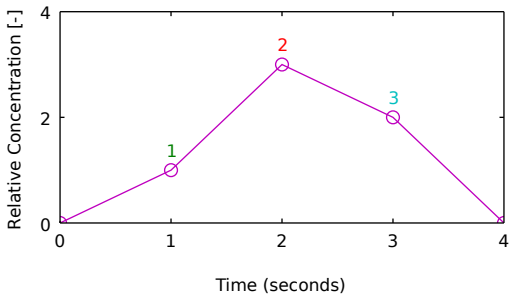

(a) Upstream concentration profile

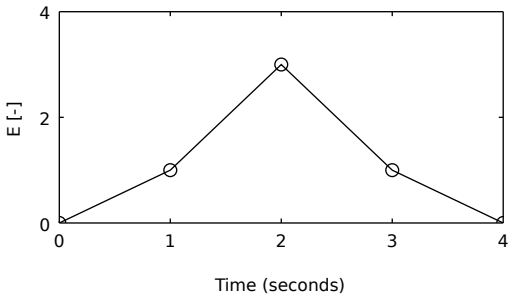

(b) The Residence Time Distribution

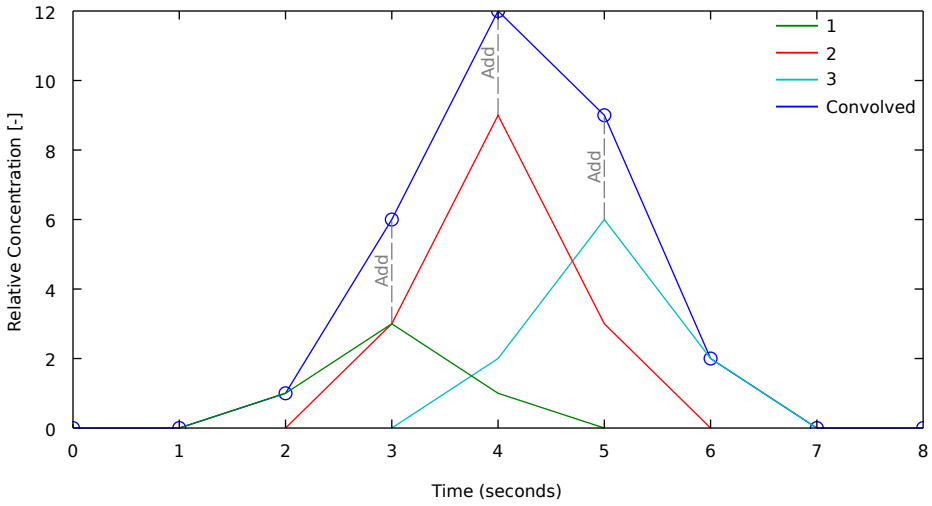

(c) The downstream convolved profile

Figure 2.6: Convolution demonstration

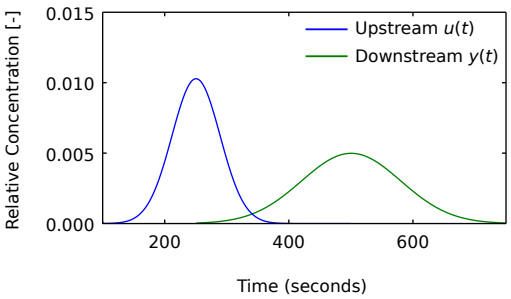

(a) Forwards in time

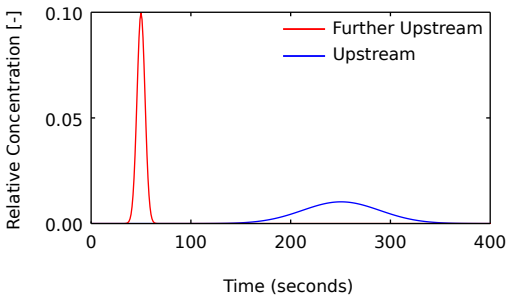

(b) Backwards in time

Figure 2.7: Concentration profiles changing with time

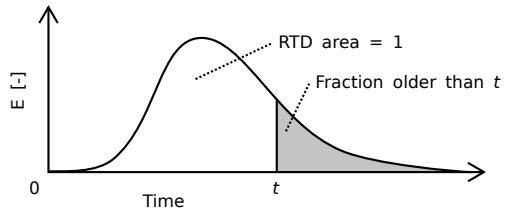

Figure 2.8: An example Residence Time Distribution, after Levenspiel (1972)

(cumulative mass-fraction) that has passed through the system. In chemical engineering the CRTD is referred to as the F curve (Levenspiel, 1972).

Figure 2.9 shows two CRTDs, one for below-threshold and one for above-threshold surcharges in an 800 mm manhole. There is a clear difference in shape between the two CRTDs, i.e. the mixing characteristics of a hydraulic structure can be characterised by the CRTD. The above-threshold CRTD rises steeply with a short tail, which corresponds to the majority of the solute short-circuiting. In the below-threshold CRTD there is only a short rise, with a long drawn out tail, reflecting more complete mixing. The exponential response is typically associated idealised perfect mixing, i.e. complete instantaneous mixing (Levenspiel, 1972).

2.5 Deconvolution

Deconvolution is the reverse process of convolution, that is to say the process of determining E given u and y. It is possible to use deconvolution on recorded experimental solute transport data to obtain an RTD with a good fit to the data.

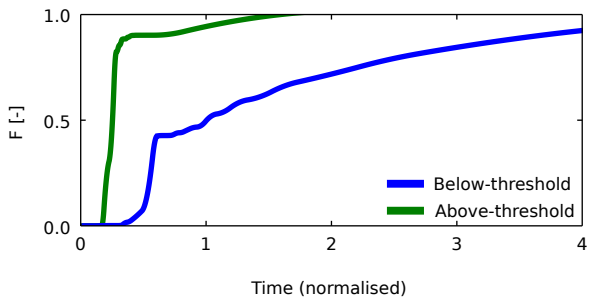

Figure 2.9: Cumulative Residence Time Distributions, showing the difference between the below-threshold and above-threshold conditions for an 800 mm manhole with 1 l/s flow (data from Guymer & Stovin, 2011)

For the ADE and ADZ models, the model parameters can be directly estimated from recorded experimental data, e.g. the method of moments (Rutherford, 1994). However, there is no equivalent direct solution for E in Equation 2.4 from experimental data as due to the presence of noise it forms an ill-posed problem (Hansen, 1998). As a result, deconvolution is generally an optimisation process, of which there are many methods. Madden *et al.* (1996) outline several, including Fourier transform based deconvolution, using Discrete Integral Least Squares to model the convolution process with a linear differential equation, constrained deconvolution using spline functions, maximum entropy deconvolution, and a Genetic Algorithm approach to deconvolution. Gooseff *et al.* (2011) used optimal Wiener filtering and geostatistical inversion in analysing solute transport in streams. Stovin *et al.* (2010b) outline and apply maximum entropy deconvolution to experimental solute transport data.

Deconvolution can be considered as a control systems engineering technique for system identification. For application to solute transport, the system under investigation (e.g. manhole) becomes analogous to a single-input single-output system and the RTD becomes the system response function (Figure 2.10). This generalisation allows deconvolution to be applied to a wide range of systems, i.e. there is no inherent predisposition towards any physical characteristics.

Compared to a theoretical hydrodynamic basis, deconvolution treats a solute transport system as a black box. This is equivalent to attempting only to *describe* the operation of a system, without explaining the *how* or *why*. A deconvolved RTD is not constrained by how the system is assumed to operate. However, the abstraction provided by the systems analogy is also a weakness. There is the temptation to ignore the underlying hydrodynamics, which should not be done.

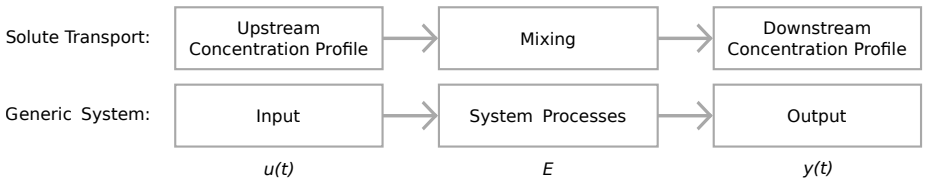

Figure 2.10: Systems analogy for solute transport systems

2.5.1 Geostatistical deconvolution

Geostatistical deconvolution is one means of obtaining an RTD from experimental solute transport data. Fienen *et al.* (2006) first applied geostatistical deconvolution to solute transport data. According to their work, geostatistical deconvolution is a stochastic approach to obtaining the RTD, allowing for the consideration of uncertainty. The geostatistical solution is formulated based on Bayes' rule and is solved using Markov chain Monte Carlo methods, giving individual values for each point on the RTD. Cirpka *et al.* (2007) proposed a different, non-linear, solution to the geostatistical deconvolution problem based on Lagrange multipliers. Payn *et al.* (2008) compare geostatistical deconvolution and Fast Fourier Transform (FFT) based deconvolution to estimate RTDs. Gooseff *et al.* (2011) compared geostatistical deconvolution to Weiner filtering. FFT based deconvolution was found to be sensitive to noise and Wiener filtering was observed to have non-real (negative) values for the RTD. These papers illustrate the validity of deconvolution and applicability of RTDs in a variety of environmental engineering contexts.

2.5.2 Maximum entropy deconvolution

Maximum entropy deconvolution as applied by Stovin *et al.* (2010b) and Guymer & Stovin (2011) to solute transport data is based on an application in pharmacokinetics by Hattersley *et al.* (2008). It is a deterministic approach that uses two time-series, one an upstream concentration profile and the other a downstream concentration profile, keyed to the same times and observed at a uniform time-step to deconvolve an RTD from non-instantaneous laboratory data. This is achieved through a non-linear optimisation process, implemented in MATLAB (The MathWorks Inc., 2011).

As the starting point for the optimisation, an initial estimate of the RTD ($\hat{E}_0$) is made so that $\int_0^\infty \hat{E}(\tau)d\tau = 1$. Solving for the RTD is carried out by the MATLAB `fmincon` function, which operates for a given number of iterations to minimise an entropy function (Hattersley *et al.*, 2008; Skilling & Bryan, 1984) that evaluates RTD smoothness. The minimisation problem is also constrained so that the recorded downstream profile matches with the predicted downstream

profile $\hat{y}(t)$. This ensures that the predicted RTD $\hat{E}$ is valid. ($\hat{y}(t)$ is calculated as the convolution of the $\hat{E}$ and the recorded upstream profile $u(t)$, Equation 2.6.)

$$\hat{y}(t) = \int_{-\infty}^{\infty} \hat{E}(\tau)u(t-\tau)d\tau \tag{2.6}$$

Before minimisation, the RTD is sub-sampled according to a logarithmic decrease in spacing until first arrival time and a logarithmic increase in spacing to the end of the data. At each step of the minimisation process, the RTD is linearly interpolated between sample points before calculating $\hat{y}(t)$. The RTD is also interpolated as the final step of deconvolution. Sub-sampling significantly reduces the time taken to find a solution, without significantly impacting on solution accuracy.

2.5.3 Choice of deconvolution methodology

Maximum entropy deconvolution is a preferable method to geostatistical deconvolution for this thesis for several reasons. In general it is a simpler methodology, which means it can be more easily applied to a range of data. It also has low computational costs. With reference to geostatistical deconvolution, Fienen *et al.* (2006) stated several days were necessary to solve for one RTD on a typical desktop PC. In comparison maximum entropy deconvolution can take less than a minute. Finally, positive previous experience with maximum entropy deconvolution also recommends it.

2.6 Aims and objectives

The primary aim of this thesis is the further exploration of maximum entropy deconvolution. To develop, validate, and extend the maximum entropy deconvolution method and subsequently use the deconvolved RTDs to improve the understanding of hydraulic processes relating to solute transport.

Specific objectives of this thesis are to:

1. Develop an understanding of and outline how maximum entropy deconvo-

lution works.

2. Design and conduct sensitivity analyses to verify the suitability of maximum entropy deconvolution.

3. Extend the maximum entropy deconvolution methodology to address any issues encountered or potential improvements discovered during Objectives 1 and 2.

4. Apply the new methodology to existing laboratory data to validate and demonstrate its use; and to develop new understanding of relevant mixing conditions through the deconvolved RTDs.

2.7 Summary

Manholes occur in many places in sewer networks and better understanding of solute transport processes within them can result in better network water quality models. Most existing research on solute transport in manholes has focussed on Advection-Dispersion Equation and Aggregated Dead Zone model parameter analysis of manhole configuration. A Residence Time Distribution forms a non-parametric model that better reflects mixing processes in manholes. Stovin *et al.* (2010b) suggests maximum entropy deconvolution as a means of obtaining the RTD from experimental solute transport data, and it has been chosen for exploration in this thesis.

The maximum entropy deconvolution methodology is explored in more detail in Chapter 5.

Chapter 3

Initial investigation

Originally presented as "The Influence of Outlet Angle on Solute Transport in Surcharged Manholes" by Sonnenwald et al. *(2011) at the 12th International Conference on Urban Drainage, Porte Alegre, Brazil, 11th–16th September 2011.*

This chapter presents an analysis of variation in manhole mixing processes with respect to outlet angle. This investigation uses maximum entropy deconvolution as described in Chapter 2 (as it existed at the start of the research), and was used to guide further work.

3.1 Introduction

As discussed in Section 2.3, Guymer *et al.* (2005) proposed that mixing in manholes might be generalised into two regimes, the below-threshold and above-threshold condition, dependent on the surcharge depth. In the below-threshold condition the flow was observed to be well-mixed. In the above-threshold condition, a submerged jet forms, which reduces mean travel times and passes part of the main body of solute through the manhole, effectively short-circuiting the surcharge volume. Stovin *et al.* (2010a) suggested that the threshold occurs at $s' = 0.258D$ for straight-through (0° outlet angle) manholes without benching.

Saiyudthong (2003) investigated the effects of varying outlet angle in benched and unbenched surcharged manholes on solute transport and head loss. The Aggregated Dead Zone model parameter analysis carried out indicated the presence of the threshold, which appeared to occur at different elevations dependent upon the outlet angle. He also suggested that travel time might be influenced by outlet angle. This aim of this chapter is to use the previously collected data with maximum entropy deconvolution to identify Residence Time Distributions. These will be used these to investigate both the elevation of the threshold as well as how the mixing changes with outlet angle by quantifying the fraction of the flow short-circuiting the surcharge volume.

3.2 Methodology

The data set was recorded using a recirculating system (Saiyudthong, 2003) with 88 mm internal diameter pipes and a 388 mm internal diameter manhole. Solute transport tests were carried out with rhodamine dye and concentration measured by fluorometers 1350 mm either side of the manhole centre line. Surcharge was measured as depth of water above the soffit using a water level follower and ranged from $s = 0$ mm to $s = 460$ mm, where s is surcharge depth. The outlet angles were 0°, 30°, 60°, and 90° and flow rates were 1, 2, 4, 6 and 8 l/s. Figure 3.1 shows the laboratory setup.

The data analysed in this chapter is the 1 l/s unbenched manhole concentration profiles and the distribution of surcharges covered is shown in Figure 3.2. The 30°, 60°, and 90° data were already pre-processed and calibrated, while the 0° data were not. Pre-processing of the 0° data was carried out as described by Saiyudthong (2003). Background was established as a linear relationship between the average of the first and last 30 seconds of the profile, then subtracted. A 6.5 second moving average was applied. The 0° data were down-sampled so that the time step would be equal to the time step of the other data at 0.15 seconds. At least three test runs were completed for each flow condition and configuration. The start of a test was defined as 1% of the peak upstream concentration and the end 1% of the peak downstream concentration.

The original laboratory fluorometer calibration function was not available to cal-

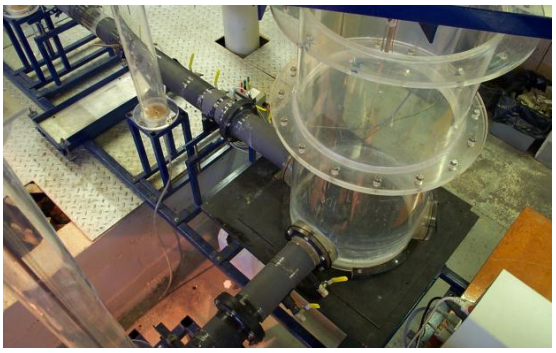

(a) The manhole in a 90° outlet angle configuration

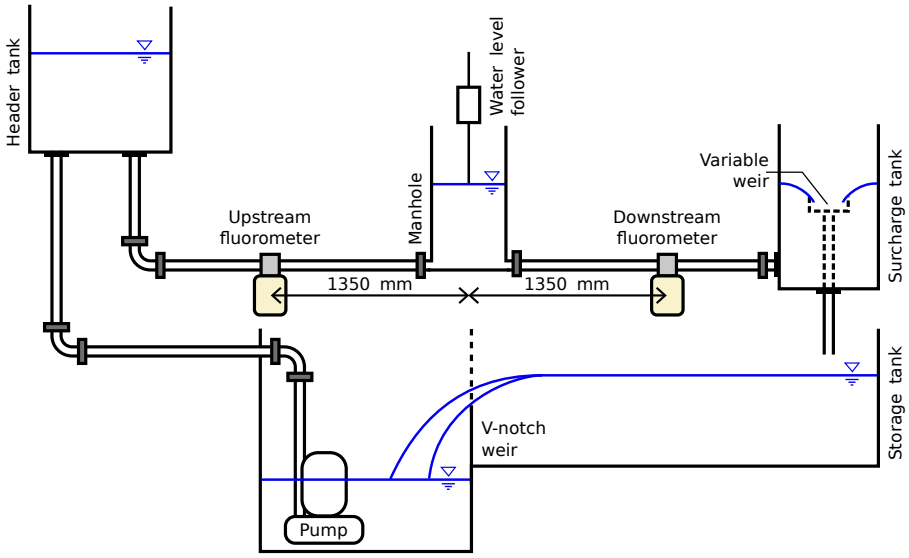

(b) Apparatus configuration

Figure 3.1: The experimental setup of Saiyudthong (2003)

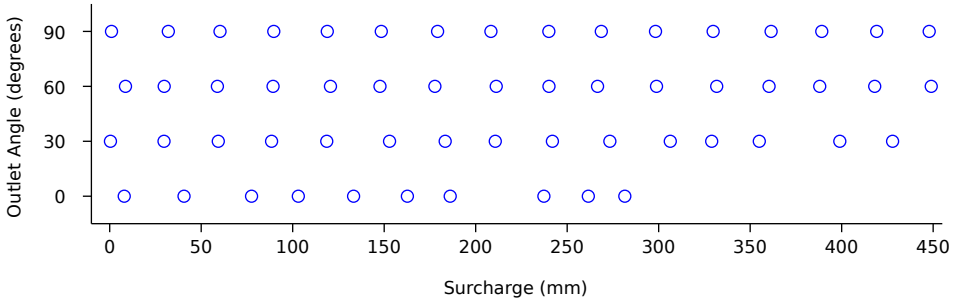

Figure 3.2: The distribution of surcharges processed

ibrate the 0° data. Instead, the concentration profile was scaled so that the area under the upstream profile and downstream profile was the same. This implies that the mass recovery is 100%, which is acceptable as the mass recovery observed in the 30°, 60°, and 90° data was generally high. The dimensionless characteristic of the RTD means that the amount of mass need not be consistent across tests.

The data were deconvolved using the deconvolution approach outlined in Section 2.5.2. Mass-balance of the deconvolved Cumulative Residence Time Distributions was enforced by scaling so that the final CRTD value equalled 1. The resulting CRTDs were grouped by the surcharges shown in Figure 3.2, with a maximum variation of ±0.5 mm, and averaged to produce a single CRTD for each configuration. The average was taken based on cumulative mass fraction rather than time, i.e. horizontal averaging—the times taken to reach a CRTD value of x were averaged. The average CRTDs were then temporally normalised according to Equation 2.5. The results are presented in Figures 3.4 to 3.7.

3.2.1 Identifying the threshold depth

As previously discussed, the above-threshold condition is characterised by short-circuiting, which typically gives rise to a two-stage CRTD. The first portion of the curve is steep and almost linear. This corresponds to the mass fraction of flow (and solute) that passes directly through (short-circuits) the manhole. There is then a clear transition in the CRTD, with the second part (i.e. the remainder of the distribution) exhibiting a more drawn out tail. In contrast, a below-threshold CRTD is a continuous curve, reflecting more complete mixing. The sharp discontinuity (point of inflection, shelf, or kink) between the two stages of the above-threshold CRTD has been used to identify the presence of short-circuiting and estimate the proportion of the flow that experiences it. This is shown in Figure 3.3, where it is estimated that approximately 45% of the flow short-circuits. The transition from below-threshold to above-threshold CRTDs provides an estimate of the threshold depth.

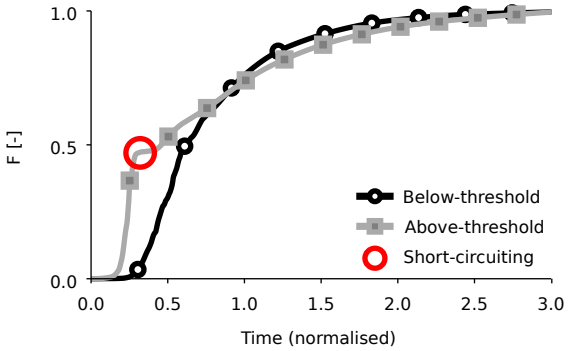

Figure 3.3: Sample plot showing angled out below-threshold and above-threshold CRTDs, highlighting the short-circuiting fraction

3.3 Results and discussion

The 0° outlet angle CRTDs (Figure 3.4) appear to be solely above-threshold. They all exhibit a rapid rise followed by a longer tail. The general lack of overall similarity between the CRTDs, particularly the initial rise, makes it especially difficult to determine if there is indeed a threshold, so no clear value can be determined for its surcharge depth. However, CRTDs at surcharge depths greater than 100 mm do appear to be more similar and may therefore match the $s' = 0.258D$ model. At sub-100 mm surcharges, the CRTDs show more below-threshold characteristics, with a gentler slope.

The initial rise of the 0° CRTDs decreases systematically with surcharge. This variation indicates that the system is not well-mixed, i.e. the main body of the flow short-circuits the manhole, passing through as a jet. For solute travelling in a short-circuiting jet, residence time is constant independent of surcharge depth, and therefore when surcharge and volume increases, as volume is in the denominator and discharge is fixed, the normalised time of the initial rise lowers. When the outlet angle is not 0° this effect is suppressed by more complex mixing processes affecting the jet.

The 30° outlet angle CRTDs (Figure 3.5) fall into two clear groups, with a few outliers. The first group ($s \geq 306$ mm) shows the characteristic steep incline and then drawn out tail, indicating it is above-threshold. The second group ($s \leq 242$ mm) is more consistent with below-threshold, appearing to be approximately exponential in form. One outlier, the single CRTD that occurs between the two

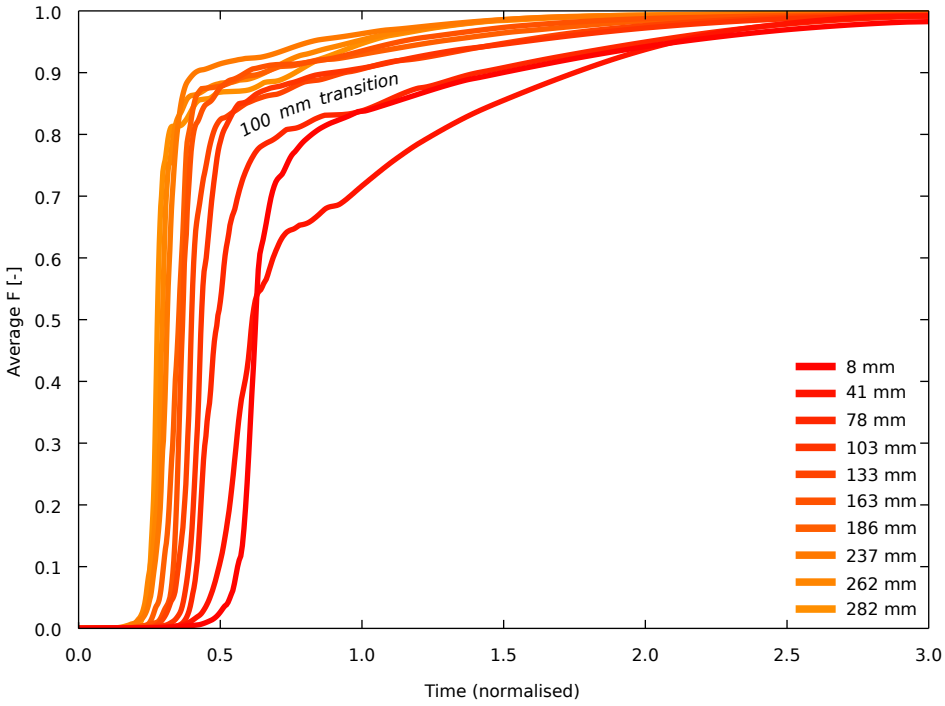

Figure 3.4: 0° outlet angle normalised average deconvolved CRTDs for 10 surcharge depths

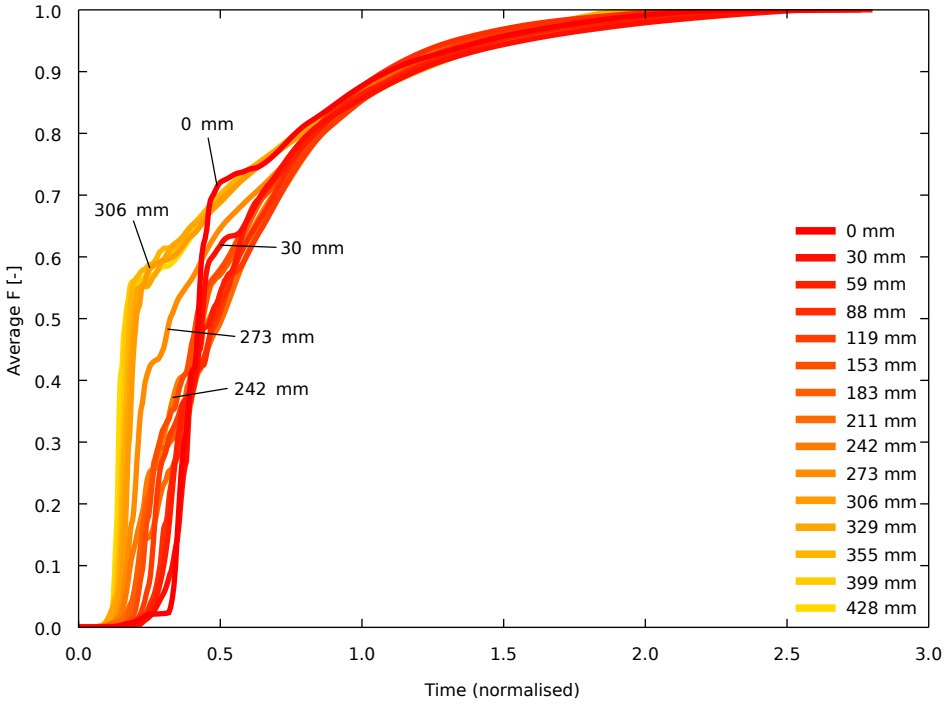

Figure 3.5: 30° outlet angle normalised average deconvolved CRTDs for 15 surcharge depths

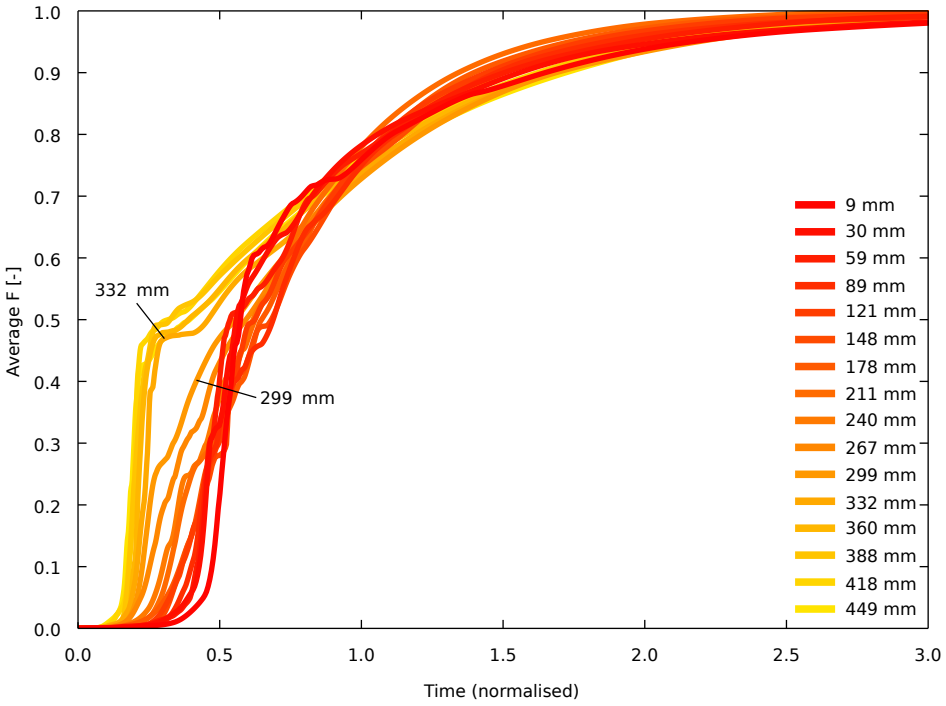

Figure 3.6: 60° outlet angle normalised average deconvolved CRTDs for 16 surcharge depths

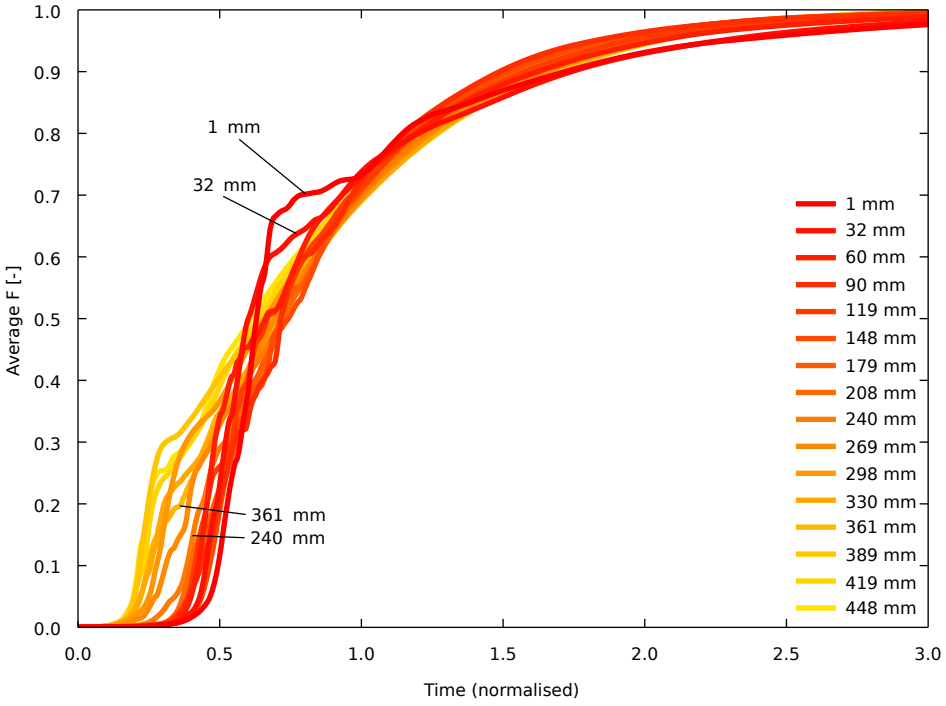

Figure 3.7: 90° outlet angle normalised average deconvolved CRTDs for 16 surcharge depths

groups ($s = 273$ mm) could be a surcharge that is around threshold, and so consists of below-threshold and above-threshold CRTDs averaged together, or could represent a transition zone. This indicates the threshold to be between the surcharges of 242 mm and 306 mm. The remaining outliers occur at low threshold ($s \leq 30$ mm) and indicate short-circuiting based on their CRTD shape (different to above-threshold short-circuiting).

The 60° outlet angle CRTDs (Figure 3.6) are similar to the 30° CRTDs and also fall into two groups, but this time without outliers. The two groups are again representative of the above-threshold and below-threshold conditions. The threshold can be determined to be between the surcharges of 299 mm and 332 mm. Closer inspection of the CRTDs reveals that passing a fraction of 0.9, the above-threshold curves take longer than the below-threshold curves, indicating that the tail is more drawn out. This appears to be unique to the 60° outlet angle.

The 90° outlet angle CRTDs (Figure 3.7) show a more gradual transition between the two different conditions compared to the 30° and 60° CRTDs. The highest surcharge depths ($s \geq 361$ mm) show the sharp discontinuity characteristic of the above-threshold condition. Similarly, the low surcharge conditions exhibit the exponential response associated with the below-threshold condition ($s \leq 240$ mm). Precise identification of the threshold elevation is not possible with this data set, although it is clearly much greater than the $s' = 0.258D$ model previously suggested for 0° manholes.

The 90° data also presents the clearest evidence of a possible third regime at very low surcharge depths, similar to above-threshold, i.e. short-circuiting. The CRTDs for the surcharges of 1 mm and 32 mm both exhibit the long first arrival times characteristic of the below-threshold condition, but their initial rises are steep. There is also the sharp discontinuity associated with the above-threshold condition. These curves are similar to the low surcharge outliers present within the 30° data. They indicate that an amount of flow travels through the manhole with the jet, the remainder experiencing full mixing. This may also be present in some of the low surcharge CRTDs from the 0° and 60° data.

The results suggest that, as outlet angle increases, the depth at which the flow transitions from the below-threshold to the above-threshold condition increases. The threshold appears to occur at 100 mm at 0° ($s' = 0.258D$), 242–306 mm

at 30° ($0.623D \leq s' \leq 0.789D$), 299–332 mm at 60° ($0.770D \leq s' \leq 0.856D$), and 240–361 mm at 90° ($0.619D \leq s' \leq 0.930D$), shown in Figure 3.8. It is clear that the previously established model of $s' = 0.258D$ is only applicable when the outlet angle is 0°.

3.3.1 Short-circuiting

Numerical values of short-circuiting mass fraction can be inferred from the CRTD plots by looking for the point at which the steep incline ceases. The short-circuiting that occurs is difficult to gauge because of the variation between individual above-threshold CRTDs. The estimated range of values is presented in Figure 3.8, which shows a possible inverse relationship between outlet angle and mass short-circuiting.

3.3.2 Physical processes

The shape of the CRTD can provide some insight as to what might be occurring within the manhole. Figure 3.9 shows potential paths of the jet for the different outlet angles in the above-threshold condition, based solely on the CRTD and some understanding of jets. These are presented as horizontal and vertical sections. The arrows indicate direction of flow and the intensity of the line indicates strength of flow.

Most of the jet is shown to pass straight through the manhole in the 0° outlet angle case (Figure 3.9a), with the edges of the jet recirculating horizontally. Vertically, some of the flow goes into surcharged volume mixing. Most of the flow continues straight through the manhole, corresponding to the observed high proportion of short-circuiting.

In the 30° outlet angle case, shown in Figure 3.9b, a portion of the jet deflects horizontally through to the outlet angle with some further small recirculation to the left of the jet flow. A larger portion of the jet recirculates on the right, setting up pressure that reinforces the deflection of the jet. Vertically there is more of the jet that passes into storage mixing, which is related to the recirculation on the right and hence a reduction in short-circuiting.

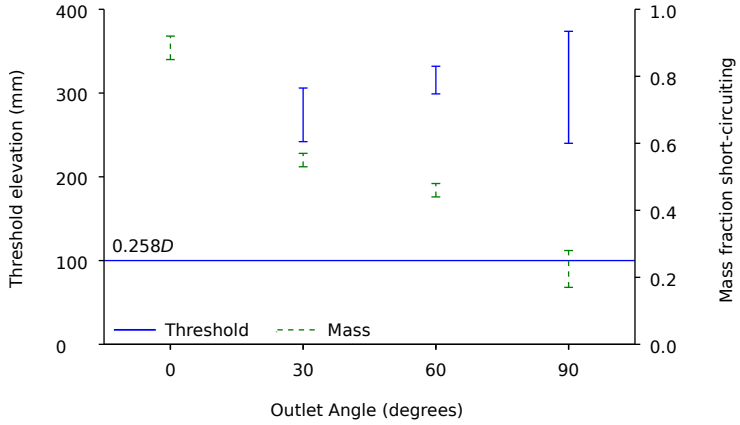

Figure 3.8: The observed threshold depth and proportion of mass short-circuiting at each outlet angle

Some recirculation to the left from the edge of the jet is thought to be possible in the 60° outlet angle case (Figure 3.9c), with flow nearer to the main body of the jet passing directly through. However, the main body itself is not forced to the outlet and instead recirculates. Correspondingly the main body of the jet also goes into vertical storage mixing and reduces the short-circuiting further.

When the outlet angle is 90°, as shown in Figure 3.9d, the jet no longer deflects, or only deflects slightly, and mainly impacts the far wall of the manhole. This sends most of the dye into surcharge storage mixing with a small amount short-circuiting, possibly due to eddies around the very edge of the jet. The vertical section shows the setup of an even larger recirculation pattern, with most of the jet going upwards as it impacts the wall. Even at low surcharge levels, the system is well-mixed.

3.4 Conclusions

- The deconvolution approach produced consistent Cumulative Residence Time Distributions for all outlet angles. Whilst not completely clear, the CRTDs suggest the presence of the previously postulated threshold and that the surcharge depth of its occurrence increases with outlet angle.
- There is some evidence of a low-surcharge short-circuiting regime.
- A significant fraction of dye that passes directly through the system due to

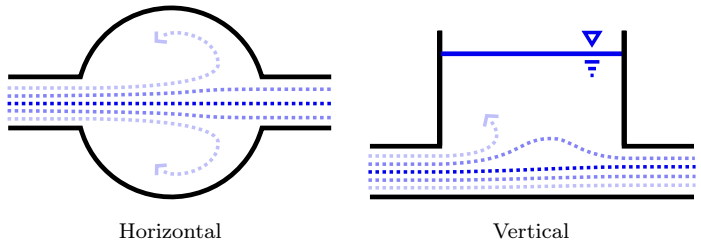

(a) 0° outlet angle

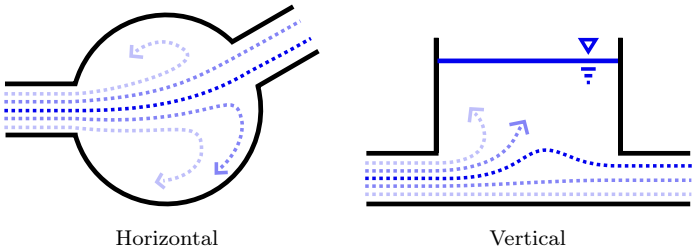

(b) 30° outlet angle

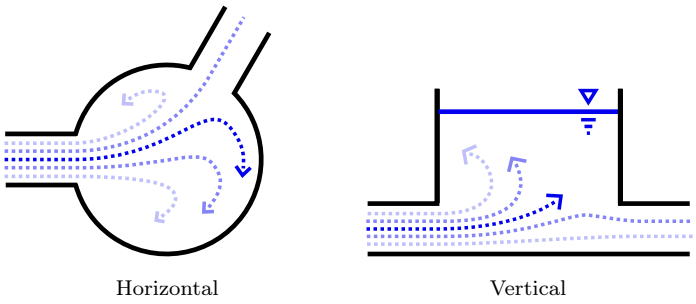

(c) 60° outlet angle

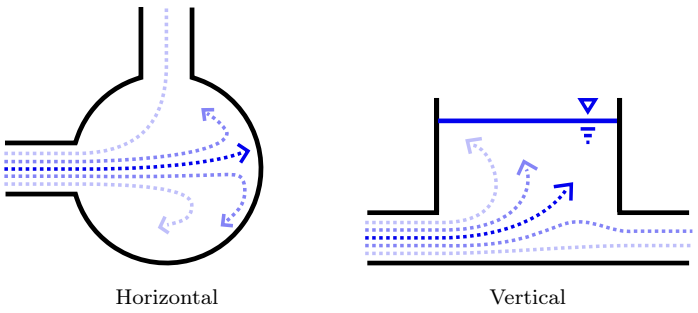

(d) 90° outlet angle

Figure 3.9: Diagram of potential path of jet, flow is left to right

short-circuiting. This is reduced at higher outlet angle.

- It is possible to suggest the behaviour of the jet to some extent based on the CRTD, and also explain the CRTD by considering the jet.

Since this investigation was conducted and the chapter detailing it was originally written, significant progress has been made on both deconvolution and interpreting CRTDs. A reanalysis of this data is presented later in Chapter 8. This experience gained carrying out this research helped to guide research in subsequent chapters.

Chapter 4

Correlation measures, model identification, and model evaluation

Originally presented as "Correlation Measures for Solute Transport Model Identification & Evaluation" by Sonnenwald et al. *(2013b) at the XXXII International School of Hydraulics, Łochów, Poland, 28nd–31st May 2012. It was subsequently published as a book chapter in* Experimental and Computational Solutions of Hydraulic Problems *in 2013 and is reproduced here with the kind permission of Springer Science+Business Media.*

Maximum entropy deconvolution relies heavily on a term that compares the known, experimental, downstream concentration profile to a downstream concentration profile predicted with an estimated Residence Time Distribution. A correlation measure compares the two profiles in each step of the minimisation process. As the comparison is responsible for ensuring an accurate RTD, correlation measures are explored here to provide understanding of how correlation value reflects differences between time-series.

4.1 Introduction

A correlation value expresses the similarity between either two separate time-series or two segments of the same time-series. They are frequently used to evaluate the goodness-of-fit for models. Within solute transport and environmental engineering, typically the R^2 (Nash & Sutcliffe, 1970), R_t^2 (Young *et al.*, 1980), and RMSD (Anderson & Woessner, 1992) correlation measures are used. The conventional understanding is that a higher or lower correlation value represents a better fit, but the reasons for the use of a specific correlation measure are typically not discussed. For example, with reference to solute transport model fitting, Fischer (1967) only specified that "the best possible agreement" be obtained, with no further guidance on how agreement is defined or assessed.

As previously discussed in Section 2.5.2, Stovin *et al.* (2010b) described a deconvolution based approach to identifying a Residence Time Distribution (RTD) from experimentally obtained upstream and downstream concentration profiles. In its original application it utilised the χ^2 parameter as the goodness-of-fit constraint (Hattersley *et al.*, 2008; Greenwood & Nikulin, 1996). For solute transport research the method was modified to use the R_t^2 correlation measure as a more familiar metric.

More information on both χ^2 and R_t^2 is necessary to determine the suitability of their application to solute transport data. Indeed, other correlation measures might prove to be better. The aim of this research, therefore, is to undertake an objective comparison of candidate correlation measures to determine which would be most suitable for use in maximum entropy deconvolution for model (i.e. RTD) identification. Correlation measures may also be used to cross-compare the identified model, and so these measures are also investigated for the subsequent evaluation of the identified RTDs.

4.1.1 Correlation measures

There are many different types of correlation/similarity measures/coefficients. They range from simple formulaic measures, which include R^2 and R_t^2, to algorithms such as Dynamic Time Warping (Berndt & Clifford, 1994), which pro-

cess the data in several steps. The most common correlation measures are based on Euclidean geometry. Euclidean based measures derive their correlation value from the Cartesian coordinate differences of the two time-series. There are also statistical and energy based measures. Statistical measures are derived from assumed probability density functions or other statistical functions. Energy based measures treat time-series data as analogous to energy states and apply energy transformations or functions developed in an energy context.

While this chapter focuses on one-dimensional solute transport data, correlation measures have applications in many fields, ranging from economic forecasting (Miskiewicz, 2010) to voice analysis (Vlachos *et al.*, 2002). Two-dimensional correlation measures (Chen *et al.*, 2005) are used when each time step has two associated values, e.g. $t(1) = \{a, b\}$. Correlation measures which operate on different time intervals or segments of the same time-series are called cross-correlation or auto-correlation measures (Movahed *et al.*, 2006). Auto-correlation measures highlight trends or repeating patterns in a time-series and as such are often used with frequency or wave form data. Correlation measures can also appear in complex number forms (Boudraa *et al.*, 2008).

Ignoring correlation measures that fall into the two-dimensional, non-linear, algorithmic, and cross/auto-correlation categories, twelve correlation measures have been identified as potentially suitable for use with solute transport data. These are summarised in Table 4.1. The measures contain a mix of non-dimensional and dimensional correlation measures. Non-dimensional correlation measures produce correlation values that have a defined meaning within a fixed range. R_t^2 is a typical examples of this, where 1 indicates a perfect correlation, and values less than or equal to 0 indicate no correlation.

4.1.2 Existing correlation measure comparisons

Christopoulos & Lew (2000) describe the problem of model fitting and outline generic models and the optimisation procedures (e.g. least squares) behind model fitting. They then describe model assessment, i.e. correlation measures, and further methods of optimisation based on model assessment. Bennett *et al.* (2012) provide an extensive review of correlation methods and measures for environmental models. They describe data constraints and then outline different meth-

Name	Symbol	Type	Reference
Burnham-Liard Criterion	BLC	S	George *et al.* (1998)
χ^2 Test	χ^2	S	Greenwood & Nikulin (1996) Hattersley *et al.* (2008)
Furthest Fitting Cost Based Similarity	FFCBS	E	Ye *et al.* (2004) *Equal weighting applied*
Nash-Sutcliffe Efficiency Index	R^2	E, D	Nash & Sutcliffe (1970)
Pearson's Product Moment Correlation Coefficient	PMCC	S, D	Rodgers & Nicewander (1988)
Root Mean Square Deviation	RMSD	S	Anderson & Woessner (1992)
Young's Coefficient of Determination	R_t^2	E, D	Young *et al.* (1980)
SimilB	SimilB	J, D	Boudraa *et al.* (2008)
Young Information Criterion	YIC	S	Cox & Boucher (1989)
MATLAB's 2-D Correlation Coefficient	CORR2	E, D	The MathWorks Inc. (2011)
Integral of Squared Error	ISE	E	Ghosh (2007)
Average Percent Error	APE	S, D	Kashefipour & Falconer (2000)

Table 4.1: List of correlation measures: (E)uclidean; Non-(D)imensional; (S)tatistical; (J)Energy

ods of comparing time-series: direct value comparisons, comparing time-series as a whole; concurrent comparisons, directly comparing data points (e.g. a scatter plot); residual methods, based on the difference between time-series data points; relative error transformations, accentuating e.g. differences at high or low values; preserving data patterns, taking into account adjacent values (e.g. cross-correlation); indirect metrics based on model parameters, coupling parameter variance and model error; and data transformation methods, moving the data into different domains (e.g. Fourier transformations). Their main focus is on providing a 5 step guideline to correctly define the comparison between data sets and then select an appropriate means of comparison. However, neither study provides insight into numerical interpretation of the correlation values that might be obtained.

Moriasi *et al.* (2007) conducted an extensive literature review compiling correlation values reported from various model fitting studies. The study provides a guideline for the use of the correlation measures found to be commonly used for watershed simulations. Through analysis of the measures used and values

obtained they recommended minimum satisfactory correlation values. However, these specific values are only of direct relevance in the context of watershed simulation performance evaluation. The study does not provide understanding of the relative sensitivity of the correlation measures.

In general there is little guidance on how correlation values obtained reflect the differences between time-series. Within deconvolution, the model identification process is based on an internal comparison between correlation values, and therefore it is straightforward to recognise higher or lower values as representing a better model. However, for evaluating the quality of different models, an additional understanding of the impact of differences between time-series on correlation value is necessary. This is particularly important for evaluating downstream concentration profile predictions made with deconvolved RTDs.

4.1.3 Correlation measure characteristics

For the purposes of using correlation measures in solute transport model identification and evaluation, certain characteristics are desirable. In model identification, several models using different model parameters are compared to the same experimental data. In this scenario, all models have the same number of sample points, so any sensitivity to this parameter can be ignored. However, when evaluating models, data may be of different lengths, so a correlation measure should not be sensitive to number of sample points. In identification and evaluation, the correlation measure should be sensitive to transformation and transformation magnitude, e.g. the correlation value obtained should indicate that the overall shape of the model is a poor fit when this is the case. In all scenarios correlation measures should not be sensitive to the noise present in natural systems. This chapter aims to systematically evaluate the 12 correlation measures in Table 4.1 against four concentration profile characteristics: number of sample points, transformation, transformation intensity, and noise.

4.2 Methodology

Three synthetic concentration profiles have been created, each representing a different solute transport scenario. The synthetic profiles were discretised, transformed, and had noise added to reflect different conditions. Correlation measures were then used to compare the unmodified concentration profiles with their modified counterparts.

4.2.1 The synthetic concentration profiles

The three synthetic concentration profiles are shown in Figure 4.1. Profile 1 consists of a normal distribution covering ±3 standard deviations (99% of the data), as generated by the MATLAB `pdf` function (The MathWorks Inc., 2011). This represents a typical response to an instantaneous input in pipe flow. Profile 2 represents a fully mixed response to a step input. It is calculated from an exponential increase and decrease. Profile 3 represents a non-ideal mixing response to an instantaneous input in the form of a 2-cell Aggregated Dead Zone (ADZ) model (Rutherford, 1994). Profile 1 is symmetric while Profiles 2 and 3 are more common asymmetric shapes.

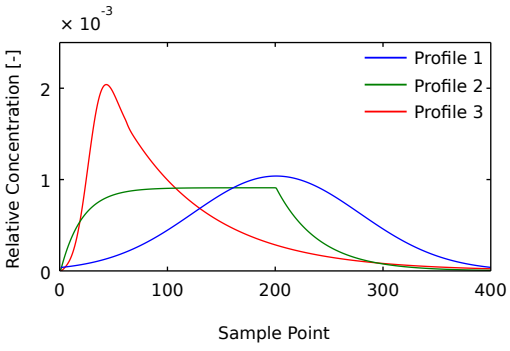

Figure 4.1: The synthetic concentration profiles

4.2.2 Generating the test data

The test data was generated from the synthetic profiles by varying four parameters: number of points; transformation; transformation magnitude; and noise level. The first step was to discretise the synthetic profiles according to the number of sample points parameter. This resulted in a total of thirty profiles, three each at 20, 40, 80, 100, 200, 400, 800, 1200, 1600, and 2000 uniformly spaced sample points. The range of number of sample points represents common solute transport time-series lengths. Each profile at each number of sample points was normalised to have unit area. This ensures that changes due to variation in number of sample points are independent of total solute volume.

From the discretised profiles, the transformed profiles were generated using five transformations, each in combination with three transformation magnitudes, 0.05, 0.10, and 0.20. Each transformation was applied in two directions, up/down or left/right (as appropriate) at magnitude times value (y-axis) or magnitude times sample points (x-axis) as appropriate, e.g. a shift or stretch of $0.20 \times 400 = 80$ sample points. Any additional sample points that were generated as a result of transformation were ignored, and in order to retain a constant time-series length, zeros were inserted when the number of sample points was reduced. Figures 4.2a–4.2e illustrate the five transformations, outlined below:

- **Scaling**, Figure 4.2a, a linear change in value that may occur when the model has errors in scale or due to poor calibration of measuring equipment;
- **Shifting**, Figure 4.2b, a temporal change that may occur when a modelled concentration profile has errors in its advection term;
- **Truncation**, Figure 4.2c, a loss of data that could be representative of not monitoring the entire experiment;
- **Stretching**, Figure 4.2d, an elongation of concentration profile that could be representative of an error in sampling frequency or an overestimation of dispersion coefficient;
- **Squeezing**, Figure 4.2e, the opposite of stretching.

Noise, e.g. Figure 4.2f, was applied to the transformed concentration profiles to

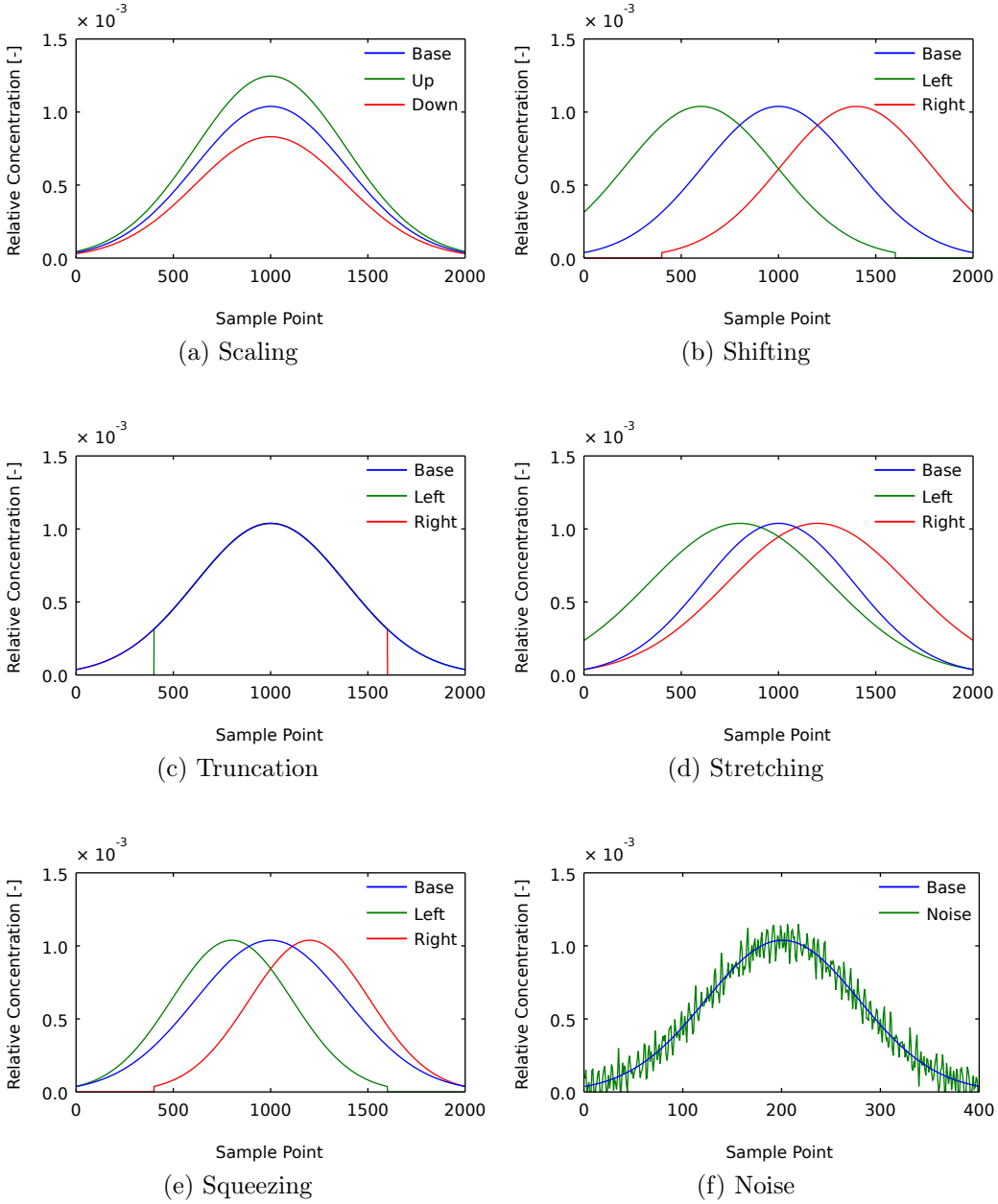

(a) Scaling (b) Shifting

(c) Truncation (d) Stretching

(e) Squeezing (f) Noise

Figure 4.2: Examples of generated data, with transformation applied at a magnitude of 0.20 and each displayed using a temporal discretisation of 400 sample points

represent the variation common in recorded data due to both instrument noise and natural systems. Noise was generated through the superposition of a random number [5, 15] of sine waves with random amplitude [-1, 1], random phase [0, π], and random frequency [0, length/2]. This was found to have a better zero mean when sub-sampling to lower numbers of sample points, and therefore better reflect natural noise than purely random computer generated noise. The noise was scaled to 0%, 5%, 10%, and 20% ratios of noise peak to discretised profile peak.

4.2.3 Generating correlation values

Correlation values are obtained from the application of a correlation measure to two time-series. In order to evaluate the correlation measures, each measure was used to compare each transformed concentration profile to the unmodified original at that number of sample points. 12 correlation measures, 3 profiles, 10 numbers of sample points, 5 transformations, 3 transformation magnitudes in 2 directions and 4 noise levels gives $12 \times 3 \times 10 \times 5 \times (3 \times 2) \times 4 = 43,200$ correlation values to be compared.

4.2.4 Comparing correlation values

Not all the correlation measures tested are non-dimensional, so a method for directly comparing all correlation values was required. Expressing the correlation value as a ratio of the perfect correlation value was rejected as for some measures a perfect correlation is indicated by 0, which would result in division by zero. Instead, correlation values were normalised into a similar range. Equation 4.1 is used to do this, where c_{norm} is a normalised correlation value, c is the correlation value to be normalised, c_{perfect} is the value of a perfect correlation between the concentration profile and itself prior to transformation and/or addition of noise, c_{max} and c_{min} are respectively the highest and lowest correlation values obtained for that profile (each either the perfect or worst correlation by definition).

$$c_{\text{norm}} = 1 - \left| \frac{c_{\text{perfect}} - c}{c_{\text{max}} - c_{\text{min}}} \right| \tag{4.1}$$

Applying Equation 4.1 results in a correlation value that is context specific for a given synthetic profile shape, number of sample points, and correlation measure. 1 will be the best match between unmodified synthetic and transformed concentration profile—0 the worst. Normalised correlation values are data set specific, and so have limited meaning outside the present analysis. An example of normalising correlation values is shown in Table 4.2. Despite very different raw correlation values, the normalised values indicate that a χ^2 of 2×10^5 represents a better match between time-series than an R_t^2 value of 0.9975.

To directly compare the large number of correlation values generated, plots showing all four parameters (number of sample points, transformation, transformation magnitude and noise) have been generated and considered. A more easily interpreted summary plot has also been generated. The sensitivity of a correlation measure to a given parameter can be expressed as the standard deviation of correlation values with respect to that parameter. For example, after taking the mean value of all correlation values for involving 20 sample points, the standard deviation of all such means for 20 to 2000 sample points. This is expressed as the standard deviation of the vector produced by Equation 4.2, where: i, j, k, and l are indices for the four parameters; and N is the number of parameter values (e.g. 10 different numbers of sample points). Equation 4.2 also takes into consideration all 3 synthetic profiles. Comparing standard deviations for each parameter and measure gives a good indication of how well the different correlation measures perform.

$$c_{\text{norm vector } i} = \frac{3}{N_j \times N_k \times N_l} \sum_{j=1}^{N_j} \sum_{k=1}^{N_k} \sum_{l=1}^{N_l} c_{\text{norm } i,j,k,l} \tag{4.2}$$

Term in Equation 4.1	Description	R_t^2 *Non-dimensional*	χ^2 *Dimensional*
c	Raw correlation value to normalise	0.9975	2×10^5
c_{min}	Lowest value in data set	0.5364	0
c_{max}	Highest value in data set	1	3.6×10^8
c_{perfect}	Perfect correlation value	1	0
c_{norm}	Normalised value	0.9946	0.9994

Table 4.2: Example correlation value normalisation

4.3 Results and discussion

There were three stages to data analysis. The first was to examine the obtained results in detail. Second was to examine trends and overall performance of the correlation measures and discard those correlation measures judged unsuitable for solute transport model identification. Finally, the correlation measures suitable for solute transport model evaluation have been examined.

4.3.1 Detailed examination

The plots for each correlation measure are made up of multiple sub-plots, each of which shows the correlation values for one of the synthetic profiles and one of the transformations. There are 3 profiles and 5 transformations so there are 15 sub-plots in total. A sub-plot before and after normalisation for R_t^2 is shown in Figure 4.3. The full normalised plot for R_t^2 is shown in Figure 4.4. As a detailed examination of all plots does not add significantly to the analysis, the remaining full normalised plots are in Appendix A.

Raw R_t^2 correlation values for the shifting transformation applied to Profile 2 are shown in Figure 4.3a, where 1 is a perfect correlation. The lines are nearly horizontal, which indicates that noise has very little influence on the correlation value obtained when Profile 2 is transformed by shifting. The greater vertical spacing between the dashed lines compared with the solid lines shows that right shifting consistently has more impact than left shifting, which is expected for this asymmetric profile. The 2000 sample point symbols are close to their lines, but the 20 sample point symbols diverge from their lines as noise increases—noise appears to have greater impact on the shifted Profile 2 when there are fewer sample points to characterise the curve. The normalised equivalent of Figure 4.3a is shown in Figure 4.3b. The normalised sub-plot in this case effectively expands the y-axis values. The occurrence of normalised values of 0 shows that shifting resulted in the lowest correlation across all transformations applied to Profile 2.

The full plot of normalised R_t^2 correlation values is shown in Figure 4.4. Shifting also has the greatest impact on Profile 1 and is about equal with squeezing in Profile 3. For Profile 2, truncation has about half the impact of shifting, and

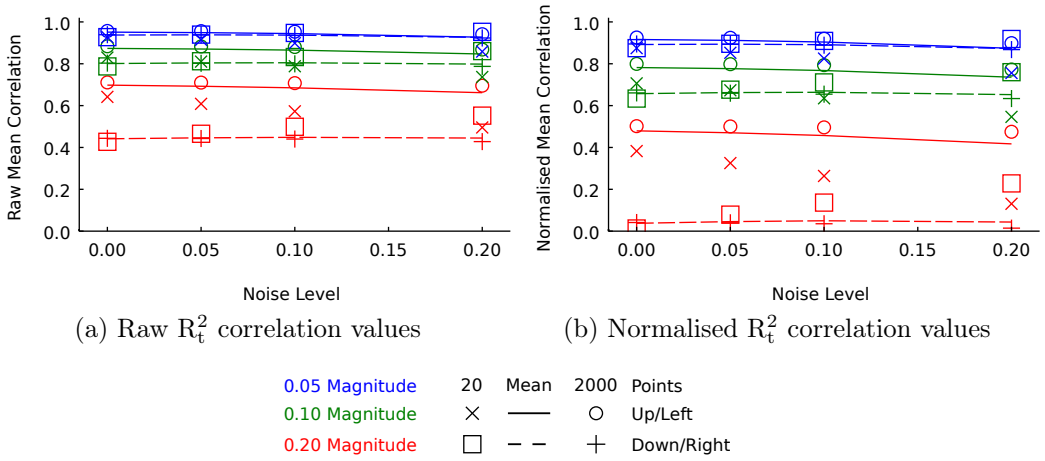

(a) Raw R_t^2 correlation values (b) Normalised R_t^2 correlation values

Figure 4.3: Shifted Profile 2 sub-plot

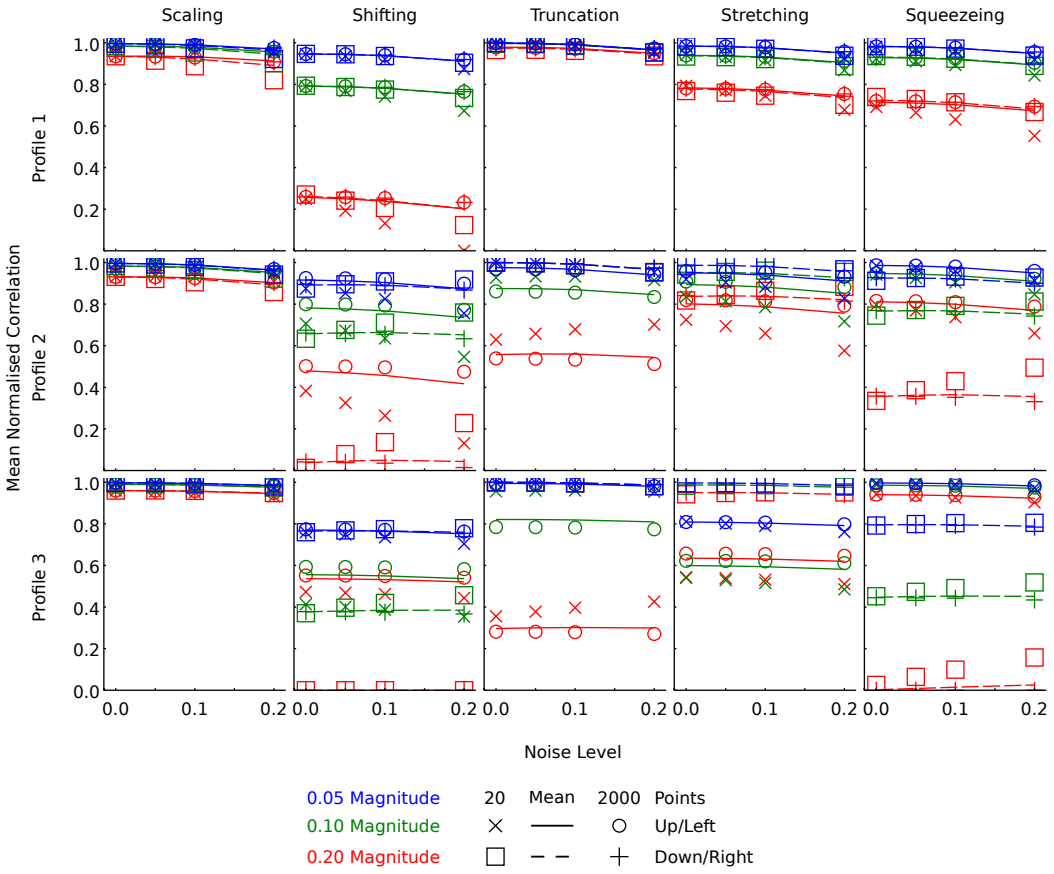

Figure 4.4: Mean normalised correlation values for R_t^2 across profile and transformation

squeezing has an influence somewhere between truncation and shifting. Stretching has the second least impact and scaling has the least impact. Sensitivity to noise is universally low. Stratification of the lines is similar across all profiles for the scaling transformation, which indicates any profiles scaled to the same degree with R_t^2 will have a similar change in correlation value, regardless of profile shape. The stratification of transformation intensity lines otherwise varies significantly. Profile 1 shows the least variation, with left/right transformations being identical and stretching and squeezing being very similar as well. Truncation of Profile 1 shows the least distinction of all the transformation/profile combinations, which implies that R_t^2 will not deal as well with identifying discrepancies associated with long tails. The long tail effect can also be seen in the right truncation of Profile 3, where again there is very little stratification. Conversely, there is a very large impact from left truncation, where the majority of the peak of Profile 3 is cut-off.

4.3.2 Correlation measure comparison

Many of the trends exhibited by R_t^2 apply to other correlation measures as well (Appendix A). The Profile 1 correlation values obtained for the up/left transformations produce nearly identical results to the down/right transformations. Increasing transformation magnitude results in decreased correlation. In most cases there is little variation with noise and small variation with number of sample points. This is also shown in Figure 4.5, which shows the standard deviation values generated with Equation 4.2. A higher value indicates that a correlation measure is more sensitive to that parameter.

The correlation measures fall into three distinct groups. Group 1 comprises BLC, FFCBS, R^2, PMCC, RMSD, R_t^2, CORR2, and APE, which all exhibit high sensitivity to transformation/transformation magnitude and low sensitivity to number of sample points/noise. Within this group: R^2 has the greatest sensitivity to transformation (change in the underlying shape); and APE shows a slightly higher sensitivity to noise. All Group 1 measures appear suitable for model identification. However, when examining the complete plots (Appendix A), PMCC and CORR2 show extremely limited sensitivity to scaling. This is attributed to these measures relying on a difference in mean value which will only change slightly

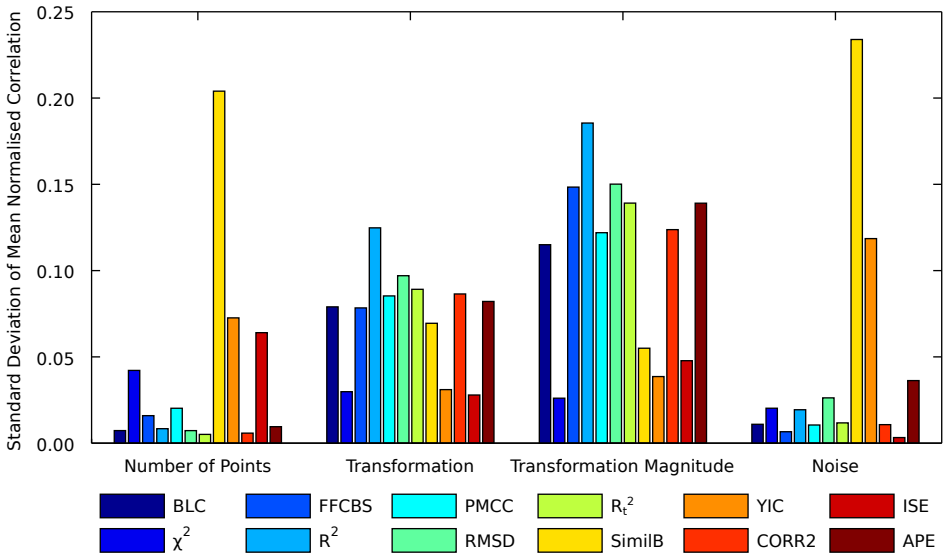

Figure 4.5: Standard deviation plot showing sensitivity of the correlation measures

when all values in a concentration profile are scaled.

Group 2 measures, χ^2 and ISE, are characterised by lower sensitivity to transformation and transformation magnitude. They appear potentially suitable for model identification despite higher sensitivity to number of sample points. The lower sensitivity to transformation/transformation magnitude is still acceptable due to the insensitivity to noise. SimilB and YIC make up Group 3, with high sensitivity to both number of sample points and noise. This, combined with lower sensitivity to transformation/transformation magnitude, make Group 3 measures unsuitable for model identification.

Overall there are eight measures which show the characteristics previously mentioned to be desirable for model identification. Six measures in Group 1 (BLC, FFCBS, R^2, RMSD, R_t^2, and APE) and the Group 2 measures (χ^2 and ISE) are all sensitive to transformation, and transformation magnitude, while insensitive to noise. They could therefore all be used for model identification, e.g. within the deconvolution method. To narrow the choice of measure further requires testing for interaction with other elements of the deconvolution process, which is carried out in Chapter 5.

For solute transport model evaluation, only the non-dimensional measures of Group 1 (R^2, R_t^2 and APE) can be recommended as these are not influenced by

number of sample points.

4.3.3 Application to model evaluation

To further investigate the correlation measures for model evaluation and provide guidance on choice of correlation measure, R^2, R_t^2, and APE have been applied to the scenarios shown in Figure 4.6. Associated (raw) correlation values are presented in Table 4.3. For APE, a lower value represents a better correlation, with 0 being the best ranging to 100. For R^2 and R_t^2, 1 is the best ranging to 0. "% Change" shows the change in correlation value between Models A2 and B2 as a percentage of the total range.

In Figure 4.6a, goodness-of-fit can be ranked by visual interpretation in order of decreasing fit as Model A1, then C1, then B1. All correlation measures correctly identify this. Model A1 shows good correlation values. For Model C1, while R_t^2 shows a somewhat lower correlation, R^2 and APE both show significantly lower correlations. For Model B1, R^2 indicates that there is no correlation at all even though B1 is clearly a temporal shift of A1. This is unique to R^2, and indicates it may actually be unsuitable for model identification. In comparison, any dimensional correlation measure would still indicate some relation.

Figure 4.6b presents a scenario in which the measured data exhibits a secondary peak representative of recirculation effects or transient storage. This scenario is common and it is essential that correlation measures indicate whether or not the model fits correctly. Model B2 can be visually described as the best as it clearly includes the secondary peak. However, the R^2 and R_t^2 correlation values imply an extremely good fit for both models. It is important to recognise what differences in correlation value indicate for these measures. In contrast, APE still

Model	A1	B1	C1	A2	B2	% Change
R^2	0.9561	0.0000	0.8386	0.9881	0.9982	1.010%
R_t^2	0.9853	0.5457	0.9459	0.9938	0.9990	0.520%
APE	12.19	73.32	23.24	9.719	3.745	5.974%

Table 4.3: Correlation values for the models presented in Figure 4.6

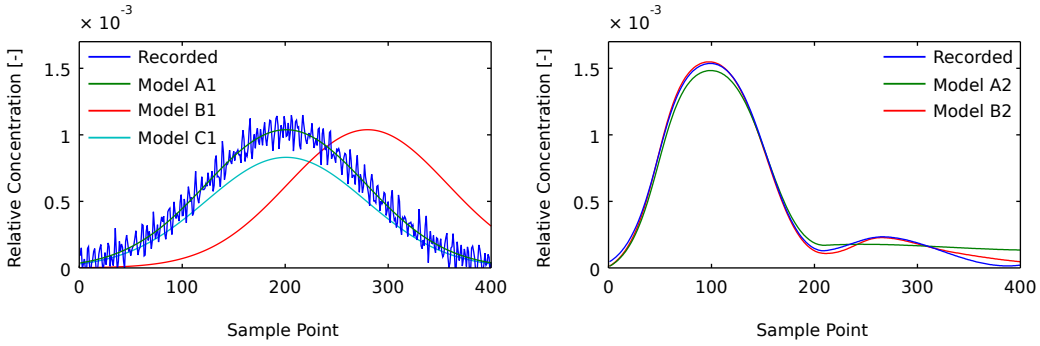

(a) Profile 1 type situation (b) Secondary peak situation

Figure 4.6: Models fit to theoretical 'recorded' data for examining correlation measures.

clearly differentiates between Model A2 and Model B2. A dimensional correlation measure would also show B2 to be the better fit, but similar to R^2 and R_t^2, it would be difficult to distinguish between the correlation values.

Each of the three correlation measures might be useful in different scenarios. R_t^2 might be most useful when model fits are expected to generally be poor as it will still indicate correlation for a wide range of transformations and magnitudes, i.e. it is flexible. APE exaggerates small differences between profiles, and so might be useful in some situations, while R^2 exaggerates larger differences. Dimensional correlation measures may perform similarly to any of these three measures, but lack the finite scale to quantify and compare correlation values. Of the three correlation measures, both R^2 and R_t^2 have been used extensively in civil engineering and therefore the values obtained can be more easily compared to existing research.

4.4 Conclusions

A systematic comparison of twelve different correlation measures using three realistic solute concentration profiles was carried out to identify measures that show high sensitivity to profile shape but limited sensitivity to noise. Eight measures (BLC, χ^2, FFCBS, R^2, RMSD, R_t^2, ISE, and APE) have been found to be potentially suitable for model identification and use in the deconvolution method. Of

these, the three non-dimensional measures, R^2, R_t^2, and APE were examined in greater detail for use in model evaluation. All three measures produced correlation values that match visual interpretation of model fit, although at different levels of sensitivity. Due to this the measures might be suitable for different scenarios, with APE exaggerating small differences, R^2 exaggerating large differences, and R_t^2 being flexible about differences between concentration profiles.

Choice of correlation measure within the deconvolution process is examined in more detail in Chapter 5.

Chapter 5

Maximum entropy deconvolution for solute transport data

Accepted for publication as "Configuring maximum entropy deconvolution for the identification of residence time distributions in solute transport applications" by Sonnenwald et al. *(2013a) in* ASCE Journal of Hydrologic Engineering*, 22nd October 2013. It is reproduced here with permission from ASCE.*

After using maximum entropy deconvolution in Chapter 3, the need for further investigation into maximum entropy parameters and applicable data was appreciated. The first step of this process was to investigate correlation measures in Chapter 4. The second step was to perform a sensitivity analysis to rigorously demonstrate the applicability of maximum entropy deconvolution to solute transport data.

5.1 Introduction

The RTD has been introduced as a model that describes solute transport in urban drainage systems, e.g. Guymer & Stovin (2011). The particular benefit

of an RTD is that, as a non-parametric model, no assumptions are made on how a system operates. Therefore, the RTD can more accurately represent the effect of complex mixing processes in a reach or structure, such as dead-zone short-circuiting (Stovin *et al.*, 2010a). Unfortunately this benefit incurs a cost, as identifying an RTD is significantly more complex than identifying the parameters of traditional models.

The general method of identifying an RTD from recorded laboratory data is deconvolution. There are many methods and applications for deconvolution. An overview of some common methods is given by (Madden *et al.*, 1996). Other applications include noise cancellation (Pandolfi, 2010) and gas chromatography (Zhong *et al.*, 2011). Within solute transport research, deconvolution techniques have been used to examine soil transfer functions (Skaggs *et al.*, 1998), bank filtration (Cirpka *et al.*, 2007), and transient storage (Gooseff *et al.*, 2011). The latter two studies used geostatistical deconvolution. Maximum entropy deconvolution, the main subject of this thesis, has previously been used to investigate solute transport in manholes in Chapter 3, as well as other studies (Stovin *et al.*, 2010b; Guymer & Stovin, 2011).

Although maximum entropy deconvolution has previously been successfully applied to solute transport data, no rigorous investigation into how the configuration settings affect the quality of the results obtained has been reported. Four maximum entropy deconvolution settings impact on the quality of the deconvolved RTD: the number of sample points; sample point distribution; constraint function; and the maximum number of iterations. Inappropriate configuration options for any of the settings may result in a poor quality RTD. Two additional settings have been found to have no impact on the deconvolved RTD: initial guess and convergence criteria.

This chapter aims to systematically identify a robust set of options that can be used to deconvolve the RTD from typical solute transport data. To this end, a sensitivity analysis has been carried out with a range of data and options for the different maximum entropy settings.

5.1.1 Maximum entropy deconvolution

Entropy is the amount of disorder in a system. It is a commonly used concept in physics and chemistry as the second law of thermodynamics, which states that the amount of order in a system will never increase. The concept of entropy is also mathematical. In this case it is an estimation of randomness of an event based on a known probability distribution. The "higher" (more negative) the entropy, the more random the result is. This is known as Shannon entropy, shown in Equation 5.1. H is the entropy of X. $P(x)$ is the probability distribution that $X = x$. (Shannon, 1948; Weisstein, n.d.).

$$H(X) = -\sum_{i} P(x_i) \ln P(x_i) \tag{5.1}$$

Maximum entropy deconvolution is a discrete computational technique developed by Skilling & Bryan (1984) for image reconstruction. They presented an altered Shannon entropy function, Equation 5.2, where S is the entropy function for deconvolution and $f_1, \ldots, f_N$ are a positive set of numerical values to be recovered. The entropy function is constructed so that any value of f_j is part of the complete image f being recovered. In this scenario, the probability p_j that f_j is a part of f is the value f_j divided by the sum of all values of f, i.e. Σf.

$$S(f) = -\sum_{j=1}^{N} p_j \ln p_j, \quad p_j = f_j / \Sigma f \tag{5.2}$$

Equation 5.2 can be interpreted in a solute transport context. In this scenario, f is the RTD. Assuming mass-balance the RTD must sum to 1 ($\int_0^\infty E(\tau)d\tau = 1$ or $\sum f = 1$), and Equation 5.2 simplifies to Equation 5.3. This can then be interpreted as an exponential measure of error. As points along the RTD have larger values, entropy increases.

$$S(f) = -\sum_{j=1}^{N} f_j \ln f_j \tag{5.3}$$

Reinterpreting the maximum entropy method of Skilling & Bryan (1984) for solute

transport data then, maximum entropy deconvolution uses regularly sampled paired upstream $u(t)$ and downstream $y(t)$ temporal concentration profiles to deconvolve the RTD. An estimate of the RTD, $\hat{E} = \{\hat{E}_1, \ldots, \hat{E}_N\}$ where N is the number of data points, is to be made as flat as possible with the only exceptions being those implied by the upstream and downstream data. Flatness of $\hat{E}$ is measured by an entropy function, Equation 5.4. This also enforces non-negativity.

A constraint function C, Equation 5.5, ensures that the RTD is a realistic result by comparing the goodness-of-fit of the predicted downstream concentration profile $\hat{y}$ against the recorded profile, where $\hat{y}$ is calculated as the convolution of $\hat{E}$ and the upstream profile (Equation 2.6). C is typically, as presented here, the chi-squared (χ^2) function, where σ is an error estimate. The RTD is identified by combining both equations in a Lagrangian function L, Equation 5.6, and maximising. λ is the Lagrange multiplier determined during the maximisation process. Sub-scripts denote specific points in discrete time.

$$S(\hat{E}) = -\sum_{i=1}^{N} \left(\frac{\hat{E}_i}{\sum_{j=1}^{N} \hat{E}_j} \right) \ln \left(\frac{\hat{E}_i}{\sum_{j=1}^{N} \hat{E}_j} \right) \tag{5.4}$$

$$C = \sum_{i=1}^{N} (\hat{y}_i - y_i)^2 / \sigma_i^2 \tag{5.5}$$

$$\hat{y}(t) = \int_{-\infty}^{\infty} \hat{E}(\tau) u(t - \tau) d\tau \tag{2.6}$$

$$L(\hat{E}, \lambda) = S(\hat{E}) - \lambda C \tag{5.6}$$

The software and methodology used for maximum entropy deconvolution of solute transport data is an evolution of a pharmacokinetics application (Hattersley *et al.*, 2008). In pharmacokinetics, data points are often collected at uneven time intervals, e.g. by a nurse making rounds. As a result, the entropy function was modified for piecewise data, where the value between points is assumed to vary linearly, and Equation 5.7 was developed. The r term is added as a base-line prediction of the RTD in the absence of other data. r takes the form of a nearest neighbour moving average where $r_i = ((\hat{E}_{i-1} + \hat{E}_{i+1})/2)$ and at $i = 0$ and $i = N$ the value

of the two nearest points, e.g. $r_N = (\hat{E}_{N-1} + \hat{E}_N)/2$. The inclusion of r results in an entropy value that evaluates smoothness rather than flatness; entropy values closer to zero indicate a smoother function.

$$S(\hat{E}) = -\sum_{i=1}^{N} \left(\frac{\hat{E}_i}{\sum_{j=1}^{N} \hat{E}_j} \right) \ln \left(\frac{\hat{E}_i / \sum_{j=1}^{N} \hat{E}_j}{r_i} \right) \tag{5.7}$$

To obtain $\hat{E}$, Hattersley *et al.* (2008) converted Equation 5.6 into an equivalent minimisation problem. This was solved using a Sequential Quadratic Programming (SQP) technique implemented within the MATLAB `fmincon` function (The MathWorks Inc., 2011). SQP is an optimisation algorithm that works by minimising a quadratic model of the problem to find the next step towards the solution (Schittkowski, 1986).

Maximum entropy deconvolution was further modified for application to solute transport data by Stovin *et al.* (2010b). The piecewise capability previously introduced was modified to create a simplified deconvolution problem where the RTD is sub-sampled. This reduces computational expense and the impact of noisy data while maintaining the benefits of a non-parametric model. The sub-sampled RTD is defined only at n sample points, spread between the start and end of the concentration data, as the length of the RTD is unknown. Sample points are otherwise placed where more variation is expected in the RTD. A full RTD is reconstructed from the sub-sampled RTD using linear interpolation.

5.2 Methodology

Equation 5.7 is used for maximum entropy deconvolution throughout this thesis. Maximum entropy deconvolution has been carried out using MATLAB, based upon the original implementation by Stovin *et al.* (2010b). It has, however, been completely recoded for this thesis to support additional configuration settings, data formats, and data analysis. The `fmincon` function is still used.

5.2.1 Configuration settings for maximum entropy deconvolution

The first two configuration settings are number and positioning of sample points. As linear interpolation is used to reconstruct the RTD, each sample point defines a change in the slope of the RTD. Therefore, changing the position and number of points is expected to have a high impact on the identified RTD.

Skilling & Bryan (1984) suggest that alternative constraint functions may be preferable to χ^2, hence this configuration setting is also examined here. As C effectively evaluates goodness-of-fit, correlation measures form suitable alternatives. Different correlation measures may place different emphasis on matching the shape, scale, or noise, discussed in Chapter 4.

`fmincon` introduces the fourth configuration setting, maximum number of iterations, which imposes an upper limit on `fmincon` so that it does not enter an infinite loop. Too few iterations, however, will stop the deconvolution process before convergence is achieved, i.e. before the RTD is identified. `fmincon` also introduces convergence criteria to determine when optimisation stops and an 'initial guess' that is the start point of the optimisation process.

5.2.1.1 Number of sample points

Stovin *et al.* (2007) suggested that as few as 7 points are necessary to define an RTD. A minimum of 10 sample points has therefore been used. 20, 40, 80, 120, 160, and 200 sample points have also been evaluated. After 200 points computational cost was observed to increase significantly. Stovin *et al.* (2010b) used 40 sample points.

5.2.1.2 Sample point distributions

Sample points are placed where more variation in the RTD is anticipated by incorporating basic assumptions about the expected RTD. Six sample point distributions have been developed using varying amounts of prior knowledge. These are described below and shown in Figure 5.1.

- **Equally spaced (ES):** A new development added for comparison, the sample points are evenly distributed across the input data. This distribution assumes no knowledge of the RTD.

- **Log from zero (LFZ):** The interval between sample points increases logarithmically from the start to the end of the input data. This distribution assumes more variation earlier in the RTD and less variation as time goes on, i.e. an exponential decay.

- **Downstream log (DwL):** From Equation 2.4 it follows that there must be some delay in the RTD if there is a delay between first arrival times. Three sample points are evenly distributed from the start of the input data until the difference in first arrival times, after which the interval between sample points increases logarithmically until the end of the downstream event. Three more sample points are evenly distributed until the end of the downstream data. First arrival time and end of event are defined as 1% of peak concentration. This is the sample point distribution previously used by Stovin *et al.* (2010b).

- **Double log (DuL):** Half of the sample points are distributed logarithmically from the start of the input data to the difference in time to peak, which is used as an estimate of delay. The other half of the sample points are logarithmically distributed away from the difference in time to peak to the end of the downstream data. A greater concentration of points around the time the RTD peak is expected allows for more uncertainty in its location.

- **Slope-based (SB):** This is a new development. An approximation of the RTD is used to distribute the sample points where its slope is expected to be greater. The approximation is computed using Fast Fourier Transformation (FFT) deconvolution (Madden *et al.*, 1996) with Blackman-Tukey Windowing (Blackman & Tukey, 1958; Harris, 1978) applied to the input data to improve accuracy, Equations 5.8-5.10, where $\mathcal{F}$ is the FFT, w is the window function, $\star$ is cross-correlation, α is length of the input data to be windowed (in this case 20%), and T is the last time or length of the input data. The absolute area of the first derivative of the approximation is evenly divided and sample points placed at the division points.

$$\hat{E}(t) = \mathcal{F}^{-1}\left(\frac{\mathcal{F}(u_{BT}(t))}{\mathcal{F}(y_{BT}(t))}\right) \tag{5.8}$$

$$\begin{aligned} u_{BT}(t) &= u(t).w(t) \star y(t).w(t) \\ y_{BT}(t) &= u(t).w(t) \star u(t).w(t) \end{aligned} \tag{5.9}$$

$$w(t) = \begin{cases} 0.5\left[1.0 - \cos\left[\pi\frac{2t}{\alpha T}\right]\right] & 0 \leq t \leq \frac{\alpha}{2}T \\ 1.0 & \frac{\alpha}{2}T \leq t \leq (1-\frac{\alpha}{2})T \\ 0.5\left[1.0 - \cos\left[\pi\frac{2t}{\alpha T}\right]\right] & (1-\frac{\alpha}{2})T \leq t \leq T \end{cases} \tag{5.10}$$

- **Double cubic (DC):** This is a new development. It is the same as the DuL distribution, but using cubic spacing. This results in a more spread out distribution, similar to the log from zero and slope-based sample point distributions, which is expected to allow greater flexibility in capturing complex profile characteristics, e.g. secondary peaks.

5.2.1.3 Constraint functions

In Chapter 4, twelve correlation measures were examined to identify potentially suitable correlation measures for solute transport model identification. Eight measures were found to be sensitive to transformation and transformation intensity while remaining insensitive to noise, and were therefore judged to be suitable as constraint functions. These are: the Burnham-Liard Criterion (BLC); χ^2; Furthest Fitting Cost Based Similarity (FFCBS); the Nash-Sutcliffe Efficiency Index

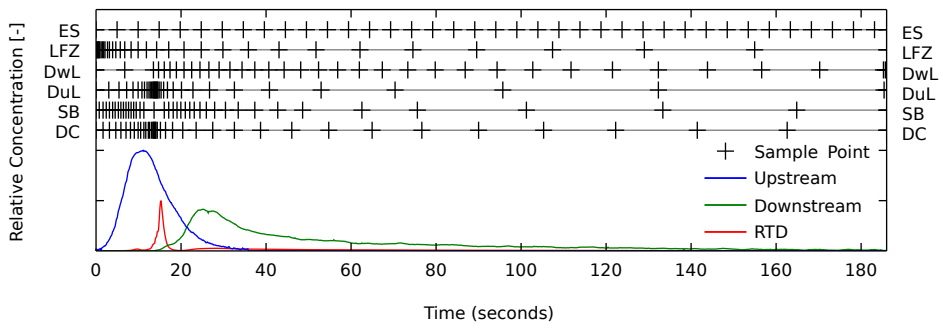

Figure 5.1: Example sample point distributions using 40 sample points

(R^2); Root Mean Square Deviation (RMSD); Young's Coefficient of Determination (R_t^2); the Integral of Squared Error (ISE); and Average Percent Error (APE). They have been converted into equivalent constraint functions for inclusion in the present sensitivity analysis. The error estimate σ of χ^2 is taken from Stovin *et al.* (2010b) as 5% of recorded value. In order to avoid confusion between R^2 values used to evaluate RTD performance (Section 5.2.3) and R^2 used as a constraint function, the latter will be referred to CR^2.

5.2.1.4 Maximum number of iterations

Maximum number of iterations in practice indicates a maximum amount of effort that should be used in deconvolving the RTD should an optimum RTD not be found earlier through convergence. 50, 100, 150, 200, 250, 300, and 350 iterations have been evaluated. A maximum of 200 iterations was used by Stovin *et al.* (2010b).

5.2.1.5 Convergence criteria

Initial testing indicated no sensitivity to convergence criteria. They have been left at `fmincon` defaults as previous work has used them successfully.

5.2.1.6 Initial guess (optimisation start point)

Initial testing indicated no sensitivity to the initial guess of the RTD. As the optimisation starting point it does not change the minimisation problem, but an initial guess that is closer to the final solution is a 'warm start' and has been shown to reduce the amount of time necessary to reach convergence in SQP algorithms (Fan *et al.*, 1988). Therefore the initial guess is fixed as the result of a FFT deconvolution with Blackman-Tukey windowing (as used in the SB distribution). Stovin *et al.* (2010b) used a flat line guess based on $\int_0^\infty E(\tau)d\tau = 1$.

5.2.2 Selection of data for sensitivity analysis

Several data sets from previously published laboratory studies were available. Within these, five mixing scenarios are represented; pipe flow (Hart *et al.*, 2013), open channel flow (Guymer, 1998), storage tank mixing (Guymer *et al.*, 2002), below-threshold (BT) surcharged manholes, and above-threshold (AT) surcharged manholes (Guymer *et al.*, 2005; Guymer & Stovin, 2011). The threshold is the surcharge depth at which hydraulic regime within a manhole switches from a fully-mixed (below-threshold) to a short-circuiting (above-threshold) system (see Section 2.3).

Two sets of typical solute transport concentration data from each of the five mixing scenarios were selected to ensure that conclusions would not be unduly influenced by a single test within each mixing scenario. The 10 paired upstream and downstream concentration profiles (henceforth referred to as 'experiments') are outlined in Table 5.1 and shown in Figure 5.2. In all cases, pre-processing of the raw data (i.e. calibration, smoothing, background removal) applied in the previous studies has been retained.

5.2.3 Analysing RTD performance

As previously stated, the full RTD is generated from the sample points via linear interpolation. A complete predicted downstream profile can then be generated by convolving the upstream profile with the full deconvolved RTD (Equation 2.6). A successful deconvolution is defined as one with high goodness-of-fit between the predicted and recorded downstream profiles, as measured by a relevant correlation measure. In Chapter 4, R_t^2, R^2 and APE were suggested as suitable for model evaluation in this context. The R^2 correlation measure has been chosen here for its high sensitivity to overall profile shape. With a perfect match, $R^2 = 1$, and for $R^2 \leq 0$ there is no correlation.

RTD shape can vary significantly without having a noticeable impact on R^2 value. As a result the entropy function (Equation 5.7) has been applied to the deconvolved RTD to evaluate smoothness. A smoother RTD is assumed to better represent a natural turbulent system, and therefore entropy values closer to zero are

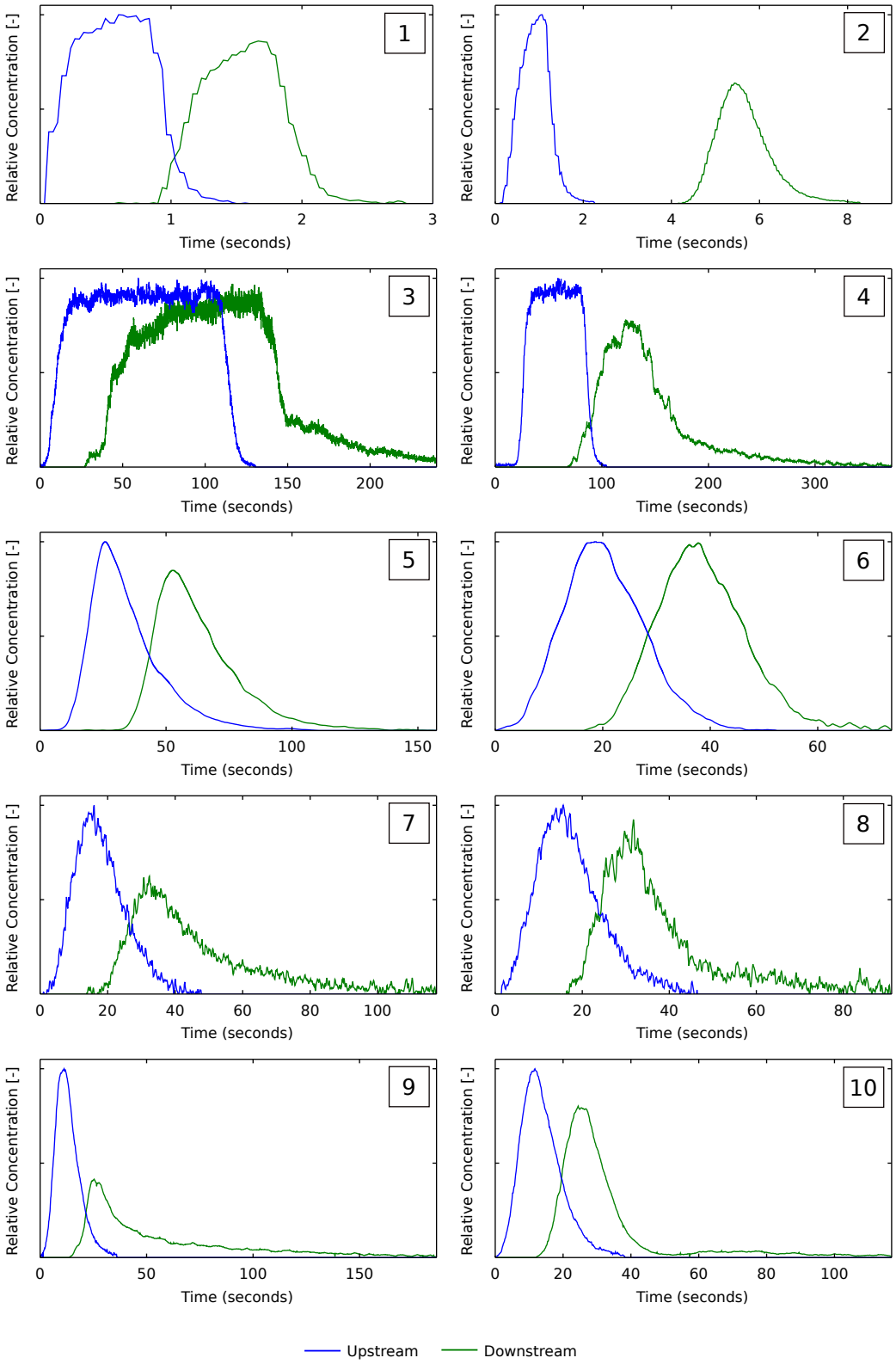

Figure 5.2: Upstream and downstream concentration profiles of experiments Time origin set to 0 and Experiment 1 and 2 zoomed in for display

Experiment	Description	Flow (l/s)*	Duration (s)	Mass recovery
1	24 mm Pipe[1]	1.084	150.0	84.42%
2	24 mm Pipe[1]	0.221	150.0	98.45%
3	Storage Tank[2]	6.9	240.2	100.00%
4	Storage Tank[2]	6	371.6	100.00%
5	Natural Channel[3]	13.7	157.3	101.96%
6	Trapezoidal Channel[3]	46.1	73.7	105.60%
7	400 mm BT Manhole[4]	1	117.3	100.00%
8	400 mm AT Manhole[4]	1	91.0	100.00%
9	800 mm BT Manhole[5]	1	186.0	100.00%
10	800 mm AT Manhole[5]	1	116.7	100.00%

[1]Hart *et al.* (2013), [2]Guymer *et al.* (2002), [3]Guymer (1998)
[4]Guymer *et al.* (2005), [5]Guymer & Stovin (2011) *As reported

Table 5.1: Summary of laboratory solute transport concentration data used

desired. An example of evaluating curve smoothness with entropy is shown in Figure 5.3.

Mass-balance of the RTDs has also been used for evaluation. Normally with perfect mass-balance, $\int_0^\infty E(\tau)d\tau = 1$. When mass recovery is not perfect, e.g. due to calibration error, then $\int_0^\infty \hat{E}(\tau)d\tau = \int_{-\infty}^\infty y(\tau)d\tau / \int_{-\infty}^\infty u(\tau)d\tau$. RTD quality was also evaluated as the ratio between the expected and actual sum of the RTD.

5.3 Results and discussion

The combination of configuration options and experiments resulted in 23,520 deconvolutions. These were carried out using batch processing on the Intel Xeon

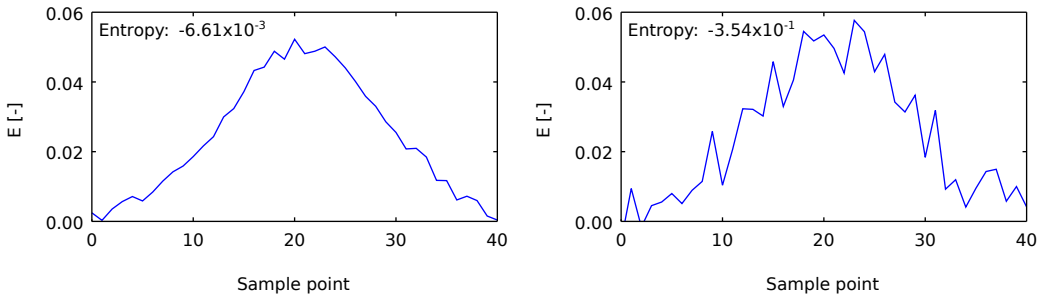

(a) Entropy closer to zero (b) Entropy further from zero

Figure 5.3: Entropy demonstration

X5650 nodes of the Iceberg parallel high-performance computing cluster at The University of Sheffield. Processing took approximately 187 days of CPU time. 61.4% of the predicted downstream profiles in comparison to the recorded downstream profiles exceed an R^2 value of 0.95 and 34.6% exceed 0.99 indicating that many combinations of configuration options are acceptable.

5.3.1 Mean and standard deviation of R^2 values

The mean (μ) and standard deviation (σ) of R^2 with respect to each configuration option are shown in Figure 5.4. Options that result in low mean R^2 values like the BLC, χ^2, ISE, and FFCBS constraints should not generally be used. They have therefore been eliminated from further consideration as robust constraint functions. The remaining configuration options are evaluated across only the CR^2, RMSD, R_t^2, and APE constraints.

Figure 5.5 illustrates the poor performance of the χ^2 and ISE constraints in contrast to R_t^2, before solution convergence. χ^2 roughly matches the shape but not scale and ISE only roughly matches shape. The performance of these two constraints does not improve with more iterations while the performance of the R_t^2 constraint does, which is typical of the other remaining constraints, CR^2, RMSD, and APE. χ^2 was originally used in maximum entropy deconvolution, but it is clear that other constraint functions perform much better.

Figure 5.4 also suggests that the DwL and ES sample point distributions perform poorly, and therefore these two distributions were eliminated from further consideration. Figure 5.6 confirms the elimination of DwL and ES by comparison to the SB distribution. Only the SB distribution fits the data for both Experiments 2 and 7. The other two distributions result in approximate fits for Experiment 7 only. For Experiment 2, DwL is mostly flat and ES is almost entirely coincident with the x-axis. This highlights the impact of poor sample point distribution choice.

After eliminating BLC, χ^2, ISE, FFCBS, DwL, and ES as configuration options, the mean R^2 values indicate improving goodness-of-fit for maximum number of iterations up to 150 iterations and near constant performance thereafter. As such, 50 and 100 iterations were also eliminated, at which point it was observed that

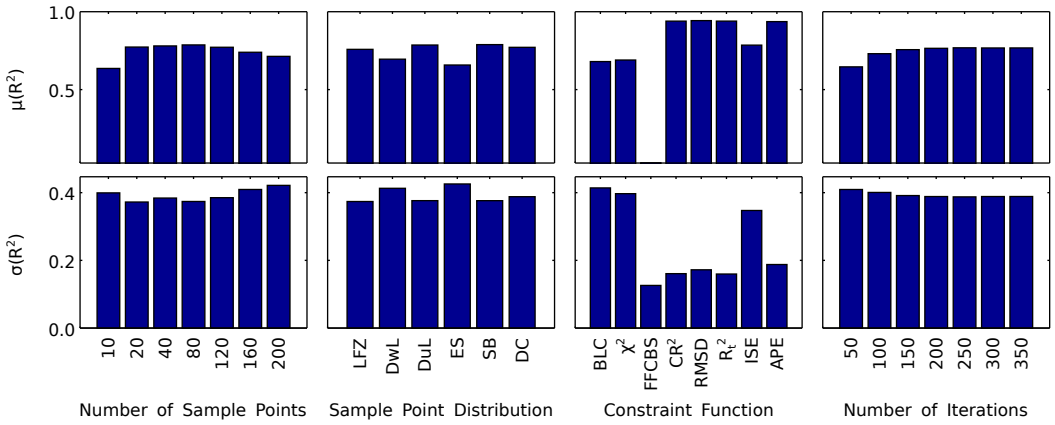

Figure 5.4: Mean (μ) and standard deviation (σ) of R^2 values by configuration option

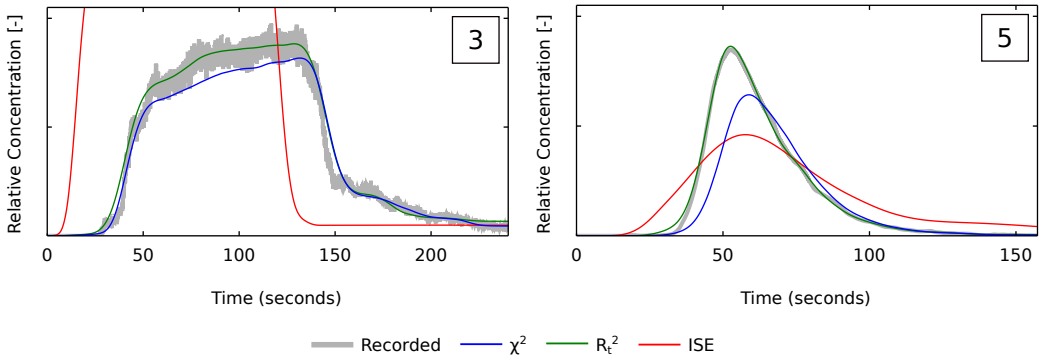

Figure 5.5: Downstream profiles of Experiments 3 and 5 predicted using RTDs deconvolved with: 40 sample points; the SB sample point distribution; 50 iterations; and the R_t^2, ISE, or χ^2 constraint

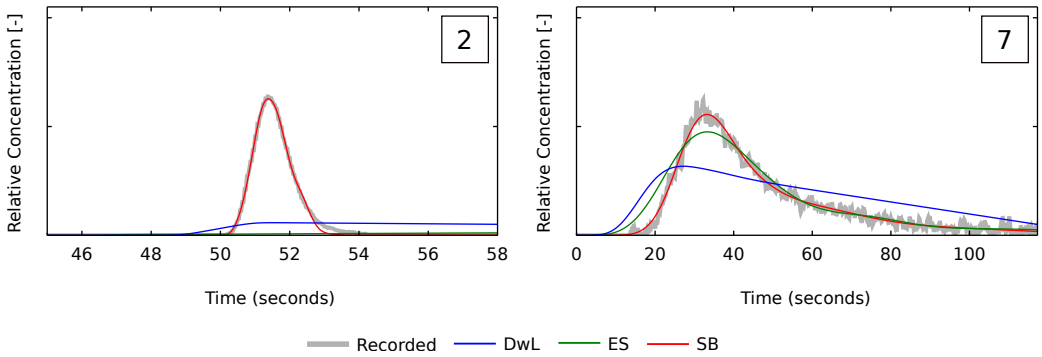

Figure 5.6: Downstream profiles of Experiments 2 and 7 predicted using RTDs deconvolved with: 10 sample points; the DwL, ES, or SB sample point distribution; 350 iterations; and the R_t^2 constraint

mean R^2 also tended to increase with number of sample points. (This is not evident in Figure 5.4.) Due to their low mean R^2, 10 and 20 sample points have been eliminated as well.

All 4,000 remaining R^2 values exceed 0.95, and 68.6% exceed 0.99. Differences in mean R^2 value are less than 0.002, and as such there is very little sensitivity of goodness-of-fit to the remaining options. This demonstrates the robustness of maximum entropy deconvolution for most combinations of 40-200 sample points, the LFZ, DuL, SB, and DC distributions, the CR^2, RMSD, R_t^2, and APE constraints, and 150-350 iterations.

5.3.2 Entropy values

Entropy values have been examined to further evaluate RTD sensitivity to the remaining configuration options. Mean entropy values for each experiment with respect to each option are shown in Figure 5.7. These are plotted for individual experiments as entropy is a dimensional measure. The figure provides insight into the sensitivity of the deconvolved RTD to the different configuration settings.

40 sample points results in the entropy closest to zero for 9 out of 10 experiments, which clearly recommends it, and therefore other numbers of sample points can be eliminated from consideration. The general trend of entropy values further from zero for increased number of sample points is consistently observed independently of data set. This is expected because a greater number of sample points provides increased potential for entropy as each sample point represents a possible change in the slope of the RTD.

The LFZ and SB distributions appear to perform almost identically across all experiments, with entropy values significantly closer to zero than the DuL and DC distributions for almost all experiments. The entropy values further from zero indicate that, although the DuL and DC distributions will generate RTDs with high goodness-of-fit, the shape of the RTDs is less smooth. They can therefore be eliminated from consideration.

Number and distribution of sample points have the highest impact on entropy and therefore on the quality of the deconvolved RTD. This is consistent with the problem formulation, i.e. changes in sample point position affect the numerical

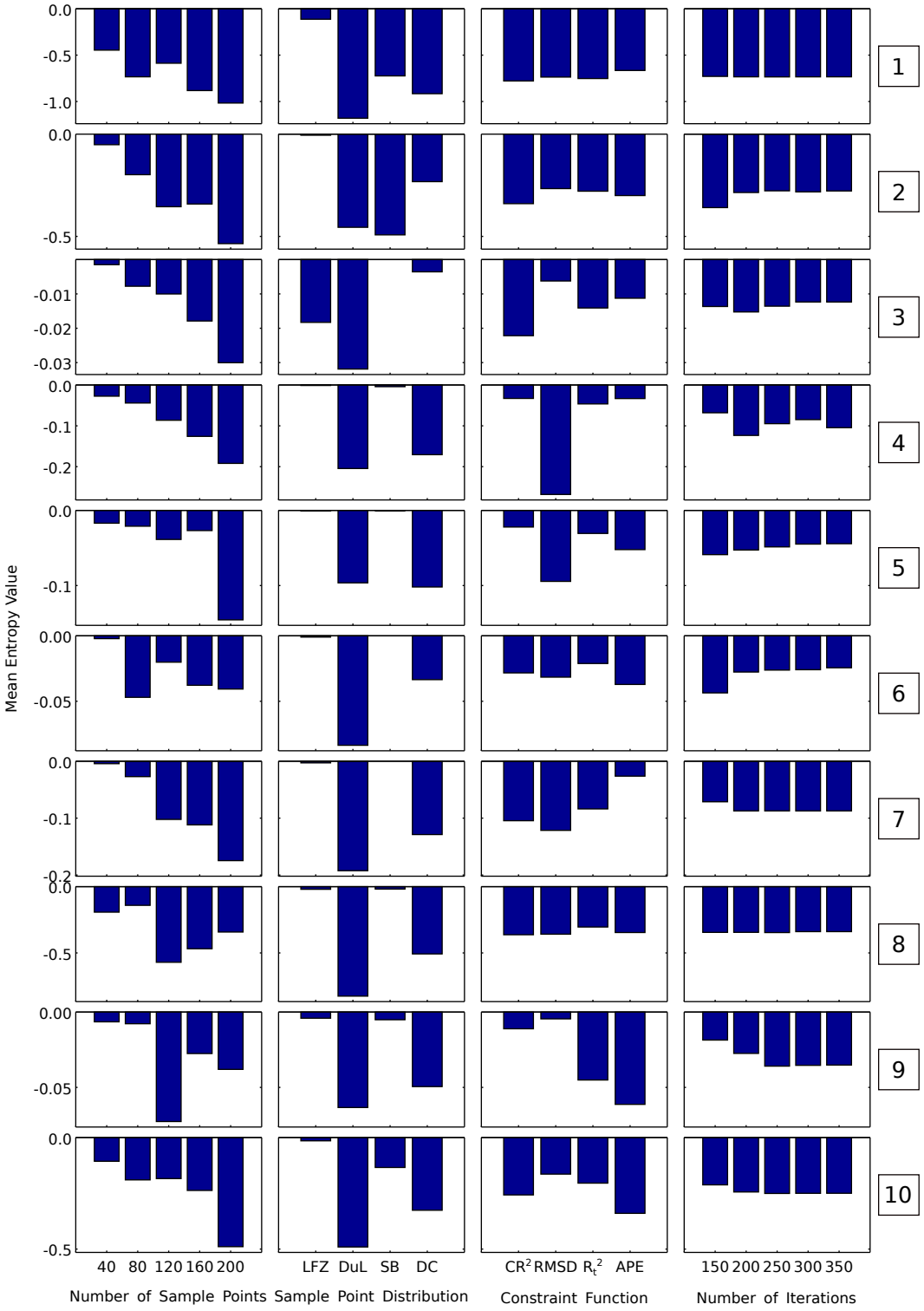

Figure 5.7: Mean entropy values by experiment and configuration option
Min $R^2 = 0.950$, mean $R^2 = 0.994$

problem being solved. Although there are multiple RTD solutions for each experiment, improved sample point positioning (and lower numbers of sample points) limits variation and results in smoother RTDs. That R^2 values remain high in these cases demonstrates the robustness of maximum entropy deconvolution as applied to solute transport.

A maximum number of iterations greater than 200 has minimal impact on RTD smoothness. Trends in smoothness with increased numbers of iterations are inconsistent. However, mean R^2 value continues to increase consistently with increased maximum numbers of iterations (Figure 5.4), and so 350 iterations can been recommended. The lack of change in RTD smoothness and predictive capability for some experiments implies that the vast majority of deconvolutions reach convergence before the maximum number of iterations is reached.

There is no clear trend in constraint function, with high variation between experiments. The smaller changes in entropy with respect to constraint are reasonable considering that constraints are interchangeable measures of error. As all of the constraint functions, CR^2, RMSD, R_t^2, and APE, are indicated to be perform similarly they are retained for further examination.

5.3.3 Mass-balance performance

Performance has been further examined by comparing the mass-balance of the remaining deconvolved RTDs, shown in Figure 5.8. The LFZ and SB distributions have been compared, using 40 sample points, the remaining four constraint functions, and 350 iterations. The SB distribution performs better, with all values close to 1, and therefore LFZ has been eliminated from consideration. The mass-balance performance shows no systematic variation with respect to constraint function.

5.3.4 Recommended configuration options

There is some evidence in the entropy data presented in Figure 5.7 that the paired experiments from each of the five data sets responded similarly to the four different constraint functions; this suggests that the optimal constraint function

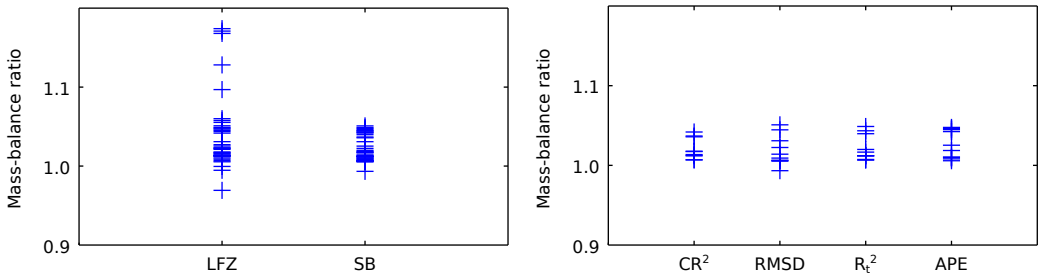

(a) Sample point distribution (b) Constraint function

Figure 5.8: Mass-balance results

may be linked to data set characteristics. However, general investigation and consideration of all results suggests that the R_t^2 constraint may perform slightly better. An additional argument in favour of R_t^2 would be that it is already a well used and understood measure in the field of solute transport. Therefore the new SB sample point distribution, 40 sample points, 350 iterations, and the R_t^2 constraint function have been identified as a robust set of configuration options.

5.4 Validation

Predicted downstream profiles and CRTDs generated with the robust configuration options (40 sample points, the new SB distribution, the R_t^2 constraint, and 350 iterations) are shown in Figure 5.9. The lower than expected final value of the CRTD for Experiment 1 is the result of the poor mass-recovery of the laboratory concentration data (Table 5.1). The predicted profiles give confidence that the identified configuration options are fit for use in deconvolution, with mean $R^2 = 0.994$.

5.5 Conclusions

Maximum entropy deconvolution has previously been successfully applied to laboratory solute transport data to identify the residence time distribution. The laboratory data was used to evaluate the impact of four different configuration settings on the deconvolved RTD. These settings are the number and distribution of

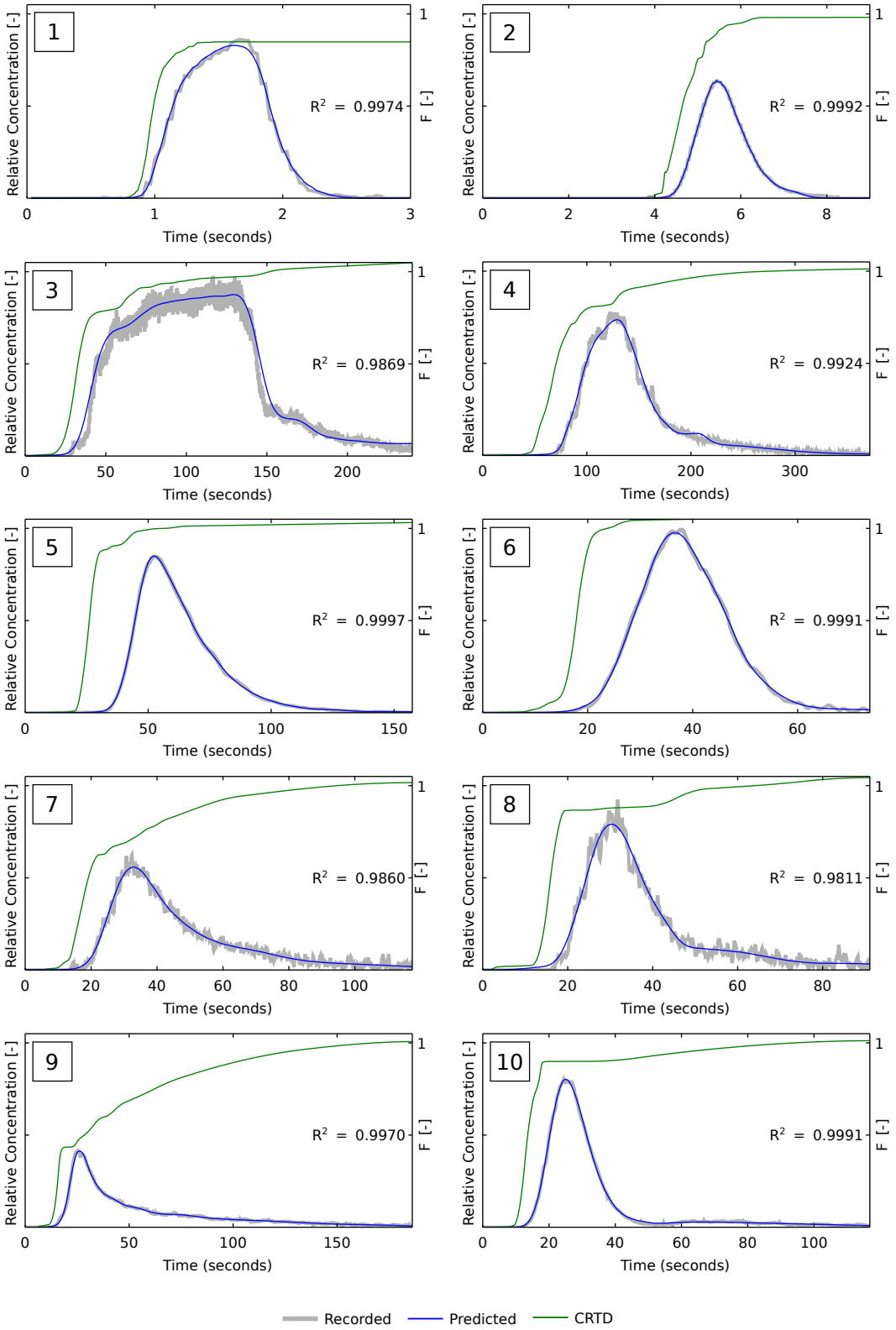

Figure 5.9: Predicted downstream profiles and deconvolved CRTDs for each experiment

sample points, the constraint function, and the maximum number of iterations.

The number and distribution of sample points particularly affects the smoothness of the deconvolved RTD, as evaluated by the entropy function. A greater number of sample points provides increased potential for noise as each point is a possible change in slope of the RTD. Smaller numbers of sample points therefore tend to result in a smoother RTD, as well as reduced computational expense. However, too few or poorly positioned sample points will result in a poor quality RTD. A new slope-based sample point distribution, where sample points are positioned based on an Fast-Fourier Transform deconvolution approximation, has been proposed and shown to perform best out of the six tested sample point distributions.

The constraint function affects the overall goodness-of-fit between the recorded downstream concentration profile and a predicted profile generated using the deconvolved RTD, here evaluated by R^2. While maximum entropy deconvolution has typically utilised χ^2 as the constraint function, alternative correlation measures place different emphasis on matching profile shape, scale, or noise. The present analysis suggests that χ^2 does not provide a robust constraint for solute transport data, but that the R^2, RMSD, R_t^2, and APE constraint functions do. There is some evidence that the optimal constraint function may be linked to specific data set characteristics, but as it is well understood in the field of solute transport, R_t^2 has been recommended as the most generically applicable constraint function. Maximum number of iterations had relatively little impact on predictive capability or RTD smoothness once 200 iterations were exceeded.

Across ten representative laboratory solute transport experiments, the recommended configuration options—40 sample points, the new slope-based sample point distribution, the R_t^2 constraint function, and a maximum of 350 iterations—result in a mean R^2 value for the predicted downstream profiles of 0.994. This confirms that maximum entropy deconvolution with the options recommended here provides a robust and effective means of identifying the RTD from laboratory solute transport data.

Chapter 6

Improvements to RTD smoothness

To extend the application of maximum entropy deconvolution for solute transport data, two improvements have been proposed. The first improvement, for RTD smoothness, is discussed here. Alternatives to the linear interpolation used to reconstruct the RTD, as well as changes to number of sample points, are suggested and evaluated. How the application of an alternative to linear interpolation affects potential over-sampling is also examined.

6.1 Introduction

In earlier chapters, deconvolved RTDs have been presented only as Cumulative Residence Time Distributions, as this allows easy interpretation of the underlying mixing processes they reflect. It becomes apparent when the RTD is plotted that there can be fluctuations in the RTD that are not necessarily visible in the CRTD (e.g. Figure 6.1). These fluctuations numerically cancel out during convolution and so do not have an impact on the predictive capability of the RTD. However, as a result of the fluctuations, the RTD may not correctly reflect the bulk mixing processes occurring when it is interpreted as a hydrodynamic model.

The presence of fluctuations in deconvolved RTDs highlights a potential issue

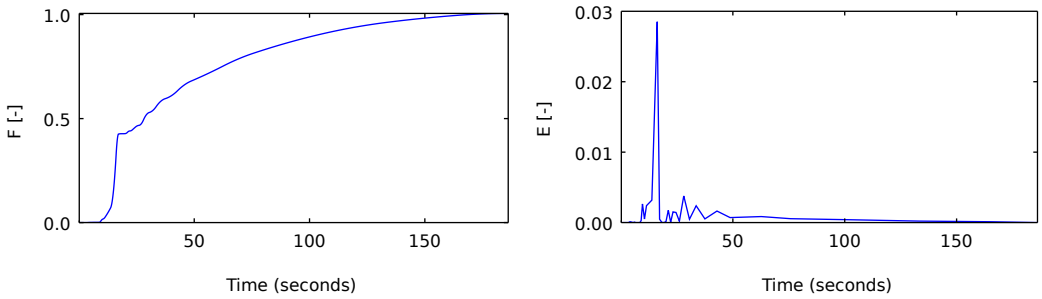

Figure 6.1: CRTD vs RTD deconvolved with linear interpolation

with the use of maximum entropy deconvolution for determining the RTD. As a black-box approach, the deconvolved RTD may provide only limited insight into hydrodynamic processes. Therefore if the deconvolution process were modified to minimise fluctuations, the quality of the deconvolved RTD and the resulting hydrodynamic interpretation should improve.

This chapter proposes an enhancement to maximum entropy deconvolution in the form of a new interpolation function and a re-evaluation of number of sample points. Several interpolation functions are presented and investigated. In a sensitivity analysis, three interpolation functions that result in a smoother RTD are investigated together with a range of sample point numbers. A second analysis, demonstrating the impact of interpolation function on over-sampled data is also carried out.

6.1.1 Factors affecting RTD smoothness

There are three main features of maximum entropy deconvolution which affect the smoothness of the RTD:

1. The r term of the objective entropy function (Equation 5.7). It is used as part of the evaluation of RTD smoothness and therefore influences final RTD shape.

2. Sample point distribution and number of sample points. Both have a high impact on RTD smoothness as shown in Figure 5.7.

3. The linear interpolation used to reconstruct the RTD from the sample

points. It affects the smoothness as it results in sharp changes in slope at sample points.

The next-neighbour average used to generate r means that in the absence of data characteristics that affect C (the deconvolution constraint, Equation 5.5), repeated iterations of the deconvolution process cause the RTD to tend towards a flat line (the lowest possible entropy). In comparison, most solute transport processes can be described with a uni-modal RTD similar to a Gaussian distribution, e.g. the ADE model (Taylor, 1954). The r term could therefore be set to a best fit Gaussian distribution to encourage a smooth RTD in that shape. This has been tested, and aside from losing some of the non-parametric benefits of having no prior assumptions about RTD shape, the impact on final RTD smoothness was consistently low and therefore it has not been investigated further.

A new sample point distribution could be developed to specifically generate a smoother RTD by incorporating additional expected RTD characteristics or forcibly increasing sample point spacing. However, this would remove some of the non-parametric flexibility of maximum entropy deconvolution. In contrast, the previous chapter showed that lower numbers of sample points could produce smoother RTDs in some cases. There is therefore scope for further adjusting the number of sample points, which could potentially also reduce computational requirements.

Neither adjusting the r term nor changing the distribution or number of sample points address the sharp changes in RTD slope caused by linear interpolation. The interpolation function can be changed to a more complex one which also smooths and—as a result—removes this effect. The interpolation function and the number of sample points have therefore been identified as key factors influencing RTD smoothness.

In Section 6.2, interpolation is investigated in more detail. Several potential alternative interpolation functions have been reviewed leading to a preliminary recommendation for further investigation in a sensitivity analysis, outlined in Section 6.3.

6.1.2 Over-sampling

When using linear interpolation, maximum entropy deconvolution can be sensitive to over-sampling. Over-sampling occurs when too large a number of sample points has been specified leading to tight temporal clustering of sample points. The tight clustering tends to result in significant oscillation between sample point values in the deconvolved RTD. The oscillation cancels out when convolved and therefore over-sampling does not affect the predicted downstream profile, but does significantly impact on RTD smoothness.

An analysis of the impact of interpolation and number of sample points on over-sampling is also outlined in Section 6.3.

6.2 Interpolation

Interpolation is the act of filling in unknown data at a given point using data from surrounding points. It is heavily used in Geographic Information Systems (GIS) and other geostatistical applications such as hydrological engineering. For example, rainfall may be estimated at a location based on the rainfall recorded at nearby rain gauges using interpolation (Teegavarapu & Chandramouli, 2005).

Within the deconvolution process, interpolation is used to generate $\hat{E}$ (the predicted RTD) to convolve the downstream predicted profile (Equation 2.6), which in turn is used to evaluating $\hat{E}$ in the constraint function (Equation 5.5). As such, interpolation is used multiple times for each iteration of the deconvolution. The maximum entropy deconvolution process is outlined in Figure 6.2, which highlights the repeated use of interpolation.

Linear interpolation, which is currently used, is the simplest type of interpolation. A straight line is drawn between the two closest sample points, and the interpolated data points are evaluated to be on that line. This has the benefit of being conceptually simple and easily executed. There are however, several more complex interpolation functions including, polynomial interpolation, Inverse Distance Weighting (IDW) and the Kriging estimation method (KEM). The latter two are the most commonly used interpolation functions in GIS applications (Zi-

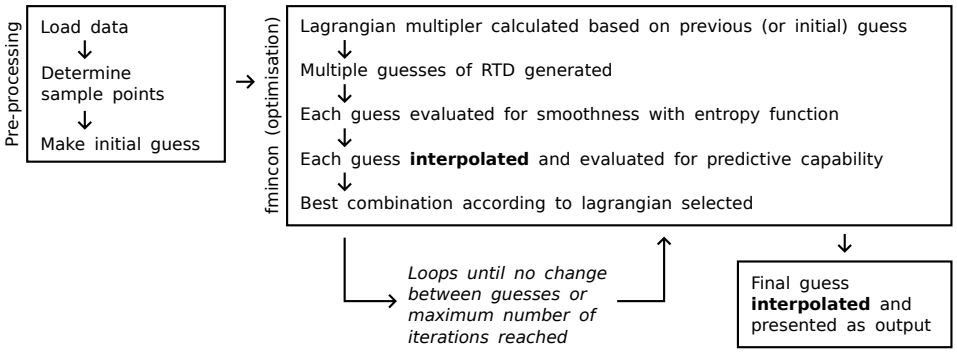

Figure 6.2: Deconvolution flowchart, highlighting interpolation

mmerman *et al.*, 1999). Both are primarily used in 2D interpolation, but can be adapted to 1D interpolation.

Linear interpolation with an Applied Moving Average (LAMA) and Gaussian Influence Estimation (GIE) are also introduced as potential replacement interpolation functions. These, and several other interpolation functions, are investigated and their suitability for maximum entropy deconvolution evaluated prior to the more detailed sensitivity analysis undertaken in this chapter.

6.2.1 Polynomial interpolation

Cubic interpolation and other polynomial interpolation schemes exist in many forms. In piecewise Hermite cubic interpolation (Fritsch & Carlson, 1980), the known sample points are used to estimate the derivatives of a cubic function that passes between them. The derivatives are then used to estimate the values at points being interpolated.

Splines can be considered a subset of regular polynomial interpolation (de Boor, 1978). They are specified to have continuous $n-1$ derivatives, so a cubic spline has continuous first and second derivatives. The result is that there are fewer possibilities for the interpolated line. Splines are commonly used in spreadsheet software to generate smooth lines in graphs.

The cubic and spline options of the MATLAB `interp1` function (The MathWorks Inc., 2011) have been used here as they are representative of the two classes of interpolation and exist as usable implementations. Examples of both methods are

shown in Figure 6.3, where they have been applied to the RTD from Figure 6.1 as a post-processing operation. The results show that spline interpolation is unsuitable for use in maximum entropy deconvolution as the interpolated RTD includes physically impossible values less than 0. However, cubic interpolation appears acceptable.

6.2.2 Inverse Distance Weighting

In IDW, the point being interpolated is a function of neighbouring point values weighted by distance (Armstrong & Marciano, 1994). As a result, IDW interpolation gives a smoothed line where closer points have a greater influence than further points, determined by the weighting function. The standard weighting function is linear, e.g. $\frac{1}{d^a}$ where d is the distance and a is an exponent (Armstrong & Marciano, 1994). Unfortunately, around the peak of the RTD, the weighting from nearby points will result in a catenary (or inverted catenary) effect between some sample points. This is unrealistic for an RTD and so IDW is judged an unsuitable interpolation function for maximum entropy deconvolution. IDW is evaluated in more detail in Appendix B.

6.2.3 Kriging Estimation Method

In KEM interpolation, a statistical model of the data being interpolated is built (Jernigan, 1986). This model is then used to predict the points being interpolated. There are several standard models, and as a result choice of model is an exercise similar to choosing either an ADE or ADZ model for solute transport data. This means on its own, model fitting is a complex exercise. Additionally, however, the uni-modal nature of the RTD further increases the complexity. This is explained in more detail in Appendix B, but in general results in KEM being unsuitable for inclusion in an automatic method such as maximum entropy deconvolution.

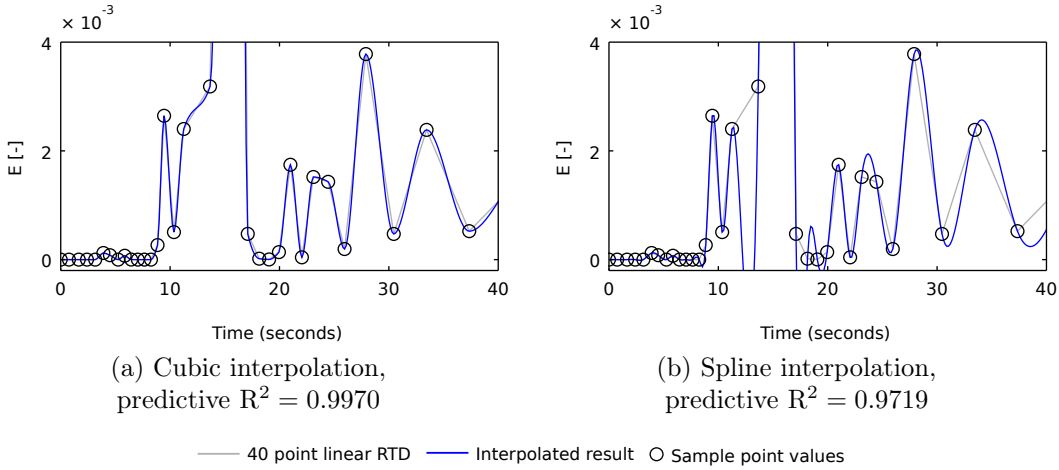

(a) Cubic interpolation, predictive $R^2 = 0.9970$

(b) Spline interpolation, predictive $R^2 = 0.9719$

Figure 6.3: Cubic and spline interpolation applied to Figure 6.1

6.2.4 Linear interpolation with an applied moving average

Linear interpolation with an applied moving average consists of firstly linearly interpolating the data and secondly applying a moving average of fixed window size. It is a practical and straightforward way of removing the sharp changes in slope in deconvolved RTDs.

Before LAMA can be applied to the RTD from Figure 6.1 as a post-processing operation, the window size must be determined. A window which is too short will produce no noticeable change from the linearly interpolated RTD, but too long and it will affect predictive capability. LAMA interpolation was tested with windows sizes up to 8 seconds. The 2 second window has almost no impact on predictive capability but improves RTD shape and so has been used. The LAMA interpolated RTD is shown in Figure 6.4.

6.2.5 Gaussian Influence Estimation

Gaussian Influence Estimation can be considered a modified IDW based approach to interpolation, specifically for use in deconvolution. It has been designed to accommodate uneven sample point spacing, including dense and sparse sample points. GIE has also been designed so that the interpolated values do not ne-

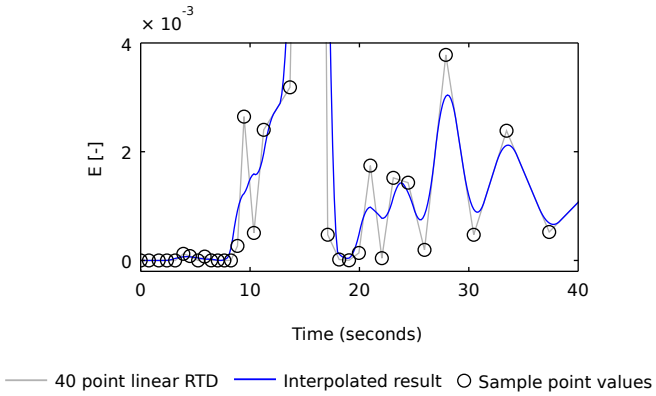

Figure 6.4: LAMA interpolation applied to Figure 6.1, predictive $R^2 = 0.9969$

cessarily pass through sample point values, allowing for more natural looking interpolation.

GIE uses weighting factors based on the distance between nearby sample points and assumes that the positive spatial autocorrelation (similarity of closer data points) of the RTD can be expressed as a Gaussian distribution centred about each point being interpolated. Closer sample points to the point being interpolated have more influence on the interpolated value according to a Gaussian distribution. The distribution for each point being interpolated is used to determine the weighting factors. The standard deviation of the Gaussian distribution is determined according to sample point spacing so that only minimal information is lost due to interpolation when sample points are close together.

GIE is presented in Equations 6.1, 6.2, and 6.3. Equation 6.1 shows the application of the weighting factors, where z_j is the point being interpolated, z_i is a known data point, and λ_i is the weighting factor for point z_i. The weighting factors are determined by Equation 6.2, where the standard deviation σ_j for the Gaussian weighting term is defined in Equation 6.3 as the mean distance between the three closest sample points a (earlier in time), b (closest), and c (later in time). This ensures that the distribution always takes into account at least two nearby sample points. If z_j coincided with sample point b, and sample points a and c were equidistant, both would be one standard deviation away.

$$z_j = \frac{\sum_{i=1}^{N} \lambda_i z_i}{\sum_{i=1}^{N} \lambda_i} \tag{6.1}$$

$$\lambda_i = \frac{1}{\sigma_j\sqrt{2\pi}} \exp\left(\frac{-(i-j)^2}{2\sigma_j^2}\right) \tag{6.2}$$

$$\sigma_j = (i_c - i_a)/4 \tag{6.3}$$

Using sample point spacing directly for the standard deviation results in sharp changes in σ as the nearest sample points change. This in turn results in an RTD with discontinuities. Taking the mid-points of plateaus in standard deviation, cubic interpolation has been successfully employed to ensure a continuous change in σ, shown in Figure 6.5, for the sample point spacing used in Figure 6.1.

In general sample points are placed farther apart when less change is expected in the RTD. This sparsity of sample points can lead to high σ values that indicate points further away than is reasonable should be taken into account, causing unrealistic variations in the interpolated result. To account for this, virtual sample points are used. They are placed equidistant between sample points when the distance between them exceeds the standard deviation of sample point spacing until this is no longer the case. The values at virtual sample points are linearly interpolated from the neighbouring real points. When GIE is applied to sequences of virtual sample points, in the worst case scenario the space between the real sample points will be effectively linearly interpolated but with a smooth transition.

GIE interpolation when applied to the RTD from Figure 6.1 as a post-processing operation is shown in Figure 6.6.

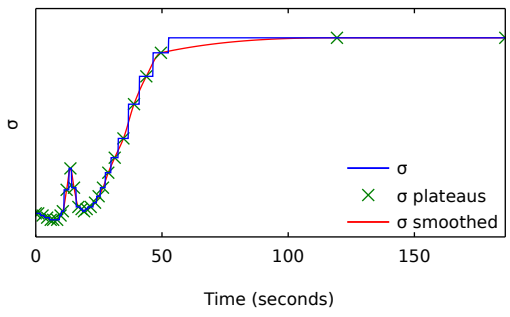

Figure 6.5: σ smoothing

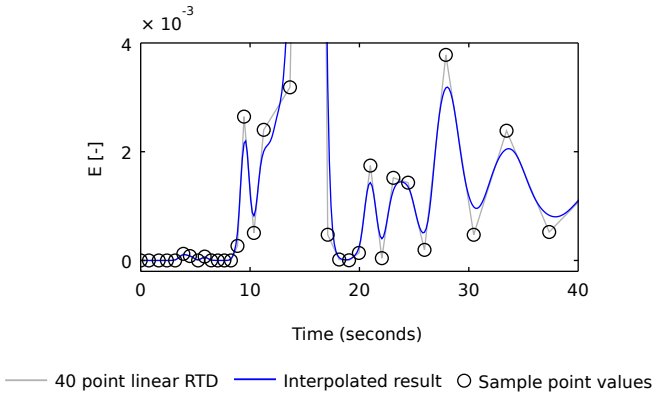

Figure 6.6: GIE interpolation applied to Figure 6.1, predictive $R^2 = 0.9965$

6.2.6 Suitable interpolation functions

Several interpolation functions have been investigated: cubic, spline, IDW, KEM, LAMA, and GIE interpolation. All of these were evaluated as a post-processing to the RTD from Figure 6.1. KEM interpolation was judged to be too complex for an automatic application. Otherwise, the remaining functions all resulted in RTDs without sharp transitions. Spline and IDW interpolation, however, produced unrealistic RTD shapes. Cubic, LAMA, and GIE produce reasonable test interpolations and so have been further evaluated for use in maximum entropy deconvolution.

6.3 Methodology

A sensitivity analysis comparing the three recommended interpolation functions (cubic, LAMA, and GIE interpolation) to the original linear interpolation function has been carried out. The analysis compares the deconvolved RTDs as predictive models using R^2 and evaluates hydraulic model quality through RTD smoothness using the entropy function. Deconvolution was carried out for all four interpolation functions using two representative solute transport data records.

To demonstrate the impact of smoothing on over-sampled data (Section 6.1.2), a second analysis has been carried out. Synthetic and laboratory concentration data has been deconvolved, with and without smoothing, at 40, and at 24 sample

points. The use of synthetic data allows for the examination of the impact of smoothing under known conditions.

6.3.1 Input data

6.3.1.1 Sensitivity analysis

Two sets of recorded laboratory upstream and downstream concentration profiles have been used; the below- and above-threshold 800 mm manhole data of Guymer & Stovin (2011), which were also used in Chapter 5 as Experiments 9 and 10. While not necessarily representative of all solute transport data, an improved interpolation function can be expected to improve the quality of the deconvolved RTDs in this case and therefore serve as a platform for investigation. The recorded data are presented again in Figure 6.7. The below-threshold data was used to generate the RTD in Figure 6.1.

6.3.1.2 Over-sampling analysis

Both synthetic and laboratory data have been used to look at the impact of interpolation on over-sampled data. To generate the synthetic data, an upstream temporal concentration profile and RTD have been generated as normal distributions. The downstream concentration profile was then created as the convolution of the upstream profile and RTD. Normal distributions were chosen as being

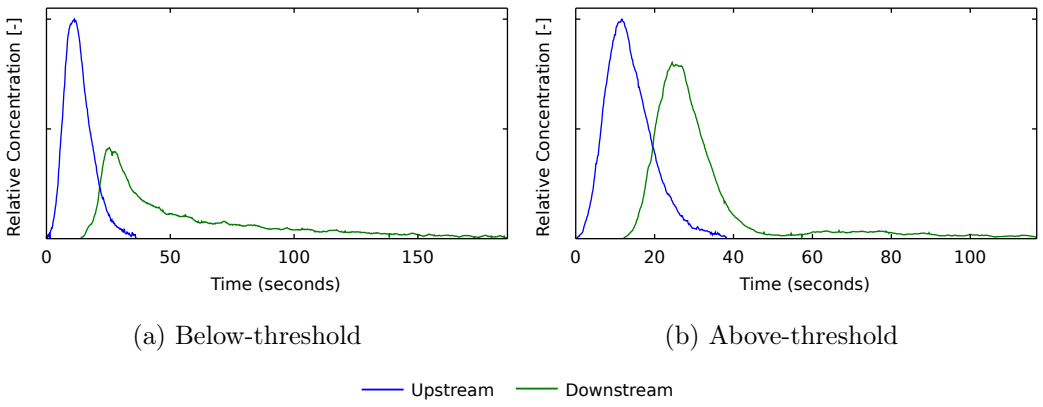

(a) Below-threshold (b) Above-threshold

Figure 6.7: Input solute transport data for sensitivity analysis

representative of pipe flow. The data is shown in Figure 6.8.

The main criterion for the synthetic data was that number of data points should be small enough to cause over-sampling when the recommended 40 sample points for deconvolution are used. As a result the synthetic upstream profile was chosen to be 50 points long and the synthetic RTD 100 points long. The convolved downstream profile is therefore 149 points long. The time step has been treated as 1 point (i.e. $dt = 1$ s). A mean of 25 points and standard deviation of 5 points has been used for the synthetic upstream profile. A mean of 50 points and standard deviation of 16.67 points has been used for the synthetic RTD. Area was normalised to 1 under both the upstream profile and RTD. In order to make a paired data record for deconvolution, the upstream profile was extended to 149 points using zeroes.

The laboratory data used was recorded from fluorometers in a 24 mm diameter pipe with a flow rate of 0.221 l/s by Hart *et al.* (2013). The data was pre-processed through calibration, the removal of background concentration levels, and the determination of start and end of the experimental event. Concentration values occurring before or after the event were set to zero. This data was also used in Chapter 5 as Experiment 2. For this study the zero concentration values were trimmed, resulting in data series 246 points long ($dt = 0.03\dot{3}$ s).

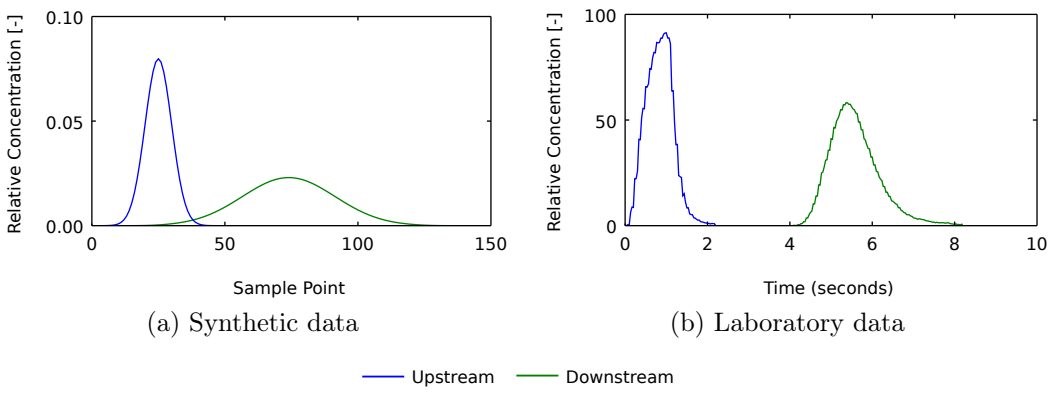

(a) Synthetic data (b) Laboratory data

Figure 6.8: Input solute transport data for over-sampling analysis

6.3.2 Deconvolution settings

6.3.2.1 Sensitivity analysis

Chapter 5 recommended the slope-based sample point distribution, 350 iterations, and the R_t^2 constraint function as robust deconvolution configuration settings, and these have been used here. 40 sample points were recommended, but the results also suggested that 20 sample points would produce good RTDs (similar predictive capability at increased RTD smoothness) with the slope-based sample point distribution. Therefore the range of 15 to 45 sample points has been chosen to include both 20 and 40 sample points. Deconvolution has been carried out in steps of 1 sample point. The alternative interpolation functions were used for all deconvolution steps shown in Figure 6.2 that require interpolation. As described in Section 6.2.4, a 2 second window size was used with LAMA interpolation. This is roughly equivalent to 20% of RTD peak width, where RTD peak width is the duration of the largest roughly Gaussian spike in the RTD.

6.3.2.2 Over-sampling analysis

Deconvolution has been carried out at both 40 and 24 sample points with linear and LAMA interpolation. LAMA interpolation has been used as it functions independently of sample point spacing. To determine window size, test deconvolutions were carried out with window size varying from 3 data points to 35 data points. The largest window size that provided a visually smooth deconvolved RTD with a high predictive capability was chosen. For both the synthetic data and laboratory data, the LAMA interpolation coincidentally used a 21 point window size. For the synthetic data this is roughly equivalent to 20% RTD peak width, and for the laboratory data 35% of RTD peak width.

6.3.3 Evaluation of predictive capability

When the deconvolved RTD is convolved with upstream data, a downstream prediction is formed (Equation 2.6). The downstream prediction was compared to the recorded downstream data using the R^2 correlation measure to give an

indication of predictive capability (see Section 5.2.3).

6.3.4 Evaluation of RTD smoothness

In Chapter 5, the entropy function (Equation 5.7) was used to evaluate RTD smoothness. The entropy function provides a dimensional measure of the difference between the RTD and a smoothed equivalent, where values closer to 0 indicate a smoother RTD. With linear interpolation, only inflection points affect entropy value as the next-neighbour moving average of a line with a linear gradient is equal to the mid-point. The entropy function therefore directly reflects the number and scale of fluctuations in the RTD. When the RTD is a continuous smooth function, entropy becomes a more complex measure.

The number of inflection points (NIPs) in the RTD can be counted. The number of points where the slope is zero provides a measure of the variation in the RTD that may be cancelled out during convolution. Both NIPs and entropy were used to evaluate RTD smoothness in the sensitivity analysis.

RTD smoothness can be directly evaluated when synthetic data is used, as a comparison can be made between the known synthetic RTD and the deconvolved RTD. Results in Chapter 4 suggest that the Average Percent Error correlation measure (Kashefipour & Falconer, 2000) is suitable for this purpose, as it exaggerates small differences between profiles. APE describes the percentage difference between two time-series, with APE = 0 indicating perfect correlation and APE $\geq$ 100 indicating no correlation. An APE comparison between the deconvolved and known RTD was used in the over-sampling analysis.

6.4 Results and discussion

6.4.1 Sensitivity analysis

In total 248 deconvolutions were carried out for the sensitivity analysis. Figure 6.9 presents the predictive R^2, entropy, and NIPs values for each combination of interpolation function and number of sample points.

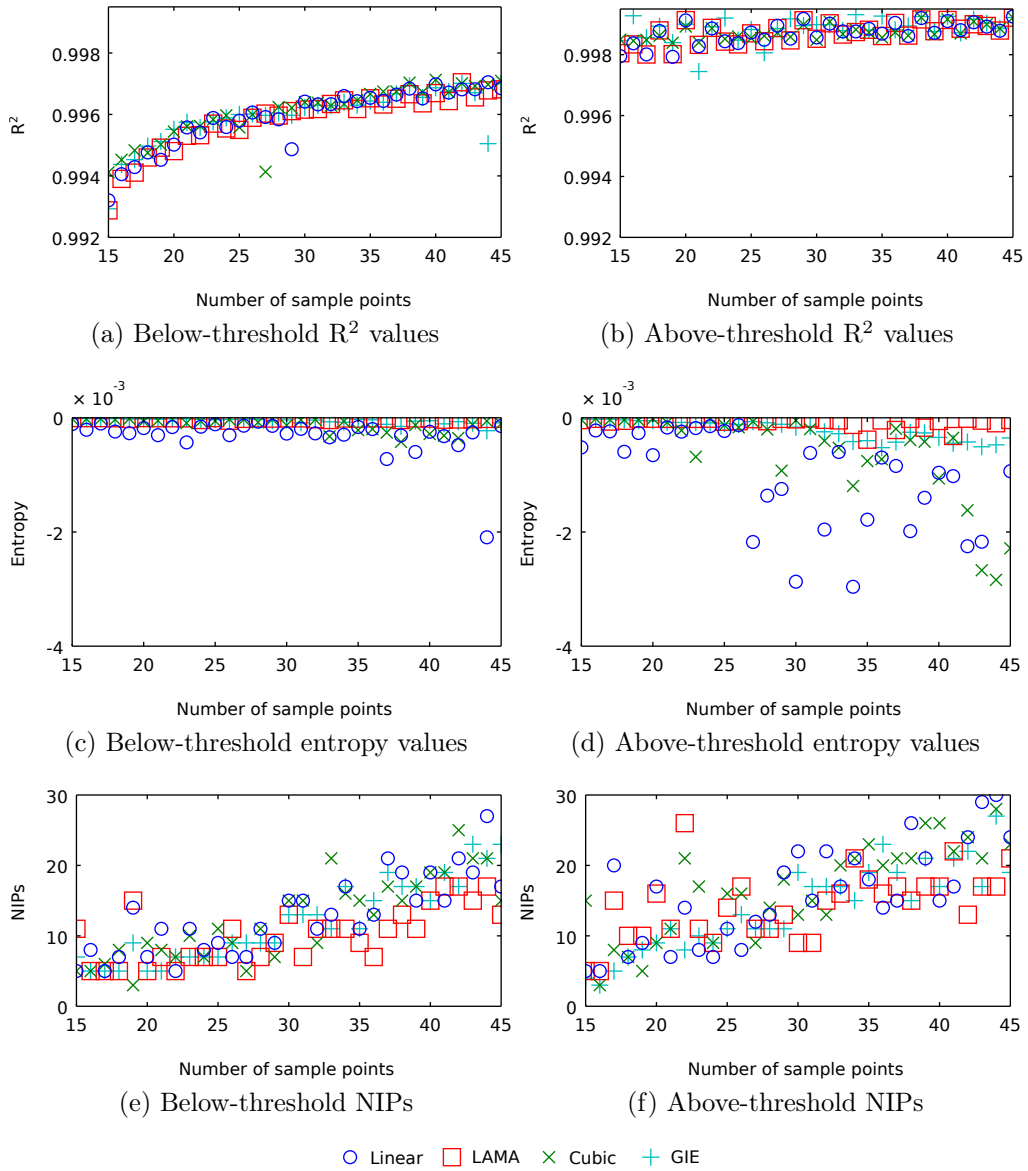

(a) Below-threshold R^2 values

(b) Above-threshold R^2 values

(c) Below-threshold entropy values

(d) Above-threshold entropy values

(e) Below-threshold NIPs

(f) Above-threshold NIPs

Figure 6.9: R^2, entropy, and NIPs values with respect to number of sample points for the below- and above-threshold data for each interpolation function

Mean R^2 value overall was 0.9973 with a minimum value of 0.9929 and maximum value of 0.9993, showing that all deconvolved RTDs form good predictive models. Figures 6.9a and 6.9b show the distribution of R^2 values with respect to interpolation function and number of sample points and in general show an increasing trend in predictive capability with more sample points. For the above-threshold RTD this is approximately linear. For this below-threshold RTD it may be broken down into two approximately linear trends, from 15 to 24 sample points, and from 24 to 45 sample points. The relative spread of R^2 values at a given number of sample points shows that interpolation function has a lower impact than number of sample points. There is no clear relationship between interpolation function and R^2 value which suggests choice of interpolation function should primarily be guided by entropy or NIPs.

Entropy trends for both the below- and above-threshold RTDs (Figures 6.9c and 6.9d) show increasing smoothness with fewer sample points, which is expected. This demonstrates the impact that number of sample points can have on RTD quality. LAMA interpolation performs best with entropy values significantly and consistently closer to zero. GIE entropy values, while not as close to zero, also show low variation with respect to number of sample points. The consistency of the entropy values suggests both the LAMA and GIE interpolation functions as good choices for a smooth RTD. Cubic and linear interpolation generally show entropy values closer to zero with lower numbers of sample points, but show significantly higher values and more variation with more sample points. The high values of entropy for linear and cubic interpolation can be attributed to the fact that both methods treat the sample points as observations of the RTD that the interpolated RTD must pass through.

Both the below- and above-threshold results show overall decreasing NIPs with fewer sample points (Figures 6.9e and 6.9f), which is consistent with the entropy results. Below-threshold NIPs values are approximately constant below 24 sample points, and increase at higher sample point numbers. This is similar to the below-threshold R^2 values. LAMA particularly appears to perform better with lower NIPs values at higher numbers of sample points. This is a result of the fixed moving average window size.

6.4.1.1 Recommendations

Higher R^2 value, entropy closer to zero, and lower NIPs are representative of smoother RTDs and are to be preferred. R^2 and NIPs primarily provide recommendation on number of sample points, while entropy provides recommendation on interpolation function. Number of sample points should be chosen (in combination with interpolation function) to provide the best balance of predictive capability and smoothness. In this instance, based on the results in Figure 6.9, 24 sample points appears to provide the best match of high predictive capability and low entropy. In the below-threshold data, 24 sample points is the change point between the two linear trends. In both cases, all four interpolation functions have similar predictive capability and NIPs values at 24 sample points. Entropy values are also low. As such it makes an excellent case for more detailed comparison. In general, LAMA and GIE can clearly be recommended over cubic and the original linear interpolation.

6.4.1.2 Visual inspection of deconvolved RTDs

Plots of the deconvolved RTDs for each interpolation function at 24 sample points are presented in Figure 6.10, together with the original 40 sample point linearly interpolated deconvolution result for comparison. Associated R^2, entropy, and NIPs values are presented in Table 6.1.

The plots show improvements in RTD smoothness. As a result of the reduced numbers of sample points the below-threshold peak RTD value is reduced. LAMA and GIE particularly show the greatest change in shape below-threshold. Above-

	Below-threshold			Above-threshold		
	R^2	Entropy	NIPs	R^2	Entropy	NIPs
Linear 40	0.9971	-2.0144×10^{-3}	21	0.9991	-9.6227×10^{-4}	15
Linear	0.9956	-1.5562×10^{-4}	8	0.9984	-1.4609×10^{-4}	7
Cubic	0.9960	-5.9767×10^{-5}	7	0.9986	-2.0130×10^{-5}	9
LAMA	0.9955	-3.8505×10^{-5}	7	0.9983	-1.5752×10^{-5}	9
GIE	0.9959	-2.6547×10^{-5}	7	0.9985	-8.8952×10^{-5}	9

Table 6.1: Deconvolution results summary for 24 sample points

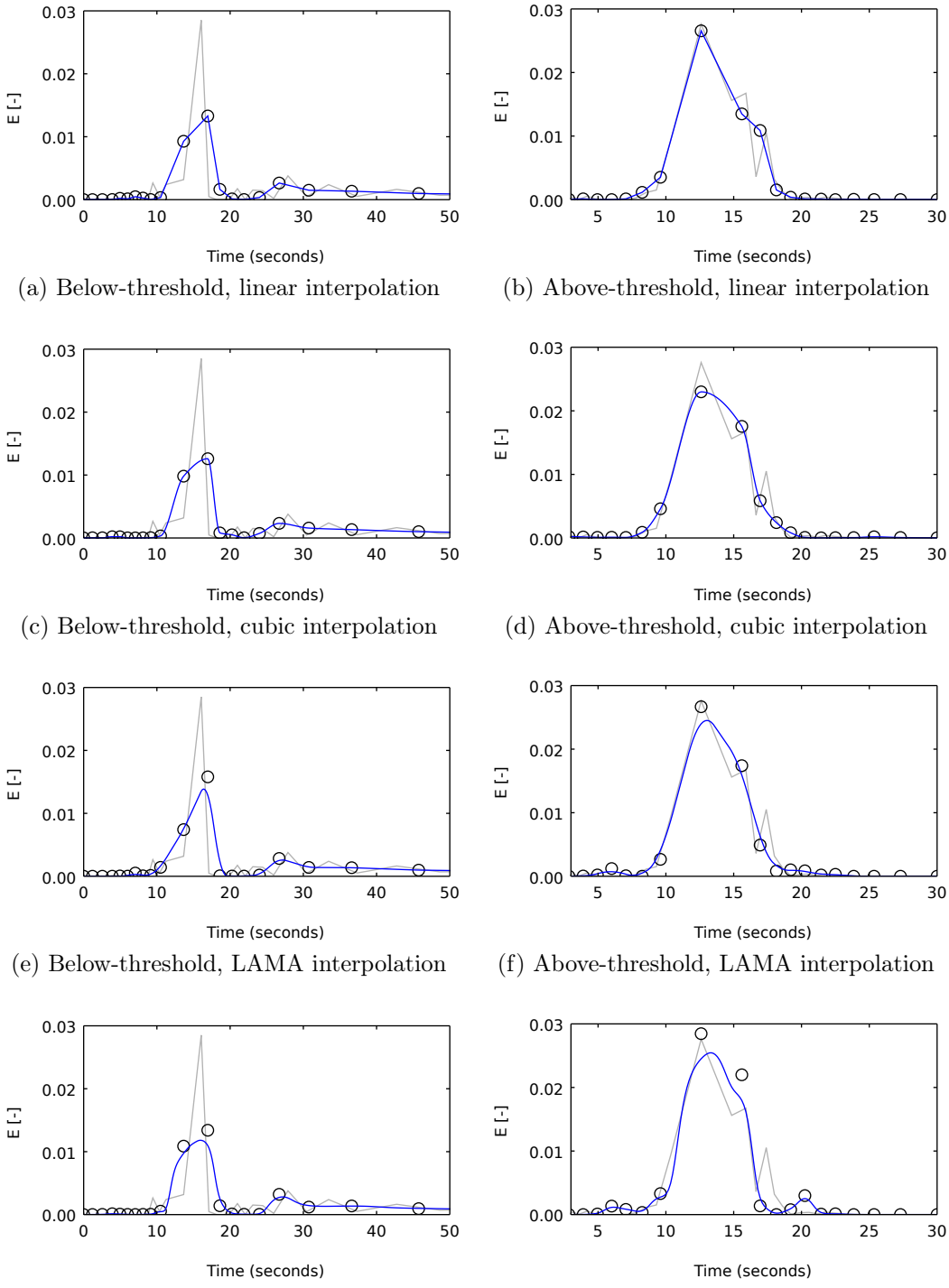

(a) Below-threshold, linear interpolation

(b) Above-threshold, linear interpolation

(c) Below-threshold, cubic interpolation

(d) Above-threshold, cubic interpolation

(e) Below-threshold, LAMA interpolation

(f) Above-threshold, LAMA interpolation

(g) Below-threshold, GIE interpolation

(h) Above-threshold, GIE interpolation

Figure 6.10: Deconvolved 24 sample point RTDs

threshold, RTD shapes are more similar across interpolation function. The small decreases in predictive capability at 24 sample points compared to 40 sample points suggests that the slope-based sample point distribution functions as designed.

Key RTD characteristics are consistently retained independent of interpolation function. Peak values and location are similar for each below- and above-threshold RTD across interpolation function. The secondary peak and tail in the below-threshold RTDs are also reproduced across interpolation function. Small secondary characteristics are evident in the above-threshold RTDs before and after the main peak with the LAMA and GIE interpolation functions only.

While peak RTD values have remained similar across interpolation function with 24 sample points, the peak values for the below-threshold RTDs are only approximately half the peak value for the 40 sample point linear RTD. The decrease is due to a sample point in the 40 point distribution not existing in the 24 point distribution. There has not been a similar decrease in peak for the above-threshold RTDs. Number of sample points, and the associated sample point positioning has played a significant role in altering RTD characteristics.

The lower number of sample points has positively influenced RTD smoothness, but potentially affected hydraulic interpretation. It may be over limiting the RTD, but there is no real indication which RTD provides the "correct" hydraulic interpretation. As with any experiment, ideally multiple runs should be carried out and deconvolved to reveal key system characteristics.

6.4.2 Over-sampling

R^2 and APE values from the over-sampling analysis, for both the synthetic and recorded data, are presented in Table 6.2.

6.4.2.1 Synthetic data

RTDs generated from the deconvolution of the synthetic data are presented in Figure 6.11. In all cases the deconvolved RTDs form excellent predictive models with $R^2 > 0.999999$, but there is significant variation in RTD shape.

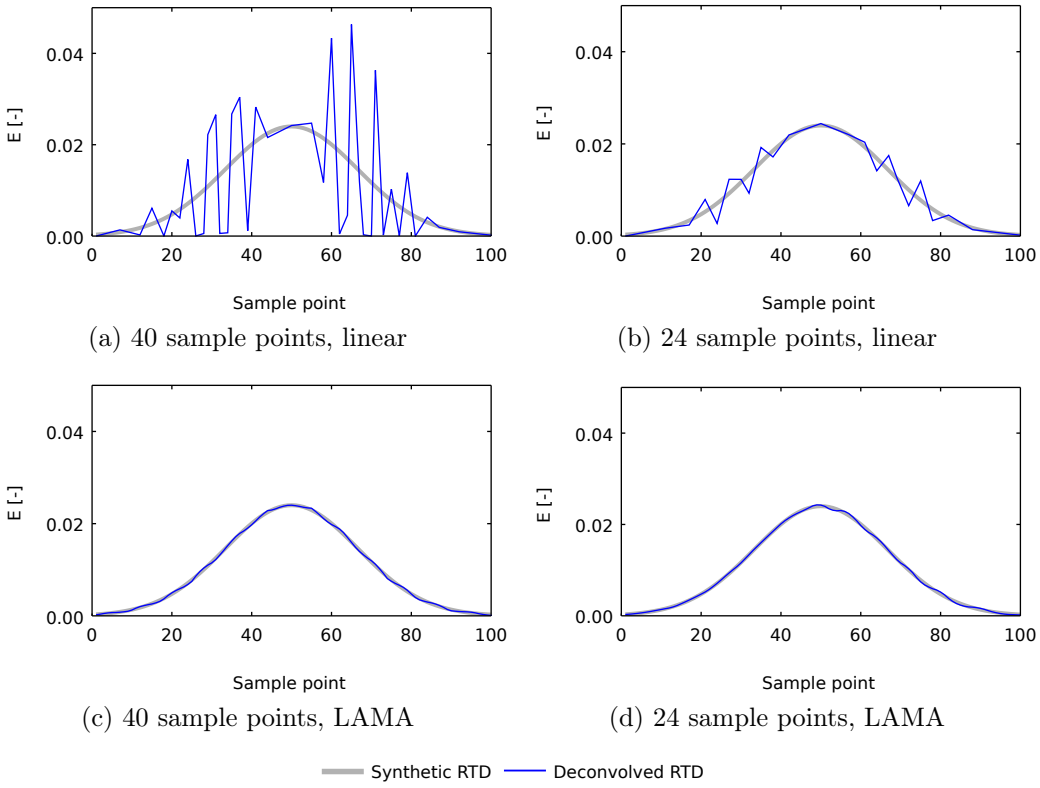

(a) 40 sample points, linear

(b) 24 sample points, linear

(c) 40 sample points, LAMA

(d) 24 sample points, LAMA

Figure 6.11: Deconvolved synthetic RTDs

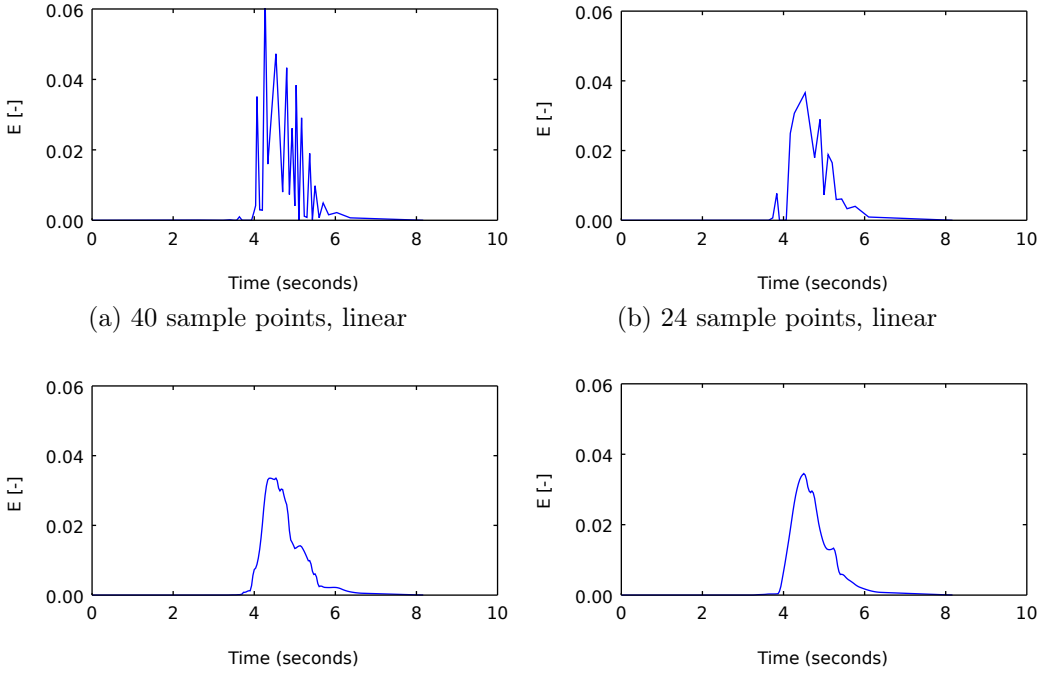

(a) 40 sample points, linear

(b) 24 sample points, linear

(c) 40 sample points, LAMA

(d) 24 sample points, LAMA

Figure 6.12: Deconvolved laboratory RTDs

Data type	Interpolation	Sample points	R^2	APE
Synthetic	Linear	40	0.9999999362	48.49
		24	0.9999991264	8.35
	LAMA	40	0.9999999556	1.65
		24	0.9999993859	1.35
Laboratory	Linear	40	0.9992231319	N/A
		24	0.9991585371	N/A
	LAMA	40	0.9991332380	N/A
		24	0.9991206907	N/A

Table 6.2: Comparison between interpolated RTDs and sample point numbers by R^2 and APE value

The RTDs deconvolved using linear interpolation show oscillation around the known synthetic RTD. The 40 sample point linear RTD shows extreme variation, reflected in a high APE value of 48.49. There is a repeating pattern of points below then above the known RTD which is the characteristic over-sampling oscillation. This is present to a much lesser extent in the 24 sample point RTD, although the APE value of 8.35 suggests that even 24 sample points may also be over-sampling in this case. However, the 24 point linearly interpolated RTD does correctly capture the basic RTD shape and could be considered satisfactory on its own.

LAMA interpolation gives a 'visually pleasing' and more accurate deconvolved RTD when using either 40 or 24 sample points. Both results show only minor variation between the known synthetic RTD and deconvolved RTD, with APE values less than 2. The 40 point LAMA RTD has a slightly higher APE value than the 24 point LAMA RTD, but both are still superior to the linear 24 point RTD in terms of shape and APE. LAMA has compensated for over-sampling.

Oscillation in the RTDs deconvolved with linear interpolation does not significantly affect predictive capability as in the convolution process as the RTD is shifted according to the integration variable τ in Equation 2.4. This can be thought of as a moving average process. Using LAMA interpolation, the moving average effect is relocated to the interpolation stages of deconvolution. The synthetic data LAMA RTDs actually also have (very) slightly higher predictive capability. LAMA interpolation could potentially result in all round better models and not just smoother RTDs.

6.4.2.2 Laboratory data

The results from the deconvolution of the laboratory data are presented in Figure 6.12. Again, the deconvolved RTDs form excellent predictive models with all $R^2 > 0.999$, and similarly there is significant variation in RTD shape.

The RTD deconvolved with the recommended 40 sample points and linear interpolation (Figure 6.12a) shows oscillation similar to its synthetic data counterpart, which is unrealistic in pipe flow. The RTD shape clearly indicates over-sampling. The 24 sample point linearly interpolated RTD shows a smoother profile that could be considered acceptable on its own, but still shows some signs of oscillation.

Similar to the LAMA interpolated synthetic RTDs, there is agreement between the LAMA interpolated 40 and 24 sample point RTDs. There is only minor variation between the two, which gives confidence that the deconvolved RTD is a good result and shows LAMA has compensated for over-sampling. Additionally, the similarity between the deconvolved LAMA interpolated RTDs based on the synthetic data and the known synthetic RTD further indicates that the RTD deconvolved from the laboratory data is a good result. Deconvolution of repeated laboratory trials could confirm this.

The non-Gaussian RTD shape could be indicative of either incomplete mixing due to less than full turbulence or due to non-Fickian advective processes dominating solute transport over short-distances (Hart *et al.*, 2013).

6.4.3 Recommendations

LAMA and GIE interpolation have both shown similar good performance. LAMA typically has a lower entropy value, but its fixed window size must be identified for each specific data set. Unfortunately this does not lend it to generic application, which otherwise is a strength of using maximum entropy deconvolution. GIE effectively uses an adaptive window size to avoid this, but it comes at the cost of slightly higher entropy and increased computational costs (longer deconvolution times). GIE also is a new measure that has not yet been proven to be robust. Either interpolation function could be recommended for specific detailed

investigation, but in general more work is needed before large scale application.

By definition, lower numbers of sample points remove the oscillation that is characteristic of over-sampling and provide an alternative to applying LAMA interpolation. This has been shown in the results where the 24 point linearly interpolated RTDs are somewhat similar to their LAMA interpolated counterparts. However, a reduction in number of sample points removes some flexibility from the deconvolution methodology. Sample point positioning becomes increasingly important and any error could result in a poor or unrepresentative RTD.

The application of LAMA allows for higher numbers of sample points to be used, avoiding over-sampling and keeping solution flexibility. Window size is critical in this case. It may be linked to RTD characteristics or sample point distribution. For practical purposes window size analysis could be conducted on one experimental configuration, and then applied to other similar configurations, e.g. similar flow rates. In the future choice of window size could potentially be automated.

24 or other lower numbers of sample points, and both LAMA and GIE interpolation can be recommended when a smoother RTD is expected or required.

6.5 Validation

Figure 6.13 shows a comparison between CRTDs generated with the recommended settings for a smoother RTD (24 sample points and GIE or LAMA interpolation) and their linearly-interpolated 40 sample point equivalents. The below-threshold rise in CRTD is less steep, and the above-threshold tail is slightly different. In both cases, however, the start and height of the steep rise are near identical and in general there is good overall agreement. The CRTDs generated from interpolated RTDs are smoother, but otherwise key CRTD characteristics are retained when using LAMA or GIE interpolation and 24 sample points in deconvolution.

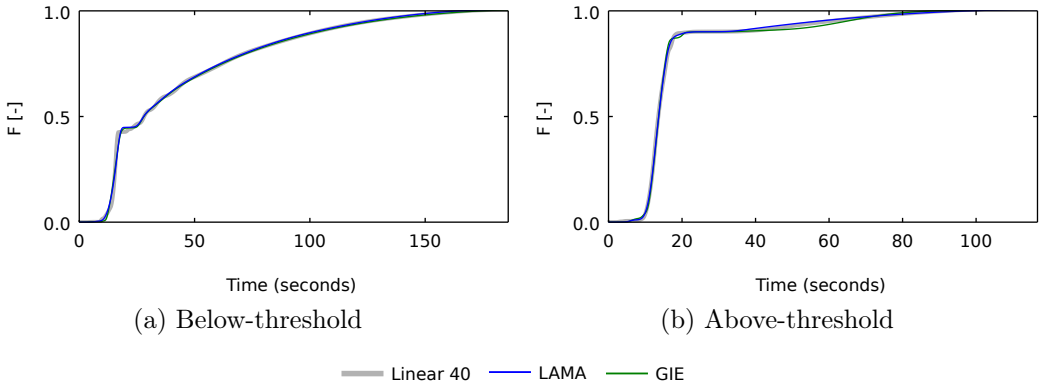

(a) Below-threshold (b) Above-threshold

Figure 6.13: CRTD comparison of interpolated results

6.6 Conclusion

Changing the interpolation function and number of sample points were proposed as means of improving the quality of RTDs deconvolved with maximum entropy deconvolution. An interpolation function which smooths gives the RTD a more realistic shape that minimises fluctuations that otherwise cancel out during convolution. Fewer sample points reduces the potential for variation and so also results in a more realistic, smoother, RTD. Several interpolation functions were initially explored, three of which were suggested for potential inclusion in maximum entropy deconvolution.

Two experimental solute transport upstream and downstream concentration profiles were deconvolved with the original linear interpolation, cubic interpolation, Linear interpolation with an Applied Moving Average (LAMA), and the specially developed Gaussian Influence Estimation (GIE) interpolation. The data were deconvolved with 15 to 45 sample points, but otherwise the previously recommended 350 iterations, R_t^2 constraint function, and slope-based sample point distribution were used. The deconvolved RTDs were compared with the Nash-Sutcliffe Efficiency Index (R^2) for evaluating predictive capability, the entropy function for evaluating smoothness, and the Number of Inflection Points (NIPs) to also evaluate smoothness.

All interpolation functions resulted in RTDs with good predictive capability. The consistent quality of results across different numbers of sample points indicates that the slope-based sample point distribution functions as designed and places

sample points effectively. R^2 and NIPs values decreased with fewer sample points, the former showing a decrease in predictive capability with smoother RTDs. The entropy values of the LAMA and GIE interpolated RTDs were much closer to zero (reflecting smoother RTDs) than linear or cubic interpolation, and so either LAMA or GIE interpolation are recommended. More detailed work may be necessary before the generic application of either, e.g. relating to the choice of LAMA window size.

In general, high R^2 values, entropy closer to zero, and low NIPs values are to be preferred as indicating smoother, good quality RTDs. Based on the results obtained, 24 sample points were found to produce smooth RTDs with high predictive capability. Examination of RTDs deconvolved with 24 sample points for each interpolation function showed that RTD shape is consistent across interpolation function, but that RTD shape varies with sample point positioning.

Synthetic solute transport data and recorded laboratory solute transport data were deconvolved with 40 and 24 sample points using linear and LAMA interpolation to investigate the possibility of reducing the effects of over-sampling in the sample point distribution. Both sets of data deconvolved with 40 sample points and linear interpolation showed signs of over-sampling, with oscillation in the deconvolved RTD. At 24 points using linear interpolation this effect was minimised, although not eliminated entirely. Using LAMA interpolation practically eliminated over-sampling effects in all cases, resulting in a smooth RTD, which in the case of the synthetic data was nearly a perfect match to the known RTD.

RTDs deconvolved with 24 sample points and LAMA or GIE interpolation are of high quality. When compared to those deconvolved with linear interpolation and 40 sample points as CRTDs all key characteristics are reproduced showing, that the interpretation of bulk mixing conditions remains similar. Either LAMA or GIE interpolation and 24 sample points can be recommended for deconvolving smoother RTDs when they are expected or required.

Chapter 7

The deconvolution of raw data

In Chapter 6, an improvement for deconvolution involving changing the interpolation function was discussed. In this chapter, as a new addition to the methodology, the potential to apply deconvolution to raw data (i.e. data without pre-processing) is explored. Different levels of pre-processing are used to investigate what, if any, pre-processing is necessary before maximum entropy deconvolution can successfully be applied to solute transport data.

7.1 Introduction

Raw data is the information collected directly from instrumentation and recorded as-is during experimental laboratory and field work, e.g. voltage readings. In most cases raw data must be pre-processed before it can be analysed. Saiyudthong (2003) describes the pre-processing of laboratory solute transport data as a complex chain of operations consisting of calibration, subtraction of background concentration levels, filtering and the trimming of the data record (reducing the length, or duration, of the record through data cut-off based on definitions of trace start and end times).

Researchers can spend significant amounts of time developing pre-processing steps that take into account their specific experimental setup. Guymer & O'Brien (2000) provide several paragraphs describing the calibration of fluorometers. Kas-

ban *et al.* (2010) clearly outlines and documents each step of the pre-processing used when obtaining the RTD using radiotracers. However, in many published papers pre-processing is only summarised, e.g. Guymer (1998), or effectively ignored, e.g. Wallis & Manson (2005). While pre-processing is generally not the specific focus of the research, it can impact significantly on the quality of the research findings. As an example of this, Joo *et al.* (2000) show how better pre-processing of data for an artificial neural network used in predicting coagulant dosing rate leads to a better learning rate, reduced error, and improved predictive capability. It is equally possible that poor pre-processing can lead to poorer results.

Given regularly sampled paired time-series experimental concentration data records for upstream $u(t)$ and downstream $y(t)$ data, maximum entropy deconvolution has been shown to robustly deconvolve the RTD from many types of pre-processed laboratory solute transport data (see Chapter 5). Assuming a linear instrument response, deconvolution of raw data should prove to be equally robust, allowing for a reduction in the time spent on, and potential errors introduced in, the application of pre-processing steps.

This chapter aims to demonstrate the applicability of maximum entropy deconvolution to raw solute transport data through a sensitivity analysis. Synthetic raw data of varying duration, noise level, background concentration level, and calibration has been generated to simulate different types of raw data. The quality of the RTDs deconvolved from the synthetic raw data have been evaluated to determine to what extent raw data can be deconvolved and whether any pre-processing steps remain necessary.

7.2 Methodology

Synthetic 'raw data' time-series have been created to investigate how input data impacts on the deconvolved RTD. An upstream profile has been convolved with a known RTD to create a downstream profile, and various pre-processing steps have then been applied in reverse.

7.2.1 Base synthetic data

The base synthetic data, analogous to pre-processed data, were created as the combination of a Gaussian upstream concentration profile ($\mu = 12.4$ s, $\sigma = 5.5$ s) and an RTD synthesised from the Advection-Dispersion Equation routing solution (Equation 2.2) using parameters $D = 0.014$ m^{2}s^{-1} and $\bar{t} = 13.5$ s. The downstream concentration profile is the convolution of the upstream profile and RTD. The data has a time step of $dt = 0.15$ s. Concentration levels below 10^{-4} have been treated as below instrument resolution and set to 0. The base data has 100% mass-recovery and is shown in Figure 7.1. It has been created to be representative of recorded laboratory pipe data with a 88 mm diameter, 5 l/s flow, and a distance between instruments of 2.7 m (Guymer & O'Brien, 2000).

7.2.2 Reversed pre-processing

Typical pre-processing of raw solute transport data follows these steps:

1. Apply calibration function
2. Subtract background concentration levels
3. Filter noise (e.g. smoothing or down-sampling)
4. Determine the start and end of the experimental event, then trim extra data

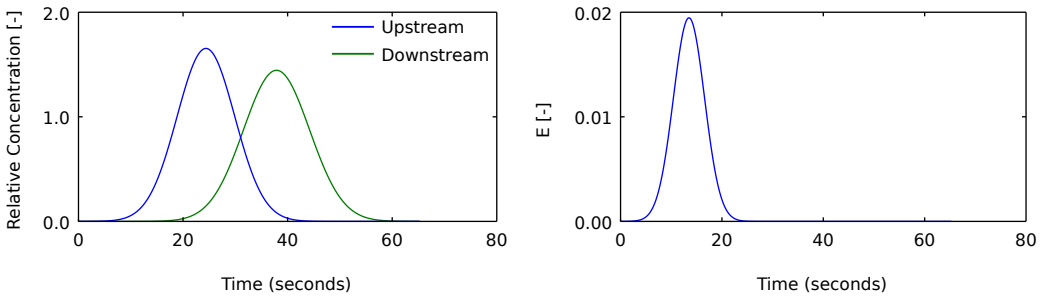

(a) Upstream and downstream profiles

(b) Known perfect RTD

Figure 7.1: Base synthetic data (representative of pipe flow)

To generate synthetic raw data these steps have been applied in reverse, as described below.

7.2.2.1 Data extension

Laboratory data is often recorded for a longer period than the created event, allowing for the start and end of the experiment to be recorded fully. With synthetic data the start and end is known, so to simulate a reversal of step 4, extra data points have been added before and after the base data, as shown in Figure 7.2, effectively extending the duration of the data record. Zeros were used in order to retain mass-balance. Data extension has been added as 0%, 10%, and 20% of record length on either side, e.g. an extension of 20% is 2 additional minutes before and after a 10 minute data record, resulting in a total duration of 14 minutes.

7.2.2.2 Addition of noise

Recorded data is subject to random variation from either within the system or due to the instrumentation, which is reflected as noise in the recorded data. Preprocessing step 3 is often used to limit the impact of noise through filtering, e.g. the application of a moving average. The base data has no noise and it must be added to simulate raw data. Random white noise has been used, as shown in Figure 7.3. Noise level is defined as peak noise intensity over peak upstream concentration. 0%, 5%, 10%, and 20% have been used. 20% noise is representative of 1 V of noise in a 5 V sensor and can be considered a conservatively high value. These levels correspond to Signal-to-Noise ratios of approximately ∞, 50, 25, and 12.5 respectively (Photon Technology International, Inc., 2005).

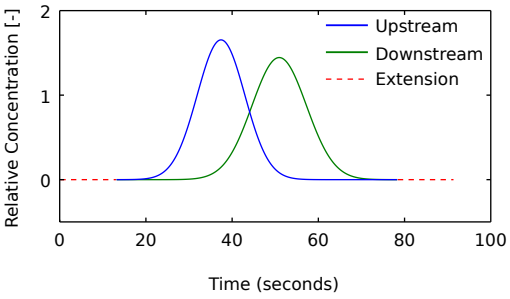

Figure 7.2: Data extension example (20%)

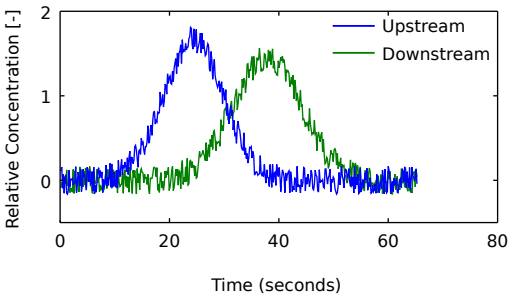

Figure 7.3: Data with 10% noise added

7.2.2.3 Addition of background

Background concentration refers to a constant or near-constant concentration level measured independently of any experimental event. It is often present in laboratory setups, particularly in those utilising recirculating systems. This step 2 of pre-processing is usually carried out to leave only the change in concentration caused by the event. This can be done by taking an assumed mean value or linear function derived from the recorded concentration levels and subtracting it.

To simulate raw data, a background concentration has been added to the base data, either as a constant value or varying linearly with time (sloped background). Constant background takes the form of a mean background concentration level, defined as a fraction of peak upstream concentration. Values of 0%, 10%, and 20% have been used. Background slope has been applied on top of each mean background level as an additional -2.5% increasing to 2.5% of peak upstream concentration for positive slope or 2.5% decreasing to -2.5% for negative slope. Addition of background is shown in Figure 7.4.

7.2.2.4 Reverse calibration

Calibrating raw data for linear sensors, pre-processing step 1, consists of multiplication by a known factor to relate sensor reading to concentration level. Therefore, to simulate raw data, multiplication by a factor has been applied ('uncalibration'). Factors have been chosen for the upstream and downstream profiles separately so that the peak values are a combination of 2, 3, 4 or 5 V, resulting in 16 combinations of uncalibration. 5 V is a representative maximum sensor value. Base data with uncalibration is shown in Figure 7.5.

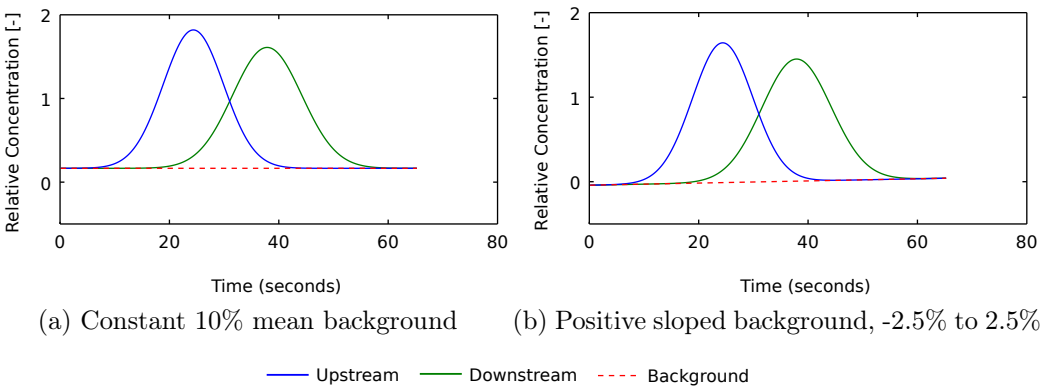

(a) Constant 10% mean background (b) Positive sloped background, -2.5% to 2.5%

Figure 7.4: Added background concentration level examples

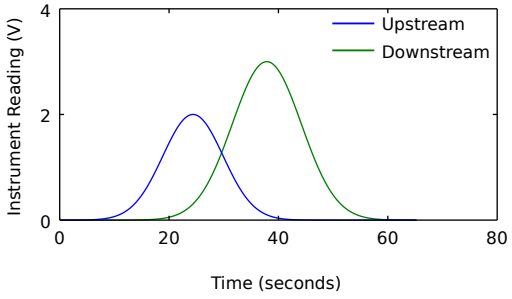

Figure 7.5: Reverse calibration example to 2 V upstream and 3 V downstream

7.2.3 Anomalous data

There are situations where laboratory data displays unusual characteristics not dealt with in routine pre-processing. Two such cases have been created and tested in order to examine how unusually low quality input data impacts on the deconvolved RTD.

The first case consists of recurring data spikes where single data points have significantly higher values, e.g. Figure 7.6a. Spikes have been introduced once every 133, 67, and 33 points (once every 20, 10, or 5 s) with intensities of 10%, 20%, and 40% of peak concentration non-coincidentally to the upstream and downstream concentration profiles. The second anomalous case consists of sequences of zero reading, e.g. short periods where sensors became unplugged (Figure 7.6b). 13, 33, and 67 consecutive points (2, 5, or 10 s durations) in both profiles have been set to zero at different times ranging through the entire data record, e.g. from 0 to 2 seconds or from 2 to 4 seconds.

The anomalous data cases have been applied to only a subset of the synthetic data, and are analysed separately from the main sensitivity analysis. The anomalous data has been applied to 6 types of raw data. These are the combinations of 0%, 5%, or 10% noise and 0% or 10% constant mean background (no slope) with an uncalibration of the upstream and downstream profiles to 3 V and 0% extension.

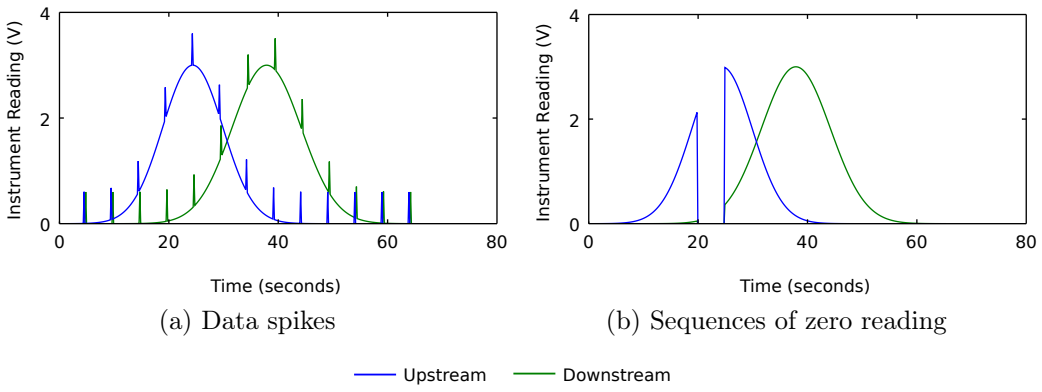

(a) Data spikes

(b) Sequences of zero reading

Figure 7.6: Anomalous data examples

7.2.4 Deconvolution settings

In Chapter 5, deconvolution was recommended to be carried out using 40 sample points, 350 iterations, the slope-based sample point distribution and the R_t^2 constraint function. However, the recommended 40 samples points has here been changed to 20 sample points to reduce the potential for noise and over-sampling (see Chapter 6) in the deconvolved RTD.

7.2.5 Analysis

7.2.5.1 Predictive capability

The RTD forms part of a predictive model (Equation 2.6), which can be evaluated through the R^2 correlation measure (see Section 5.2.3). For this analysis, the deconvolved RTD is scaled by the mass-balance of the synthetic raw data from which it was derived to account for uncalibration. The base upstream profile is then convolved with the scaled deconvolved RTD to generate a predicted downstream concentration profile, which is then compared with the original downstream concentration profile.

7.2.5.2 RTD comparison

Considering that the RTD used to generate the synthetic raw data is known, a direct evaluation of RTD quality can be made by comparing the scaled deconvolved RTD with the original synthesised RTD using the APE correlation measure (see Section 6.3.4).

7.2.6 Validation

To verify the applicability of the results obtained to a wider range of raw data, e.g. data with asymmetric and other more complex RTD profiles, genuine raw laboratory data has been deconvolved. As discussed in Section 2.3, Guymer *et al.* (2005) suggested that surcharged manholes experience two hydraulic mixing re-

gimes dependent on surcharge depth, a below-threshold fully mixed condition and an above-threshold short-circuiting condition. These conditions have previously been shown to have differing RTDs when deconvolved from pre-processed data, e.g. Figure 2.9. The raw recorded solute transport data from a below- and above-threshold surcharged 800 mm manhole at a 0.88 l/s flow rate have therefore been selected for deconvolution from O'Brien (1999), shown in Figures 7.7a and 7.7b.

Minimal pre-processing has been applied. This comprises a sloped background subtraction based on the mean of the first and last 5 seconds of data as background concentration level estimations. The raw data after minimal pre-processing is shown in Figures 7.7c and 7.7d. Noise level has been estimated as around 13% for both data records. Deconvolution was carried out with the previously recommended settings. 40 sample points are used to account for the longer data record, and as the RTD does not need specifically to be inspected.

7.3 Results and discussion

The different combinations of synthetic input data with different levels of data pre-processing resulted in 1,728 deconvolutions being carried out. The anomalous data resulted in an additional 816 deconvolutions.

7.3.1 Predictive capability

Figure 7.8a shows all of the R^2 values evaluating the comparison between the base and predicted downstream profiles. These values exclude the anomalous data. Each group of 3 columns represents a mean background level, and each individual column corresponds to a different background slope (i.e. positive, no slope, or negative). Each column contains all combinations of uncalibration. Every nine columns represent a specific noise level.

Overall predictive capability is excellent, with mean $R^2 = 0.9958$. There is a clear trend of decreasing predictive capability with increasing noise and increasing mean background level. The greater spread in the columns further to the right indicates that the impact of uncalibration increases with greater background levels

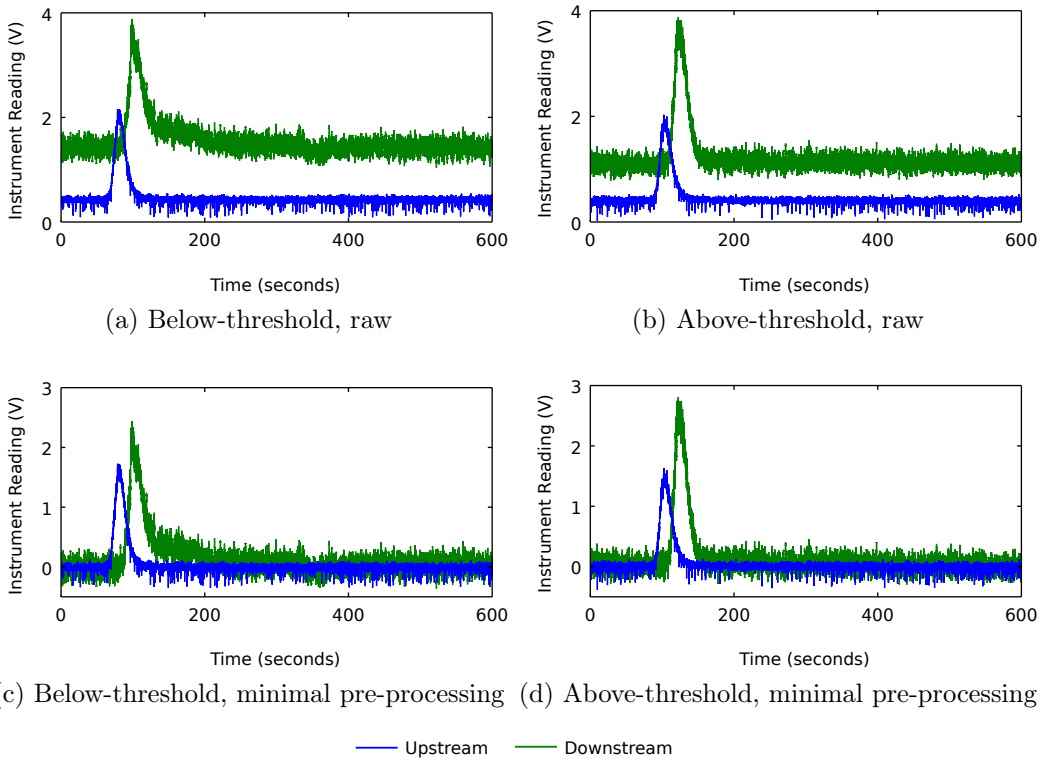

(a) Below-threshold, raw

(b) Above-threshold, raw

(c) Below-threshold, minimal pre-processing

(d) Above-threshold, minimal pre-processing

Figure 7.7: Raw data records for validation

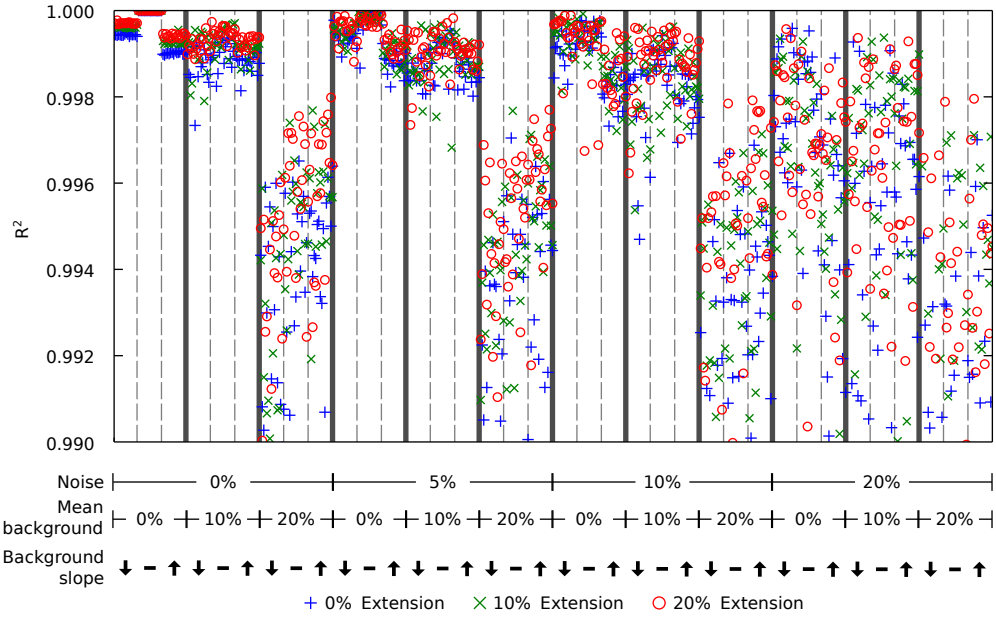

(a) R^2 values comparing the perfect downstream profile with a predicted downstream profile created using the perfect upstream profile and a deconvolved RTD

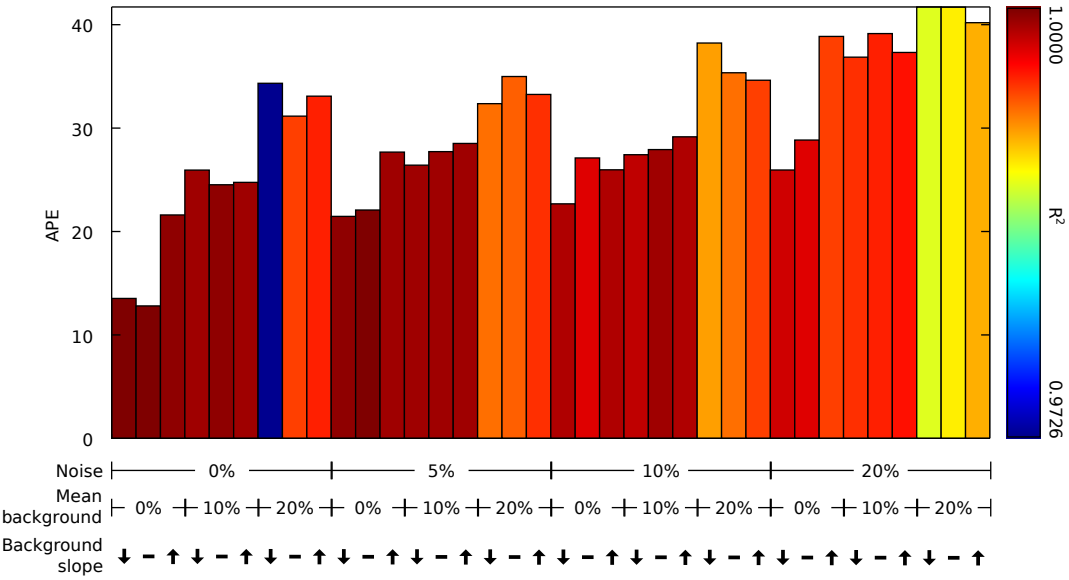

(b) Mean APE value, comparing recovered and known RTD

Figure 7.8: Impact of reversed pre-processing on R^2 and APE value

and noise, but does not appear to be systematic. Background slope and extension have relatively little impact on predictive capability, but may be explained.

A positive background slope leads to lower R^2 values than a negative background slope when mean background level is 0%, independent of uncalibration. The negative portion of the downstream profile with a negative background slope cannot be matched in the deconvolution process, while the greater positive portion due to a positive background slope can be. RTDs deconvolved from the latter will more greatly over predict mass-balance than the former will under predict it. The greater over-prediction results in poorer R^2 values.

The increase of R^2 with extension at no background and no noise may be explained by the wider spacing of sample points that results from the same 20 points being distributed over a longer profile. This reduces the relative potential for noise, leading to an improvement in RTD quality with extension. When there is non-zero background, there is a consistent period of time at the start of the profile when the downstream prediction does not match the synthetic raw data. This period is fixed in length regardless of total duration and therefore, as extension increases, represents a proportionately smaller period of time. The period of poor fit therefore has less negative influence on the R^2 value at greater extension, increasing R^2 values overall.

7.3.2 RTD quality

Mean APE values for the comparison between the known and deconvolved RTDs are shown in Figure 7.8b. The effects of extension and uncalibration have been combined as they have no impact on predictive R^2 value in the ideal scenario of no background and no noise. Those RTDs are therefore assumed to be of similar quality, although realistically there is some variation due to the deconvolution process. Bars are coloured by mean predictive R^2 value (from Figure 7.8a), showing the relationship between RTD quality and predictive quality.

Figure 7.8b shows similar trends to Figure 7.8a, breaking down into clear groups in RTD quality around noise and mean background level. The lowest observed mean APE value is 13.00, indicating that the deconvolved RTD will always vary from the actual RTD. APE value approximately doubles with either the addition

of 10% constant background or 10% noise. As background and noise level increase further so does APE value. In general, background concentration appears to have a greater impact on RTD quality than noise level as 20% noise with 0% mean constant background has a lower mean APE value than 0% noise and 20% mean background level.

The variation in RTD quality due to background slope can be seen again. APE values for positive background slope are significantly higher than their negative background slope counterparts due to the greater over-prediction of the RTD when there is a positive background slope. Despite relatively small variations in R^2 value, the larger difference in APE value shows significant change in RTD shape.

7.3.3 Visual inspection

Figure 7.9 shows the predicted concentration profiles and deconvolved cumulative residence time distributions (CRTDs) for three cases. The first case has 5% noise and no background. The second case has 10% noise and 10% mean background (no slope). The third case has 20% noise and 20% mean background (no slope).

The figures show decay in predictive capability and RTD quality with increased noise and background. Lower noise and background levels should therefore be preferred to keep RTD quality high. This confirms the results shown in Figures 7.8a and 7.8b, suggesting 10% noise and 10% background levels as limits for a fit-for-purpose deconvolved RTDs. This corresponds to approximate lower limit cut-offs of $R^2 = 0.998$ and APE = 30 for this data set. Higher noise levels may be acceptable with no background concentration.

7.3.4 Data anomalies

In data that includes the spike and sequence of zero reading anomalies, the trend of decreasing predictive capability and RTD quality with increased noise and background level remains.

When random data spikes are applied, there is no overall significant change in

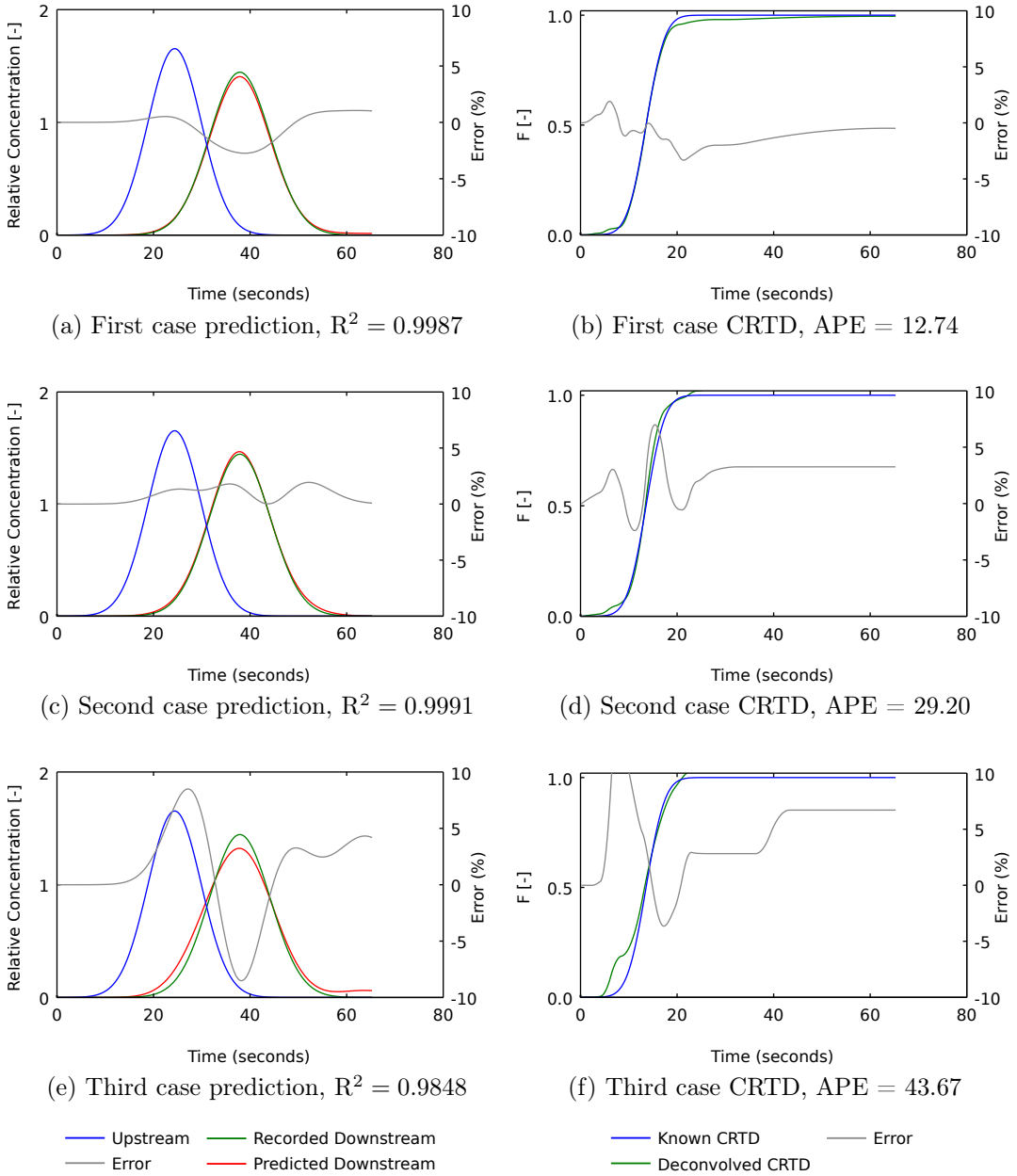

(a) First case prediction, $R^2 = 0.9987$

(b) First case CRTD, APE = 12.74

(c) Second case prediction, $R^2 = 0.9991$

(d) Second case CRTD, APE = 29.20

(e) Third case prediction, $R^2 = 0.9848$

(f) Third case CRTD, APE = 43.67

Figure 7.9: Test cases showing deconvolved CRTD and predicted downstream profiles for visual inspection

predictive capability, with mean $R^2 = 0.9985$. RTD quality also remains acceptable with a mean APE value of 26.67. The greatest impact occurs on RTD quality with a spike frequency of 5 s, with an increase in APE value of 5. The decrease in R^2 value is minimal. Greater spike size affects only R^2 value, causing slightly lower values.

Impact due to the sequences of zero reading is much clearer, with predictive capability and RTD quality varying widely depending on the location of the zeros. Across the 6 tested data records, a 10 s sequence of zeros replacing the peak of downstream profile impacts on the deconvolved RTD the greatest, with mean R^2 of 0.2400 and mean APE value of 100. A 2 s sequence replacing the upstream peak results in a mean R^2 of 0.9828 and APE of 30.39. If the sequence of zero readings is at the start or end of the profile, R^2 and APE value are unaffected. Impact is minimised as the sequences of zero reading move away from the peak of the profile and as sequence length decreases. The impact of sequences of zero reading on the upstream profile is lower than on the downstream profile, which indicates that downstream profile quality is more important for obtaining a good RTD.

7.3.5 Raw data analysis recommendations

10% noise and 10% background have been suggested as input data quality limits for deconvolving a fit-for-purpose RTD, with calibration and extension having minimal impact. Spikes are suggested to have a similar impact to noise, while sequences of zero readings can significantly affect the RTD. To ensure sufficient input data quality, minimal pre-processing to the data should be applied based on these findings.

Background concentration has a high impact on RTD and is a common occurrence, so it is the most important data quality issue to address. Background concentration should be subtracted as part of minimal pre-processing. This subtraction should take into account background slope, but in general need not be overly precise as at very low background levels noise will have a greater impact on RTD quality.

Pre-processing for noise is indicated to be unnecessary as long as background

subtraction has taken place. Even at noise levels higher than 10% the RTD has been observed to remain good. In the event of significantly greater noise levels, some filtering should be applied, e.g. a moving average. Additional steps of down-sampling or cutting may be required for computational reasons when time-series are of significant length. However, in most cases no other pre-processing should be required.

7.3.6 Validation

The applicability of maximum entropy deconvolution to raw solute transport data has been carried out using raw laboratory data. Figure 7.10 shows the downstream profiles from Figure 7.7 with predicted output from the deconvolved RTDs. The R^2 values in this case are much lower than those obtained in the sensitivity analysis, but by visual examination the predicted downstream profile clearly matches the recorded profile. The lower R^2 values are the result of noise captured by the high sampling frequency of 166 Hz. The high sampling frequency also causes high numbers of data points, which results in long deconvolution times. As previously mentioned, sub-sampling of the concentration data may be advisable in these situations for practical purposes.

Figure 7.11 shows the deconvolved CRTDs. While there is no way to make a numerical evaluation of RTD quality, they can be evaluated in comparison to each other based on the previously presented below- and above-threshold CRTDs, e.g. Figure 2.9. In both figures, the above-threshold CRTD rises steeply, while the below-threshold CRTD only has a short rise followed by a drawn out tail.

Deconvolution can be successfully applied to raw solute transport data to obtain fit-for-purpose predictive models and CRTDs that reflect hydraulic system characteristics.

7.4 Conclusions

Data pre-processing is an important step that converts raw data records into a form suitable for analysis. Typical solute transport data pre-processing steps have

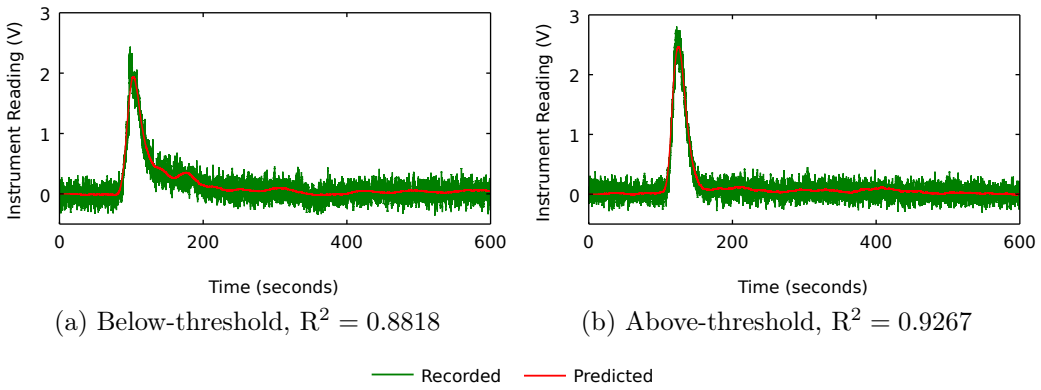

(a) Below-threshold, $R^2 = 0.8818$ (b) Above-threshold, $R^2 = 0.9267$

Figure 7.10: Predicted downstream profiles from experimental validation data (Figure 7.7)

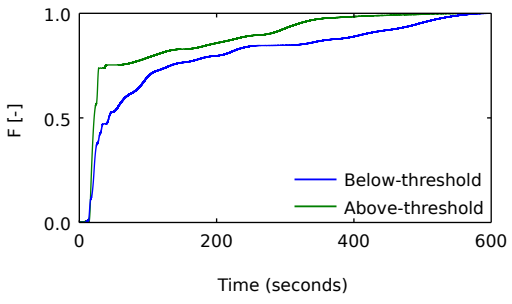

Figure 7.11: Deconvolved CRTDs from experimental validation data: 800 mm manhole, 0.88 l/s flow, mass-balanced

been identified and applied in reverse to generate synthetic raw data. Maximum entropy deconvolution has then been used to deconvolve the synthetic raw data in order to evaluate how input data quality affects the quality of the deconvolved RTD. Anomalous data were also tested.

Predictive capability of the deconvolved RTD is generally good, but degrades with increases in noise and background concentration level. Differences in uncalibration and extension impact on the deconvolved RTD, but do so in an unsystematic fashion. Increasing background concentration levels with time particularly influence the deconvolved RTD, causing over estimation of the RTD and a corresponding reduction in RTD quality and predictive capability.

RTD quality, assessed using a direct comparison to a known RTD, shows similar trends to predictive capability, decreasing with increased noise and background concentration level. Even with no noise or background, however, there is a slight degradation in the quality of the deconvolved RTD with a mean APE value of 13.00. This degradation approximately doubles with 10% noise or background. RTD quality and predictive capability are clearly linked.

A visual inspection of the predicted downstream profiles and deconvolved CRTDs was carried out. Combined, the results suggest that 10% noise and background are limits for deconvolving a fit-for-purpose RTD. Higher noise levels may be acceptable, providing the mean background concentration level is low, as noise appears to less severely impact on deconvolved RTD. Minimal pre-processing is suggested to take the form of a background concentration level subtraction that takes into account background slope.

Provided minimal pre-processing is done, and the instrumentation used to collect the raw data has a linear response, maximum entropy deconvolution can be successfully applied to raw solute transport data to extract the RTD. This has been demonstrated with independent laboratory data.

A more thorough test of the deconvolution of raw data is carried out in Chapter 8.

Chapter 8

Mixing in surcharged manholes

This chapter serves as a demonstration of the applicability of maximum entropy deconvolution towards deconvolving large amounts of raw data and the identification of hydraulic processes occurring in surcharged manholes. The partial data set previously analysed in Chapter 3 is re-analysed together with the complete data set, and an enhanced understanding of both the deconvolution process and Residence Time Distributions is used to draw new conclusions.

8.1 Introduction

In combined sewer networks surcharged manholes experience complex mixing conditions. To correctly model the effect of manholes in hydraulic models, research has been conducted on energy losses in manholes and several relationships have been proposed. However, due to the complex nature of mixing processes in manholes, no clear theoretical relationship has emerged for water quality modelling and as such most water quality models simply use a plug flow assumption through manholes.

To date, mixing in manholes has been characterised primarily for unbenched, straight through manholes. A brief summary of this work was given in Section 2.3. Of particular interest is research carried out by Saiyudthong (2003) on the effects of outlet angle and benching on mixing characteristics. Benching is a manhole

feature incorporated to reduce the chance of settling. A significant amount of solute tracer data was collected and the raw data saved in a form suitable for re-analysis with deconvolution (see Chapter 7). Complementary data collected by Dennis (2000) is also suitable. This chapter aims to combine existing research with new deconvolution analysis to present a more complete picture of mixing processes in surcharged manholes by including results from angled and benched manholes.

8.1.1 Solute transport in manholes

Guymer *et al.* (2005) described two mixing conditions in unbenched manholes. A below-threshold well-mixed condition and an above-threshold short-circuiting condition. Stovin *et al.* (2010a) identified a hydraulic threshold for this change in mixing regime at $s' = 0.258D$, where s' is threshold surcharge depth and D is manhole diameter. Stovin *et al.* (2013) used validated CFD models to show that the below-threshold well-mixed condition does not occur in manholes when $D/D_p < 4.4$, where D_p is pipe diameter. Instead, flow is short-circuiting (above-threshold) for all surcharge depths. Manhole to pipe diameter ratios below this $D/D_p = 4.4$ cut-off are more common in sewer networks than manholes with a higher ratio. The CFD models also showed that for manholes where $D/D_p \geq 4.4$, the threshold occurred at $s' = 0.2D$. This corresponds directly with theoretical jet expansion according to Albertson *et al.* (1950).

The results of Stovin *et al.* (2013) were shown through Cumulative Residence Time Distribution analysis and through normalised t_{50} values. The t_{50} value is the residence time at which CRTD = 0.5, i.e. the time taken for 50% of the mass to pass through a system or $\int_0^{t_{50}} E(\tau)d\tau = 0.5$. The CRTDs indicated that in the below-threshold condition ($D/D_p \geq 4.4$), there was systematic variation in mixing that should be taken into account. Stovin *et al.* (2013) hypothesised that as surcharge depth increased there was more jet expansion promoting better mixing until the above-threshold condition was reached, fully damping most jet mixing effects. They also showed K energy loss coefficients (discussed in Section 8.1.2) that corresponded well to normalised t_{50} values, and as a result hypothesised that, given solute transport processes and energy losses are both factors of system hydrodynamics, it should be possible to correlate the results to predict one from

the other.

A third "very low surcharge" mixing condition was observed at surcharge depths of 10–20 mm in unbenched manholes by Stovin *et al.* (2013) when $D/D_p \geq 4.4$. This condition was indicated by CRTDs similar in shape to those of the above-threshold condition, also indicating short-circuiting. Analogous CRTDs at low surcharge depth were also shown in Chapter 3 for unbenched manholes at 0°, 30°, and 90° outlet angles with flow at 1 l/s. This condition was first reported by Jones (2011) when investigating unsteady-state flow conditions in unbenched surcharged straight through manholes.

8.1.2 Energy losses

Stovin *et al.* (2013) suggested a link between mixing processes and energy losses. Pedersen & Mark (1990) suggested that energy losses in manholes could be accounted for using submerged jet theory. They developed a theoretical basis for relating energy losses (head loss) in manholes to a single energy loss coefficient K in Equation 8.1, where $\triangle h$ is head loss, g is the acceleration due to gravity, and V_x is mean longitudinal pipe velocity. After establishing this, they proceeded to investigate relationships between K and manhole geometry. Several other studies have also related the K value to manhole characteristics (e.g. Arao *et al.*, 2012; Zhao *et al.*, 2006; Wang *et al.*, 1998), and as such it is the standard coefficient for describing energy losses in manholes.

$$\triangle h = K\frac{V_x^2}{2g} \tag{8.1}$$

Other previous work also suggests that K values change with the hydraulic threshold (Lindvall, 1986; Arao & Kusada, 1999). In terms of system hydraulics, flow at high surcharge depths has visually been observed to have a smooth water surface (less turbulence) (Johnston & Volker, 1990), resulting lower K values. This is likely a case of above-threshold flow and less well-mixed manhole outflow. It should be possible to use K to further examine mixing processes in conjunction with the RTD.

Specifically of interest is work by Arao & Kusada (1999), who studied the effect

of outlet angle, water depth, and manhole drop on energy loss in an unbenched manhole. They investigated a 0° outlet, 45° outlet and two different types of 90° outlet with a $D/D_p = 3.6$. For a 0° outlet angle with no drop, their results show an increase in K with surcharge depth up to $s = 0.278D$, where s is surcharge depth, after which it decreases to a near constant value. This is consistent with the well-mixed below-threshold condition $0.2D \leq s' \leq 0.285D$ proposed by Stovin *et al.* (2010a) and Stovin *et al.* (2013). For a 90° outlet angle with no drop they show increasing K with surcharge depth until $s = 0.833D$, after which K drops to a steady value. This is consistent with the threshold depth reported in Chapter 3 for a 90° outlet angle. They conclude that there are clear differences in K with water depth.

8.1.3 Energy dissipation

Saiyudthong (2003) suggested an energy dissipation value as a link between the mixing processes and energy losses, but did not conduct a detailed analysis, particularly with reference to system hydraulics. The rate of energy dissipation G for a unit of water is known as the velocity gradient and has the units s^{-1} (Equation 8.2). It was originally derived by Camp & Stein (1943) to relate power input to mixing in the context of flocculation.

Droste (1997) provides a good explanation and basic derivation for G. Force equations and power equations are balanced for an elemental volume of water, and pressure terms used to combine them. This is linked to shear forces, which are in turn linked to velocity through the stress-strain relationship of Newton's law of viscosity, i.e. assuming a Newtonian fluid, shear is related to velocity by the dynamic viscosity. Velocity is then linked to power dissipation through flow, resulting in Equation 8.2, where, ν is kinematic viscosity, and t_n is the nominal retention time.

$$G = \sqrt{\frac{g \triangle h}{\nu t_n}} \tag{8.2}$$

G when combined with $\triangle h$ from a system is a mean value. Although energy dissipation varies throughout a system, it is assumed that G scales with work

input and therefore mean G also scales with power input. This is the basis of the use of G as a criterion for design of flocculation vessels.

8.1.4 Cumulative Residence Time Distributions

F, the CRTD is the cumulative sum of the RTD, expressed in Equation 8.3. The CRTD has been used to distinguish between different mixing conditions, but previous manhole related research has not discussed how to interpret mixing conditions through CRTD analysis.

$$F(t) = \int_0^t E(\tau)d\tau \tag{8.3}$$

8.1.4.1 Normalised time

Danckwerts (1953) implicitly introduces the concept of normalised time as a mechanism for analysing CRTDs that takes into account volume and flow rate. Normalised time was introduced in Chapter 2 as Equation 2.5. $t_{nz} = 1$ is equivalent to the nominal retention time $t_n = VQ^{-1}$.

$$t_{nz} = tQV^{-1} \tag{2.5}$$

Normalised time is expected to allow for CRTD scaling provided three conditions are met: geometric similarity, Reynolds number similarity, and fluid similarity (fluids at the model scale and at full scale behave the same). Stovin *et al.* (2010a) investigated CRTDs as a dimensionless predictive model of unbenched manholes and showed them to be applicable provided similar flow fields existed (e.g. all below-threshold). Manhole CRTDs with different flow rates and surcharge depths were shown to collapse onto a common shape (or line) when normalised time was used. An example of this is shown in Figure 8.1.

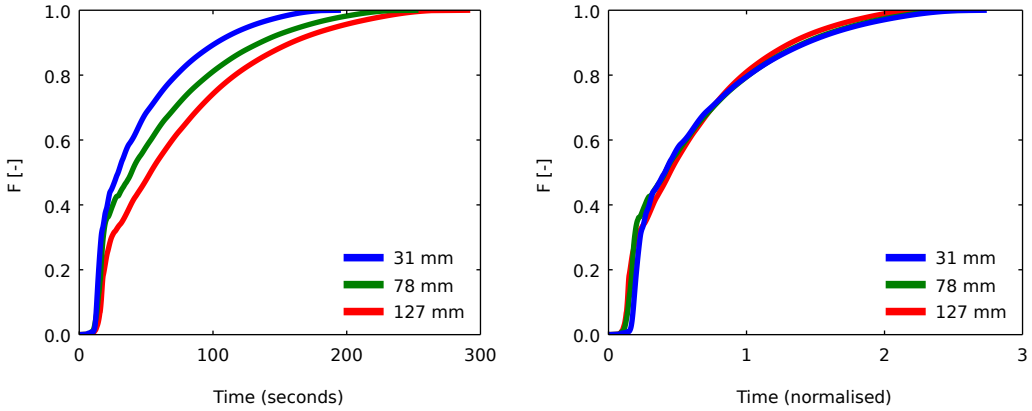

(a) 1 l/s

(b) 1 l/s in normalised time

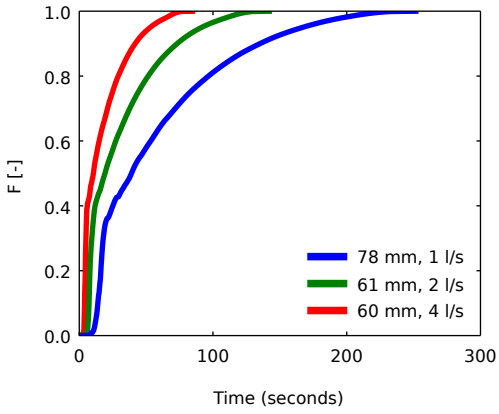

(c) Similar surcharge depth

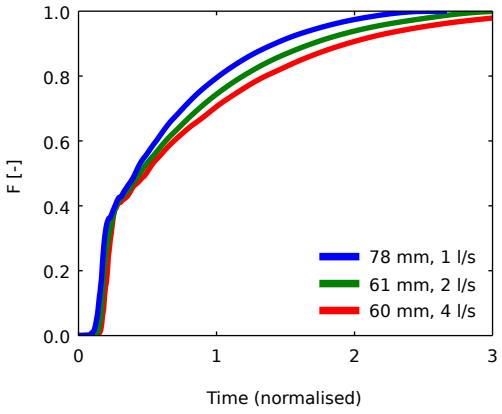

(d) Similar surcharge depth in normalised time

Figure 8.1: CRTD demonstration of normalised time for below-threshold CRTDs from unbenched 800 mm manhole data (Guymer & Stovin, 2011)

8.1.4.2 Interpreting CRTDs

Knowledge of general CRTD shapes can be used in interpreting deconvolved CRTDs to infer underlying mixing processes. Both Danckwerts (1953) and Levenspiel (1972) discuss certain fundamental flow regimes and the CRTD shapes that reflect them. These are outlined below, increasing in complexity.

- Plug flow, shown in Figure 8.2a. The CRTD rises from 0 to 1 at $t_{nz} = 1$. Pure advection with no dispersion. All particles share the same travel time.
- Pipe flow, shown in Figure 8.2b. The CRTD rises gradually from 0 near $t_{nz} = 1$, rises more steeply around $t_{nz} = 1$, and then continues on to gradually approach 1. Advection with some Fickian dispersion, e.g. Taylor (1954). The bulk of particles travel around the mean pipe velocity.
- Complete mixing, shown in Figure 8.2c. All particles are mixed instantaneously throughout the available mixing volume, and gradually exit. This is expressed by Equation 8.4.

$$F(t_{nz}) = 1 - e^{-t_{nz}Q/V} \tag{8.4}$$

- Short-circuiting flow, shown in Figure 8.2d. The bulk of the particles travel through significantly more rapidly than $t_{nz} = 1$, while a small fraction of the particles are trapped in a dead zone and so have a higher retention time.
- Arbitrary flow, shown in Figure 8.2e. There is no single dominating flow path. Instead, particles can potentially travel along several different paths and/or through dead zone(s).

8.1.4.3 Short-circuiting

The concept of short-circuiting has been previously introduced in Chapter 2 to explain the above-threshold flow field, e.g. Figure 2.9. Several different CRTD parameters to quantify short-circuiting have been developed, e.g. Persson (2000). In general these rely on at least one of two key CRTD features, both of which can be seen in Figure 8.2d. The first of these is a steep rise in CRTD, which

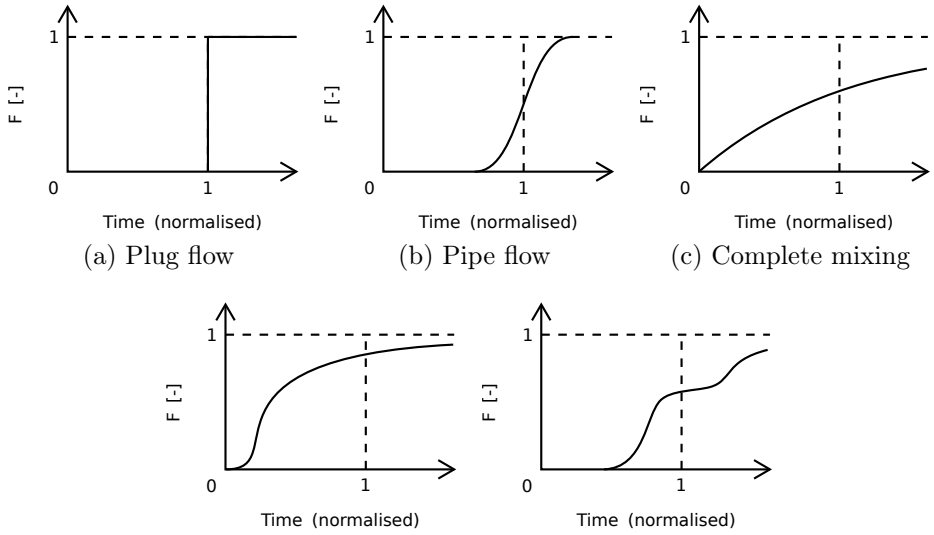

(a) Plug flow (b) Pipe flow (c) Complete mixing

(d) Short-circuiting flow (e) Arbitrary flow

Figure 8.2: Different mixing conditions expressed as CRTDs, after Danckwerts (1953); Levenspiel (1972)

can be numerically expressed as a high ratio of t_{16}/t_{50} (Ta & Brignal, 1998). Unfortunately this could also indicate something similar to plug flow, e.g. Fig 8.2a, or a single dominating flow path (Stovin *et al.*, 2008). A more reliable indicator is that the bulk of the CRTD occurs prior to $t_{nz} = 1$ (Holland *et al.*, 2004). In this scenario flow has moved through the system more rapidly through the system than the nominal retention time would indicate. A short-circuiting flow field in manholes is typically indicated by both features.

While a CRTD contains features that indicate short-circuiting, this does not on its own imply what underlying flow field may be causing the short-circuiting. As indicated by the variety of CRTD parameters that have been proposed, more of the context of these features must be considered as well. This chapter introduces a second type of short-circuiting flow field occurring within manholes. Both the original and new fields are shown in Figure 8.3.

Type I short-circuiting is the previously introduced above-threshold short-circuiting, where flow passes directly through the manhole according to the jet. This matches the PLIF imagery shown in Figure 2.5b. As such, Type I short-circuiting is specifically characterised by the rise in CRTD corresponding to the equivalent pipe travel time, i.e. $t_{16} \approx t_{50} \approx 0.25\pi D D_p^2 Q^{-1}$. As this time is independent of surcharge volume, when CRTDs reflecting Type I short-circuiting are normalised,

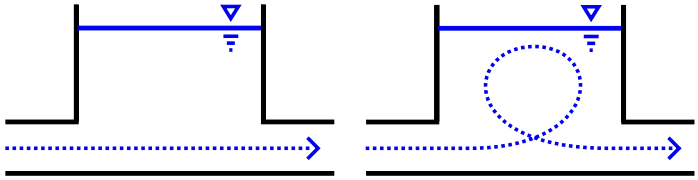

(a) Type I (b) Type II

Figure 8.3: Short-circuiting flow fields

they do not collapse e.g. Figure 3.4.

Type II short-circuiting appears on a CRTD plot nearly identically to Type I short-circuiting, with a similar steep rise in CRTD, and again the bulk of the solute passes through the manhole at $t_{nz} < 1$. However, in Type II short-circuiting the flow path is different. Flow is still dominated by a jet core, but in this case it circulates throughout the manhole surcharge volume. As a result, the time at which the steep rise occurs is much later than the equivalent pipe travel time. Additionally, as Type II short-circuiting is a volume effect, the flow path changes with surcharge depth and therefore when CRTDs showing Type II short-circuiting are normalised they do collapse.

The primary difference therefore between Type I and Type II short-circuiting CRTDs is not the shape but instead that Type II CRTDs will collapse due to volume effects when normalised while Type I CRTDs will not.

8.1.4.4 CRTD balance

Danckwerts (1953) showed that one of the fundamental properties of the CRTD is that the area under the CRTD for $t_{nz} \leq 1$ is equal to the area above the CRTD for $t_{nz} > 1$, as shown in Figure 8.4. While this applies to all CRTDs, many plots, such as those in Figure 8.2, are truncated and therefore do not show this. The area A can be expressed as Equation 8.5 (Denbigh & Turner, 1984).

$$A = \int_0^{t_n} F(\tau)d\tau = \int_{t_n}^{\infty} [1 - F(\tau)]d\tau \tag{8.5}$$

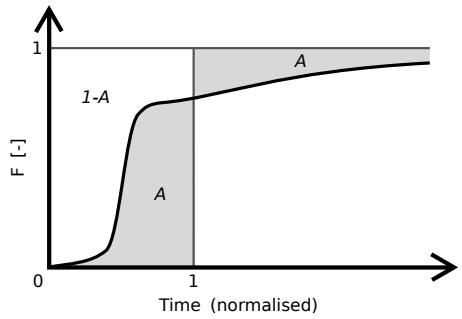

Figure 8.4: CRTD area balance, after Danckwerts (1953)

8.1.5 Chapter aims

This chapter aims to demonstrate the large scale applicability of maximum entropy deconvolution to raw solute transport data; infer the mixing processes occurring in angled and un/benched manholes through CRTD analysis; and to further investigate the link between energy losses and mixing processes in manholes.

8.2 Methodology

Raw experimental data has been previously collected by Dennis (2000) and Saiyudthong (2003) on both a benched and unbenched 388 mm manhole with an 88 mm diameter pipe and outlet angles of 0°, 30°, 60°, and 90° at varying flow rates and surcharge depths. Fluorometers were placed 1.35 m up- and downstream of the manhole centre and dye tracer tests were run. The experimental apparatus is shown in Figure 3.1, and the benching in Figure 8.5. The experimental configurations are shown in Figure 8.6, indicating where head loss and solute tracer data were collected. The 0° unbenched data consists of 5 repeat trials, while the rest of the data consists of 3 repeat trials. The 0° benched data was unavailable for reanalysis. Data was not collected at combinations of low surcharge depth and high flow rate due to pipe friction losses. (At high flow rates, friction losses in the downstream pipe were so great as to cause additional surcharge in the manhole irrespective of system configuration for low surcharges.) The 1 l/s data of Saiyudthong (2003) for the 30°, 60°, and 90° outlet angles was previously analysed as pre-processed data in Chapter 3.

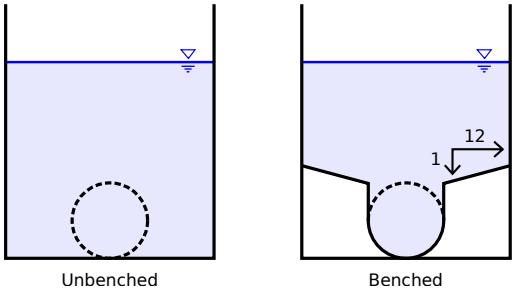

Figure 8.5: Benched manhole diagram for Saiyudthong (2003)

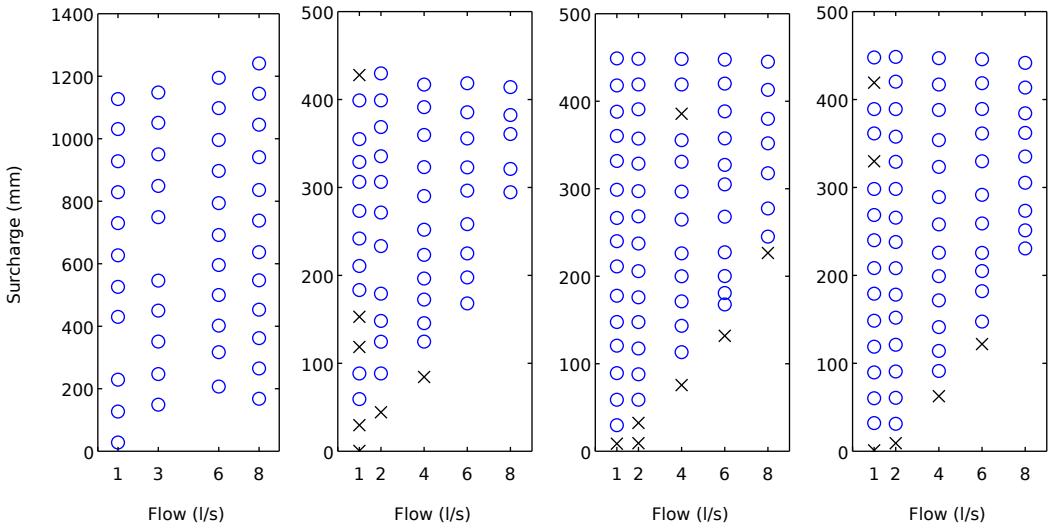

(a) 0° unbenched (b) 30° unbenched (c) 60° unbenched (d) 90° unbenched

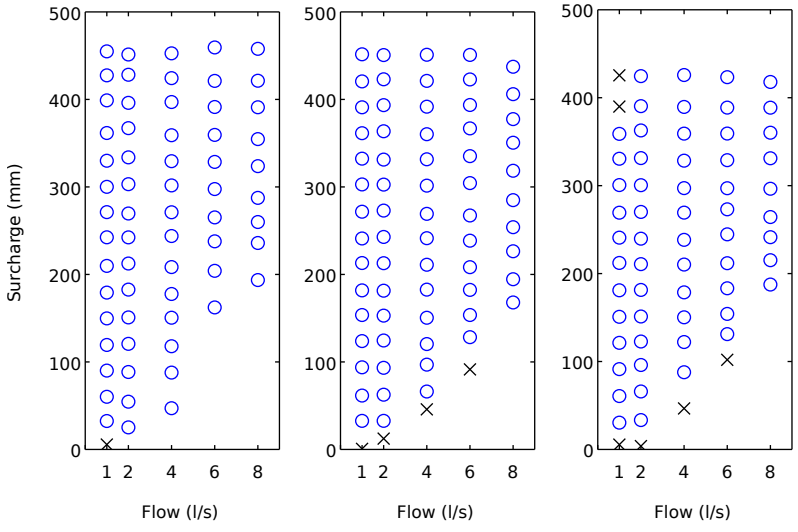

(e) 30° benched (f) 60° benched (g) 90° benched

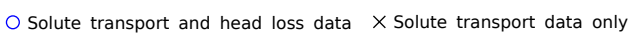

Figure 8.6: Data set summary

8.2.1 Maximum entropy deconvolution

In Chapter 5, 40 sample points, the slope-based sample point distribution, 350 iterations, and the R_t^2 constraint function were recommended as robust configuration settings, and these have been used. In Chapter 7 raw data was deconvolved successfully with only minimal pre-processing applied. This has been used to reduce potential errors that may otherwise be introduced during pre-processing. The minimal pre-processing used was the recommended background concentration level subtraction as a linear function from the mean of the first 5 seconds of data to the last 5 seconds of data. Additionally, due to the record length and high sampling frequency in comparison to the experimental event, the record has been trimmed. The cut-offs were conservatively determined as the first ten data points below 0.5% of peak concentration from profile peak outwards.

8.2.2 Scaling and normalisation of CRTDs

As the data is deconvolved without calibration, the sum of the CRTD will not equal one (as should be the case). For most data, mass-balance can be assumed, and therefore the deconvolved RTDs can be scaled so that $\int_0^\infty E(\tau)d\tau = 1$. After scaling the RTDs and converting them to CRTDs, the CRTDs from each trial of each experimental configuration were averaged on a cumulative percentage basis, i.e. the mean of the residence time (t_x) for each 0.1% mass fraction has been calculated. They have then been temporally normalised according to Equation 2.5 to allow cross-comparison of different surcharge depths and flow rates.

8.2.3 Additional CRTD scaling

In some cases, scaling the CRTD to one produces an inaccurate result, e.g. Figure 8.7. In the scenario shown, Trial 1 varies significantly from Trials 2 and 3. Whilst it is possible that this is a genuine result, visual examination of the upstream and downstream data shows similar concentration profiles for all three trials. As such, similar mass recovery levels would be expected across the three repeats even though it is raw data. However, Table 8.1 shows that Trial 1 has a much higher mass-balance ratio.

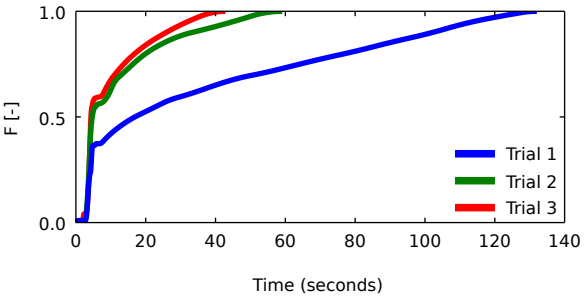

Figure 8.7: Inaccurate CRTD scaling

Trial	Upstream	Downstream	Ratio
1	486.0	712.4	1.466
2	476.0	432.2	0.908
3	429.4	393.4	0.916

Table 8.1: Raw-data mass-balance for Figure 8.7

Further inspection shows that this is due to a background concentration level offset in the downstream data, but not in upstream data. In order for the deconvolution goodness-of-fit constraint to be met, the RTD 'creates' extra mass, i.e. $\int_0^\infty E(\tau)d\tau \gg 1$. This causes the scaling to produce the inaccurate result as the mass-balance assumption is no longer true.

The mass creation effect is in direct contrast to results presented in Chapter 7, which showed that small background offsets still produced an RTD close to the known RTD. The mass creation effect was unobserved as for that comparison the RTD was cut-off at the end point of the known RTD. Therefore the deconvolved CRTD is still representative of the system hydraulics if the cut-off point can be determined. An accurate guess of true CRTD length (the necessary cut-off point) can be made by scaling it to achieve the balance shown in Figure 8.4 via Equation 8.5. The scaling process is outlined below and shown in Figure 8.8.

- Assume the CRTD is scaled based on factor f, i.e. $\hat{F} = F \times f$, where $\hat{F}$ is a scaled estimate of the CRTD. The initial estimate of f, $f_0 = 1/\int_0^\infty E(\tau)d\tau$. If $\int_0^\infty E(\tau)d\tau \gg 1$ then f_0 is an under estimation, which explains the significantly different shape of Trial 1 in Figure 8.7.

- Let the end of the CRTD, L, occur when $\hat{F}(t_{nz}) = 1$. This will be the last

point in the CRTD when F is scaled with f_0.

- Let the area under the left side ($t_{nz} \leq 1$) of CRTD $\int_0^{t_n} \hat{F}(\tau)d\tau$ be "left" and the area over the right side ($t_{nz} > 1$) of the CRTD $\int_{t_n}^{\infty}[1 - \hat{F}(\tau)]d\tau$ be "right".

- Increase f in small increments until left $\geq$ right, recalculating L with each increase in f as the new point at which $\hat{F}(L) = 1$.

The results of this process are shown in Figure 8.9. It has been used on the few (5 out of 1378) trials where normal mass-balance is not appropriate, rather than discarding the data. These trials have been identified manually as those having significantly higher mass-balance than other repeats, e.g. a single mass-balance of 0.9 compared to two of 0.7.

8.2.4 CFD modelling

CFD modelling on two configurations (32 mm and 330 mm surcharge depths in the unbenched 90° outlet angle manhole) has been carried out as part of this chapter to gain additional insight into the flow fields that deconvolved CRTDs represent. The modelling was carried out in ANSYS Fluent 14.5 (ANSYS, Inc., 2012) according to Stovin *et al.* (2013). Specifically, previously validated model parameters were used, including the $k-\varepsilon$ Realisable turbulence model and a fixed lid (friction free) approximation of the free surface. The mesh size used follows the approximate recommendation of $D_p/8$, for a mesh size of 10 mm. Particle tracking of very small neutrally buoyant particles was used to obtain theoretical CRTDs. These settings have been validated by Bennett (2012).

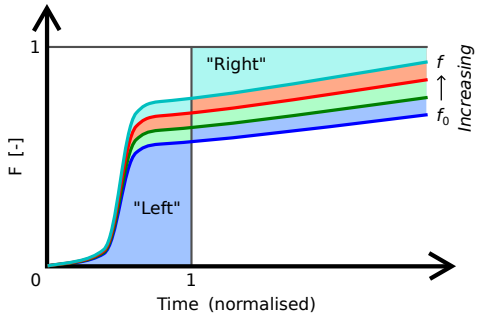

Figure 8.8: CRTD scaling process

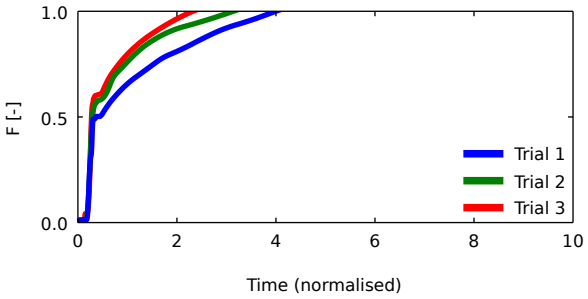

Figure 8.9: Corrected CRTD scaling

8.2.5 Energy dissipation

Equation 8.2 has been applied to obtain G values for each outlet angle, flow rate and surcharge depth, using t_{50} instead of t_n as the latter does not take into account the reduced mixing that arises due to deviation from plug flow, e.g. short-circuiting. Mean values of $\triangle h$ across repeat trials are used.

8.3 Deconvolution results

Averaged deconvolved CRTDs are presented in this section. As the first large scale application of the novel deconvolution of raw data, a visual comparison has been made to the results previously presented in Chapter 3. Equivalent plots of the pre-processed unbenched 30°/60°/90° 1 l/s data shown in Figures 3.5/3.6/3.7 are shown in Figures 8.12a/8.13a/8.14a.

The four key CRTD shapes previously identified using pre-processed data are visible in the new figures derived from raw data. At low surcharge depths ($s <$ 60 mm) CRTDs exhibit short-circuiting characteristics with a steep rise in CRTD. At high surcharge depths ($s >$ 300 mm) CRTDs also exhibit short-circuiting characteristics. CRTDs similar to the complete mixing shape occur at other depths ($60 < s <$ 270 mm). A transitional CRTD is present in both the pre-processed and raw data at $s \approx$ 270 mm, occurring in between the high surcharge short-circuiting and the lower surcharge complete mixing. The overall similarity of CRTD shapes deconvolved from both pre-processed and raw data demonstrates that successful applicability of the novel deconvolution of raw data for large data sets.

Larger versions of the plots shown in this section are presented in Appendix C.

8.3.1 CRTDs for unbenched manholes

8.3.1.1 0° outlet angle

0° outlet angle normalised CRTDs are presented in Figure 8.10. In general the normalised CRTDs show a trend of decreasing first arrival time with increased surcharge depth, which indicates volume independent flow. As volume increases, the travel time does not, resulting in a lower t_{nz}. This is consistent with the above-threshold surcharge hydraulic regime. Travel time is lower as it is the jet core passing through the manhole, which will be travelling at greater than the mean velocity. Degree of short-circuiting increases with increased surcharge depth.

The CRTDs do not collapse, indicating Type I short-circuiting. Non-normalised CRTDs have been plotted in Figure 8.11. The steep rises clearly overlap for each flow rate. Mean pipe travel times have also been plotted and they are similar to the steep rise in CRTD, particularly at higher flow rates. The steep rise and its position are further consistent with Type I short-circuiting. The CRTDs indicate that the mixing volume is bypassed almost entirely.

A well-mixed condition (below-threshold) is expected at lower surcharge depths ($s' \leq 0.258D$) (Stovin *et al.*, 2010a), however this data set has only one straight through configuration at the sub-100 mm surcharge level, which is 28 mm at 1 l/s. While the CRTD does indicate more thorough mixing occurs, it is unclear to what extent this is related to the below-threshold surcharge condition as it is only one configuration.

8.3.1.2 30° outlet angle

30° outlet angle normalised CRTDs are presented in Figure 8.12. There appear to be 4 types of CRTD, and hence mixing conditions present, at 1 l/s: a low surcharge Type I short-circuiting condition ($s < 60$ mm) similar to that observed by Stovin *et al.* (2013); a well-mixed condition ($60 < s < 250$ mm); a transitional condition ($s \approx 270$ mm); and a Type II short-circuiting condition ($s > 300$ mm).

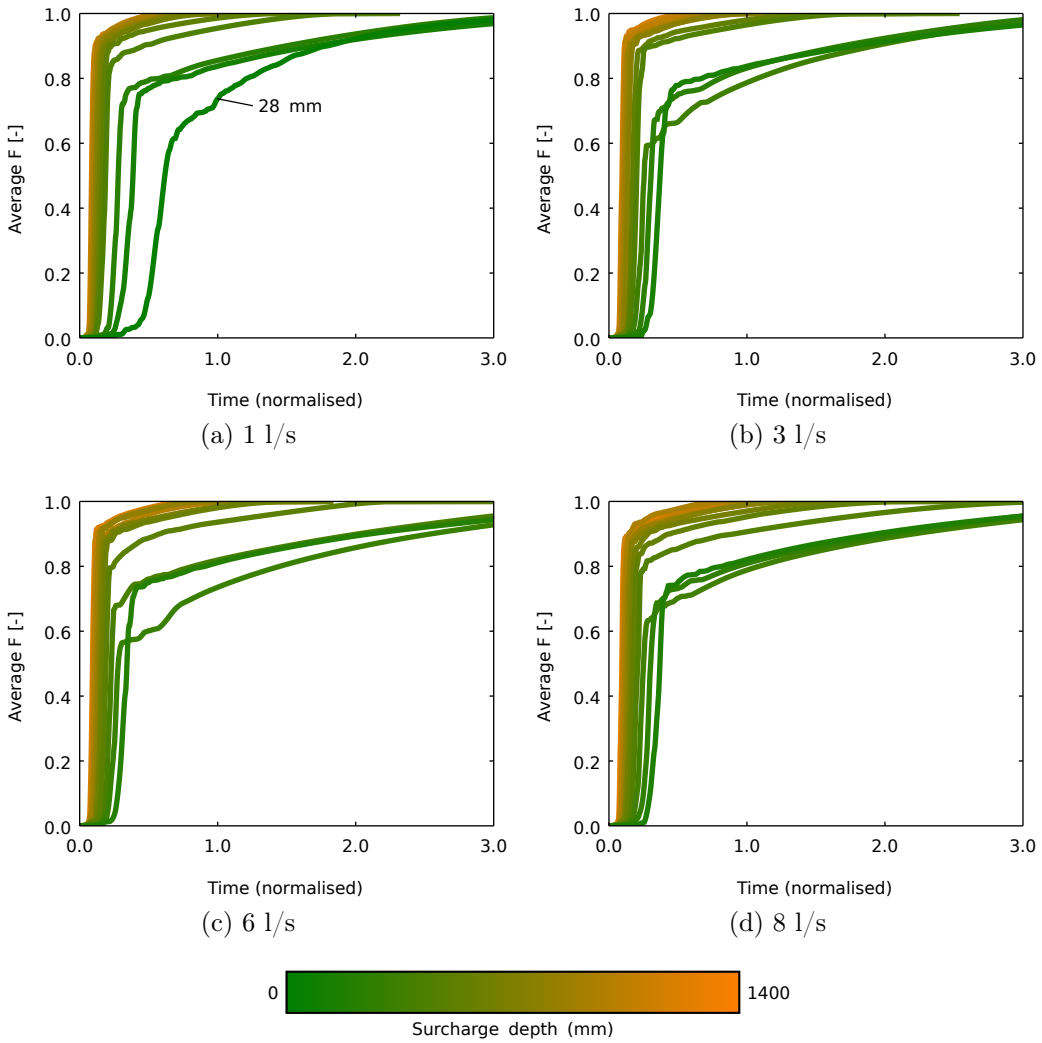

(a) 1 l/s (b) 3 l/s

(c) 6 l/s (d) 8 l/s

Figure 8.10: Unbenched 0° outlet angle normalised average CRTDs

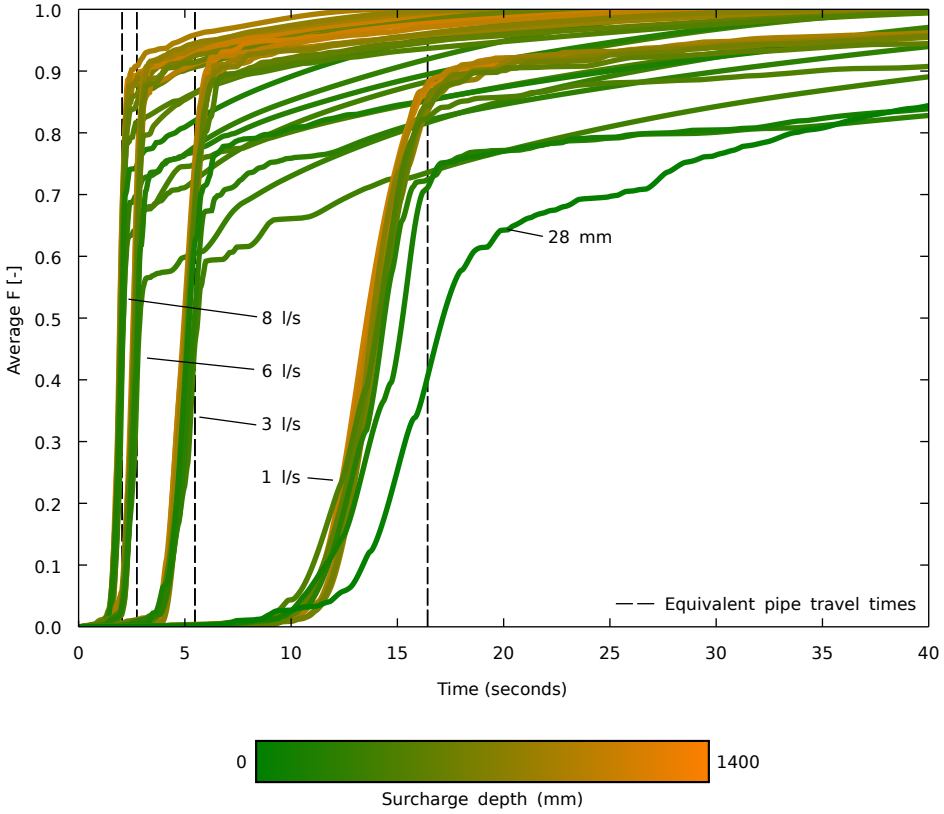

Figure 8.11: Unbenched 0° outlet angle non-normalised average CRTDs

The well-mixed CRTDs almost entirely overlap, although the first arrival times (e.g. t_5) seem to transition smoothly to the Type II short-circuiting CRTDs. The overlap of the high surcharge CRTDs indicate that the mixing processes scale as the mixing volume increases and hence these CRTDs are inferred to correspond to Type II short-circuiting.

At 2 l/s, only three conditions are observed, with no low surcharge Type I short-circuiting. The well-mixed, transitional, and Type II short-circuiting conditions are still clearly defined. At 4 l/s there is more variation in the well-mixed CRTDs and there is no transitional CRTD. Four CRTDs here were identified for the additional RTD scaling (Section 8.2.3), one of the three trials each at surcharge depths of 290 mm, 322 mm, and two trials at 360 mm. Results for 6 l/s and 8 l/s appear to show only Type II short-circuiting. One CRTD at 6 l/s and 296 mm surcharge depth was identified for the additional RTD scaling.

The lack of the low surcharge Type I short-circuiting CRTDs at flow rates greater than 1 l/s and the lack of well-mixed CRTDs at 6 and 8 l/s is attributable to the lack of experimental configurations for lower surcharges at high flow rates. However, these conditions are assumed to be present as previous work has indicated that below- and above-threshold flow regimes occur at all flow rates (Guymer & Stovin, 2011) and therefore that flow field is flow rate independent, which must be true in order for normalisation of CRTDs to apply.

8.3.1.3 60° outlet angle

60° outlet angle normalised CRTDs are presented in Figure 8.13. Only three CRTD shapes, and hence flow regimes, are present at 1 l/s. These follow the same surcharge cut-offs as for the 30° outlet angle. The three shapes present are for low surcharge Type I short-circuiting, well-mixed, and Type II short-circuiting. There are no transitional CRTDs. Instead, the well-mixed CRTDs gradually shift towards the transitional CRTD shape. All four CRTD shapes are visible at 2 l/s, back down to three shapes at 4 l/s, 6 l/s, and 8 l/s, with no low surcharge Type I short-circuiting. Similar to the 30° outlet angle there were no experimental configurations at these low surcharge depths for higher flow rates.

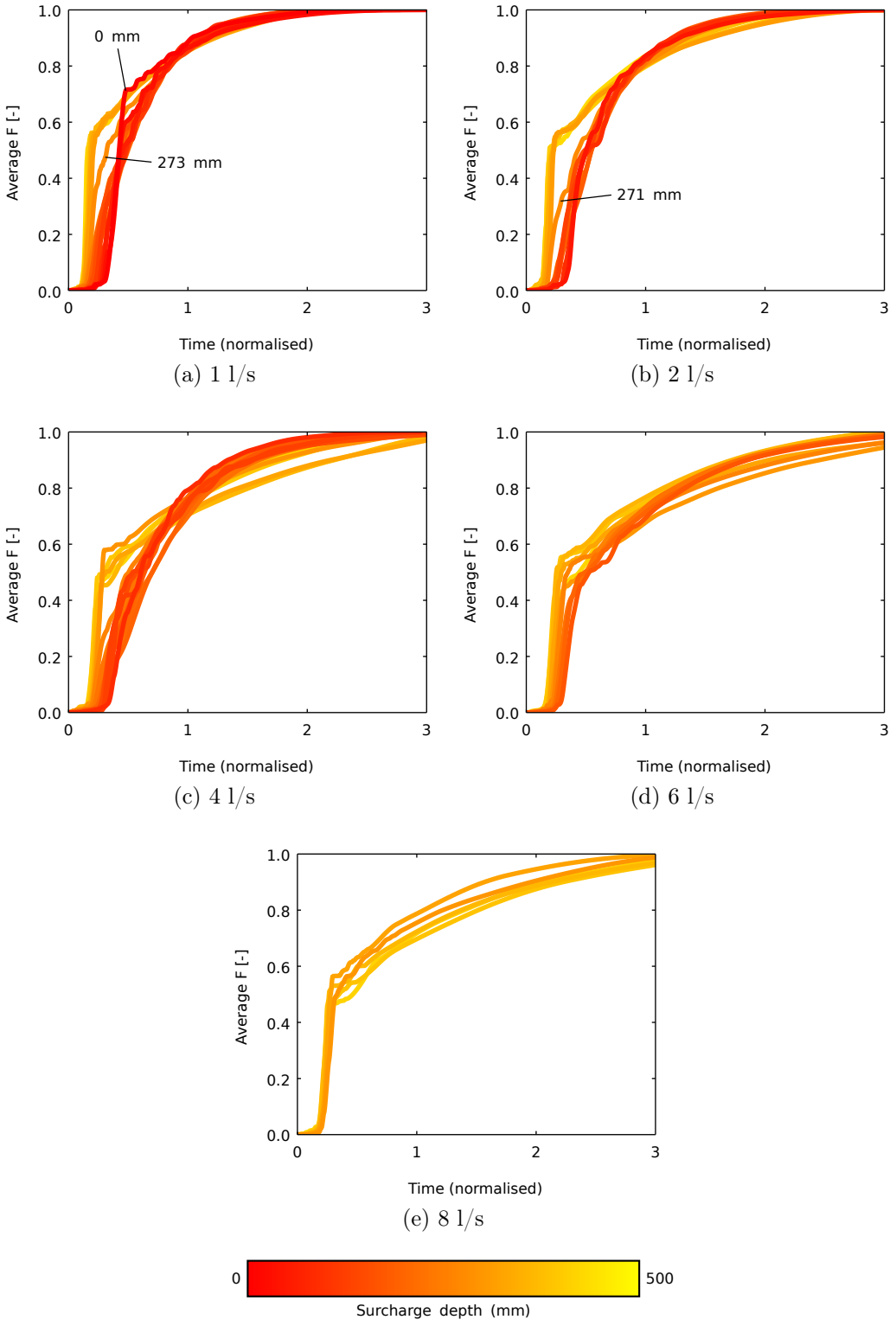

(a) 1 l/s

(b) 2 l/s

(c) 4 l/s

(d) 6 l/s

(e) 8 l/s

Figure 8.12: Unbenched 30° outlet angle normalised average CRTDs

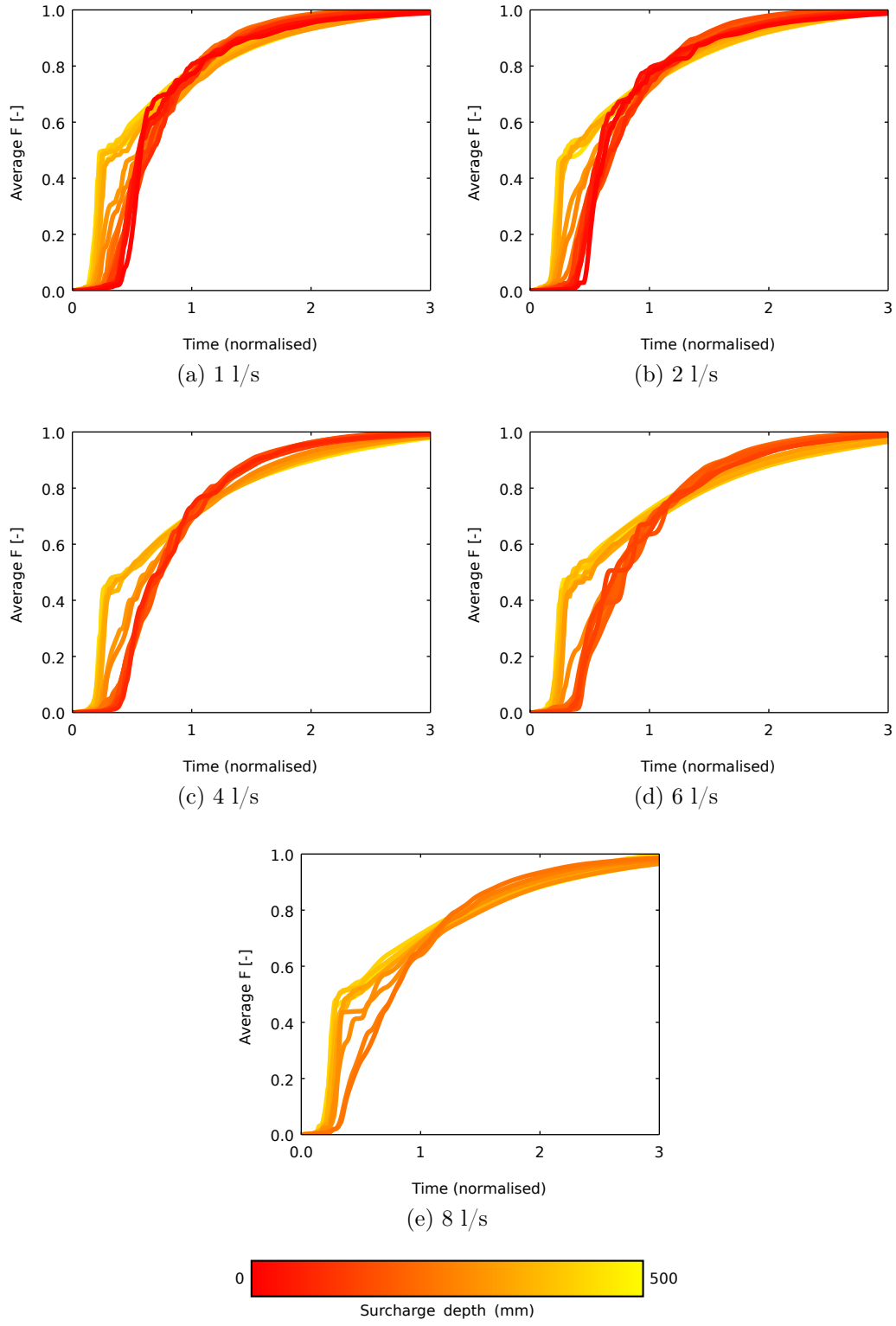

(a) 1 l/s

(b) 2 l/s

(c) 4 l/s

(d) 6 l/s

(e) 8 l/s

Figure 8.13: Unbenched 60° outlet angle normalised average CRTDs

8.3.1.4 90° outlet angle

90° outlet angle normalised CRTDs are presented in Figure 8.14. At 1 l/s there are three CRTD shapes visible: the low surcharge Type I short-circuiting; well-mixed; and Type II short-circuiting. The latter is poorly defined at 1 l/s, as the rise in CRTD is not very steep. At 2 l/s all four shapes are again visible. 4 l/s, 6 l/s, and 8 l/s do not show the low surcharge Type I short-circuiting condition as there were no experiments at those surcharge depths, otherwise the three conditions, with multiple transitional CRTDs are shown.

8.3.2 CRTDs for benched manholes

8.3.2.1 0° outlet angle

As previously mentioned, the benched 0° outlet angle data is unavailable for reanalysis.

8.3.2.2 30° outlet angle

Benched 30° outlet angle normalised CRTDs are presented in Figure 8.15. Similar to the 0° outlet angle unbenched manholes, the normalised 30° CRTDs shown a trend of decreasing first arrival time with increased surcharge depth. Again similarly, the CRTDs do not collapse, indicating Type I short-circuiting. Short-circuiting fraction increases with surcharge depth from at least 65%.

Non-normalised benched 30° outlet angle CRTDs are presented in Figure 8.16. The steep rises with short-circuiting clearly overlap. First arrival time is consistently less than the equivalent pipe travel time. There is also a CRTD (6 mm surcharge depth and 1 l/s) that is similar to the unbenched 30°, 60°, and 90° outlet angle results, indicating low surcharge Type I short-circuiting.

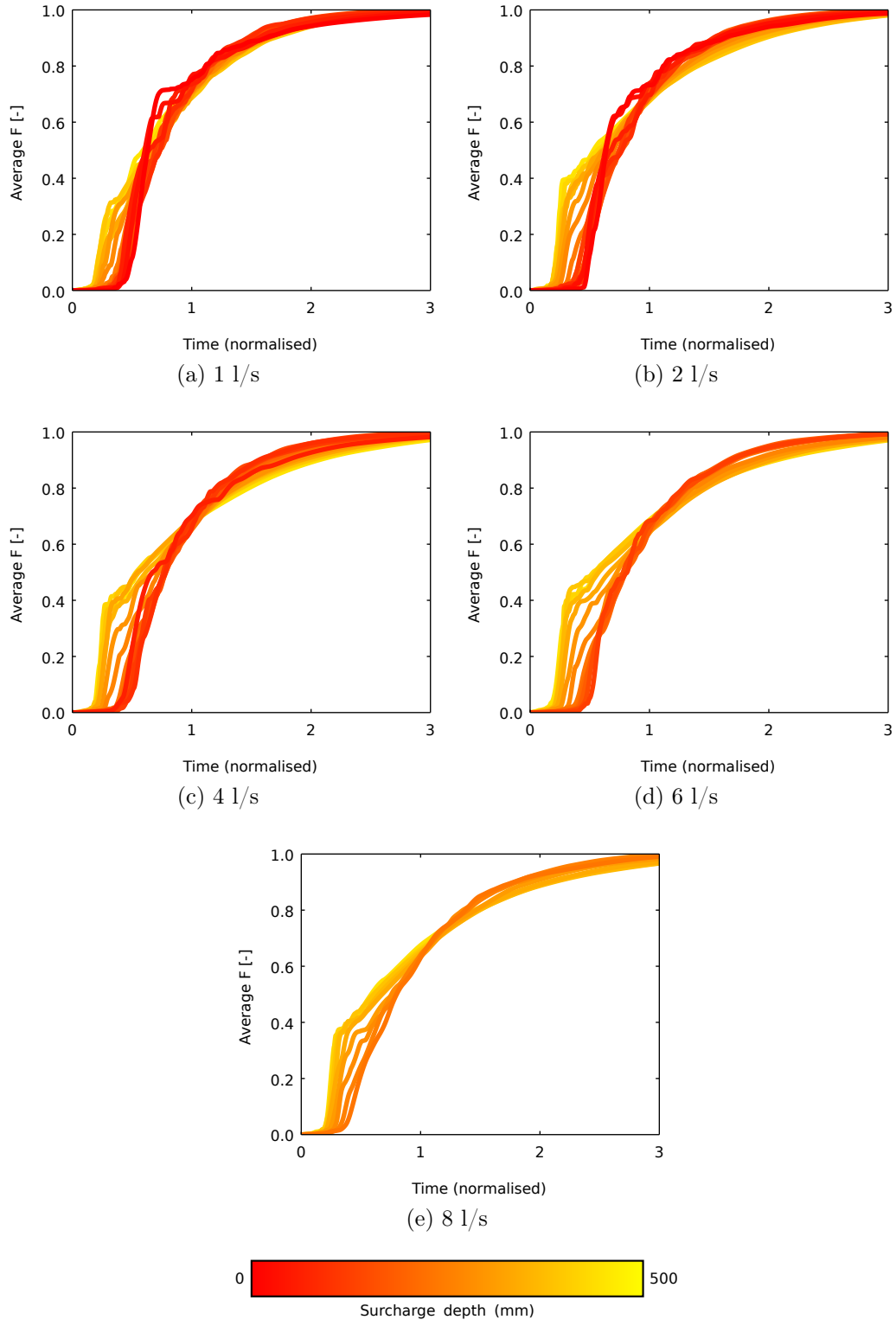

(a) 1 l/s

(b) 2 l/s

(c) 4 l/s

(d) 6 l/s

(e) 8 l/s

Figure 8.14: Unbenched 90° outlet angle normalised average CRTDs

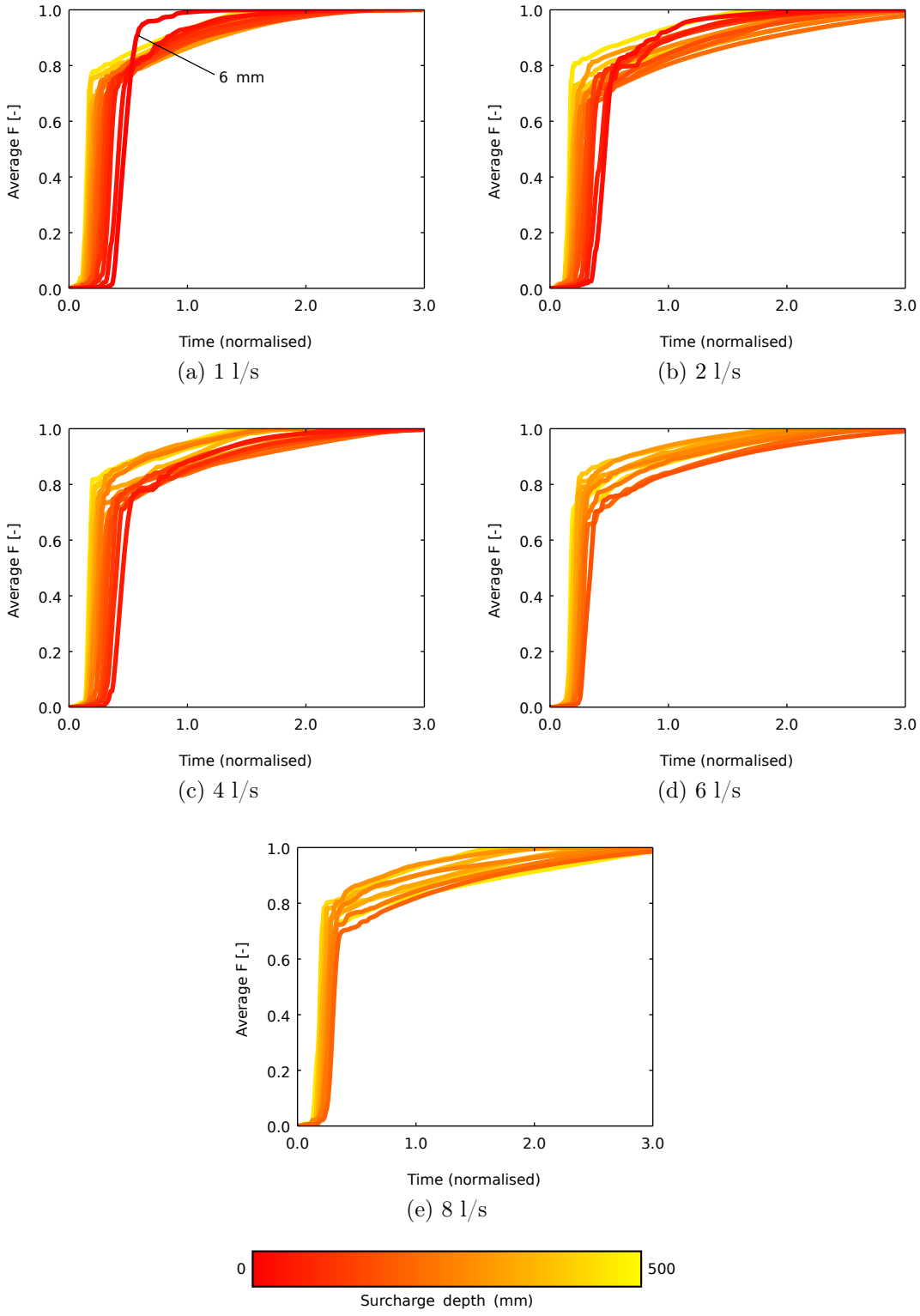

(a) 1 l/s

(b) 2 l/s

(c) 4 l/s

(d) 6 l/s

(e) 8 l/s

Figure 8.15: Benched 30° outlet angle normalised average CRTDs

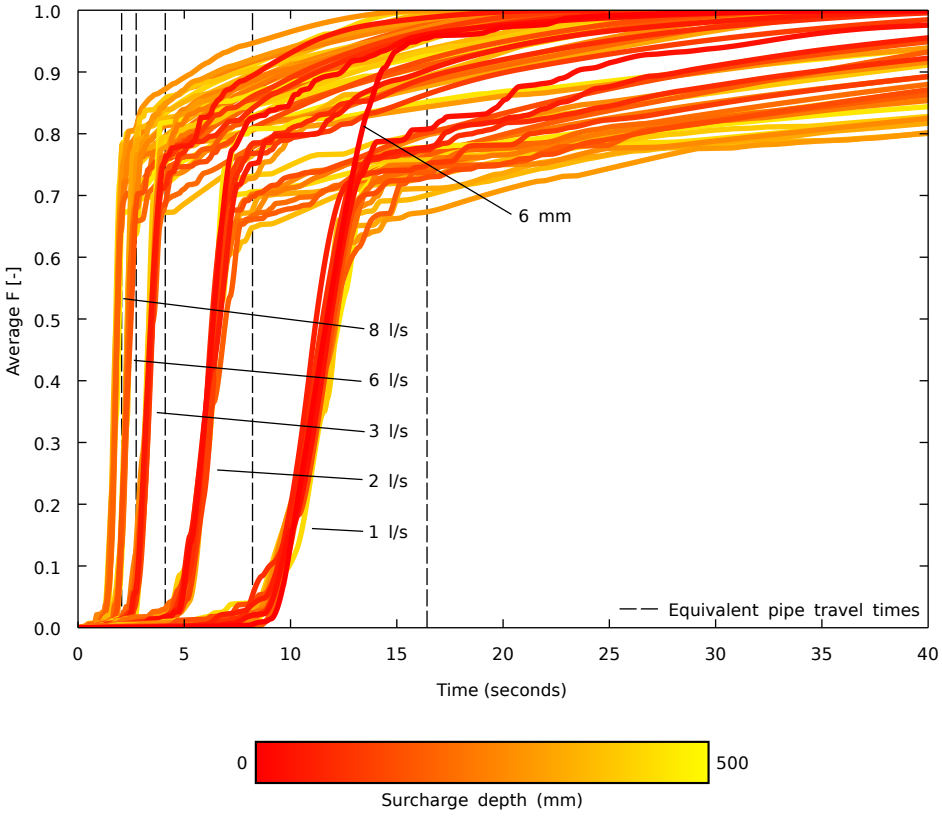

Figure 8.16: Benched 30° outlet angle non-normalised average CRTDs

8.3.2.3 60° outlet angle

Benched 60° outlet angle normalised CRTDs are presented in Figure 8.17. The decreasing travel time with increased surcharge depth is the normalised equivalent of the overlapping lines shown in the 0° unbenched and 30° benched results. This is indicative of Type I short-circuiting. At the 1, 2, and 4 l/s flow rates, there is a gradual transition in CRTD shape from low surcharge Type I short-circuiting at $s \leq 100$ mm to CRTDs with both the rise indicative of Type I short-circuiting and an overlapping exponential tail at $s > 100$ mm. The Type I short-circuiting rise and the exponential tail combined indicate a two-part bifurcating flow. In bifurcating flow, water takes two distinct paths that do not directly interact. The fraction of short-circuiting is significantly lower (around 55%).

The 1 l/s 1 mm and 2 l/s 12 mm surcharge depth CRTDs appear to be almost cumulative Gaussian in shape and similar to pipe flow, showing the low surcharge Type I short-circuiting in this case to be almost purely an effect of the benching. There were no experimental configurations conducted, but this is expected at the higher flow rates as well. In contrast to the unbenched 60° outlet angle results, there are no CRTDs that indicate well-mixed flow.

8.3.2.4 90° outlet angle

Benched 90° outlet angle normalised CRTDs are presented in Figure 8.18. They follow the same pattern as the benched 60° outlet angle CRTDs, but with a lower fraction of short-circuiting (around 40%). At 2 l/s the 4 mm CRTD, indicative of low surcharge Type I short-circuiting, is almost perfectly cumulative Gaussian in shape. In contrast to the unbenched 90° outlet angle results, there are no CRTDs that indicate well-mixed flow.

8.3.3 Retention time values

8.3.3.1 Unbenched manholes

Normalised t_{50} values for the unbenched manholes are shown in Figure 8.19. They can provide an indicator of hydraulic regime with respect to surcharge depth,

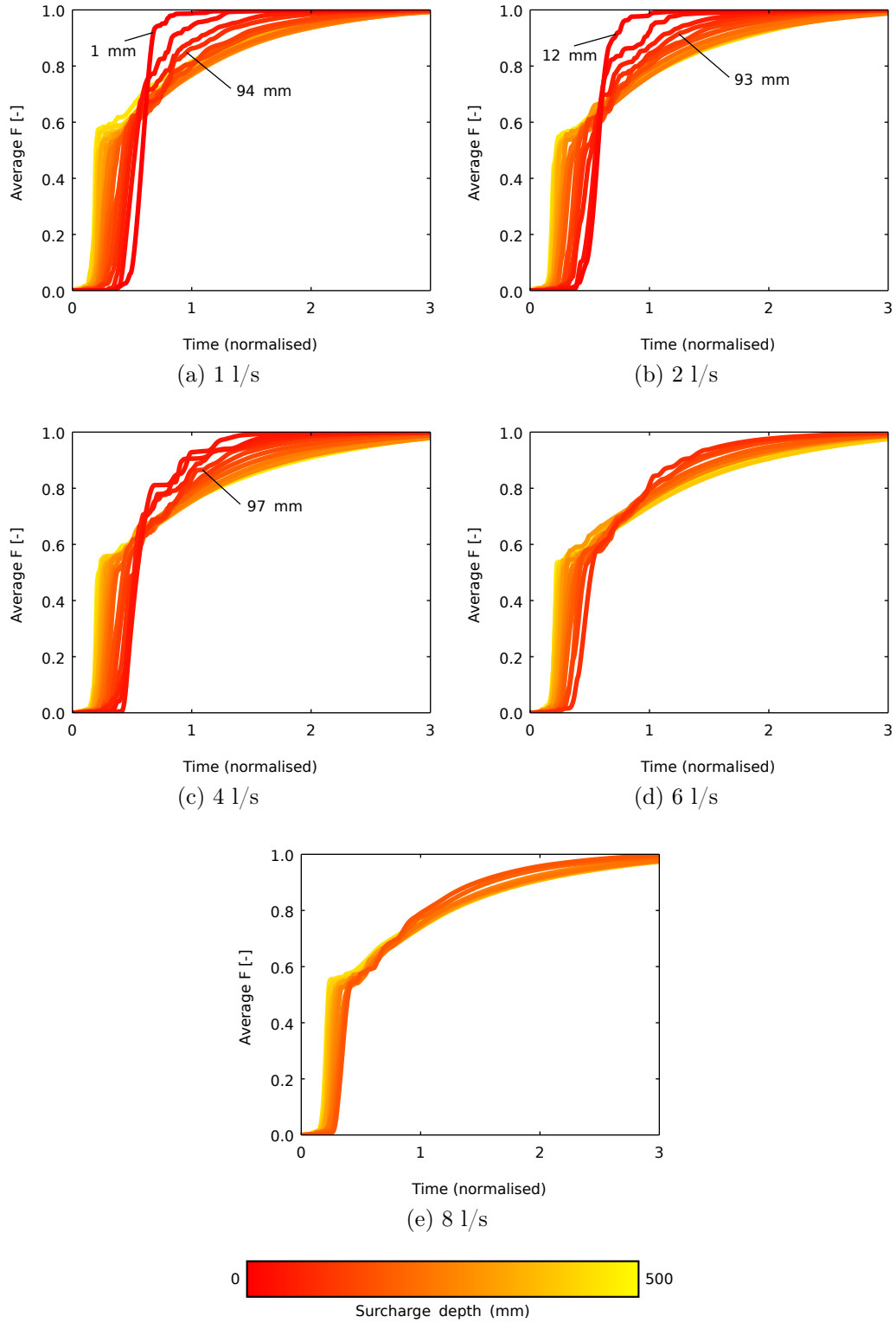

(a) 1 l/s

(b) 2 l/s

(c) 4 l/s

(d) 6 l/s

(e) 8 l/s

Figure 8.17: Benched 60° outlet angle normalised average CRTDs

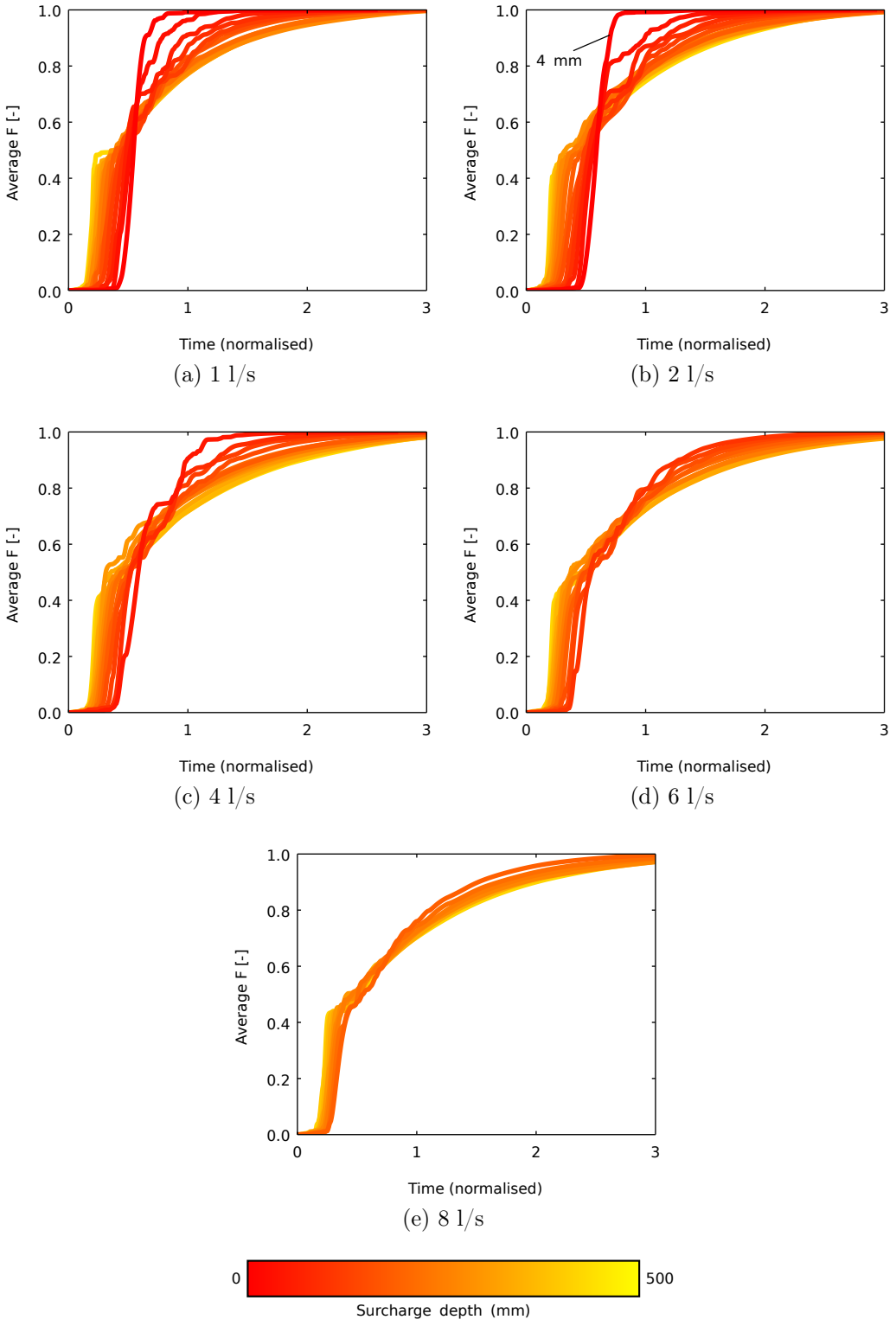

(a) 1 l/s

(b) 2 l/s

(c) 4 l/s

(d) 6 l/s

(e) 8 l/s

Figure 8.18: Benched 90° outlet angle normalised average CRTDs

e.g. indicate the presence of short-circuiting (Bennett, 2012; Stovin *et al.*, 2013). Immediately apparent is a difference between the 0° outlet angle and 30°/60°/90° outlet angle results. The 0° outlet shows a steady decay in t_{50} with increasing surcharge depth, which is consistent with the shifting in the normalised CRTDs caused by increasing surcharge volume in the denominator of Equation 2.5. For the 30°/60°/90° outlet angles though, the t_{50} lines are consistent across surcharge depth, i.e. they scale with surcharge volume as the complete mixing volume.

At non-zero outlet angles, there appears to be a consistent decrease in t_{50} at $s > 300$ mm, which is consistent with the transition in CRTD shape from those representing well-mixed flow to those indicating Type II short-circuiting. The less clear transition at the 90° outlet angle is due to the t_{50} value occurring in the exponential tail of the CRTD. As a result, t_{20} values are shown in Figure 8.20, where the decrease at $s > 300$ mm is more readily apparent. Both t_{50} and t_{20} values at $s < 60$ mm for the 60° and 90° outlet angles give some indication of the low surcharge Type I short-circuiting.

The differences in t_{50} and t_{20} values between the straight and angled manholes, combined with the differences in how the normalised CRTDs collapse and the pipe travel times confirms a difference in flow field between straight through and angled manholes. The higher t_x values for the angled manholes compared to the straight through manhole indicate a longer flow path. That the values are near constant with surcharge depth is consistent with utilising the full surcharge volume for mixing (e.g. the collapsing of normalised CRTDs). Similarities between the 30°, 60°, and 90° times correspond to visual similarities between the CRTDs providing additional evidence of similar flow fields despite differing outlet angles.

8.3.3.2 Benched manholes

t_{50} values for the benched manholes are shown in Figure 8.21 and t_{20} values are shown in Figure 8.22. There is overall the same exponential decrease with increasing surcharge depth as with the straight through unbenched manhole for all outlet angles. This corresponds to Type I short-circuiting.

The t_{50} values at the 90° outlet angle start to level out at $s > 150$ mm. This is due to the fraction of short-circuiting being less than 50%. At surcharge depths

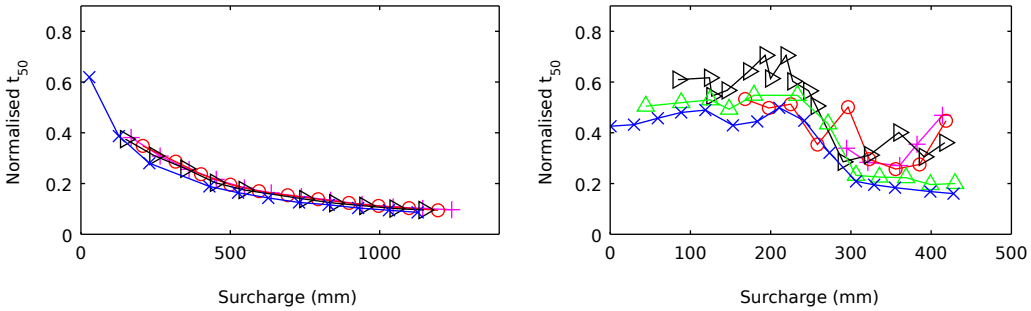

(a) 0° outlet angle (b) 30° outlet angle

(c) 60° outlet angle (d) 90° outlet angle

Figure 8.19: Unbenched normalised t_{50} values

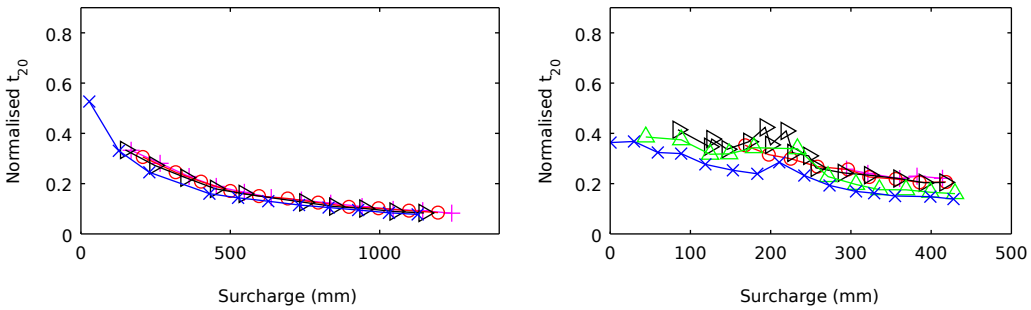

(a) 0° outlet angle (b) 30° outlet angle

(c) 60° outlet angle (d) 90° outlet angle

Figure 8.20: Unbenched normalised t_{20} values

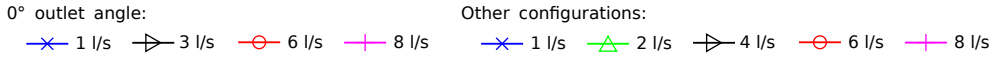

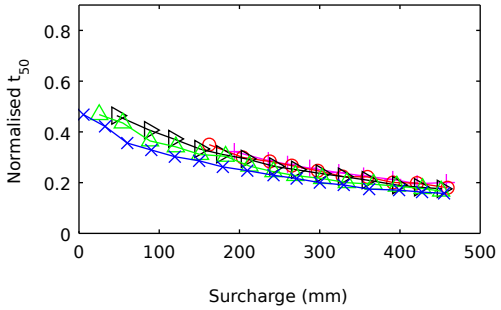

(a) 30° outlet angle

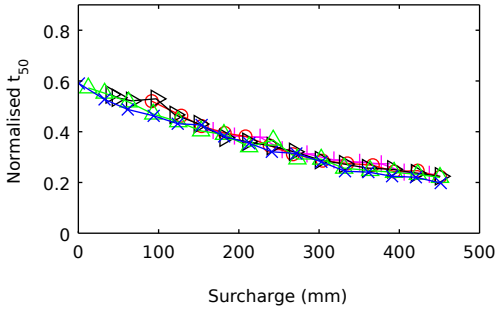

(b) 60° outlet angle

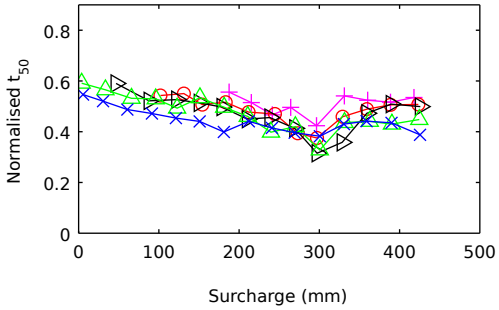

(c) 90° outlet angle

Figure 8.21: Benched normalised t_{50} values

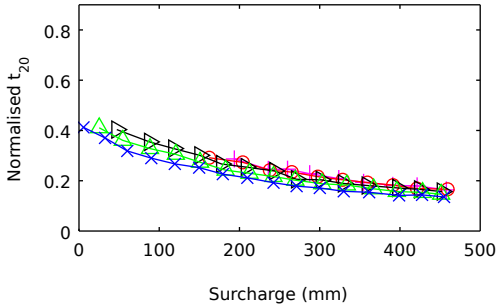

(a) 30° outlet angle

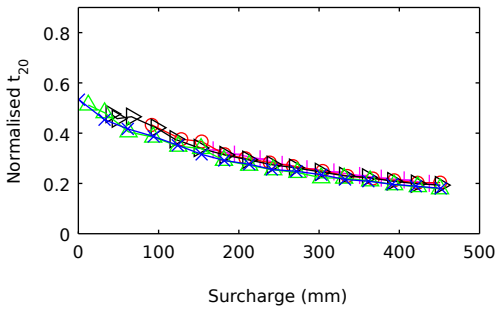

(b) 60° outlet angle

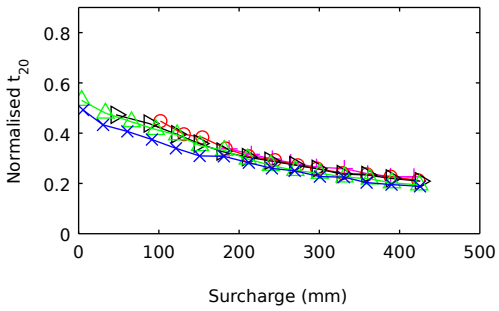

(c) 90° outlet angle

Figure 8.22: Benched normalised t_{20} values

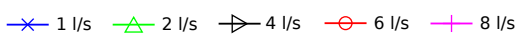

around 100 mm for the 60° outlet angle, a slight discontinuity in both t_{20} and t_{50} values is present. This is consistent with the transition from CRTD shapes indicating low surcharge Type I short-circuiting ($s < 100$ mm) to the CRTDs showing combined Type I short-circuiting and a well-mixed tail ($s > 100$ mm).

8.3.3.3 Variation in repeat trials

The t_x values of individual trials can be used to give an indication of the repeatability both of the experiments and of deconvolution. Figures 8.23 shows the standard deviation between repeat trials of $t_{20}/t_{50}/t_{80}$ values divided by the length of the longest RTD for each trial. Higher values indicate that repeats were less consistent. σt_{20} and σt_{50} values are consistently low. σt_{80} values are typically higher as a result of the variation present in CRTD tails. The maximum σt_{80} is less than 0.1. As most CRTDs are longer than $t_{nz} = 3$, at worst variation between the CRTDs deconvolved from repeat trials is around $3.3\dot{3}\%$. Overall the standard deviation values indicate that both the experimental trials and the deconvolution process produce consistent and repeatable results.

8.4 Energy

8.4.1 Energy loss coefficient

Energy loss coefficients (K values) derived from laboratory manometer data by Dennis (2000) and Saiyudthong (2003) are shown in Figure 8.24 for unbenched and Figure 8.25 for benched manholes. It is unclear to what extent the high variation visible is related to mixing characteristics, but previous research does indicate more consistent values should be expected. In particular, the 1 l/s K values for the unbenched 0° outlet angle are inconsistent with those of the 3, 6, and 8 l/s values, as well as those in other literature (e.g. Pedersen & Mark, 1990; Arao & Kusada, 1999).

Variation in energy loss with surcharge depth may be consistent with different flow fields. 0° outlet angle values are all similar (ignoring 1 l/s), which could correspond to a similar flow field across surcharge depth. A decrease in K for

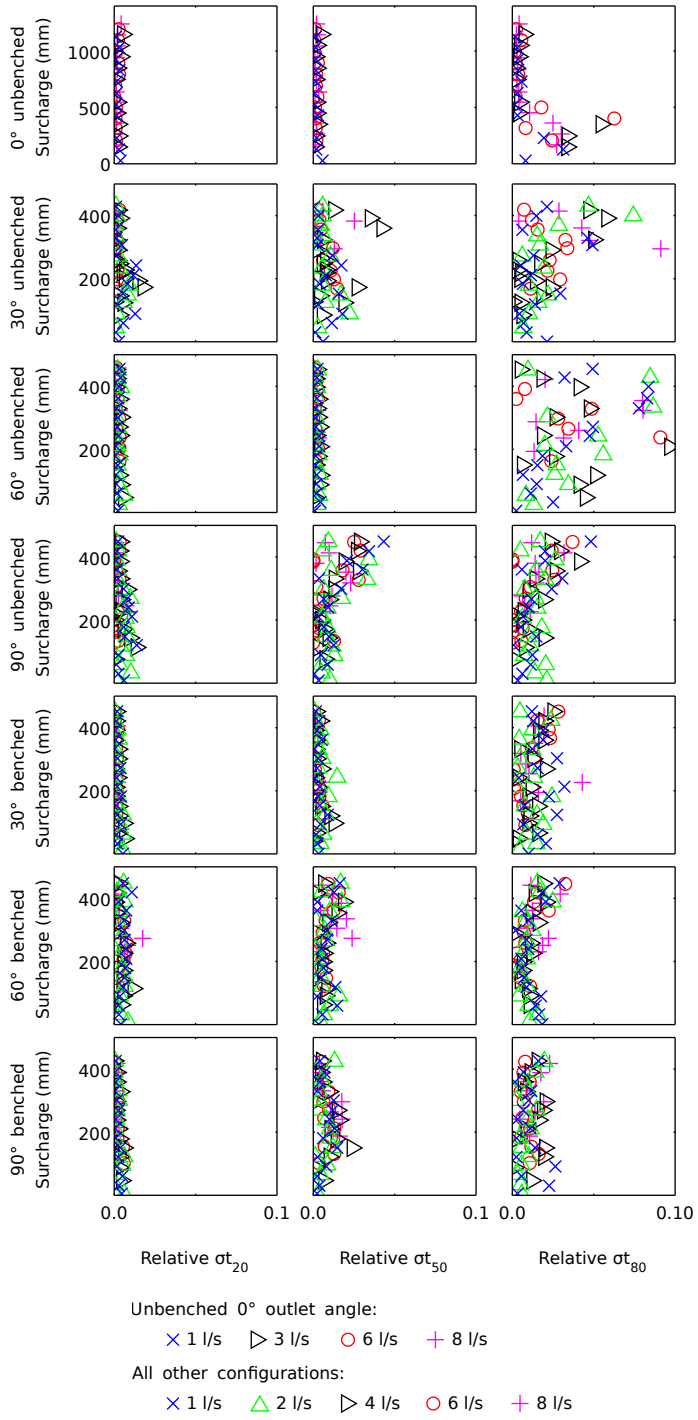

Figure 8.23: Variation in t_{20}, t_{50}, and t_{80} values

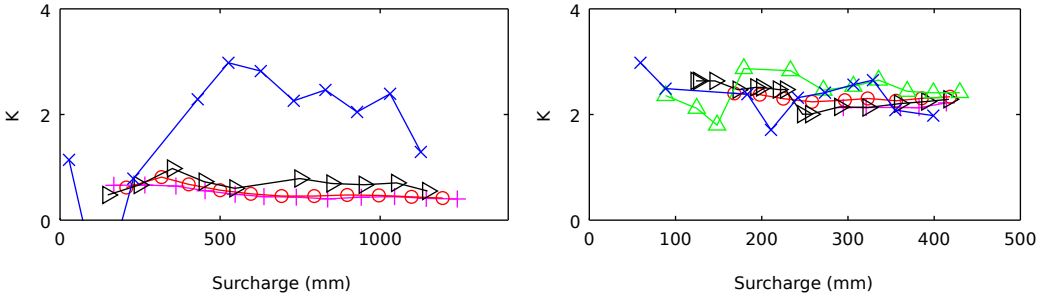

(a) 0° outlet angle

(b) 30° outlet angle

(c) 60° outlet angle

(d) 90° outlet angle

Figure 8.24: Unbenched K values

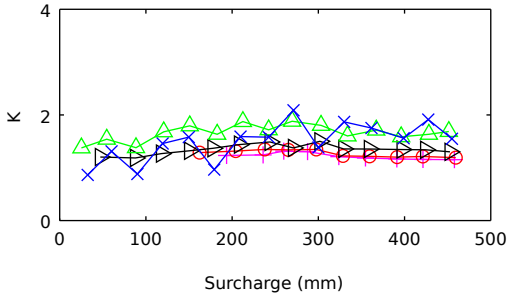

(a) 30° outlet angle

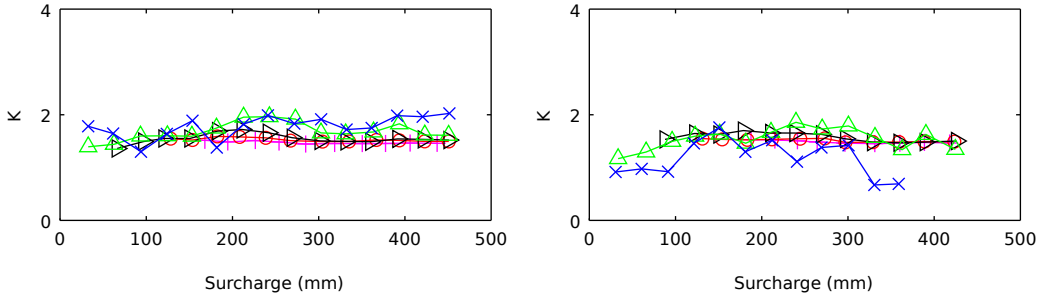

(b) 60° outlet angle

(c) 90° outlet angle

Figure 8.25: Benched K values

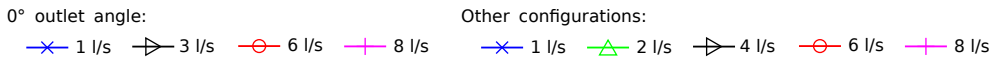

the the 1, 2, 4, and 6 l/s flow rates at the unbenched 60° and 90° outlet angles at $s > 300$ mm indicates there is a change in head loss with surcharge depth, which could be associated with the transition from well-mixed flow to Type II short-circuiting CRTDs.

In general benched manholes have lower K values than their unbenched counterparts, indicating lower energy losses overall. This could be attributed to the confinement and flow direction provided by the benching. K values at $s < 100$ mm depth in the benched manholes at 1 and 2 l/s in the 90° outlet angle, and slightly lower K values in the 60° outlet angle could correspond to low surcharge Type I short-circuiting CRTDs.

8.4.2 Energy dissipation

Velocity gradient (G) values are presented in Figures 8.26 and 8.27. A line for mean value at each flow rate is also plotted. Due to the high variability in the energy loss data, it is uncertain as to how reliable the obtained G values are, but there is a clear trend of higher G with higher flow rates.

The lowest G values are found for the straight through manhole, which due to Type I short-circuiting, has relatively low head loss and short travel times. G value rises greatly at the 30° outlet angle, and then drops as outlet angle increases. This is likely due to longer travel times at higher outlet angles. There is no large systematic variation with surcharge depth, and specifically nothing that corresponds to the previous established $s' = 0.258D$ (100 mm) threshold depth (Stovin *et al.*, 2010a) or any of the other transitional depths identified. Considering the magnitude of the values obtained, any variation could be lost in noise.

Figure 8.28 shows mean G values for each combination of benching, outlet angle, and flow rate. From this, it may be possible that G value could be used as a rough estimate of t_{50} provided an estimate of head-loss was also feasible.

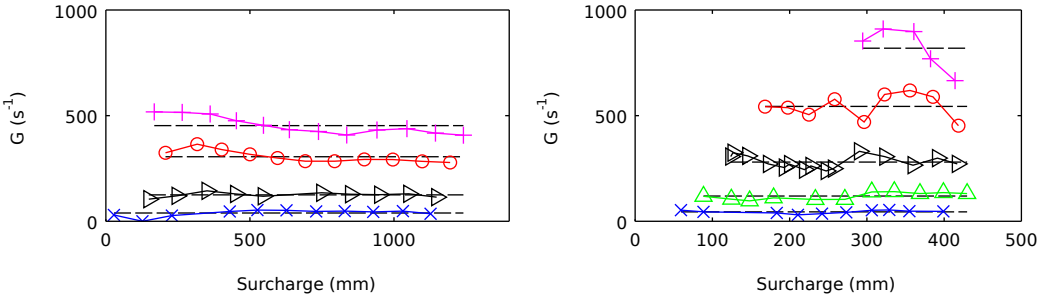

(a) 0° outlet angle (b) 30° outlet angle

(c) 60° outlet angle (d) 90° outlet angle

Figure 8.26: Unbenched G values

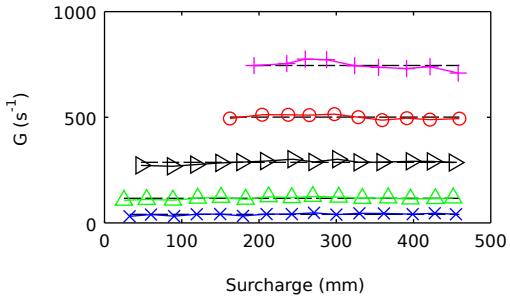

(a) 30° outlet angle

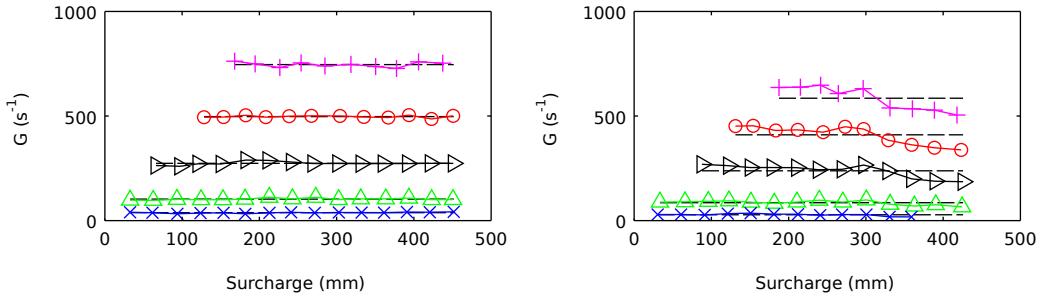

(b) 60° outlet angle (c) 90° outlet angle

Figure 8.27: Benched G values

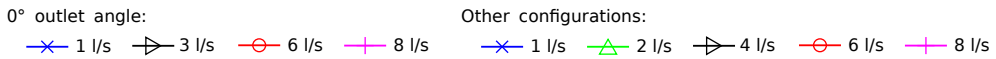

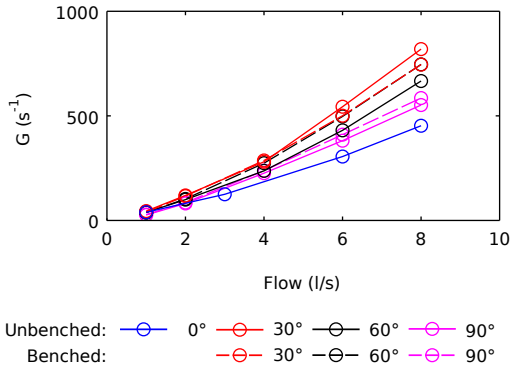

Figure 8.28: Relationship between Q and G

8.5 Previous data set analyses

The current data set has undergone two previous related analyses. The deconvolution analysis undertaken in Chapter 3, and a traditional ADE/ADZ analysis by Saiyudthong (2003).

8.5.1 Comparison to Chapter 3

In Chapter 3, the unbenched 1 l/s 0°, 30°, 60°, and 90° outlet angle configurations were analysed. Short-circuiting fractions and surcharge depths for the below-/above-threshold transition were proposed. This analysis relied on an assumption that below-threshold well-mixed and the above-threshold Type I short-circuiting flow fields were applicable to angled manholes. The threshold depth was found to increase with increased outlet angle, and short-circuiting fraction to decrease with increased outlet angle. Based on the results obtained and assuming jet deflection, the work proposed horizontal and vertical flow fields.

The current work analyses a more comprehensive data set and clearly indicates that what was considered the threshold in Chapter 3 occurs at a consistent surcharge depth across outlet angle and flow rate in angled manholes. Furthermore, a greater understanding of CRTD shapes indicates that the flow fields that develop in angled manholes are not the previously assumed below- and above-threshold fields. Instead, well-mixed flow transitions to Type II short-circuiting. The fraction of short-circuiting otherwise is consistent with the new results. The low

surcharge Type I short-circuiting CRTDs previously found at the 30° outlet angle is found at other angles and flow rates. The low surcharge Type I short-circuiting was also reported by Stovin *et al.*, 2013.

8.5.2 Comparison to Saiyudthong (2003)

Saiyudthong (2003) both collected and analysed the current data set. The analysis was carried out across flow rate, surcharge depth, outlet angle and benching. K values and optimised best-fit Aggregated Dead Zone (ADZ) model parameters were used to compare the differences between configuration. Some CFD work and comparison of G values was also carried out.

K values were identical to those presented here, and a comparison was made to theoretical and empirical models predicting K. No correlation between K and flow field (e.g. below-/above-threshold) was made. Instead K was examined in comparison to a CFD simulation, and only with reference to unbenched manholes. Minor trends in K value previously unexplained have now been referenced to potential flow fields according to CRTD results. As a result, the previous recommendation of mean K values for each outlet angle across surcharge depth can no longer be made.

The G values that were calculated show similar patterns to the current work. A better appreciation of the implications of G value remaining constant across surcharge depth can also therefore be developed, although it still needs further investigation.

Of particular interest the comparison of mixing processes inferred from ADZ model parameters to those indicated by the deconvolved CRTDs and therefore of any potential limitations of traditional parameter analysis.

8.5.2.1 Travel times

Travel time $\bar{t}$ is the time from the centroid of the upstream concentration profile to the centroid of the downstream concentration profile. Saiyudthong (2003) analysed best fit values to the data and in general found travel time to increase linearly with surcharge depth. For the unbenched 30° and 60° manholes, travel

time dropped to a constant value when surcharge depth exceeded 275 mm and 325 mm, respectively. This corresponds to the 300 mm change in shape observed in the deconvolved CRTDs, which was otherwise unobservable with travel time analysis. Saiyudthong (2003) wrote that this...

> "...might suggest that after the surcharge was above the threshold [between linearly increasing and constant travel time], the travel time was independent of the surcharge and influenced by the dominant core zone. In other words, it may be interpreted that after the surcharge pass the threshold, it was beyond the effective mixing volume by the diffusion of solute."

CRTD analysis has indicated that this effect is due to Type II short-circuiting. While it is controlled by a dominant core zone, it also utilises the full manhole volume at all surcharge depths.

No similar drop in travel time is shown for the benched manholes at the 60° or 90° outlet angle. As they result in bifurcating flow, the well-mixed volume that increases with surcharge depth will increase the travel time, which cancels out the portion of solute that arrives earlier due to short-circuiting. Benched manholes in general had lower travel times, which...

> "...might be caused by the benching confining the jet diffusion zone. In other words, the benching reduced the volume of the diffusion..."

This can be confirmed by the Type I short-circuiting portion of the CRTDs from benched manholes in comparison to the well-mixed flow of the unbenched manhole, i.e. the benched manhole is shown to have a shorter flow path, shown in Figure 8.29. This is also reflected in lower t_{50} values for benched manholes.

8.5.2.2 Reach time delay

Reach time delay is the difference in first arrival time, i.e. the time it takes for the first dye observed at the upstream fluorometer to be observed at the downstream fluorometer. Saiyudthong (2003) reports that optimised values of reach time delay

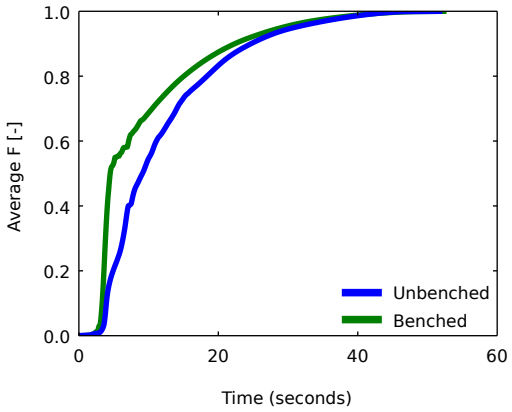

Figure 8.29: 60° unbenched 265 mm vs benched 241 mm 4 l/s manhole average CRTDs

is roughly constant for the unbenched 0° outlet angle manholes, but for the 30°, 60°, and 90° angles increases with surcharge depth up to around 300 mm and then decreases to a roughly constant value. This is consistent with the transition from well-mixed flow to Type II short-circuiting observed in the deconvolved CRTDs.

At the benched 30° outlet angle, reach time delay was observed to be constant, which is consistent with and indicative of the Type I short-circuiting observed in the deconvolved CRTDs. At the benched 60° and 90° outlet angles, reach time delay decreased with increasing surcharge depth, which is inconsistent with the deconvolved CRTDs (predicting roughly constant first arrival time.) Saiyudthong (2003) theorised that the decreasing reach time delay could be due to flow directly over the benching, but there is no CRTD evidence to support this.

8.5.2.3 Dispersive fraction

Dispersive fraction is the ratio of residence time to travel time. Saiyudthong (2003) reports optimised values to be higher in all unbenched than benched manhole configurations, except for surcharges of 100–300 mm in the 60° and 90° benched configurations. The increase in dispersive fraction could be related to the change from low surcharge Type I short-circuiting, to well-mixed flow, to Type II short-circuiting. In the benched manholes dispersive fraction could break down into a linearly increasing trend from 0–100 mm then a second linear trend with lower slope after 100 mm. The link to flow field is only apparent however

after having the additional insight provided by the deconvolved CRTDs.

Saiyudthong (2003) hypothesised that...

> "This may be because the benching at the moment worked as a baffle to provide a circulation or secondary flow in the manhole. [...] The circulation made more mixing in the benched manholes than in the unbenched manholes."

The first statement reflects the flow field inferred from the benched CRTDs, but the second does not accurately reflect the differences in mixing between benched and unbenched manholes. Comparing unbenched and benched CRTDs, e.g. Figure 8.29, the unbenched CRTDs are more exponential in shape, indicating more mixing in the benched manholes. The greater dispersive fraction of the benched manholes from 100–300 mm is therefore not an accurate indicator of the mixing taking place in this scenario.

8.5.2.4 Two-cell ADZ

Saiyudthong (2003) suggested and demonstrated that a two-cell ADZ model could be used to better model solute transport in unbenched manholes at surcharge depths exceeding 300 mm, i.e. Type II short-circuiting. A...

> "Head profile will be dominated by the advection process as it comes first and contains the peak of the downstream profile. Meanwhile, Tail profile is the remaining part of the whole downstream profile, in which dispersion might be a major process. In other words, this two cell technique was to quantify the amounts of solute concentration travelling in the core zone, dominated by advection process, and the diffusion zone, dominated by dispersion process, in jet flow..."

This is in effect a model and description of the two separate processes identified through examination of the deconvolved CRTDs. The sharp rise in CRTD of short-circuiting as the Head advection dominated process and the exponential Tail dispersion dominated process.

8.6 Flow fields

It is possible with the aid of the CRTDs to infer what flow fields might be occurring at different surcharge depths, at different outlet angles, and with or without benching. Six characteristic CRTD shapes have been observed to occur at different configurations in the data analysed here:

1. Type I short-circuiting flow (above-threshold)
2. Low surcharge Type I short-circuiting flow
3. Type II short-circuiting flow
4. Well-mixed flow (below-threshold)
5. Transitional flow
6. Bifurcating flow, combining Type I short-circuiting and well-mixed flow

Representative CRTDs for each are shown in Figure 8.30. The figure also has the two representative CRTDs presented by Stovin *et al.* (2010a) for comparison. The 2010 CRTDs have had pipe mixing effects subtracted, and so do not directly match the other CRTDs shown here. Pipe subtraction can be thought of as a shift on the time axis towards zero for making a quick comparison. The different CRTD shapes and their associated flow fields are discussed in the following sections.

8.6.1 Type I short-circuiting flow (above-threshold)

Type I short-circuiting flow CRTDs are present in the straight through unbenched and benched 30° outlet angle manhole results. They are consistent with what have been previously shown to be above-threshold CRTDs, shown in Figure 8.30. The Type I short-circuiting flow field they represent occurs at $s > 0.285D$ in 0° unbenched manholes according to Stovin *et al.* (2010a), and has been found here at surcharge depths greater than 6 mm ($s > 0.025D$) in the benched 30° manhole.

In short-circuiting flow the majority of the solute passes directly through the manhole. A small portion of the solute enters the storage volume to be released

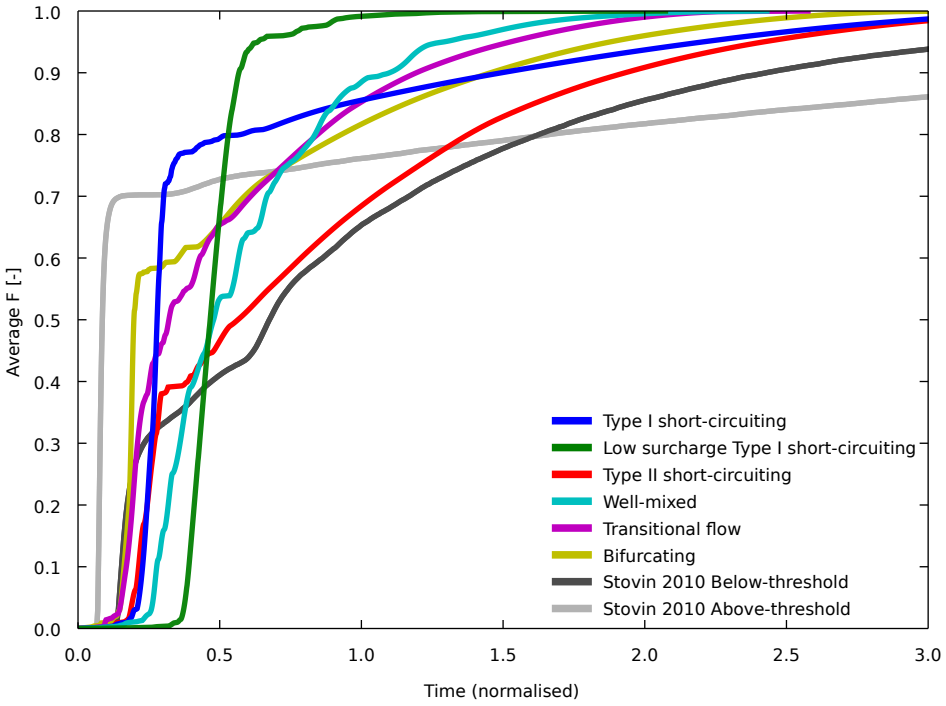

Figure 8.30: Different characteristic CRTD shapes, with the below-/above-threshold CRTDs of Stovin *et al.* (2010a)

again slowly. This indicates very little shear interaction between the inflow jet and storage volume. In the straight through unbenched manhole this can be attributed to confining pressure and in the benched manholes to the confinement provided by the benching.

8.6.2 Low surcharge Type I short-circuiting flow

Low surcharge Type I short-circuiting CRTDs occur at $s < 0.025D$ in straight through manholes according to Stovin *et al.*, 2013. They have been observed at below 60 mm ($s < 0.155D$) in angled unbenched manholes and below 100 mm ($s < 0.258D$) in angled benched manholes in the results. They are characterised by their occurrence at low surcharge depths, and in angled manholes by a higher short-circuiting fraction than the Type II short-circuiting that occurs at higher surcharge depths.

Particle tracking in a CFD model allows for a comparison between experimental and theoretical CRTDs and can be used to verify flow fields that have been inferred from the CRTDs. The unbenched 90° outlet angle 1 l/s 32 mm surcharge configuration has been modelled with a CFD simulation, and the CRTD obtained from the model is shown in Figure 8.31a. The theoretical CRTD obtained from the CFD shows good agreement with the deconvolved experimental CRTDs, particularly in the reproduction of the amount of short-circuiting and the variation in the exponential tail.

Figure 8.31b shows velocity vectors in the horizontal plane section at mid-pipe depth. The bulk of the flow is shown to directly short-circuit due to jet deflection and a recirculation zone forms. Both the short-circuiting and the recirculation are shown in the CRTD. The latter is represented by the small variations in the CRTD tail, the frequency of which are probably consistent with the recirculation time as tracer is entrained from the jet into the zone then back into the jet after a complete circulation. This can be thought of as an effective dead zone, with cell size increasing with surcharge depth until well-mixed flow develops.

The presence of primarily horizontal recirculation rather than vertical recirculation is what distinguishes low surcharge Type I short-circuiting from regular Type I short-circuiting.

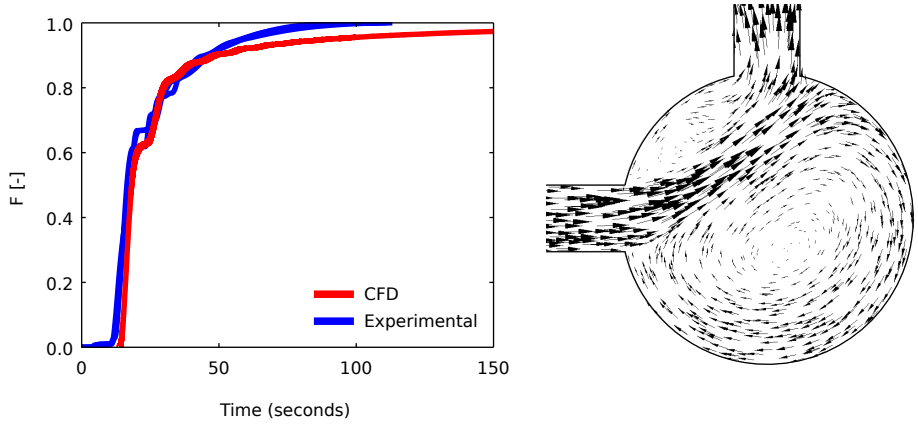

(a) CRTD comparison

(b) Horizontal plane section (cutting pipe diameter)

Figure 8.31: CFD model of 32 mm surcharge in a 90° unbenched manhole at 1 l/s, showing low surcharge Type I short-circuiting

8.6.3 Type II short-circuiting flow

CRTDs indicating Type II short-circuiting occur in unbenched angled manholes at surcharge depths greater than 300 mm ($s > 0.773D$). Type II short-circuiting is distinguished from Type I by the collapse of the CRTDs when normalised, showing that the flow path passes through the surcharge volume.

A CFD model of the unbenched 90° outlet angle 1 l/s 330 mm surcharge configuration was run to verify the presence of Type II short-circuiting. Model results are shown in Figure 8.32. The theoretical and experimental CRTDs show reasonable agreement with similar first arrival times. The tail of the CRTD is slightly delayed in the CFD model, but is of a similar shape. The velocity vectors in the vertical section through the inlet pipe (cutting the pipe diameter) show a circulating field forms, covering the entire volume. The jet impacts the far wall then curls around. The core of the jet travels through this field, resulting in a mass of solute with similar travel time and corresponding rise in CRTD.

The formation of the recirculating field may be due to water depth reaching manhole diameter, i.e. $s + D_p \approx D$. It is possible that at lower surcharge depths there is interaction between the jet curling around and the water surface that in this case prevents the circulation zone from establishing.

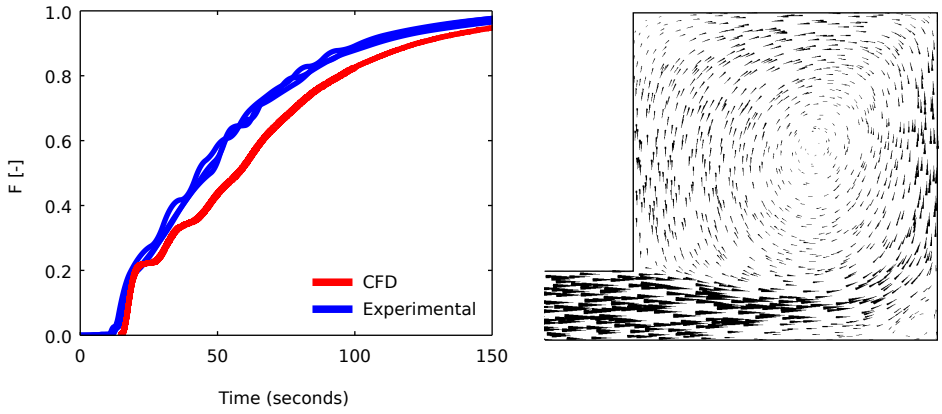

(a) CRTD comparison

(b) Vertical inlet plane section (cutting pipe diameter)

Figure 8.32: CFD model of 330 mm surcharge in a 90° unbenched manhole at 1 l/s, showing Type II short-circuiting

8.6.4 Well-mixed flow (below-threshold)

Well-mixed CRTDs have only been observed in unbenched manholes. They occur in straight through unbenched manholes below-threshold ($s < 0.2D$) (Stovin *et al.*, 2013) and occur in angled unbenched manholes at surcharge depths between 60 mm and 250 mm ($0.155D < s < 0.696D$) in these results.

According to previous work, at a range of surcharge depths an expanding jet meets the water surface promoting mixing, i.e. well-mixed flow (Stovin *et al.*, 2013). In angled manholes $D/D_p < 4.4$ the jet is theorised to hit the far wall as jet length is greater than manhole diameter, causing turbulence. As flow rate increases there is likely to be increased turbulence as the inlet velocity of the water is dissipated. This is reflected in the t_x times in Figures 8.19 and 8.20 that do not collapse perfectly on top of each other for angled manholes, but instead increase slightly with flow rate.

The 2010 below-threshold CRTD shown in Figure 8.30 appears to be more consistent with the Type II short-circuiting CRTD. The more drawn out tail indicates a greater dead zone effect occurring. As the 2010 CRTD is from a straight through manhole, the dead zone effect may be due to the areas either side of the jet, similar to what is shown in Figure 8.31b.

8.6.5 Transitional flow

Transitional CRTDs have been found in these results in angled unbenched manholes around the surcharge depth of 270 mm ($s \approx 0.7D$). They are exponential in shape, similar to the well-mixed CRTDs, but are characterised by earlier first arrival times.

The transitional CRTD shape between well-mixed and Type II short-circuiting CRTDs may be an effect of averaging CRTDs. However, investigation of the repeat trials before averaging indicates that this is not the case as CRTD shape is consistent between repeats. The CRTDs may potentially indicate oscillation in the manhole between the two neighbouring mixing conditions, in effect an averaging taking place at the system level. Alternatively, the transitional CRTDs may otherwise indicate some sort of unique flow field occurring. It is not understood what mechanism may cause this.

8.6.6 Bifurcating flow

CRTDs indicating bifurcating flow have only been observed to occur in these results for the benched 60° and 90° outlet angle manholes at surcharge depths greater than 100 mm ($s > 0.258D$). In bifurcating flow, the flow path splits. Bifurcating CRTDs indicate a flow field combining Type I short-circuiting with well-mixed flow, characterised by a roughly 50/50 split, i.e. a consistent 50% short-circuiting mass fraction.

In bifurcating flow CRTDs, the steep rise associated with short-circuiting clearly shifts in normalised time, with higher surcharges having earlier normalised first arrival times. Simultaneously, the normalised exponential portions of the CRTD collapse nearly perfectly when normalised. The combination of these two separate CRTD characteristics indicates bifurcating flow. Saiyudthong (2003) hypothesises the Type I short-circuiting component is caused by the inlet jet being redirected to the outlet by the benching. The well-mixed component occurs as a portion of the jet not redirected by the benching enters the surcharge volume.

8.6.7 Flow field summary

6 different CRTD shapes have been identified, indicating different combinations of Type I short-circuiting, Type II short-circuiting, and well-mixed flow. While some of these CRTDs reflect fundamentally similar flow fields, they are caused by different hydrodynamics. The flow fields are summarised in Table 8.2 and Figure 8.33.

Of the different experimental configurations, the 30° benched manhole has the simplest flow field, consisting entirely of short-circuiting flow. The 60° and 90° benched manholes transition from low surcharge Type I short-circuiting to a bifurcating flow field combining Type I short-circuiting with well-mixed flow. The 0° unbenched manhole transitions from low surcharge Type I short-circuiting to below-threshold well-mixed flow to above-threshold Type I short-circuiting flow. The 30°/60°/90° unbenched manholes experience the most complicated mixing processes, from low-surcharge Type I short-circuiting to well-mixed flow to transitional to Type II short-circuiting.

These flow fields have been inferred from the CRTDs deconvolved from raw data at one manhole diameter ($D/D_p = 4.4$). However, given the results of Stovin *et al.* (2013) showing changes in flow field with manhole diameter, these flow fields may not form at all ratios of D/D_p. Type II short-circuiting may not form at higher diameter ratios as it may depend on jet impact on the far wall. Redirection of the jet for very low surcharge short-circuiting in angled manholes may also not form at higher diameter ratios due to jet core dissipation.

Figure 8.33 also shows results from Arao & Kusada (1999) where changes in K value may indicate a change in hydraulic regime. These values provide supporting

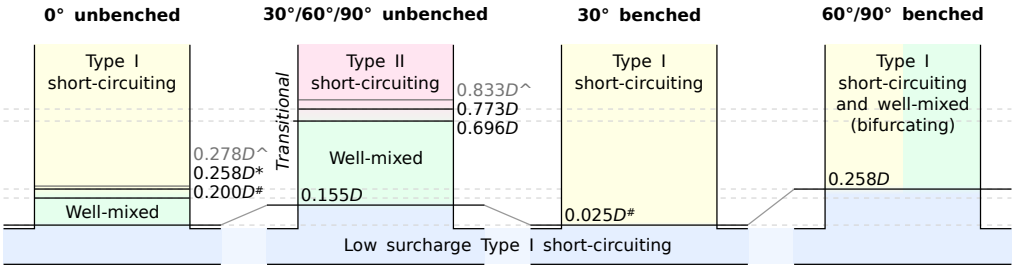

Figure 8.33: Flow field summary

^Arao & Kusada (1999), *Stovin *et al.* (2010a), #Stovin *et al.* (2013)

Flow field	Alternative names	First proposed by	Evidence
Type I short-circuiting flow	Post-threshold Above-threshold	Guymer *et al.* (2005)	Unbenched 0° outlet angle CRTDs, Sub-subsection 8.3.1.1 Benched 30° outlet angle CRTDs, Sub-subsection 8.3.2.2
Low surcharge Type I short-circuiting flow	Very low surcharge	Jones (2011) Stovin *et al.* (2013)	Unbenched 30° outlet angle CRTDs, Sub-subsection 8.3.1.1 Unbenched 90° outlet angle CRTDs, Sub-subsection 8.3.2.2 Benched CRTDs, Subsection 8.3.2 32 mm 90° outlet angle CFD work, Subsection 8.6.2
Type II short-circuiting flow			Unbenched 30°/60/90° outlet angle CRTDs, Sub-subsections 8.3.1.2–8.3.1.4 330 mm 90° outlet angle CFD work, Subsection 8.6.3
Well-mixed flow	Pre-threshold Below-threshold	Guymer *et al.* (2005)	Unbenched 30°/60/90° outlet angle CRTDs, Chapter 3 and Sub-subsections 8.3.1.2–8.3.1.4
Transitional flow		Sonnenwald *et al.* (2011)	Unbenched 30°/60/90° outlet angle CRTDs, Chapter 3 and Sub-subsections 8.3.1.2–8.3.1.4
Bifurcating flow			Benched 60°/90° outlet angle CRTDs, Sub-subsections 8.3.2.3–8.3.2.4

Table 8.2: Flow field summary

evidence for a relationship between head loss and flow field.

8.7 Conclusions

In general, the current work elaborates on previous results and provides additional insight into hydrodynamic processes occurring in angled and benched manholes. A review of existing solute transport and manhole flow field research was carried out and a need for a comprehensive analysis identified. The novel deconvolution of raw data was used to extract Cumulative Residence Time Distributions from previously collected raw solute transport data. The deconvolution of raw data was verified by comparison to the deconvolution of identical, pre-processed, data. CRTD scaling was successfully applied as necessary. Additional understanding of how the CRTD reflects flow field was used to identify how mixing characteristics vary with surcharge depth, outlet angle, and benching. Analysis of retention times was carried out to further examine differences in mixing characteristics. Similar analyses of energy losses (K) and energy dissipation (G) were carried out.

Retention time values match mixing characteristics. t_{50} and t_{20} were found to be reliable indicators of change in flow field. Similar retention time values across experimental trials indicate consistent repeatability of both the experimental data and the deconvolution analysis. The experimental K values are inconsistent for some configurations, but to some extent also reflect differences in mixing characteristics. Experimental G values do not show much variation, and may therefore hint at a link between $\triangle h$ and t_{50}. More work in this area is required to better establish the link between energy losses and mixing characteristics.

Comparison with traditional ADZ model parameter analysis, Saiyudthong (2003), reveals that while it does not fully capture the differences in mixing characteristics observed through CRTD analysis, several key features were observed with both analyses. Travel time analysis suggested that constant values in unbenched manholes were due to a dominant core zone, which has been confirmed by the presence of short-circuiting. Similarly, lower travel times in benched manhole suggested that benching confined the jet, confirmed by the presence of short-circuiting in the deconvolved benched manhole CRTDs. Changes in reach time delay also reflected changes in mixing characteristics in some cases.

Saiyudthong (2003) found dispersive fraction to be higher in benched manholes, indicating greater mixing. However, the comparison of benched and unbenched CRTDs shows lower short-circuiting fractions for unbenched manholes, indicating greater mixing taking place.

Overall, six characteristic CRTDs were identified, reflecting different mixing conditions. Based on these, a Type I short-circuiting flow field can be inferred to occur at $s > 0.258D$ in straight through unbenched manholes and at $s > 0.025D$ in 30° benched manholes, characterised by a steep rise in the CRTD close to the equivalent pipe travel time. Low surcharge Type I short-circuiting can be inferred to occur at $s < 0.025D$ in straight through manholes and in 30° benched manholes, at $s < 0.155D$ in 30°/60°/90° unbenched manholes and at $s < 0.258D$ in 60°/90° benched manholes.

Well-mixed flow has been inferred to occur in 0° unbenched manholes at $0.025 < s < 0.258D$ and in 30°/60°/90° unbenched manholes at $0.155D < s < 0.696D$, but not in benched manholes. It is caused by jet expansion reaching the surface resulting in turbulence that promotes mixing. Deconvolved CRTDs also infer a transitional flow field forming in surcharge depths between well-mixed flow and Type II short-circuiting flow at $s \approx 0.7D$, characterised by lower first arrival times. It is potentially due to an oscillation between the neighbouring flow fields.

Type II short-circuiting can be inferred to occur at $s > 0.773D$ for all of 30°/60°/90° unbenched manholes. This is in contrast to results from Chapter 3 that indicated that the threshold depth varied with outlet angle. Type II short-circuiting is a circulating flow field that carries mass through the surcharge volume at similar travel times. A bifurcating flow field can be inferred to form in 60° and 90° benched manholes, combining Type I short-circuiting flow and well-mixed flow at $s > 0.258D$. This flow field is caused by portions of the jet being redirected by benching, either towards the outlet or upwards into the surcharge volume. As it is caused by the benching, it does not occur in unbenched manholes.

These flow fields have been observed only at $D/D_p = 4.4$. It is possible they may not form at all manhole to pipe diameter ratios. However, results from Arao & Kusada (1999) with $D/D_p = 4.1$ concur with those obtained for the straight through and unbenched 90° outlet manholes.

Chapter 9

Conclusions and further work

This chapter summarises the work carried out within this thesis. Afterwards conclusions are presented, and then suggestions for possible further work are outlined. Finally, key outcomes of this thesis are listed.

9.1 Summary

The introduction of Chapter 1 provides background information and establishes the wider context for the research undertaken. It introduces the concept of the Residence Time Distribution as a potential means of increasing the understanding of the mixing processes underlying solute transport, and deconvolution as a potential means of obtaining an RTD from experimental data.

Chapter 2 specifically described how deconvolution and RTDs fit within the context of solute transport research and hydraulic modelling. The RTD was presented and compared to the Advection-Dispersion Equation and Aggregated Dead Zone models in Figure 2.4, showing how the RTD is an improved way to describe mixing processes and potentially therefore infer hydrodynamic processes. Deconvolution in general is outlined, and maximum entropy deconvolution specifically is explained as a means of obtaining an RTD from experimental data. The aims and objectives of this thesis are also listed in Chapter 2.

Objective 1 was to develop and convey an understanding of maximum entropy deconvolution, which was partially carried out in Chapter 2. In addition, a practical examination of how maximum entropy deconvolution functioned was made through a study of the effects on solute transport of varying manhole outlet angle, presented in Chapter 3. This helped to build an understanding of how maximum entropy deconvolution works, as well as establishing the guiding questions for what parts of deconvolution needed to be examined in greater detail.

Objective 2 involved conducting sensitivity analyses to verify the suitability of maximum entropy deconvolution as applied to solute transport data. As a result of the work carried out for Chapters 2 and 3, two analyses were conducted in support of Objectives 1 and 2. A detailed examination of correlation measures was undertaken in Chapter 4, and a detailed examination of deconvolution configuration options was undertaken in Chapter 5.

The detailed examination of correlation measures provides an understanding of how differences between recorded and predicted concentration profiles are reflected by a single value. This is fundamental to any model fitting exercise, and in a deconvolution context is partially responsible for ensuring that a realistic RTD is generated (Equation 5.5). Correlation measures are also used for evaluation of the resulting RTDs, i.e. by comparing the fits of the predicted downstream profile across repeated trials.

The second sensitivity analysis conducted for Objective 2 forms the core of the thesis. In Chapter 5, maximum entropy deconvolution is fully and completely outlined, finally satisfying Objective 1. The potential configuration options for maximum entropy deconvolution are tested with a range of representative solute transport data. The purpose of this is two-fold: to simultaneously verify the applicability of maximum entropy deconvolution; and to identify a single set of robust configuration options. Both purposes are realised, and credence is lent to those results as Chapter 5 has been published as a peer reviewed journal article (Sonnenwald *et al.*, 2013a).

Chapters 2 to 5 established the suitability of maximum entropy deconvolution. At this point, as part of Objective 3, improvements to the methodology were considered and two explored. Chapter 6 addresses RTD smoothness. By default, maximum entropy deconvolution uses linear interpolation between sample points,

which results in sharp changes in the RTD that are inconsistent with natural mixing processes. Alternative RTD interpolation functions remove this effect, and simultaneously reduce the effects of over-sampling. Chapter 7 investigates the deconvolution of raw data. Data pre-processing is often time consuming and complex. A sensitivity analysis was conducted to find out the limits to data that can be deconvolved without pre-processing.

Objective 4, the demonstration of maximum entropy deconvolution to obtaining new results, is addressed in the penultimate chapter (Chapter 8). Recommended deconvolution settings from Chapter 5 are combined with the ability to deconvolve raw data from Chapter 7 to perform a complete reanalysis of the data that was partially analysed in Chapter 3. The refined and validated deconvolution methodology is used to recover RTDs and analyse the affects of benching and outlet angle on mixing characteristics in surcharged manholes. Energy loss data is also combined with the analysis. Comparisons are made to the original data analyses.

9.2 Conclusions

Several conclusions can be drawn relating to maximum entropy deconvolution and RTDs. Other conclusions about the systems under investigation can also be drawn. Conclusions regarding maximum entropy deconvolution and RTDs include:

- Correlation measures used for model identification should be insensitive to noise, while remaining sensitive to transformation and transformation magnitude. 8 correlation measures examined in this thesis meet these criteria: BLC, χ^2, FFCBS, R^2, RMSD, R_t^2, ISE, and APE (Chapter 4).

- Correlation measures used for model evaluation should share characteristics with those used for identification, but additionally be non-dimensional in order to allow for the relative comparison of model fit across different data sets. The R^2, R_t^2, and APE correlation measures meet these criteria, with varying sensitivity to different time-series characteristics. Of the three: R^2 is extremely sensitive to overall profile shape; APE is sensitive to small dif-

ferences in profile; and R_t^2 is flexible, indicating greater differences between profile are similar (Chapter 4).

- Maximum entropy deconvolution has several configuration options, of which four were found to have significant impact on the deconvolved RTD. These are: number of sample points; sample point distribution; maximum number of iterations; and constraint function (Chapter 5).
  - Greater numbers of sample points result in RTDs that have better predictive capability. However, greater numbers of points also result in RTD entropy further from zero—they are less smooth. Numbers of sample points below 40 in many cases result in reduced predictive capability, and so 40 sample points was recommended as the best balance of RTD predictive capability and smoothness (Chapter 5).
  - Sample point distribution has a significant impact on RTD quality as it fundamentally changes the deconvolution problem. Of the six distributions examined, two performed poorly in almost all cases, the equally spaced and downstream log distributions. The remaining four (the double log, double cubic, slope-based, and log from zero) distributions all produced RTDs with excellent predictive capability. The double log and double cubic distributions, however, had significantly reduced smoothness and the log from zero distribution had poor mass balance. As a result, the new slope-based distribution was recommended as a robust configuration option (Chapter 5).
  - Maximum number of iterations had the smallest impact on RTD quality. Any number of iterations greater than 150 produced an acceptable result. RTD smoothness varied inconsistently with increased iterations. However, in some cases predictive capability continued to increase with more iterations, so 350 iterations was recommended (Chapter 5).
  - Constraint function affected RTD predictive capability. Of the 8 tested constraint functions (determined in Chapter 4), 4 performed equally well. These are the R^2, RMSD, R_t^2, and APE constraint functions. Although there is some indication that constraint function is linked to data characteristics, it is weak and so R_t^2 is recommended as a function, based on it being a well understood and used measure in solute transport research (Chapter 5).

- Maximum entropy deconvolution works with a range of source data types. Manhole, storage tank, channel, and pipe data (Table 5.1) were all successfully deconvolved with high predictive capability shown by the deconvolved RTDs (Chapter 5).

- Interpolation function was investigated as a means of producing smoother RTDs and two alternate interpolation functions were suggested to replace the original linear interpolation: Gaussian Influence Estimation (GIE); and Linear interpolation with an Applied Moving Average (LAMA). Both produce RTDs of similar quality with entropy closer to zero (smoother) and low Numbers of Inflection Points. Their performance was far superior to both linear interpolation and the third alternate, cubic interpolation (Chapter 6).

- Fewer sample points can also result in smoother RTDs without affecting predictive capability. This additionally confirms the suitability of the slope-based sample point distribution (Chapter 6).

- The use of a smoothing interpolation function can effectively eliminate any effects of over-sampling, where higher numbers of sample points negatively impact upon RTD smoothness (Chapter 6).

- Changing interpolation function or reasonably reducing number of sample points does not adversely impact upon the predictive capability of deconvolved RTDs. It affects only RTD shape, giving smoother RTDs that arguably better reflect mixing processes in detail. However, as CRTD shape remains unaffected, GIE or LAMA need be used only when a smooth RTD is specifically required (Chapter 6).

- Data pre-processing comprises several different steps. These can be reversed to evaluate whether raw can be directly deconvolved. Data extension, addition of noise, addition of background concentration, and reverse calibration have been examined in a sensitivity analysis. The analysis has demonstrated that raw data can be successfully deconvolved, provided sensors with a linear response are used (Chapter 7).

- The predictive capability of an RTD deconvolved from raw data decreases with increases in noise and background concentration level. The latter has greater impact, and particularly sloped background concentration levels will

negatively impact the deconvolved RTD. Differences in uncalibration and extension also affect predictive capability, but do so in an unsystematic fashion (Chapter 7).

- Comparison of the deconvolved RTD with its known counterpart was made to directly evaluate RTD quality. This shows similar trends to predictive capability and the two are clearly linked. However, even with perfect input data, there is still a slight degradation in deconvolved RTD quality. This degradation doubles with either 10% noise or a mean background concentration level of 10% (Chapter 7).

- Combining predictive capability and RTD quality results, 10% noise and 10% mean background are recommended as minimum quality limits for raw data. However, higher noise levels may be acceptable with lower mean background concentration levels. Minimal pre-processing is recommended to subtract background, particularly to take into account changes in background concentration level with time (Chapter 7).

- Deconvolution of raw data with only minimal pre-processing was applied on a large scale. Comparison to identical pre-processed data showed that the novel deconvolution of raw data was successful (Chapter 8).

- A CRTD scaling algorithm can be applied to CRTDs when the input data has a background offset resulting in 'mass creation' (Chapter 8).

- CRTDs, and other CRTD based parameters (e.g. t_{20}), were successfully used to infer flow fields and underlying system hydrodynamics (Chapter 8).

- CRTD analysis provides understanding that is consistent with traditional ADZ parameter analysis. It also provides additional insight into the changes in ADZ parameters caused by changes in flow field (Chapter 8).

Conclusions regarding mixing processes:

- Short-circuiting fraction decreases with increased manhole outlet angle in unbenched manholes (Chapter 3).

- Six CRTDs were identified as representing the range of flow fields that could be inferred in surcharged, unbenched 0°/30°/60°/90° outlet angle and

benched 30°/60°/90° outlet angle, manholes with $D/D_p = 4.4$ at a range of flow rates (Chapter 8).

- At surcharge depths of $s > 0.258D$ in straight through unbenched and $s > 0.025D$ in 30° outlet angle benched manholes, CRTDs indicate Type I short-circuiting. In this flow field the majority of the solute passes directly through the manhole at close to equivalent pipe travel times. It has been previously referred to as above-threshold short-circuiting (Chapter 8).
- At surcharge depths of $s < 0.025D$ in straight through unbenched manholes (Stovin *et al.*, 2013), $s < 0.155D$ in angled unbenched manholes, and at $s < 0.258D$ in angled benched manholes, CRTDs indicate low surcharge Type I short-circuiting. In the unbenched manholes it is caused by the inlet jet core passing directly to the outlet as a result of horizontal recirculation zones forming. In the benched manhole the field forms as a result of the benching confining the jet (Chapter 8).
- At surcharge depths of $s > 0.773D$ in angled unbenched manholes, CRTDs indicate the formation of a Type II short-circuiting flow field. In this flow field, a vertical circulation field forms throughout the manhole volume. It entrains the jet, and as a result, a bulk of mass entering the circulation exits with similar residence times (Chapter 8).
- At surcharge depths of $s < 0.2D$ in straight through unbenched manholes (Stovin *et al.*, 2013) and $0.155D < s < 0.696D$ in angled unbenched manholes CRTDs indicate well-mixed flow. In this flow field, additional turbulence caused by the inlet jet interacting with the surface or far wall keeps the recirculation zones from forming (Chapter 8).
- At surcharge depths of $s \approx 0.7D$ in angled unbenched manholes, CRTDs indicate a transitional flow field forms, with characteristics of both well-mixed flow and Type II short-circuiting CRTDs. It is not understood what causes this (Chapter 8).
- At surcharge depths of $s > 0.258D$ in 60° and 90° outlet angle benched manholes, CRTDs indicate a bifurcating flow field forms. Part of the flow experiences Type I short-circuiting as a result of the benching and passes directly through the manhole. The other part of the flow impinges upon the benching and is deflected upwards into the surcharge

volume resulting in a well-mixed flow portion (Chapter 8).

- Energy loss co-efficient K values recorded by Arao & Kusada (1999) in a manhole with $D/D_p = 4.1$ change at $s = 0.278D$ in a straight through unbenched manhole, and at $s = 0.833D$ in a 90° outlet angle unbenched manhole. These correspond with results obtained from CRTD analysis, providing evidence for a link between mixing processes and energy losses (Chapter 8).

9.3 Suggestions for further work

There are several additional areas of research that could be followed up directly. Topics that have been either briefly touched upon or otherwise not included in the thesis are discussed in this section.

9.3.1 Dynamic sample point spacing

Currently, maximum entropy deconvolution uses sample point positions based on assumed RTD characteristics. The slope-based sample point distribution is the main exception to this, which uses a quick FFT-based deconvolution to estimate sample point positions. There is no reason that a quick maximum entropy deconvolution could not be used instead. Alternatively, dynamic spacing could be achieved through the inclusion of additional optimisation constraints, allowing for more optimal sample point positioning. A genetic algorithm approach to sample point positioning might also be suitable.

9.3.2 Pipe subtraction

All of the RTDs deconvolved from experimental manholes data take into account the mixing volume between two fluorometers. This includes a short segment of pipe on either side of the manhole. While the manhole is the controlling structure, all of the RTDs presented within this thesis include the small amount of dispersion taking place in each short reach of pipe. Guymer & Stovin (2011) introduce

the concept of subtracting the pipe dispersion to give an RTD that reflects the mixing processes occurring in the manhole only. This would be a step towards the application of manhole RTDs in larger network models.

Unfortunately while conceptually simple, the practical application of pipe subtraction is significantly more complex. Currently it appears to require significantly more accurate flow data than is available. The validity of applying the ADE model at such a short scale needs more investigation within the deconvolution context. A vena contracta is also observed to form in the manhole's downstream pipe in PLIF images and CFD models. In angled manholes, momentum from within the manhole also continues to affect the flow in the downstream pipe. All of these effects must be considered in more detail.

9.3.3 Stepped manholes

Dennis (2000) collected solute transport data for a 388 mm straight through manhole which was analysed in Chapter 8. He also collected data with a downstream step height of $0.5D_p$, $1.0D_p$, $1.5D_p$, and $2.0D_p$. The analysis of mixing characteristics could easily be extended to include the effects of step change to give further information about mixing processes in manholes. In general, additional manhole configurations could also be analysed.

9.3.4 LAMA window size

GIE interpolation works well, but is complex and slow. LAMA interpolation is much faster, but requires manual specification of a window size for the moving average. Work carried out for Chapter 6, as well as other work not contained within this thesis, suggests that optimal window size may be a function of sample point spacing and other data set characteristics, e.g. the difference in first arrival times. It may be possible to automatically determine window size, which would make the application of LAMA far more generic.

9.3.5 CRTD scaling

The algorithm used in Chapter 8 to identify the end of the CRTD when the mass-balance was incorrect was applied manually in specific instances. Defining a specific criterion for its application would allow for it to be included as an optional automatic part of the deconvolution software. Determining exactly to what extent the resulting CRTD is still an over-estimation could be used to further improve the scaling algorithm as well.

9.3.6 Engineering application of Chapter 8

Work in Chapter 8 identified several flow fields which develop as a function of manhole outlet angle, the presence of benching, and surcharge depth. This is in contrast to the previously identified two mixing regimes (below-/above-threshold) and could potentially increase the complexity of manhole solute transport modelling. An analysis of to what extent this additional refinement benefits practical modelling outcomes should be conducted so that a unified modelling guideline can be produced.

9.3.7 Energy losses

Head loss data has been collected simultaneously with solute transport data in a number of instances in order to try to establish a link between the two. If a link is successfully established, a well calibrated hydraulic model could result in a significantly improved linked water quality model. The theoretical basis for such a relationship is that the hydrodynamic processes occurring within a manhole control both the energy losses and mixing characteristics.

To a certain extent this was investigated in Chapter 8. However, this was an empirical approach that did not produce particularly clear results. Other research, e.g. Pedersen & Mark (1990); Arao & Kusada (1999); Stovin *et al.* (2013), suggests that a better link should be possible.

The proper starting point for additional investigation of the link between energy losses and mixing characteristics should be through a theoretical examination

of the ADE work of Taylor (1954), which effectively produces an RTD, and the Darcy-Weisbach equation (Prasuhn, 1987), which gives energy losses due to friction in pipes. Denbigh & Turner (1984) suggest that such a link exists, but it needs to be examined in greater detail. If successfully linked, RTD or CRTD parameters (e.g. t_{50}) should be linkable to head loss characteristics for pipes. This could then be applied to deriving RTDs for more complex structures.

9.4 Key outcomes

Key outcomes of this research are:

1. A demonstration and explanation of maximum entropy deconvolution as a robust means of obtaining an RTD from experimental solute transport data.

2. A recommended set of configuration options for maximum entropy deconvolution, including the R_t^2 constraint function, 40 sample points, the new slope-based sample point distribution, and 350 iterations.

3. Refinements to maximum entropy deconvolution to enable the deconvolution of smooth RTDs.

4. A demonstration that maximum entropy deconvolution can successfully be applied to either raw or minimally pre-processed solute transport data.

5. A new examination of the effects of outlet angle and benching on mixing processes in surcharged manholes.

References

Albertson, M. L., Dai, Y. B., Jensen, R. A., & Rouse, H. (1950). Diffusion of submerged jets. *Transactions of the American Society of Civil Engineers*, 115(1), 639–664.

Anderson, M. & Woessner, W. (1992). *Applied groundwater modeling: simulation of flow and advective transport.* London: Academic Press, Inc.

Andrés-Doménech, I., Múnera, J., Francés, F., & Marco, J. (2010). Coupling urban event-based and catchment continuous modelling for combined sewer overflow river impact assessment. *Hydrology and Earth System Sciences Discussions*, 7(3), 3281–3328.

ANSYS, Inc. (2012). *ANSYS Fluent 14.5.* Cecil Township, PA.

Arao, S. & Kusada, T. (1999). Effects of pipe bending angle on energy losses at two-way circular drop manholes. In *Proc. the Eighth International Conference on Urban Storm Drainage.*

Arao, S., Kusuda, T., Moriyama, K., Hiratsuka, S., Asada, J., & Hirose, N. (2012). Energy losses at three-way circular drop manholes under surcharged conditions. *Water Science and Technology*, 66(1), 45–52.

Armstrong, M. P. & Marciano, R. (1994). Inverse-distance-weighted spatial interpolation using parallel supercomputers. *Photogrammetric engineering and remote sensing*, 60(9), 1097–1104.

Beer, T. & Young, P. C. (1983). Longitudinal dispersion in natural streams. *Journal of environmental engineering*, 109(5), 1049–1067.

Bennett, N. D., Croke, B. F., Guariso, G., Guillaume, J. H., Hamilton, S. H., Jakeman, A. J., Marsili-Libelli, S., Newham, L. T., Norton, J. P., Perrin, C., *et al.* (2012). Characterising performance of environmental models. *Environmental Modelling & Software*, 40, 1–20.

Bennett, P. (2012). *Evaluation of the Solute Transport Characteristics of Surcharged Manholes using a RANS Solution.* PhD thesis, The University of Sheffield.

Berndt, D. J. & Clifford, J. (1994). Using dynamic time warping to find patterns in time series. In *Technical Report WS-94-03* (pp. 359–370). Melno Park, California: The AAAI Press.

Blackman, R. B. & Tukey, J. W. (1958). *The measurement of power spectra, from the point of view of communications engineering.* Dover books on engineering and engineering physics. Dover Publications.

Boudraa, A.-O., Cexus, J.-C., Groussat, M., & Brunagel, P. (2008). An energy-based similarity measure for time series. *Eurasip Journal on Advances in Signal Processing*, 2008:135892.

Camp, T. R. & Stein, P. C. (1943). Velocity gradients and internal work in fluid motion. *Journal of the Boston Society of Civil Engineers*, 85, 219–37.

Chadwick, A., Morfett, J., & Borthwick, M. (2004). *Hydraulics in civil and environmental engineering.* London, UK: Spon Press, fourth edition edition.

Chen, L., Ozsu, M. T., & Oria, V. (2005). Robust and fast similarity search for moving object trajectories. In J. Widom, F. Ozcan, & R. Chirkova (Eds.), *Proceedings of the ACM SIGMOD International Conference on Management of Data* (pp. 491–502). Baltimore, MD.

Chow, V. T. (1959). *Open-channel hydraulics.* McGraw-Hill, second edition edition.

Christopoulos, A. & Lew, M. J. (2000). Beyond eyeballing: fitting models to experimental data. *Critical Reviews in Biochemistry and Molecular Biology*, 35(5), 359–391.

Cirpka, O. A., Fienen, M. N., Hofer, M., Hoehn, E., Tessarini, A., Kipfer, R., & Kitanidis, P. K. (2007). Analyzing bank filtration by deconvoluting time series of electric conductivity. *Ground Water*, 45(3), 318–328.

Cox, C. S. & Boucher, A. R. (1989). Data based models: An automatic method for model structure determination. In *IEE Colloq. Model Validation Contr. Syst. Design Simulation* (pp. 2/1–2/4). London, U.K.

Cross, H. (1936). Analysis of flow in networks of conduits or conductions. *University of Illinois Bulletin*, 34(22).

Danckwerts, P. V. (1953). Continuous flow systems: distribution of residence times. *Chemical Engineering Science*, 2(1), 1–13.

Davis, P. M., Atkinson, T. C., & Wigley, T. M. L. (2000). Longitudinal dispersion in natural channels: 2. The roles of shear flow dispersion and dead zones in the River Severn, UK. *Hydrology and Earth System Sciences Discussions*, 4(3), 355–371.

de Boor, C. (1978). *A practical guide to splines*. Springer-Verlag New York.

Denbigh, K. G. & Turner, J. C. R. (1984). *Chemical Reactor Theory*. Cambridge University Press.

Dennis, P. (2000). *Longitudinal Dispersion due to Surcharged Manholes*. PhD thesis, The University of Sheffield.

DHI (2012). *MIKE 2012*. Hørsholm, Denmark.

Dirckx, G., Thoeye, C., De Gueldre, G., & Van De Steene, B. (2011). CSO management from an operator's perspective: a step-wise action plan. *Water Science and Technology*, 63(5), 1045–1053.

Droste, R. L. (1997). *Theory and practice of water and wastewater treatment*. John Wiley & Son, Inc.

Fan, Y., Sarkar, S., & Lasdon, L. (1988). Experiments with successive quadratic programming algorithms. *Journal of Optimization Theory and Applications*, 56(3), 359–383.

Fienen, M. N., Luo, J., & Kitanidis, P. K. (2006). A bayesian geostatistical transfer function approach to tracer test analysis. *Water Resources Research*, 42(7).

Fischer, H. B. (1967). The mechanics of dispersion in natural streams. *Journal of the Hydraulics Division, A.S.C.E.*, 93(6), 187–215.

Fischer, H. B. (1979). *Mixing in Inland and Coastal Waters*. Elsevier.

Fritsch, F. N. & Carlson, R. E. (1980). Monotone piecewise cubic interpolation. *SIAM Journal on Numerical Analysis*, 17(2), 238–246.

George, S., Burnham, K., & Mahtani, J. (1998). Modelling and simulation of hydraulic components for vehicle applications - a precursor to control system design. In *Simulation '98. International Conference on (Conf. Publ. No. 457)* (pp. 126 –132).

Ghosh, A. K. (2007). *Intro. to Linear & Digital Control Systems*. Prentice-Hall Of India Pvt. Ltd.

Gooseff, M. N., Benson, D. A., Briggs, M. A., Weaver, M., Wollheim, W., Peterson, B., & Hopkinson, C. S. (2011). Residence time distributions in surface transient storage zones in streams: Estimation via signal deconvolution. *Water Resources Research*, 47.

Greenwood, P. & Nikulin, M. (1996). *A guide to chi-squared testing*, volume 280. Wiley-Interscience.

Guymer, I. (1998). Longitudinal dispersion in sinuous channel with changes in shape. *Journal of Hydraulic Engineering*, 124(1), 33–40.

Guymer, I., Dennis, P., O'Brien, R., & Saiyudthong, C. (2005). Diameter and surcharge effects on solute transport across surcharged manholes. *Journal of Hydraulic Engineering-Asce*, 131(4), 312–321.

Guymer, I. & O'Brien, R. (2000). Longitudinal dispersion due to surcharged manhole. *Journal of Hydraulic Engineering*, 126(2), 137–149.

Guymer, I., Shepherd, W. J., Dearing, M., Dutton, R., & Saul, A. J. (2002). Solute retention in storage tanks. In *Proceedings of 9th International Conference on Urban Drainage, Portland, Oregon, USA*.

Guymer, I. & Stovin, V. R. (2011). One-dimensional mixing model for surcharged manholes. *Journal of Hydraulic Engineering*, 137(10), 1160–1172.

Hansen, P. C. (1998). *Rank-deficient and discrete ill-posed problems: numerical aspects of linear inversion*. Society for Industrial and Applied Mathematics.

Harris, F. J. (1978). On the use of windows for harmonic analysis with the discrete fourier transform. *Proceedings of the IEEE*, 66(1), 51–83.

Hart, J., Guymer, I., Jones, A., & Stovin, V. R. (2013). Longitudinal dispersion coefficients within turbulent and transitional pipe flow. In P. Rowinski (Ed.), *Experimental and Computational Solutions of Hydraulic Problems*: Springer.

Hattersley, J. G., Evans, N. D., Hutchison, C., Cockwell, P., Mead, G., Bradwell, A. R., & Chappell, M. J. (2008). Nonparametric prediction of free-lightchain generation in multiple myelomapatients. In *17th International Federation of Automatic Control World Congress (IFAC)* (pp. 8091–8096). Seoul, Korea.

Holland, J. F., Martin, J. F., Granata, T., Bouchard, V., Quigley, M., & Brown, L. (2004). Effects of wetland depth and flow rate on residence time distribution characteristics. *Ecological Engineering*, 23(3), 189–203.

Innovyze (2010). *InfoWorks CS 11*. Broomfield, CO.

Jarvis, C. H. & Stuart, N. (2001). A comparison among strategies for interpolating maximum and minimum daily air temperatures. part ii: The interaction between number of guiding variables and the type of interpolation method. *Journal of Applied Meteorology*, 40(6), 1075–1084.

Jernigan, R. W. (1986). *A Primer on Kriging*. U.S. Environmental Protection Agency, Washington, DC.

Johnston, A. J. & Volker, R. E. (1990). Head losses at junction boxes. *Journal of hydraulic engineering*, 116(3), 326–341.

Jones, A. (2011). *Solute Dispersion across Manholes under Time-Varying Flow Conditions*. PhD thesis, University of Warwick.

Joo, D., Choi, D., & Park, H. (2000). The effects of data preprocessing in the determination of coagulant dosing rate. *Water Research*, 34(13), 3295–3302.

Kasban, H., Zahran, O., Arafa, H., El-Kordy, M., Elaraby, S. M. S., & Abd El-Samie, F. E. (2010). Laboratory experiments and modeling for industrial radiotracer applications. *Applied Radiation and Isotopes*, 68(6), 1049–1056.

Kashefipour, S. & Falconer, R. (2000). An improved model for predicting sediment fluxes in estuarine waters. In *Proceedings of the Fourth International Hydroinformatics Conference, Iowa, USA*.

Lau, J., Butler, D., & Schütze, M. (2002). Is combined sewer overflow spill frequency/volume a good indicator of receiving water quality impact? *Urban water*, 4(2), 181–189.

Lau, S., Stovin, V., & Guymer, I. (2008). Scaling the solute transport characteristics of a surcharged manhole. *Urban Water Journal*, 5(1), 31–40.

Levenspiel, O. (1972). *Chemical Reaction Engineering*. John Wiley & Son, Inc.

Lindvall, G. (1986). *Energiförluster i ledningsbrunnar - Laboratoriemätninger*. Geohydrologiska forskningsgruppen 81, Chalmars Tekniska Högskola. (In Swedish.).

Madden, F. N., Godfrey, K. R., Chappell, M. J., Hovorka, R., & Bates, R. A. (1996). A comparison of six deconvolution techniques. *Journal of Pharmacokinetics and Biopharmaceutics*, 24(3), 283–299.

Mailhot, A., Beauregard, I., Talbot, G., Caya, D., & Biner, S. (2012). Future changes in intense precipitation over Canada assessed from multi-model NARCCAP ensemble simulations. *International Journal of Climatology*, 32(8), 1151–1163.

Miskiewicz, J. (2010). Entropy correlation distance method. The euro introduction effect on the consumer price index. *Physica a - Statistical Mechanics and Its Applications*, 389(8), 1677–1687.

Moriasi, D. N., Arnold, J. G., Van Liew, M. W., Bingner, R. L., Harmel, R. D., & Veith, T. L. (2007). Model evaluation guidelines for systematic quantification of accuracy in watershed simulations. *Transactions of the Asabe*, 50(3), 885–900.

Movahed, M. S., Jafari, G. R., Ghasemi, F., Rahvar, S., & Tabar, M. R. R. (2006). Multifractal detrended fluctuation analysis of sunspot time series. *Journal of Statistical Mechanics-Theory and Experiment*, (2).

Nash, J. E. & Sutcliffe, J. V. (1970). River flow forecasting through conceptual models part I - A discussion of principles. *Journal of Hydrology*, 10(3), 282–290.

O'Brien, R. T. (1999). *Dispersion due to Surcharged Manholes*. PhD thesis, The University of Sheffield.

Pandolfi, L. (2010). On-line input identification and application to active noise cancellation. *Annual Reviews in Control*, 34(2), 245–261.

Payn, R. A., Gooseff, M. N., Benson, D. A., Cirpka, O. A., Zarnetske, J. P., Bowden, W. B., McNamara, J. P., & Bradford, J. H. (2008). Comparison of instantaneous and constant-rate stream tracer experiments through non-parametric analysis of residence time distributions. *Water Resources Research*, 44(6).

Pedersen, F. B. & Mark, O. (1990). Head losses in storm sewer manholes: Submerged jet theory. *Journal of Hydraulic Engineering*, 116(11), 1317–1328.

Persson, J. (2000). The hydraulic performance of ponds of various layouts. *Urban Water*, 2(3), 243–250.

Photon Technology International, Inc. (2005). *The Measurement of Sensitivity in Fluorescence Spectroscopy*. Retrieved from `http://www.pti-nj.com/LaserStrobe/TechNotes/MeasurementSensitivity.pdf`.

Prasuhn, A. L. (1987). *Fundamentals of Hydraulic Engineering*. Holt, Rinehart and Winston, New York, NY.

Pyrcz, M. & Deutsch, C. (2003). The whole story on the hole effect. *Geostatistical Association of Australasia Newsletter*, 18, 3–5.

Rieckermann, J., Neumann, M., Ort, C., Huisman, J. L., & Gujer, W. (2005). Dispersion coefficients of sewers from tracer experiments. *Water Science and Technology*, 52(5), 123–133.

Rodda, J., Little, M., Rodda, H., & McSharry, P. (2010). A comparative study of the magnitude, frequency and distribution of intense rainfall in the united kingdom. *International Journal of Climatology*, 30(12), 1776–1783.

Rodgers, J. L. & Nicewander, W. A. (1988). Thirteen ways to look at the correlation coefficient. *The American Statistician*, 42(1), 59–66.

Rutherford, J. C. (1994). *River mixing.* Chichester, England: John Wiley & Son Ltd.

Saiyudthong, C. (2003). *Effect of Changes in Pipe Direction across Surcharged Manholes on Dispersion and Head Loss.* PhD thesis, The University of Sheffield.

Schittkowski, K. (1986). Nlpql: A fortran subroutine solving constrained nonlinear programming problems. *Annals of Operations Research*, 5(2), 485–500.

Shannon, C. E. (1948). The bell system technical journal. *A mathematical theory of communication*, 27, 379–423.

Sherman, L. K. (1932). Streamflow from rainfall by the unit-graph method. *Engineering News Record*, 108, 501–505.

Skaggs, T. H., Kabala, Z. J., & Jury, W. A. (1998). Deconvolution of a non-parametric transfer function for solute transport in soils. *Journal of Hydrology*, 207(3-4), 170–178.

Skilling, J. & Bryan, R. K. (1984). Maximum-entropy image-reconstruction - general algorithm. *Monthly Notices of the Royal Astronomical Society*, 211(1), 111–124.

Sonnenwald, F., Stovin, V., & Guymer, I. (2011). The influence of outlet angle on solute transport in surcharged manholes. In *12th International Conference on Urban Drainage.* Porte Alegre, Brazil.

Sonnenwald, F., Stovin, V., & Guymer, I. (2013a). Configuring maximum entropy deconvolution for the identification of residence time distributions in solute transport applications. *Journal of Hydrologic Engineering.* (Oct. 24, 2013).

Sonnenwald, F., Stovin, V., & Guymer, I. (2013b). Correlation measures for solute transport model identification & evaluation. In P. Rowinski (Ed.), *Experimental and Computational Solutions of Hydraulic Problems*: Springer.

Stovin, V., Bennett, P., & Guymer, I. (2013). Absence of a hydraulic threshold in small-diameter surcharged manholes. *Journal of Hydraulic Engineering*, 139(9), 984–994.

Stovin, V., Guymer, I., & Lau, S. D. (2010a). Dimensionless method to characterize the mixing effects of surcharged manholes. *Journal of Hydraulic Engineering*, 136(5), 318–327.

Stovin, V. R., Grimm, J. P., & Lau, S.-T. D. (2008). Solute transport modeling for urban drainage structures. *Journal of Environmental Engineering*, 134(8), 640–650.

Stovin, V. R., Guymer, I., Chappell, M. J., & Hattersley, J. G. (2010b). The use of deconvolution techniques to identify the fundamental mixing characteristics of urban drainage structures. *Water Science and Technology*, 61(8), 2075–2081.

Stovin, V. R., Guymer, I., & Lau, D. (2007). Cumulative concentrations modelling longitudinal dispersion - an upstream temporal concentration profile-independent approach. In *Proceedings of The 5th International Symposium on Environmental Hydraulics* Tempe, Arizona.

Ta, C. & Brignal, W. (1998). Application of computational fluid dynamics technique to storage reservoir studies. *Water Science and Technology*, 37(2), 219–226.

Taylor, G. (1953). Dispersion of soluble matter in solvent flowing slowly through a tube. *Proceedings of the Royal Society of London Series a-Mathematical and Physical Sciences*, 219(1137), 186–203.

Taylor, G. (1954). The dispersion of matter in turbulent flow through a pipe. *Proceedings of the Royal Society of London. Series A: Mathematical and Physical Sciences*, 223(1155), 446–468.

Teegavarapu, R. S. & Chandramouli, V. (2005). Improved weighting methods, deterministic and stochastic data-driven models for estimation of missing precipitation records. *Journal of Hydrology*, 312(1), 191–206.

The MathWorks Inc. (2011). *MATLAB R2011a.* Natick, MA.

U.S. EPA (2010). *SWMM 5.0.* Cincinnati, OH.

Valentine, E. M. & Wood, I. R. (1977). Longitudinal dispersion with dead zones. *ASCE J Hydraul Div*, 103(9), 975–990.

Vlachos, M., Kollios, G., & Gunopulos, D. (2002). Discovering similar multidimensional trajectories. In R. D. K. N. A. H. H. Agrawal (Ed.), *18th International Conference on Data Engineering, Proceedings* (pp. 673–684). IEEE Computer Society.

Wallis, S. & Manson, R. (2005). Modelling solute transport in a small stream using discus. *Acta Geophysica Polonica*, 53(4), 501.

Wallis, S. G., Young, P. C., & Beven, K. J. (1989). Experimental investigation of the aggregated dead zone model for longitudinal solute transport in stream channels. *Proceedings of the Institution of Civil Engineers (London).*, 87 pt 2(MAR.), 1–22.

Wang, K. H., Cleveland, T. G., Towsley, C., & Umrigar, D. (1998). Hhead loss at manholes in surcharged sewer systems. *JAWRA Journal of the American Water Resources Association*, 34(6), 1391–1400.

Weisstein, E. W. (n.d.). MathWorld: Entropy. Wolfram Research, Inc. [online] Retrieved from `http://mathworld.wolfram.com/Entropy.html` (7 Nov 2013).

Ye, J. C., Tang, Y., Peng, H., & Zheng, Q. L. (2004). FFCBS: A simple similarity measurement for time series. In *Proceedings of the 2004 International Conference on Intelligent Mechatronics and Automation* (pp. 392–396).

Young, P., Jakeman, A., & McMurtrie, R. (1980). An instrumental variable method for model order identification. *Automatica*, 16(3), 281–294.

Zhao, C.-H., Zhu, D. Z., & Rajaratnam, N. (2006). Experimental study of surcharged flow at combining sewer junctions. *Journal of hydraulic engineering*, 132(12), 1259–1271.

Zhong, W. J., Wang, D. H., Xu, X. W., Wang, B. Y., Luo, Q., Senthil Kumaran, S., & Wang, Z. J. (2011). A gas chromatography/mass spectrometry method for the simultaneous analysis of 50 phenols in wastewater using deconvolution technology. *Chinese Science Bulletin*, 56(3), 275–284.

Zimmerman, D., Pavlik, C., Ruggles, A., & Armstrong, M. P. (1999). An experimental comparison of ordinary and universal kriging and inverse distance weighting. *Mathematical Geology*, 31(4), 375–390.

Appendix A

Mean normalised correlation value plots

These plots show the full range of correlation values for the analysis carried out in Chapter 4. Horizontally, different transformations are shown, while the different profiles are shown vertically.

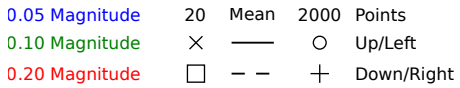

Figure A.1: Legend

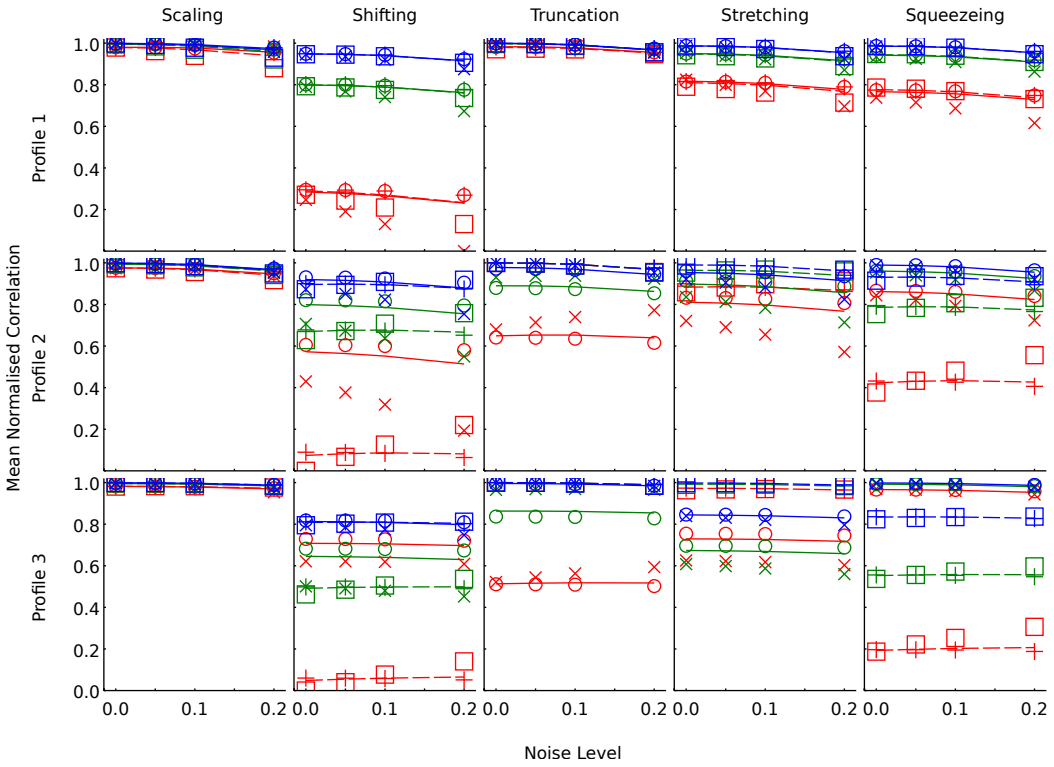

Figure A.2: Mean normalised correlation values for BLC

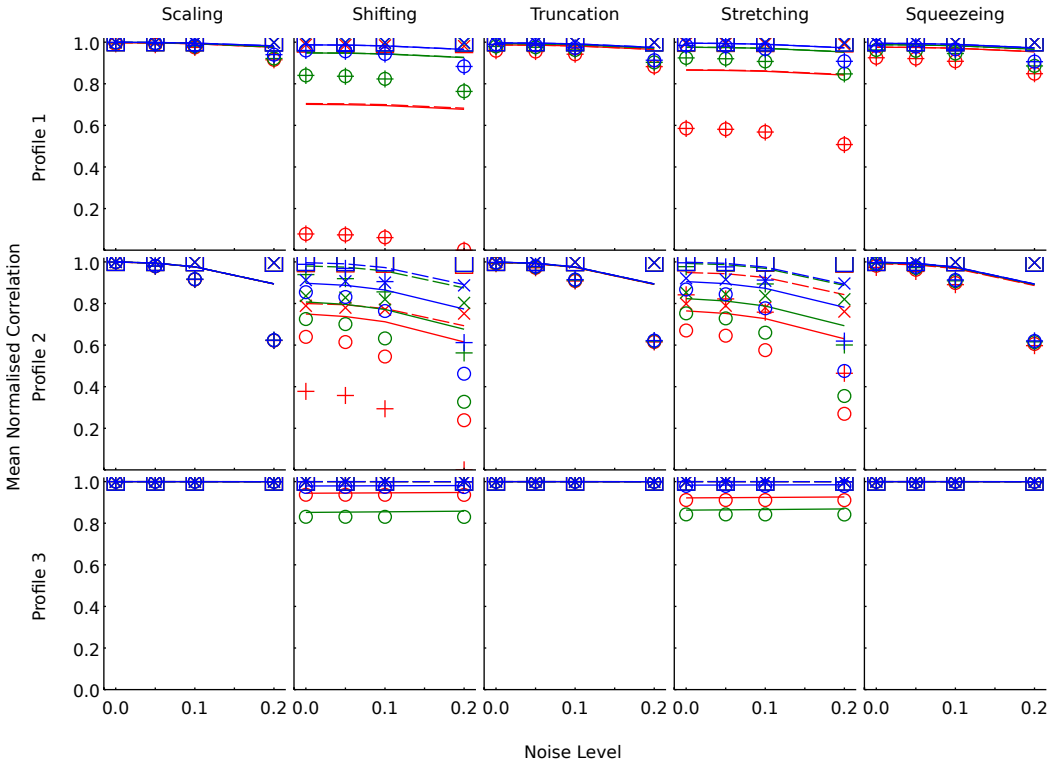

Figure A.3: Mean normalised correlation values for χ^2

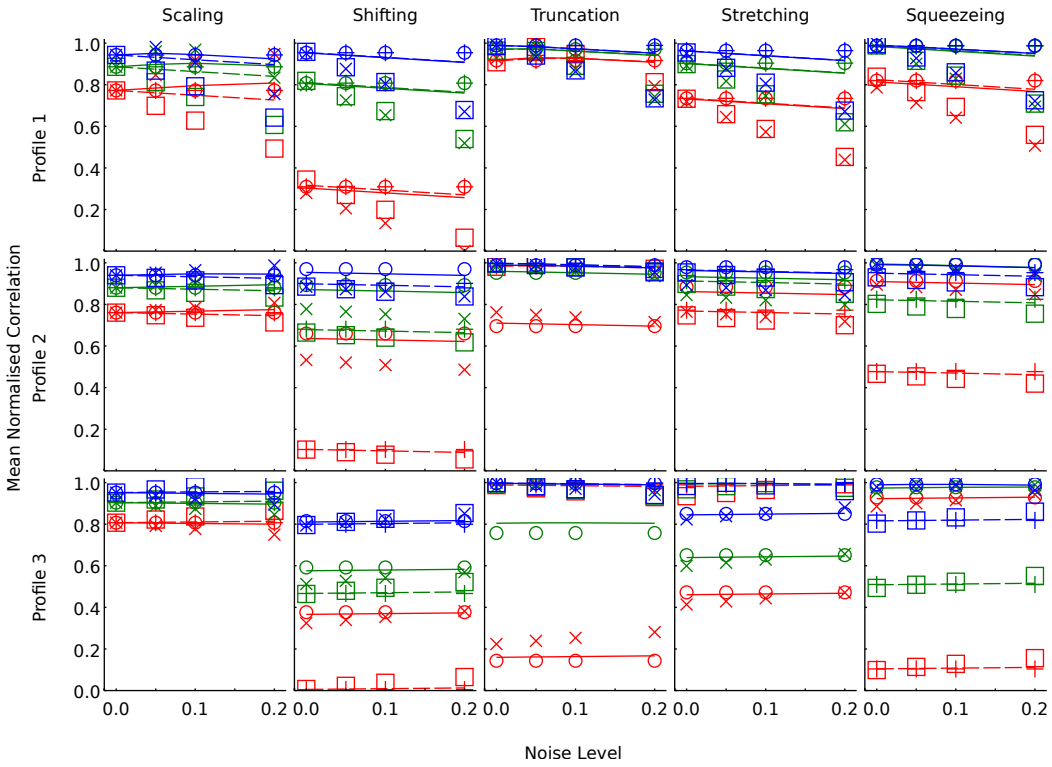

Figure A.4: Mean normalised correlation values for FFCBS

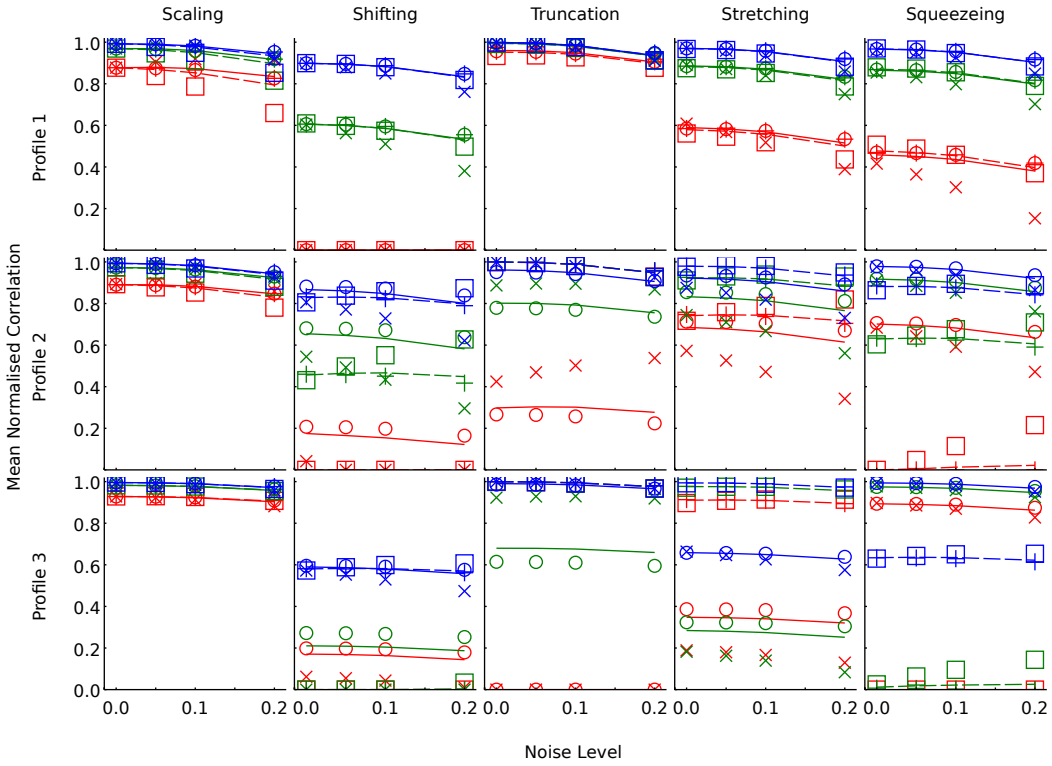

Figure A.5: Mean normalised correlation values for R^2

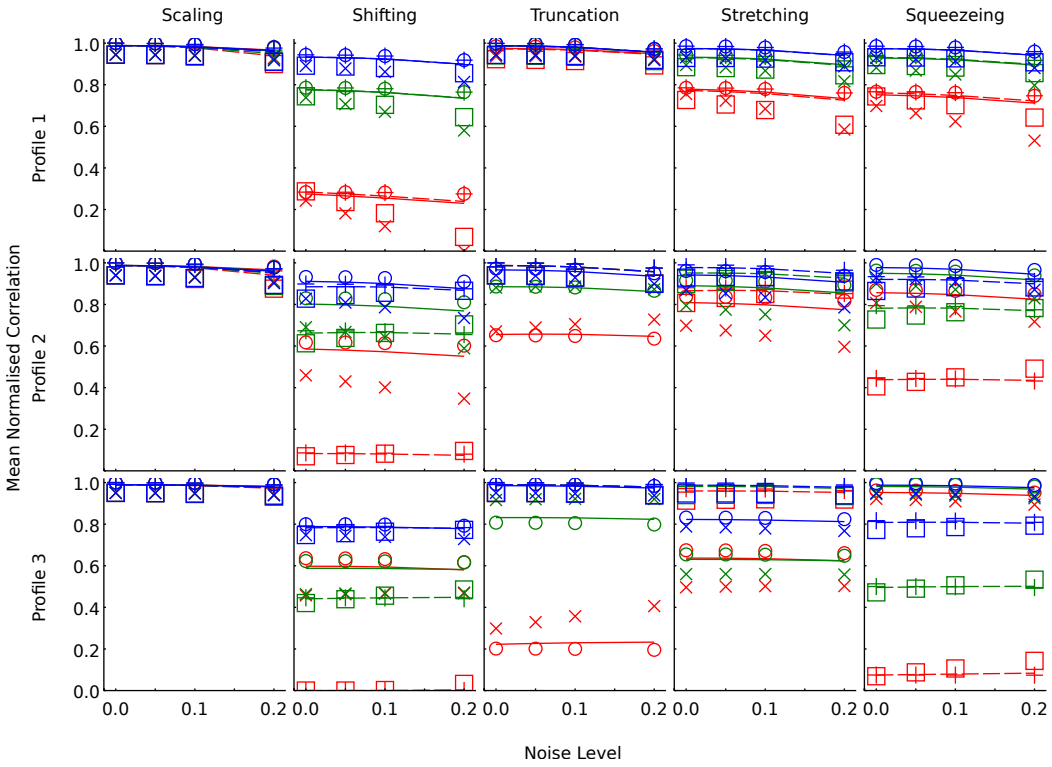

Figure A.6: Mean normalised correlation values for PMCC

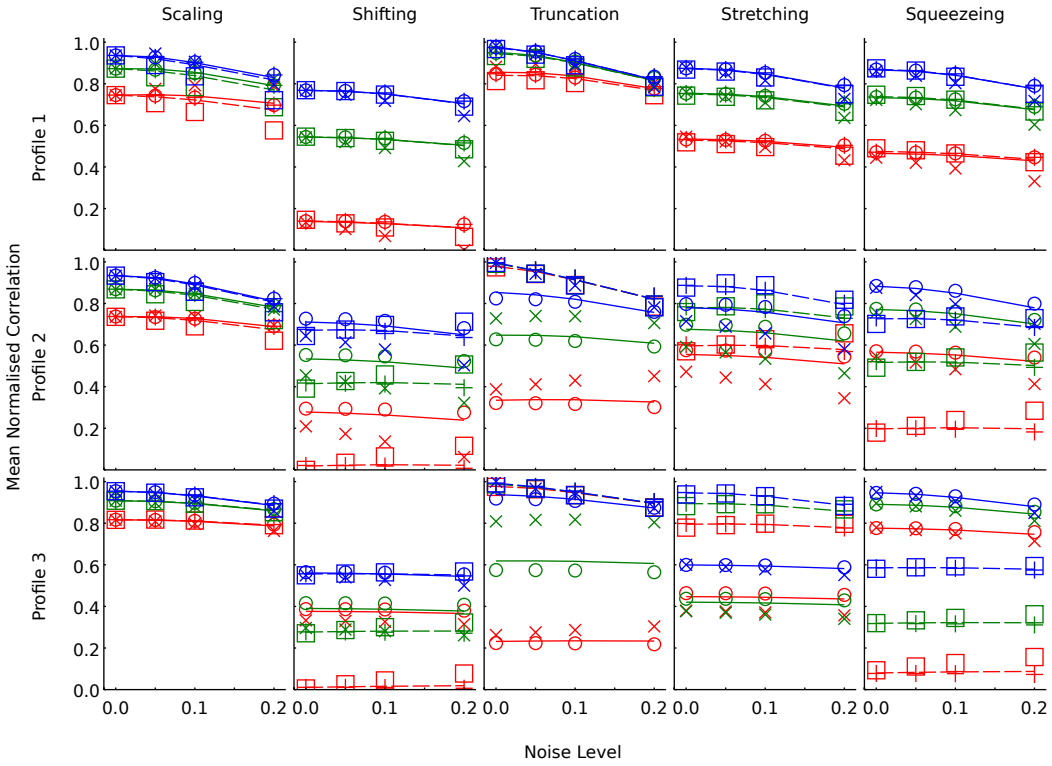

Figure A.7: Mean normalised correlation values for RMSD

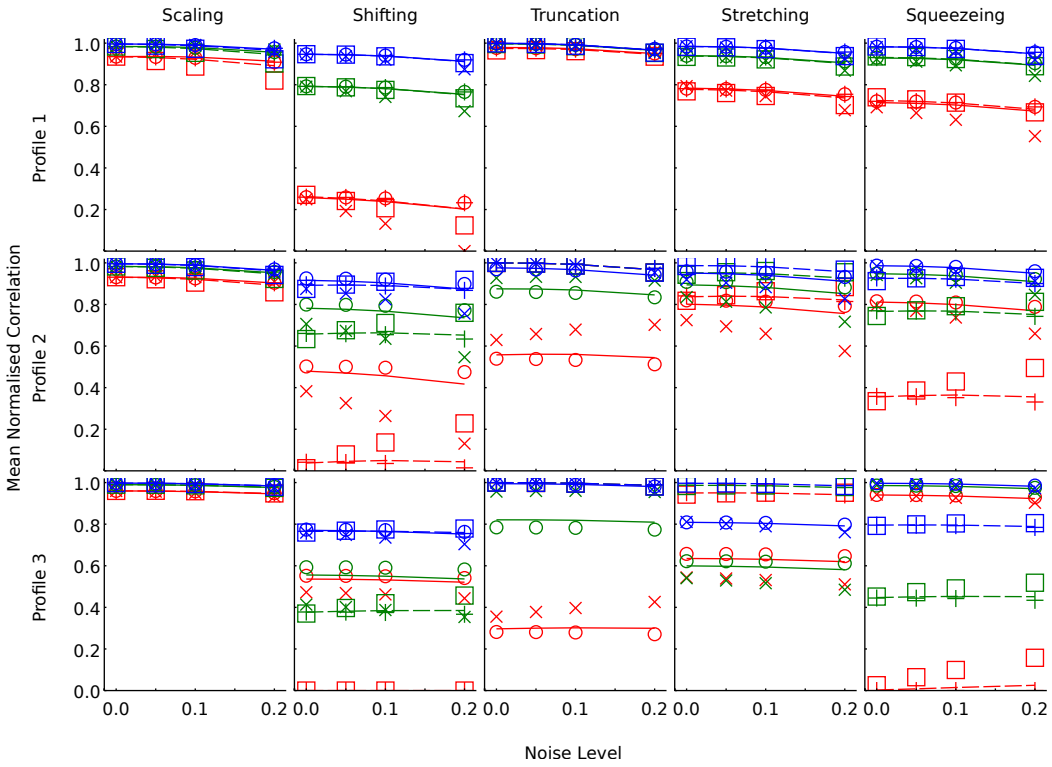

Figure A.8: Mean normalised correlation values for R_t^2

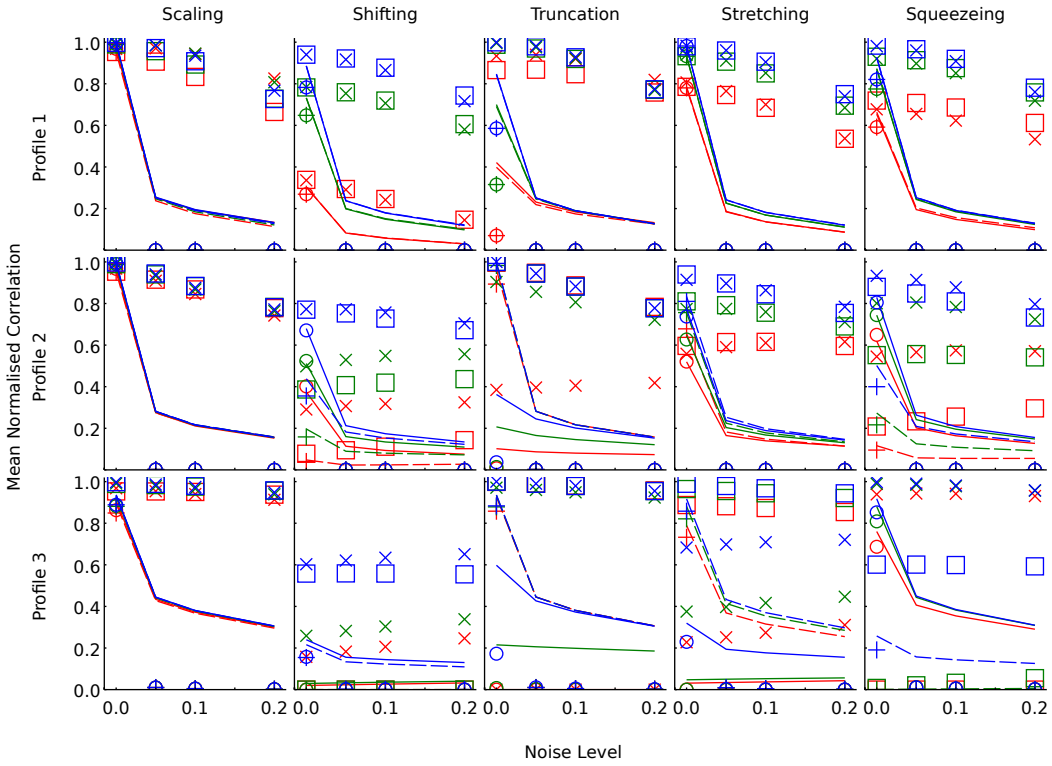

Figure A.9: Mean normalised correlation values for SimilB

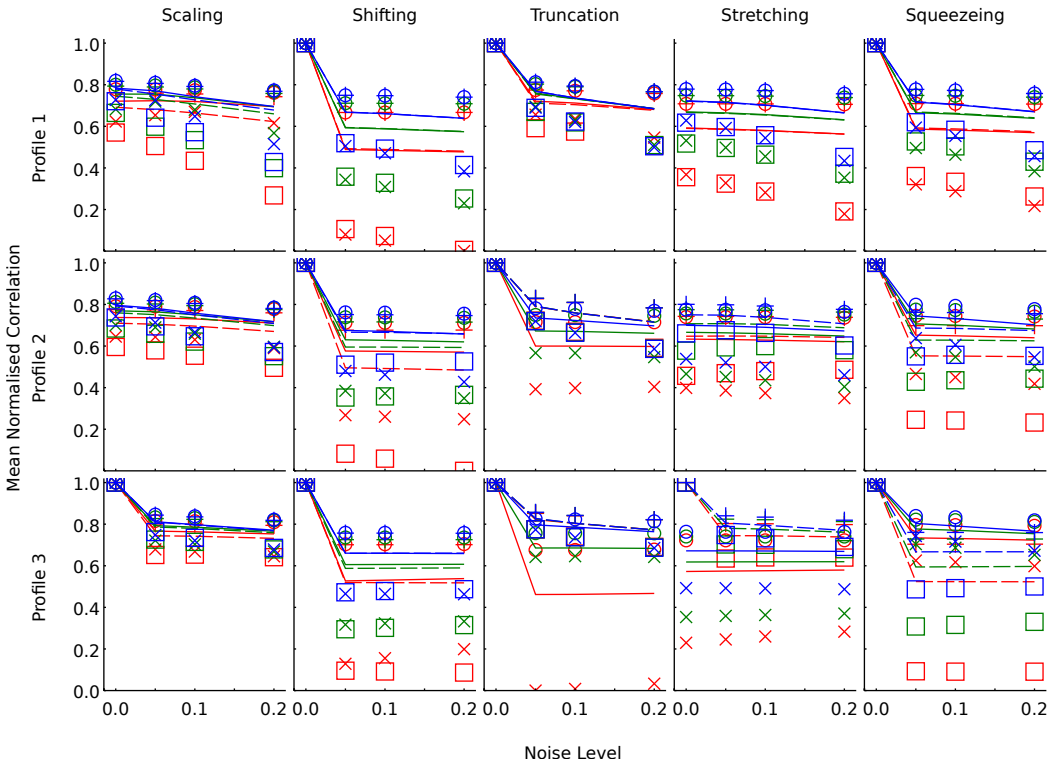

Figure A.10: Mean normalised correlation values for YIC

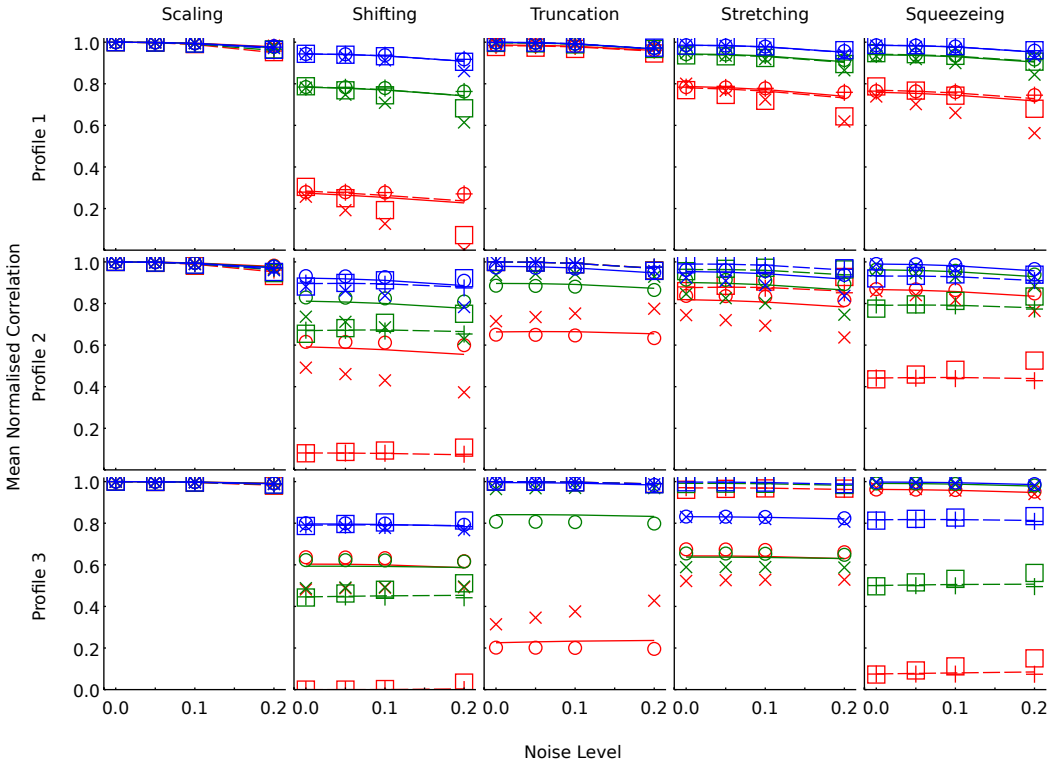

Figure A.11: Mean normalised correlation values for CORR2

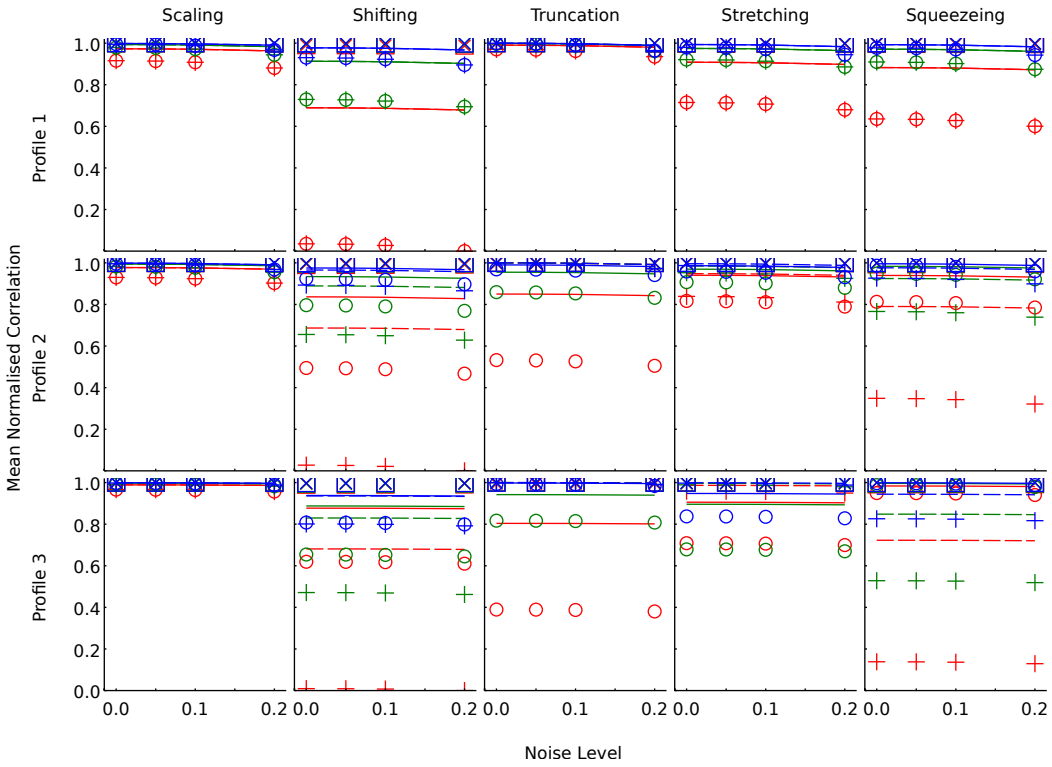

Figure A.12: Mean normalised correlation values for ISE

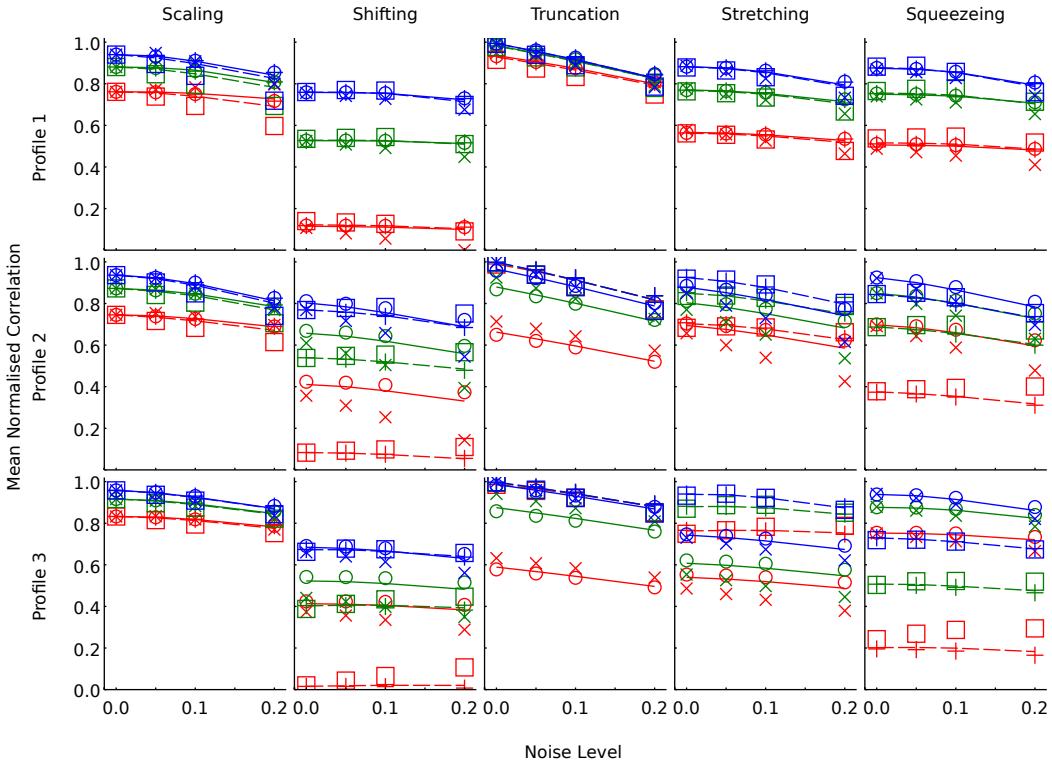

Figure A.13: Mean normalised correlation values for APE

Appendix B

GIS INTERPOLATION FUNCTIONS

Inverse Distance Weighting (IDW) and Kriging Estimation Method (KEM) are introduced in Chapter 6. Like the other interpolation functions, they are a potential means of obtaining a smoother RTD, but are rejected as being unsuitable for maximum entropy deconvolution. The detailed evaluations of both functions are covered in this appendix.

B.1 Inverse Distance Weighting

In IDW, Equation B.1, the point being interpolated z_j is defined as the summation of neighbouring points z_i relative to the distance d between the point z_j and the other points z_i to the power of a, where a is a factor typically between 1 and 2, although higher values can be used (Armstrong & Marciano, 1994). The number of neighbouring points k can vary, ranging from a fixed number of points or even all points (Jarvis & Stuart, 2001). IDW results in a smoothed line where closer points have a greater influence than further points on the value being interpolated.

$$z_j = \frac{\sum_{i=1}^{k} z_i/d^a}{\sum_{i=1}^{k} 1/d^a}, \quad d = |i-j| \tag{B.1}$$

An example of IDW when applied to the RTD from Figure 6.1 as a post-processing operation is shown in Figure B.1. IDW shows a similar flaw to spline interpolation

where a catenary (or inverted catenary) effect is visible between some sample points. These interpolated values are unrealistic for an RTD and so IDW was judged unsuitable.

B.2 Kriging Estimation Method

The KEM is a more complex interpolation method where the data points being interpolated are calculated based on a model of the data (Jernigan, 1986). The existing data is used to generate a semivariogram using Equation B.2, where d is lag distance and $n(d)$ is the number of points at that lag. Lag is the x-axis difference between two points and γ is the semivariance at a given lag, which is half the squared difference in value. There is often only one lag value for each precise distance, so lag bins are used, grouping together lags so that a mean semivariance value is taken for that lag range. The semivariance is a measure of the similarity between values with respect to the distance between them.

$$\gamma(d) = \frac{1}{2}\frac{1}{n(d)}\sum_{i=1}^{n(d)}(z_{i+d} - z_i)^2 \tag{B.2}$$

After creating the semivariogram, a semivariogram model is fit to it. Most semivariogram models have three properties, the nugget (C_0), sill (C_1), and range (a). This is illustrated in Figure B.2, which shows the spherical semivariogram model, Equation B.3 (Jernigan, 1986). The nugget value is indicative of discontinuities in the data (at very small lag distances a non-zero semivariance). The sill is the point at which the semivariance stabilises, usually the maximum semivariance value. The range is the distance at which the stabilisation of semivariance takes place.

$$\gamma(d) = \begin{cases} C_o + C_1\left(3d/2a - d^3/(2a^3)\right) & d \leq a \\ C_o + C_1 & d > a \end{cases} \tag{B.3}$$

Once the model is fit, it allows for the semivariance to be predicted at any arbitrary lag distance. This can be turned into covariance with respect to lag by using

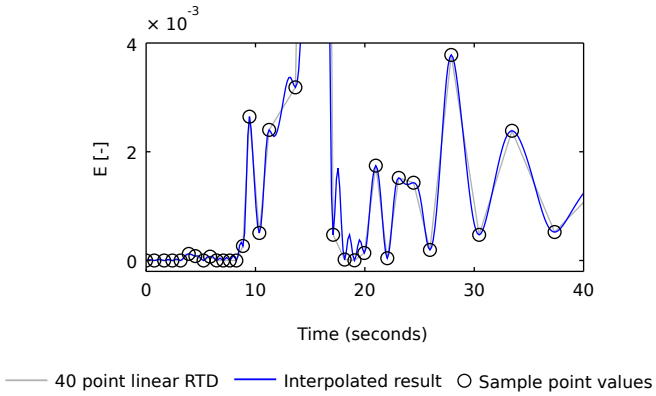

Figure B.1: IDW interpolation applied to Figure 6.1, predictive $R^2 = 0.9611$, $k = 40$, $a = 2$

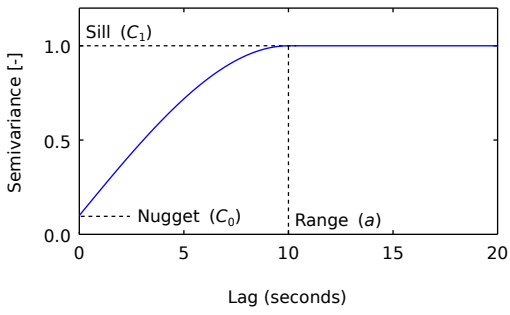

Figure B.2: Example spherical semivariogram model, labelled with model components

the sill minus the semivariance ($C_1 - \gamma$). Covariance beyond the range is 0. The covariance is used to determine the weighting factors λ through Equation B.4, where $\mathbf{K}$ is a NxN matrix of semivariance values for the lag distances between sample points and $\mathbf{k}$ is a Nx1 matrix of semivariance values for the lag distances between the point being interpolated and the sample points. The weighting values are then used in Equation B.5 to calculate the final interpolated value, similar to IDW.

$$\mathbf{K}\lambda = \mathbf{k} \tag{B.4}$$

$$z_j = \sum_{i=1}^{N} \lambda_i z_i \tag{B.5}$$

As the first step to applying KEM interpolation to the RTD from Figure 6.1 for evaluation, a semivariogram must be generated. The expected shape of the semivariogram normally increases with lag then levels off, indicating a decreasing relationship between sample point values with sample point separation. Figure B.3 shows the semivariogram for the sample points underlying Figure 6.1. It demonstrates a "hole effect" where semivariance rises then lowers, which is typically associated with periodic data (Pyrcz & Deutsch, 2003). In this scenario, the semivariogram indicates that points further apart are more similar than points closer together, which is unrealistic.

There are two potential courses of action when the hole effect makes it difficult

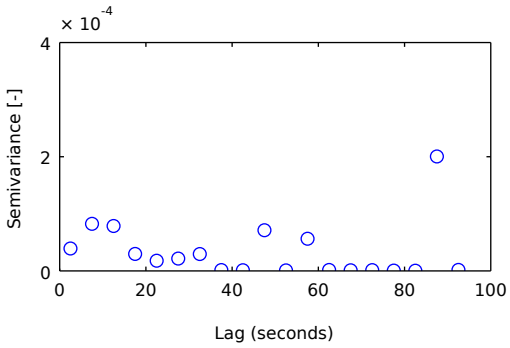

Figure B.3: RTD semivariogram for Figure 6.1 using 5 second bins

to fit a semivariogram model. The semivariogram could be considered to be cut at the peak of the hole, i.e. fixing the range and fitting a simple model until that point only. Alternatively, additional post-processing could be used to compensate for the low semivariance values obtained through some sort of averaging. The general complexity of KEM makes KEM interpolation unsuitable for an automatic process like maximum entropy deconvolution.

Appendix C

Large normalised CRTD plots for Chapter 8

This appendix contains larger and more detailed deconvolved CRTD plots corresponding to those presented in Chapter 8 (Figures 8.11 to 8.18). They show mean, normalised CRTDs for each surcharge depth at each outlet angle and flow rate.

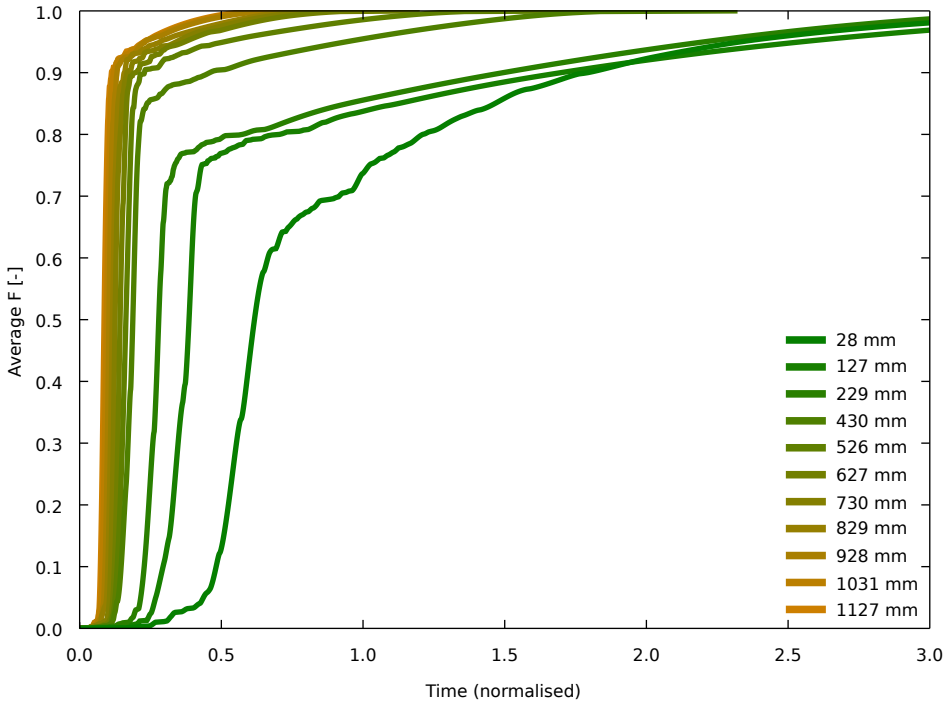

Figure C.1: 0° unbenched, 1 l/s

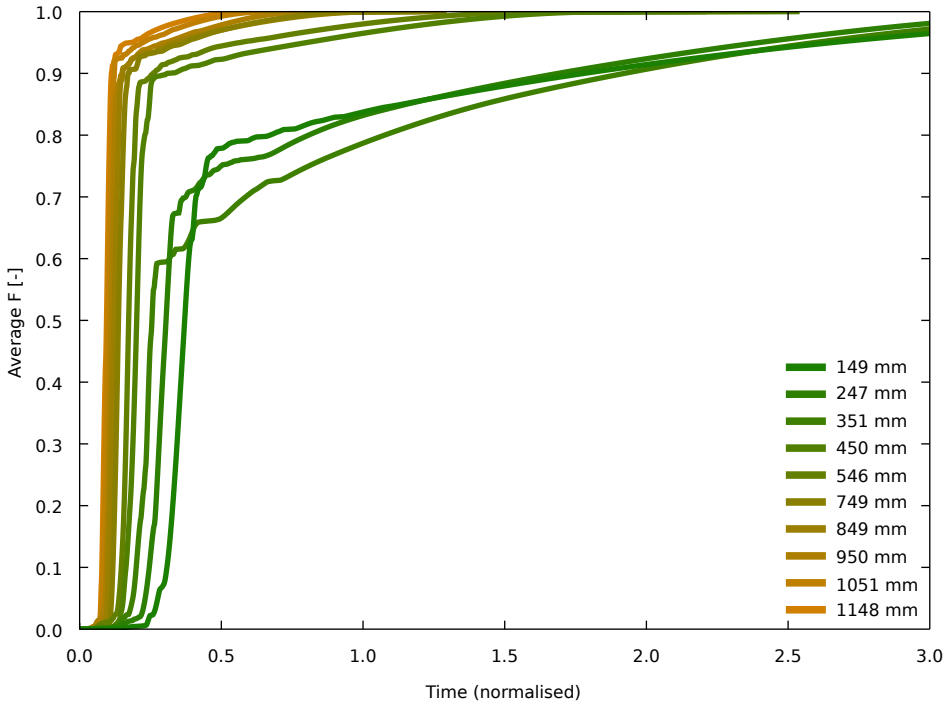

Figure C.2: 0° unbenched, 3 l/s

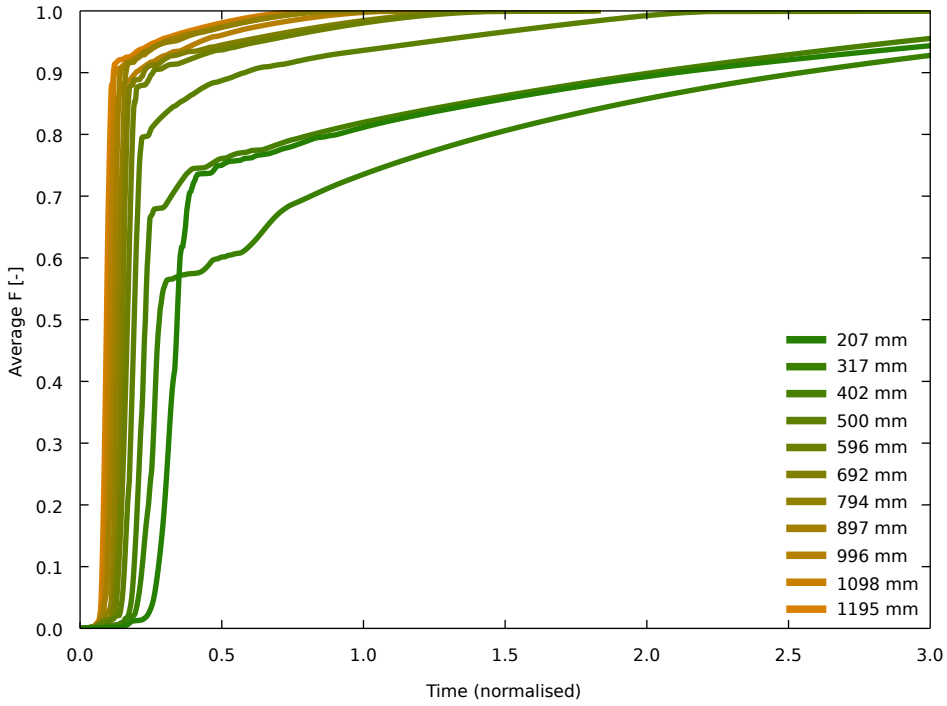

Figure C.3: 0° unbenched, 6 l/s

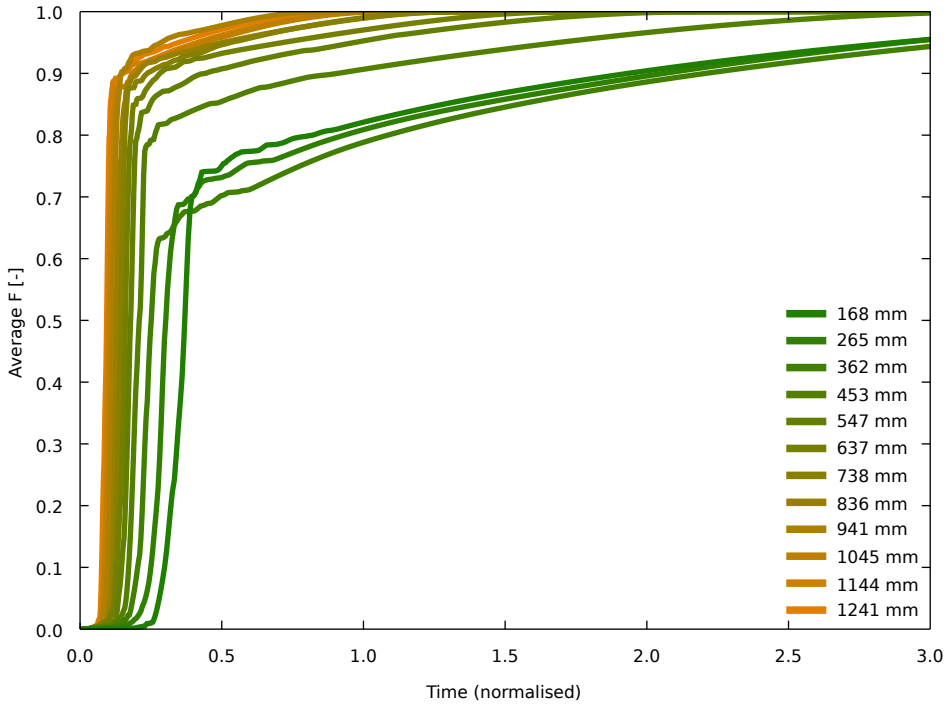

Figure C.4: 0° unbenched, 8 l/s

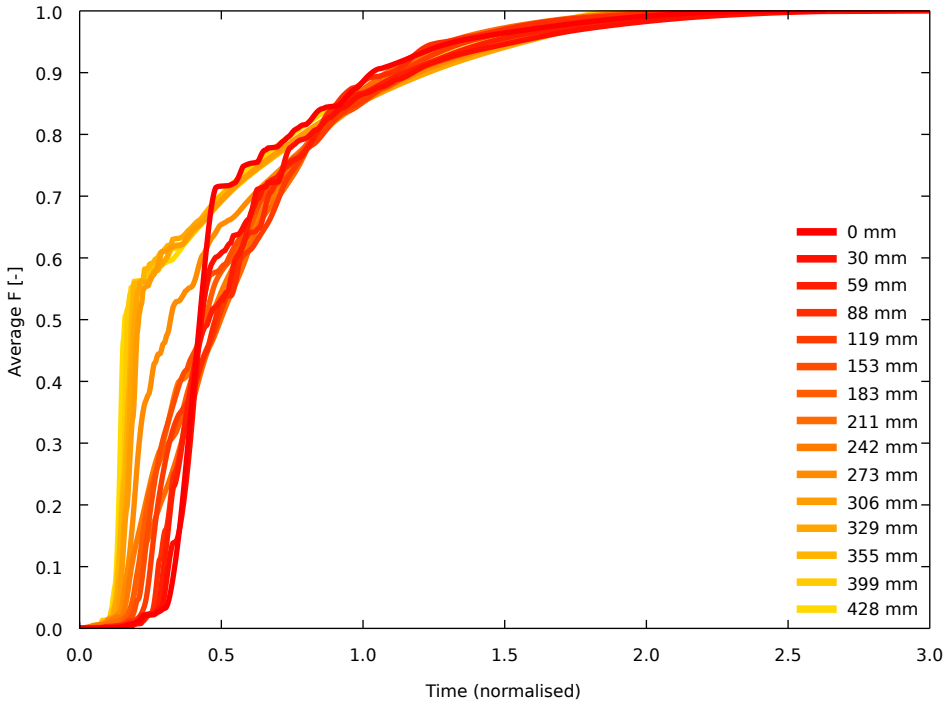

Figure C.5: 30° unbenched, 1 l/s

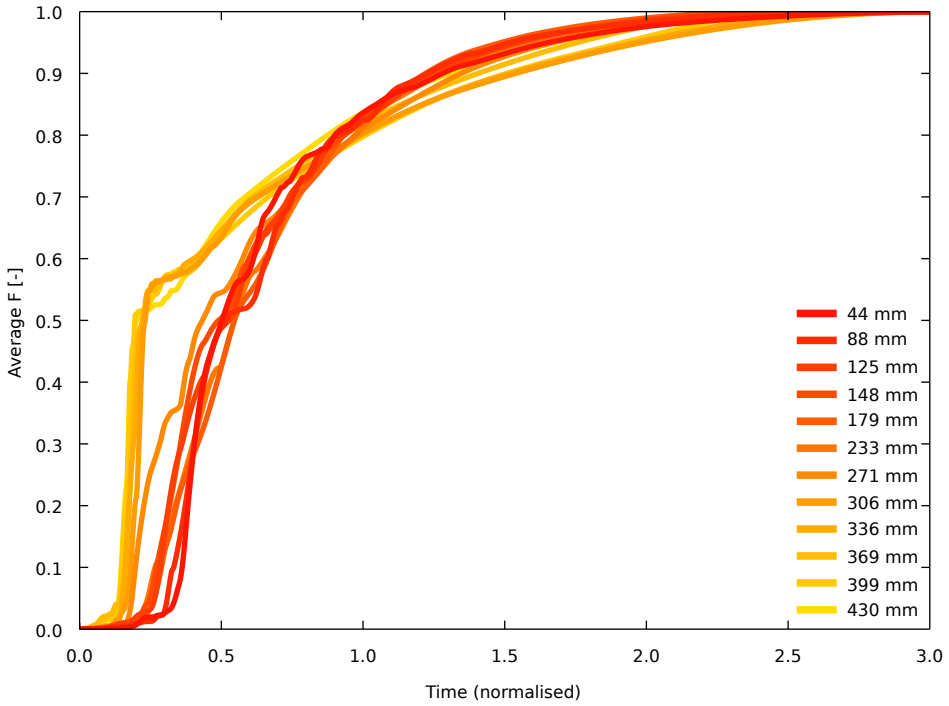

Figure C.6: 30° unbenched, 2 l/s

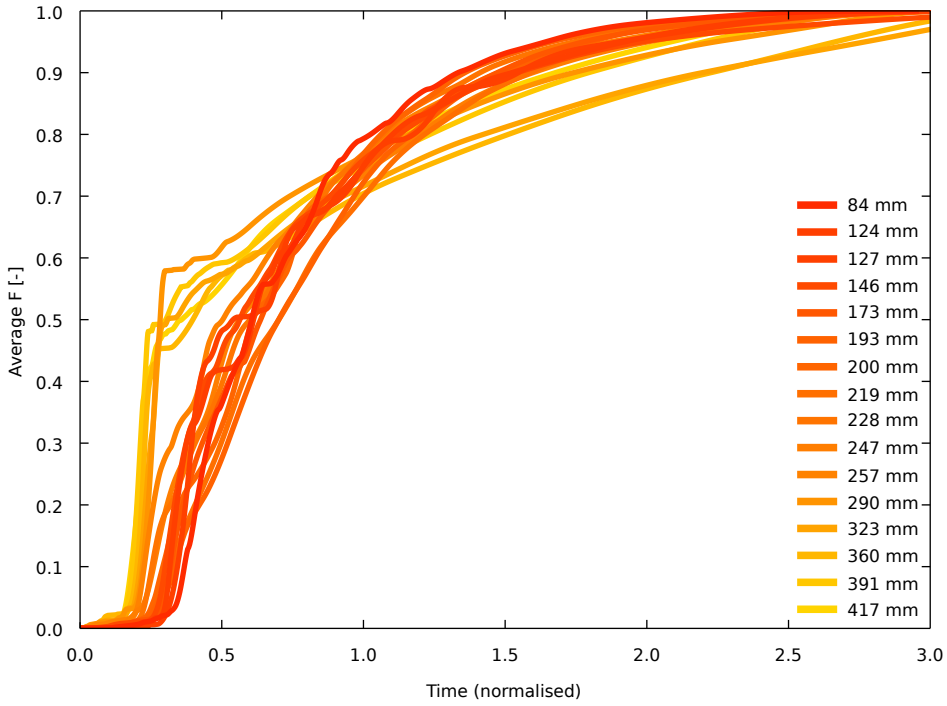

Figure C.7: 30° unbenched, 4 l/s

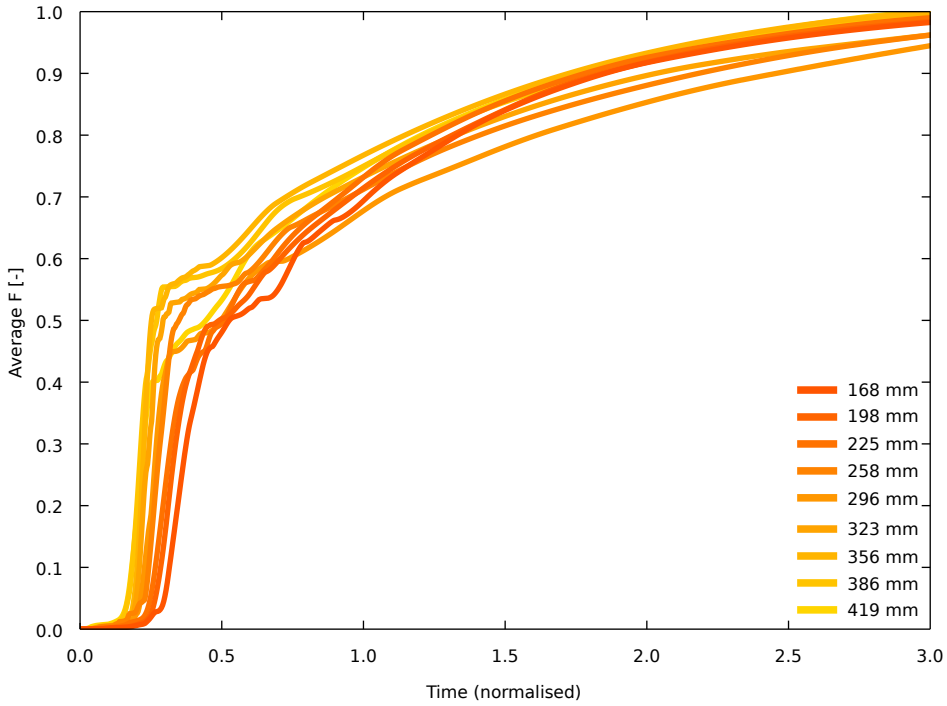

Figure C.8: 30° unbenched, 6 l/s

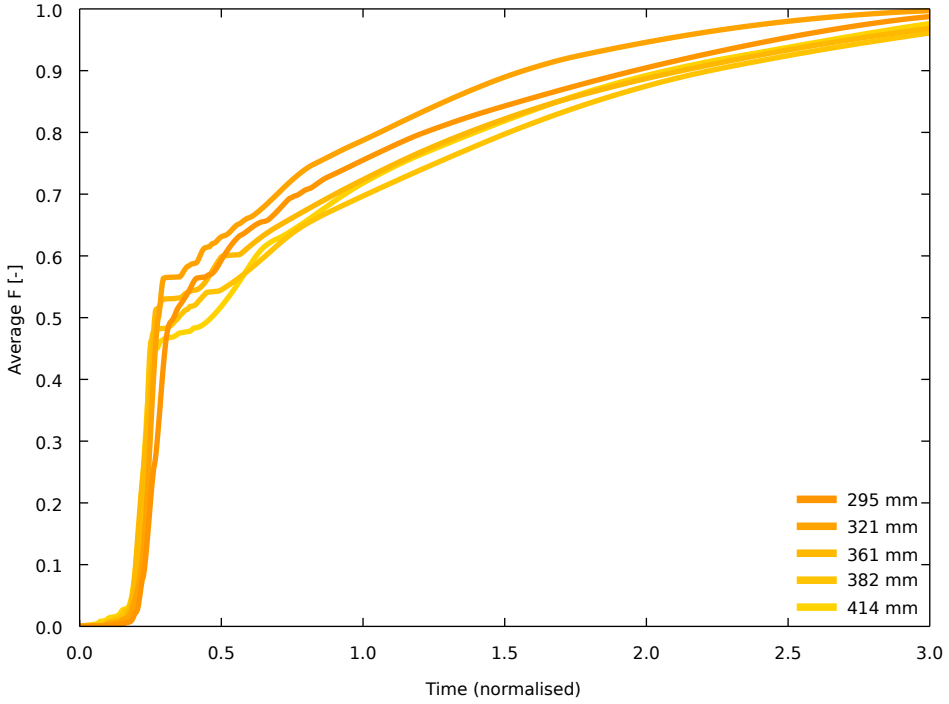

Figure C.9: 30° unbenched, 8 l/s

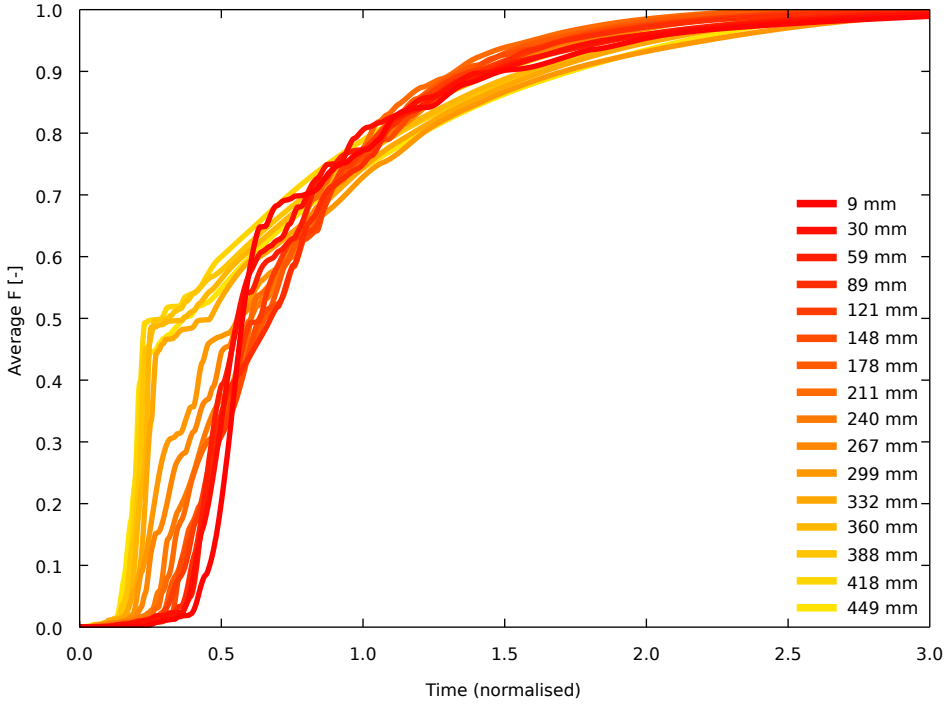

Figure C.10: 60° unbenched, 1 l/s

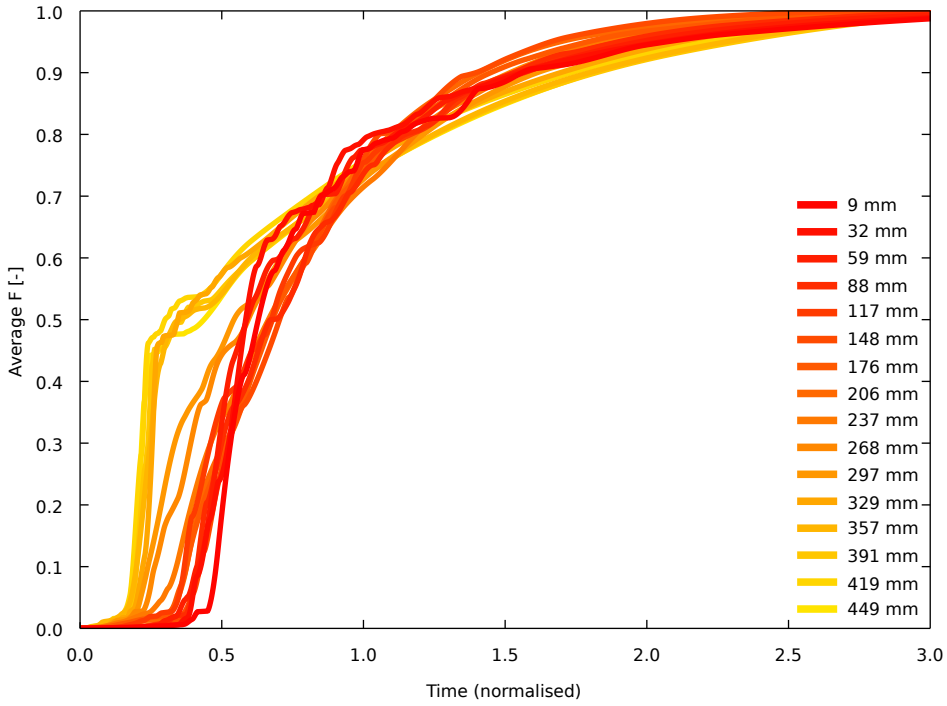

Figure C.11: 60° unbenched, 2 l/s

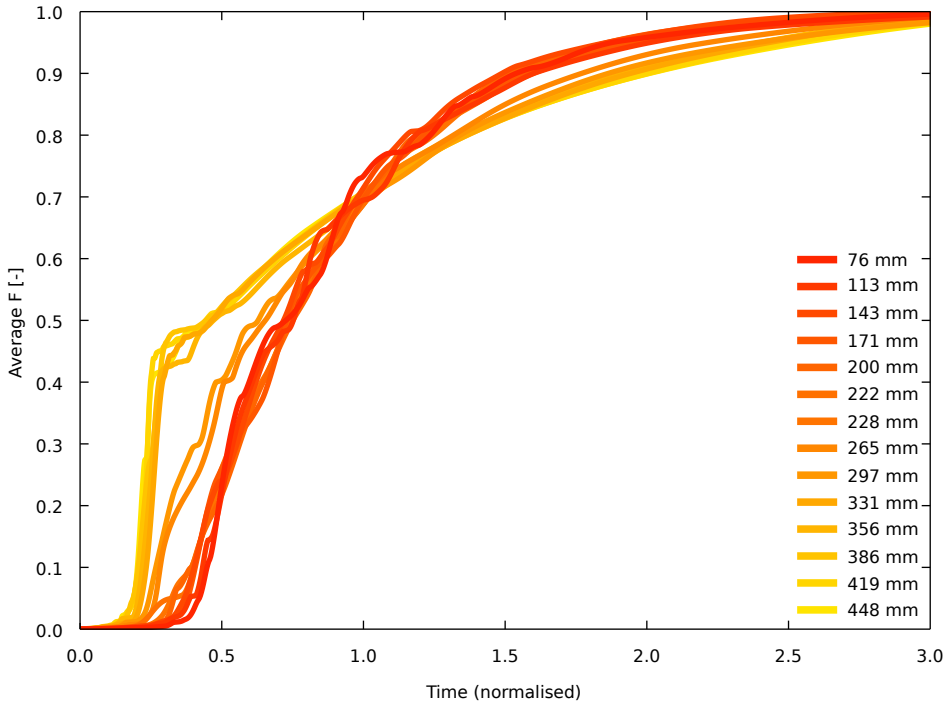

Figure C.12: 60° unbenched, 4 l/s

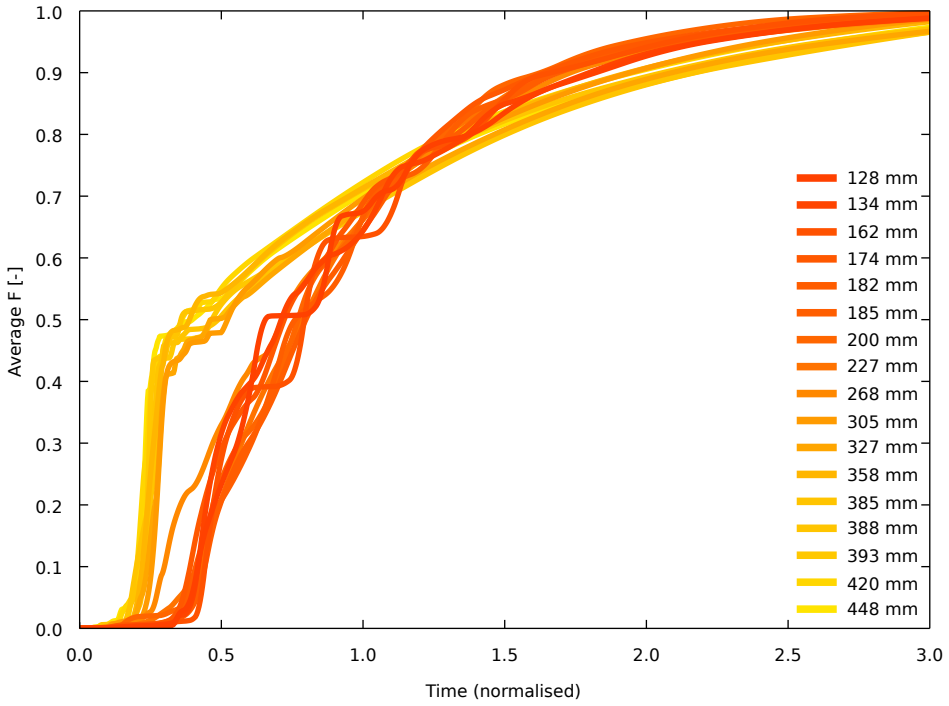

Figure C.13: 60° unbenched, 6 l/s

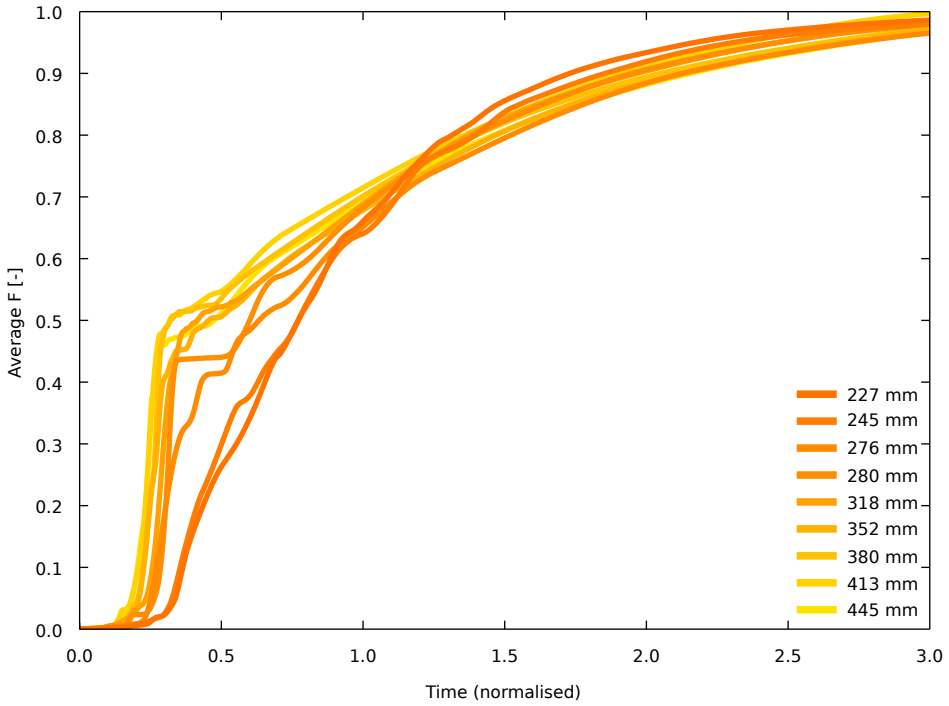

Figure C.14: 60° unbenched, 8 l/s

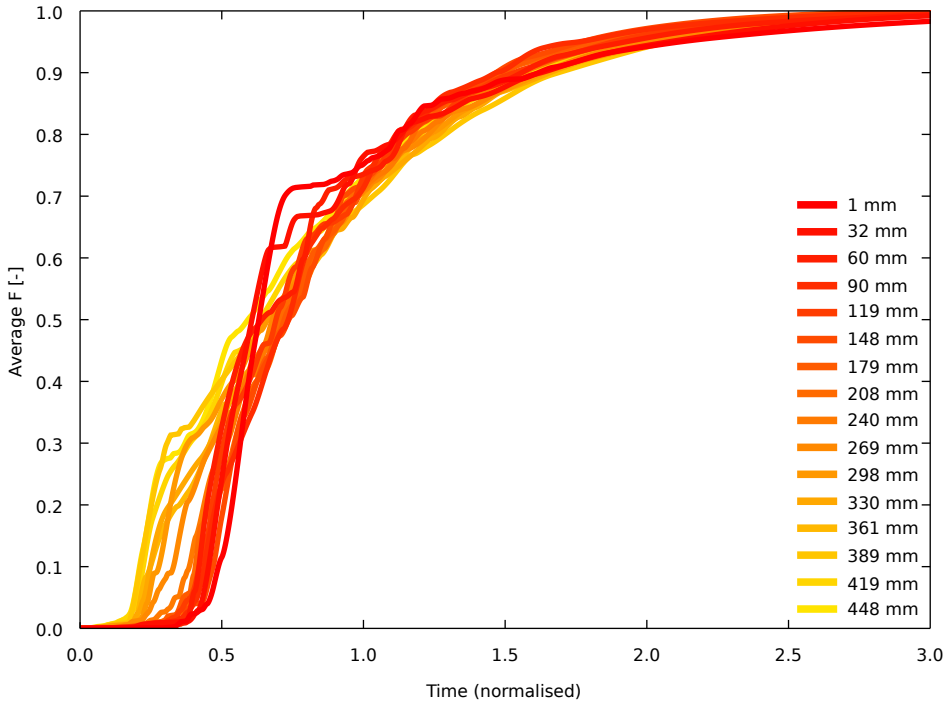

Figure C.15: 90° unbenched, 1 l/s

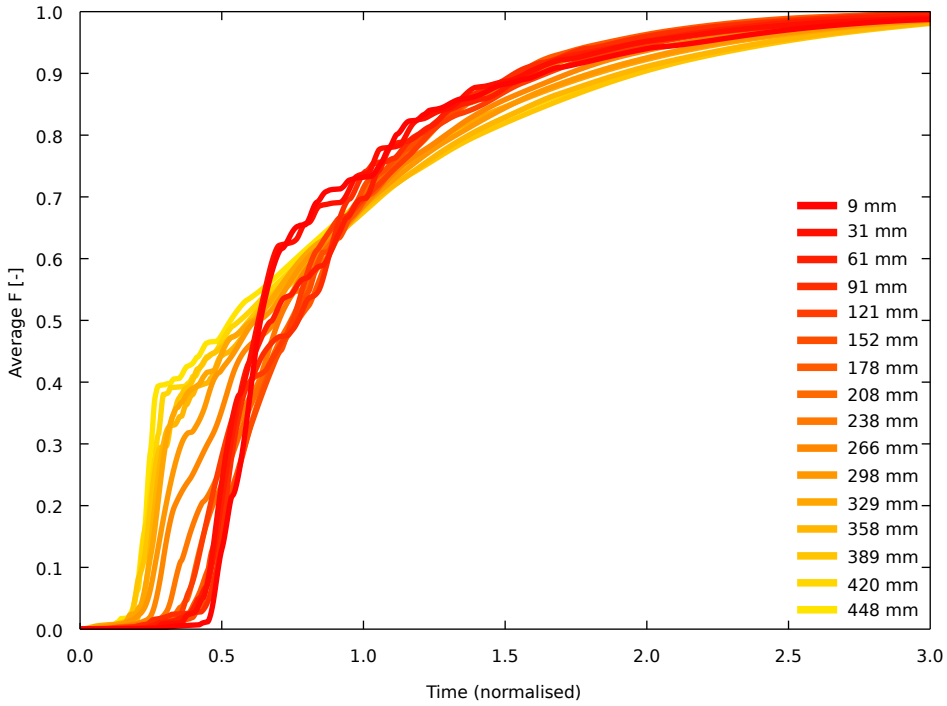

Figure C.16: 90° unbenched, 2 l/s

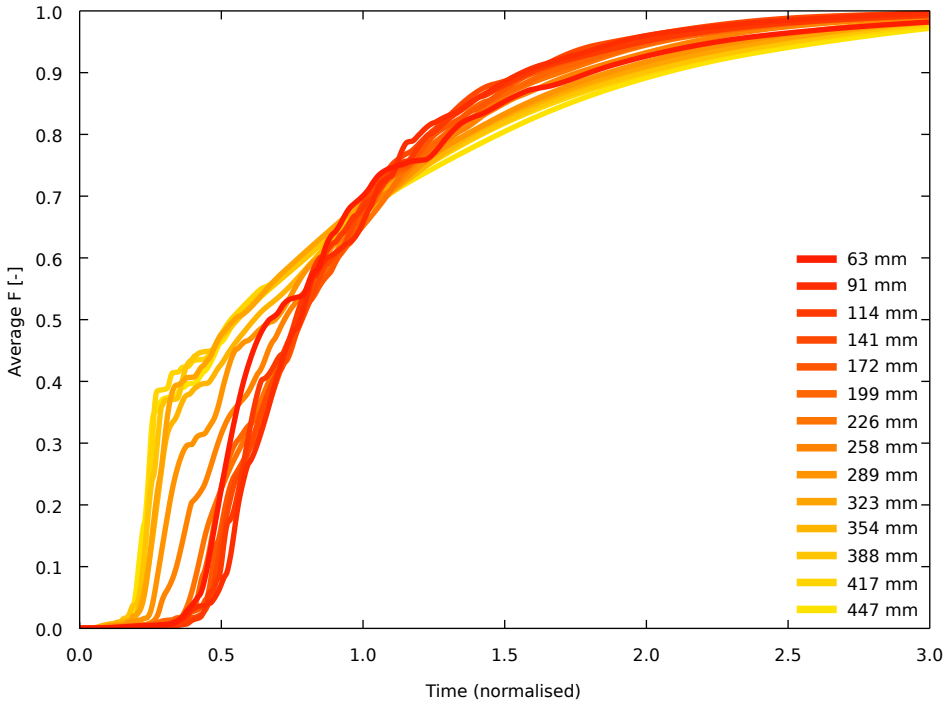

Figure C.17: 90° unbenched, 4 l/s

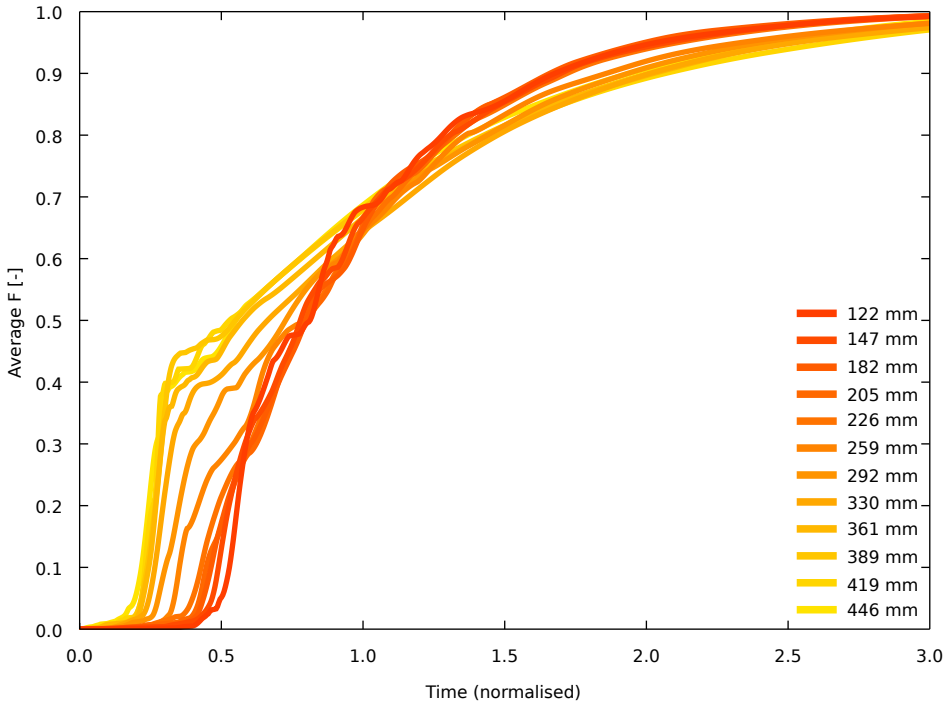

Figure C.18: 90° unbenched, 6 l/s

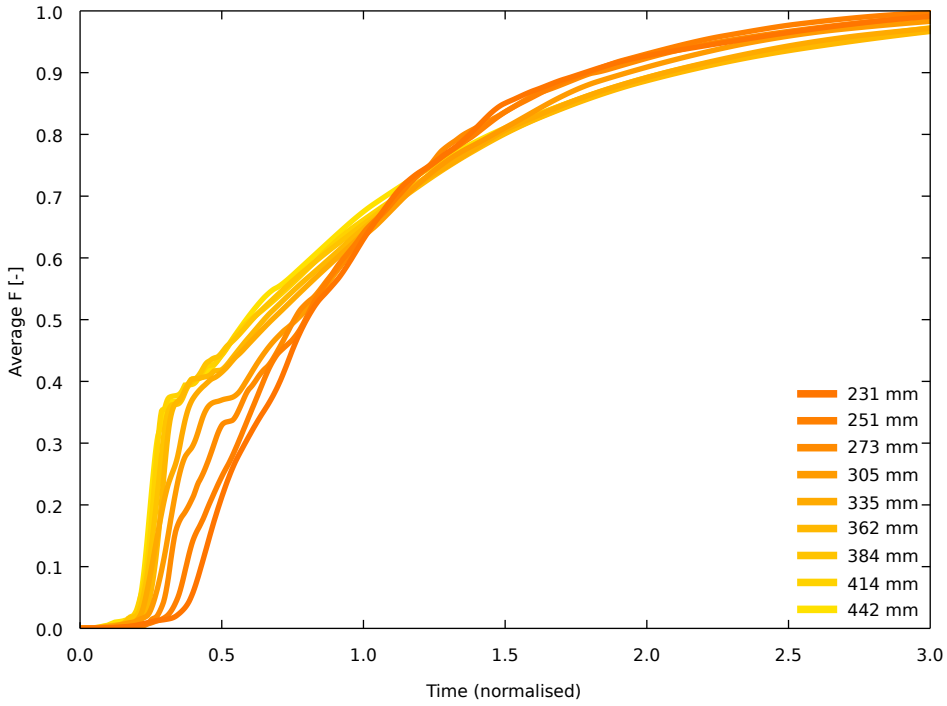

Figure C.19: 90° unbenched, 8 l/s

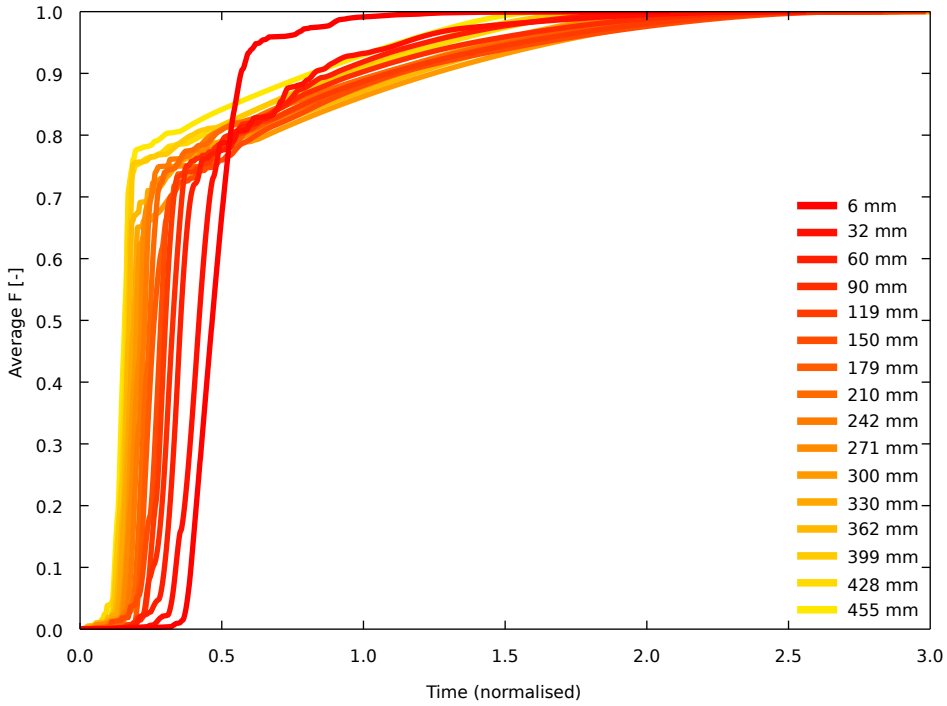

Figure C.20: 30° benched, 1 l/s

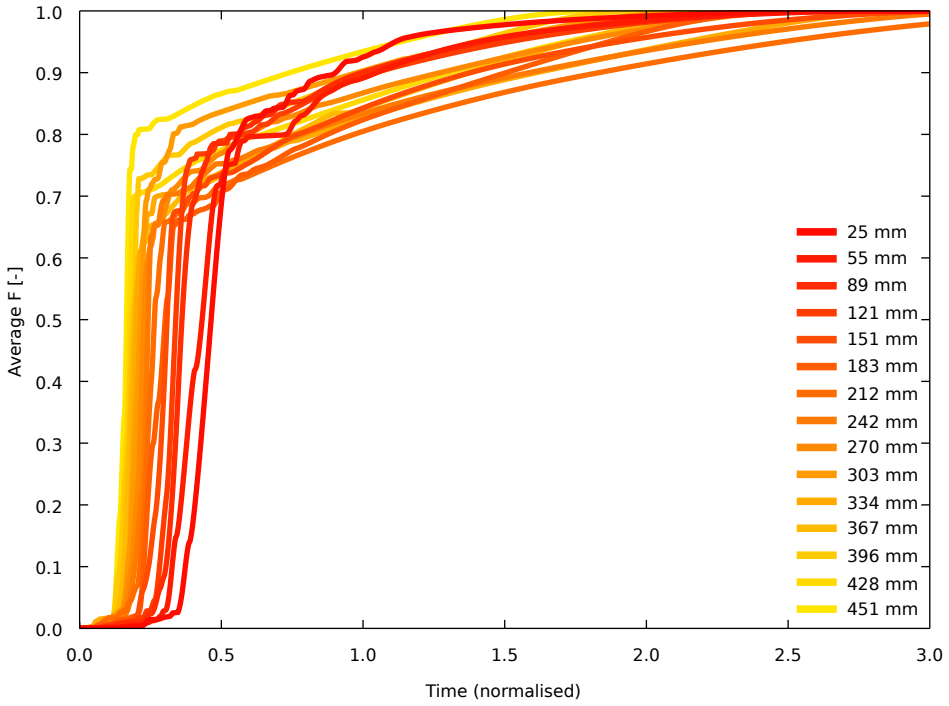

Figure C.21: 30° benched, 2 l/s

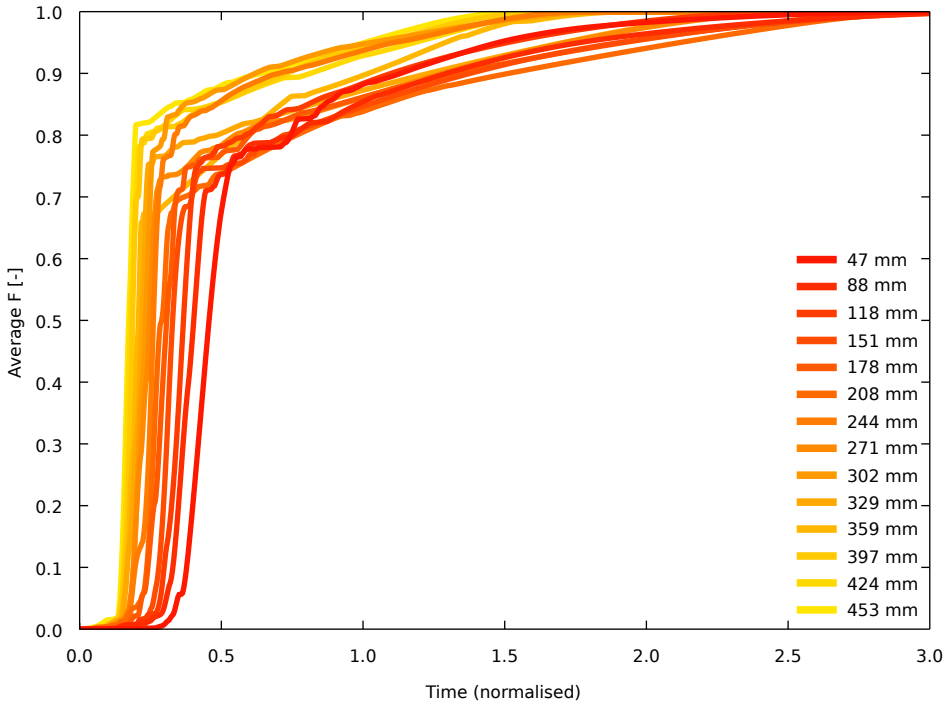

Figure C.22: 30° benched, 4 l/s

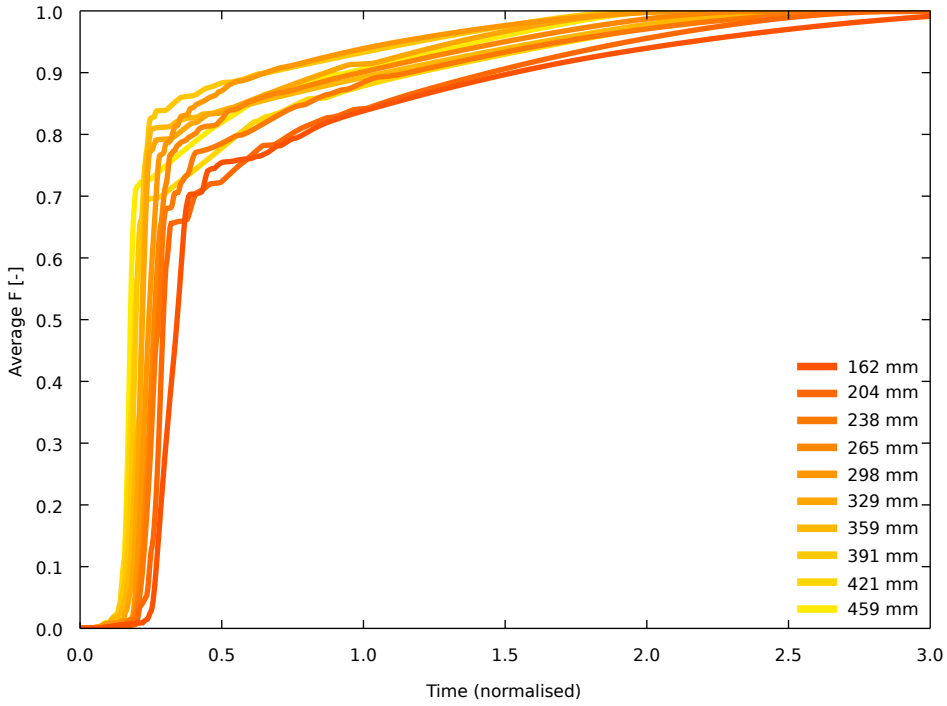

Figure C.23: 30° benched, 6 l/s

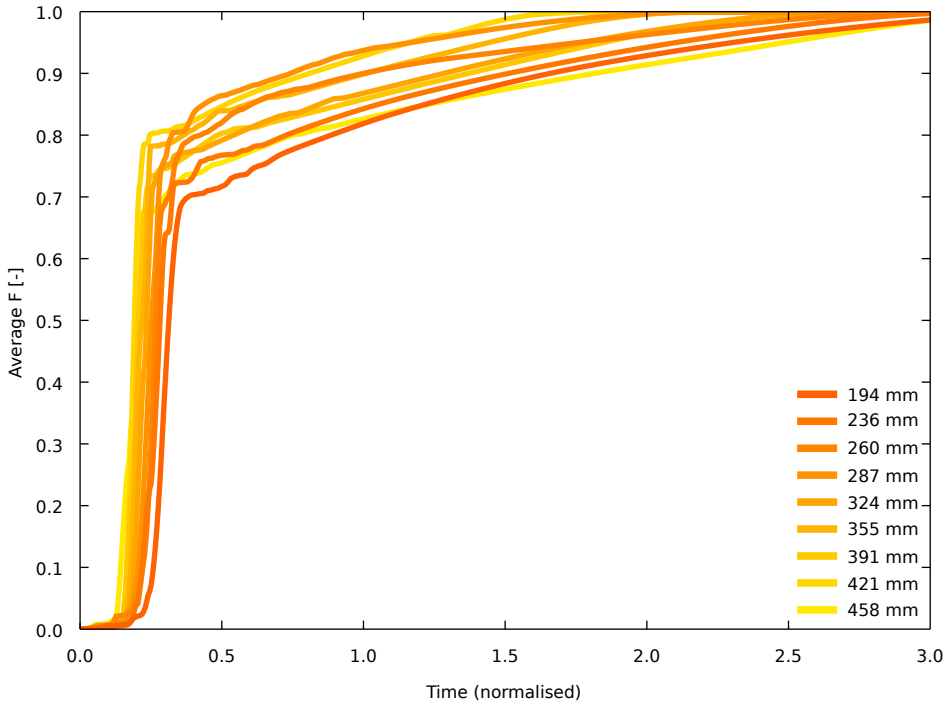

Figure C.24: 30° benched, 8 l/s

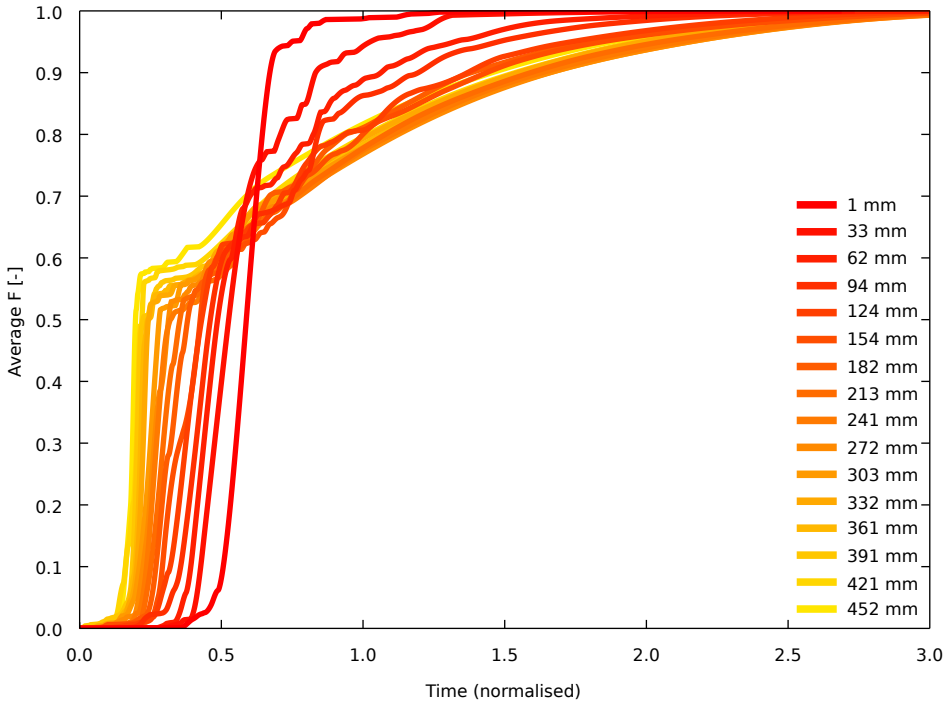

Figure C.25: 60° benched, 1 l/s

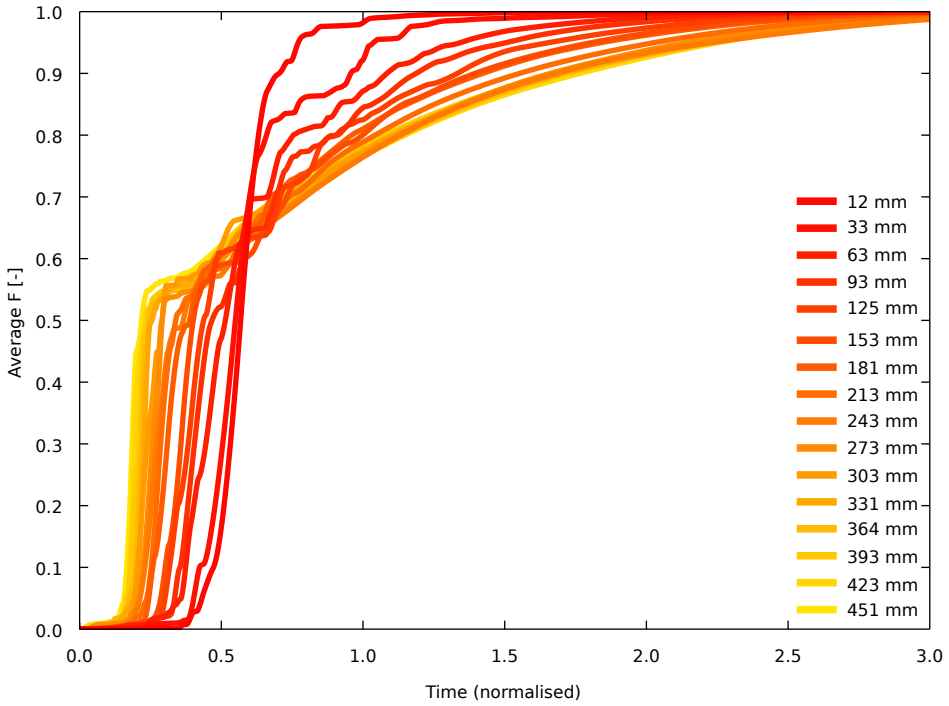

Figure C.26: 60° benched, 2 l/s

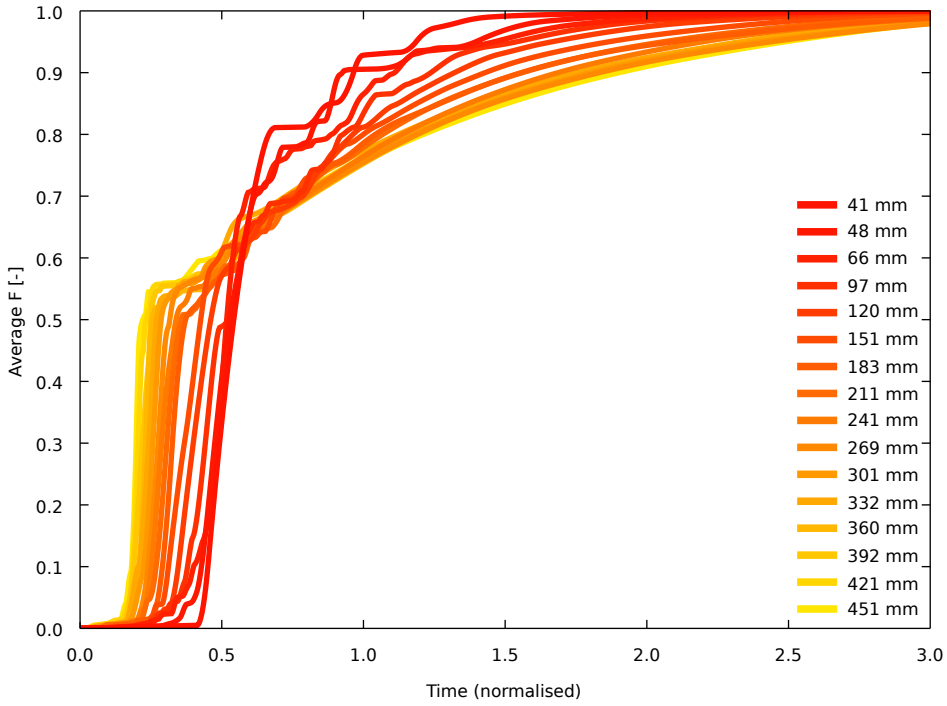

Figure C.27: 60° benched, 4 l/s

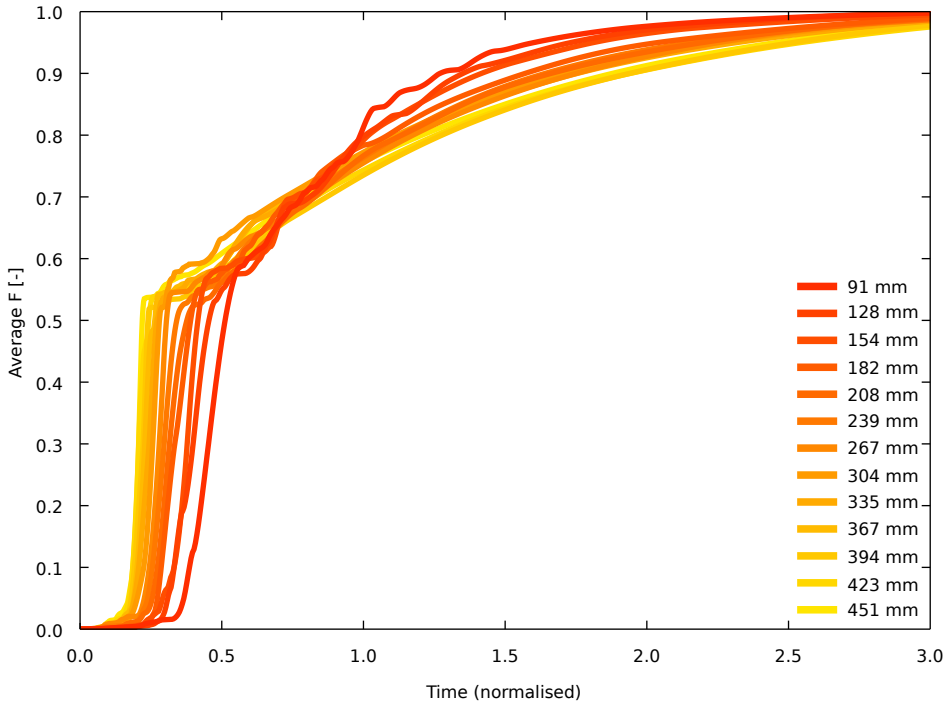

Figure C.28: 60° benched, 6 l/s

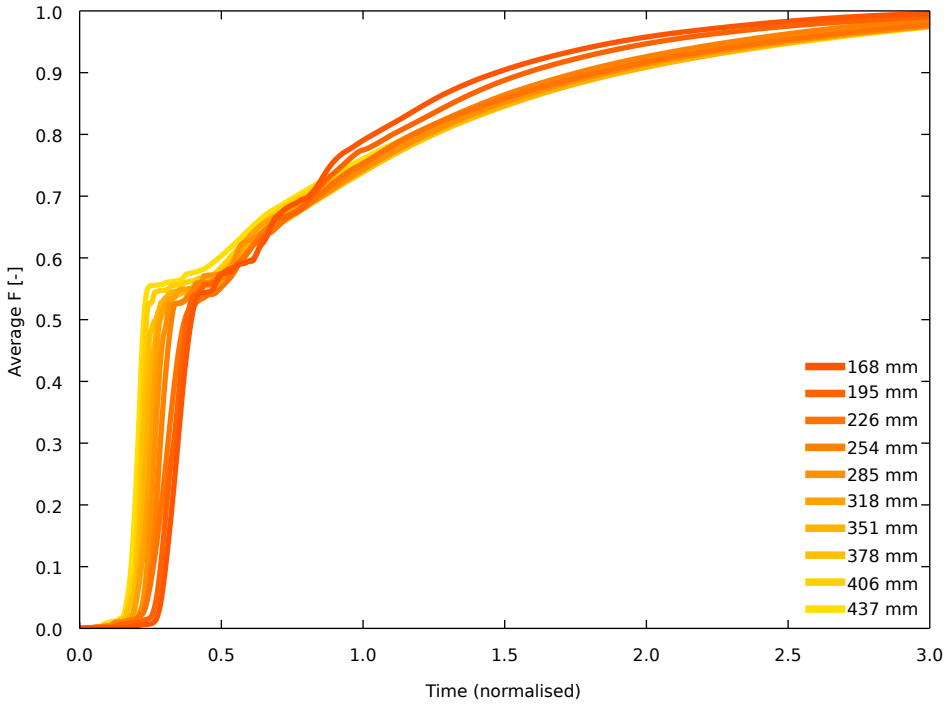

Figure C.29: 60° benched, 8 l/s

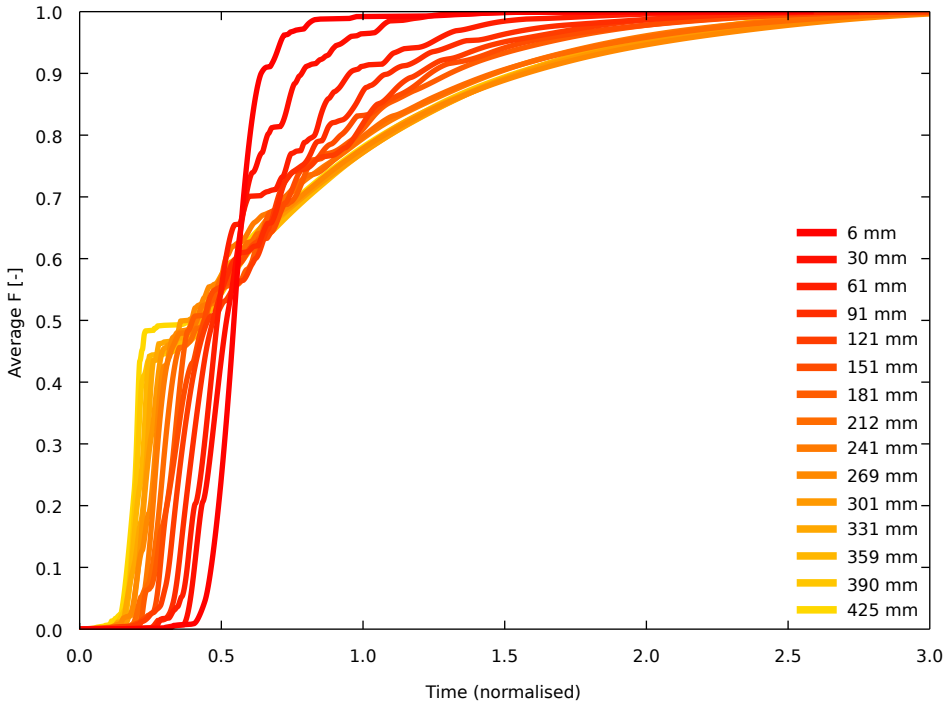

Figure C.30: 90° benched, 1 l/s

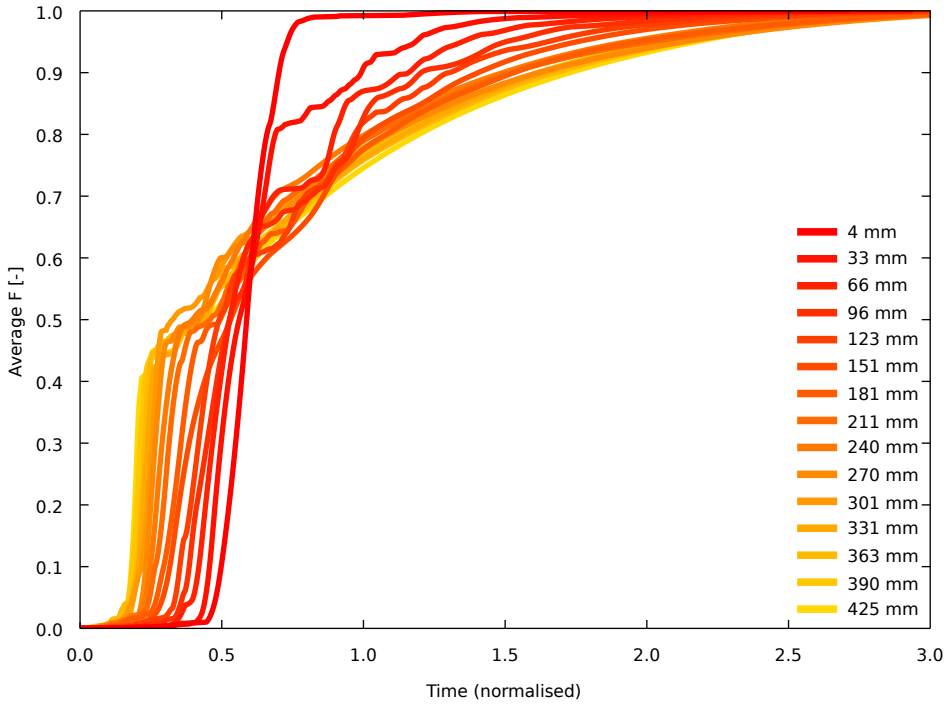

Figure C.31: 90° benched, 2 l/s

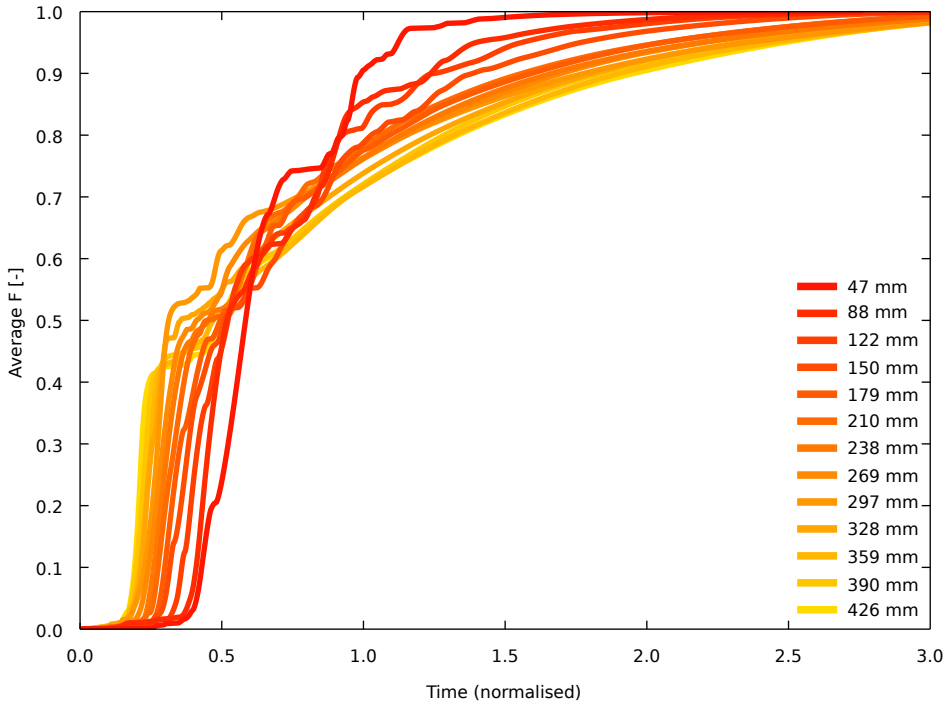

Figure C.32: 90° benched, 4 l/s

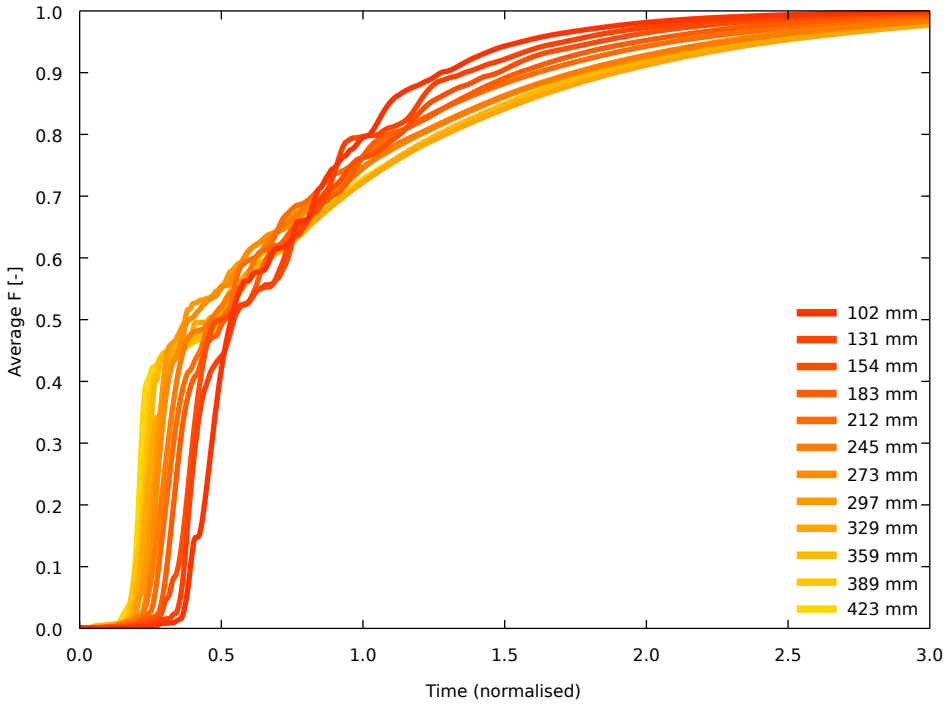

Figure C.33: 90° benched, 6 l/s

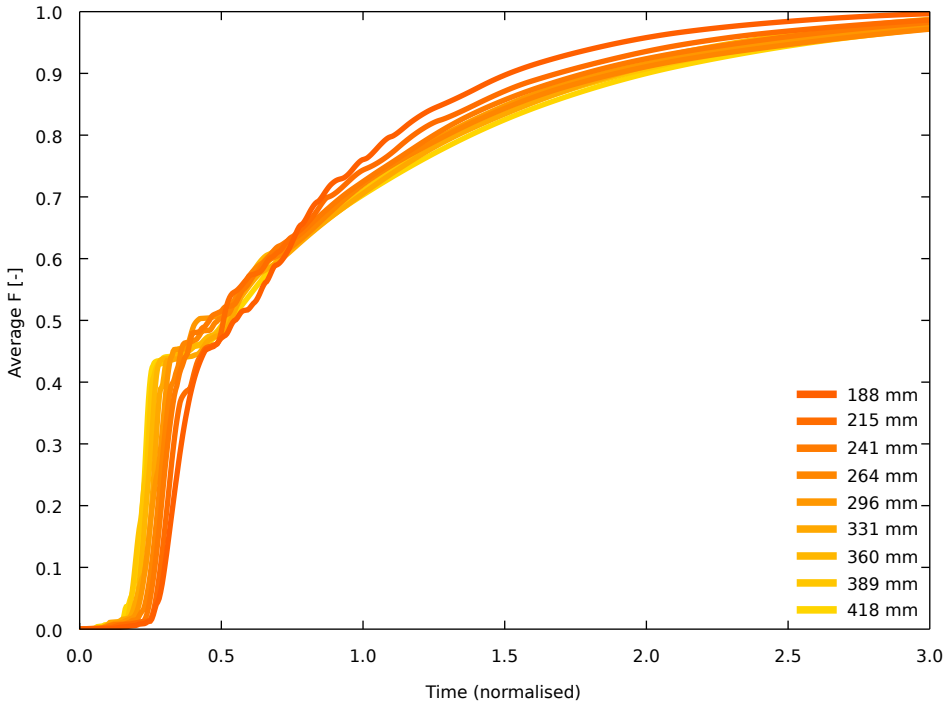

Figure C.34: 90° benched, 8 l/s